Spherical carbons as model supports for Fe, Co and Fe-Co Fischer-Tropsch catalysts

Mbongiseni William Dlamini

A thesis submitted to the Faculty of Science, University of the Witwatersrand, Johannesburg, in fulfilment of requirements for the Degree of Doctor of Philosophy.

DECLARATION

I hereby declare that the work reported in this thesis is my own unaided work.

It is being submitted to the Faculty of Science

University of the Witwatersrand, Johannesburg,

in fulfilment of requirements for the

Degree of Doctor of Philosophy.

_____	31 / 10 / 2016
Candidate	Date
(Mbongiseni W. Dlamini - 325971)	
_____	31 / 10 / 2016
Supervisor	Date
(Neil J. Coville)	

ABSTRACT

The production of liquid transportation fuels and chemicals by the Fischer-Tropsch (FT) synthesis continues to garner attention due to its economic and environmental benefits. This interest is also compounded by the flexibility to use readily available materials as feedstocks for synthesis gas production, with coal, natural gas, biomass and recently shale gas being used. Although this process is over 90 years old, challenges still remain. In this study, we have attempted to understand several FT synthesis challenges by exploring the use of carbon spheres as a model support for Co, Fe and Fe-Co FT catalysts. Thus the synthesis, characterization and application of carbon spheres with distinct architectures are described.

The synthesis of solid carbon spheres using a sucrose precursor yielded materials that were mono-dispersed (600 nm) and adopted a necklace-like accreted conformation. Upon further investigation, it was demonstrated that annealing is useful for tuning the properties of the as-prepared materials to have high surface areas (> 500 m^2/g), good thermal stability (>660 °C) and a mesoporous (> 2 nm) pore structure. Deposition of a Fe-Co bimetallic catalyst yielded oxides of the monometallic species with relatively small crystallites, with sizes in the range 7.9 – 14.4 nm. Reduction of the bimetallic samples was monitored by using in situ PXRD and TPR techniques, which revealed that a Co-Fe type-alloy is one of the phases formed on Co-rich samples at T > 450 °C. Interestingly, high relative abundances of this alloy did not correlate with high C_{5+} selectivities in Fischer-Tropsch synthesis; instead Co-rich/Fe-poor catalysts gave the best selectivity.

The effect of the support morphology in heterogeneous catalysis was investigated by using high surface area solid and hollow carbon spheres (>560 m^2/g) prepared from a resorcinol-formaldehyde precursor as support material. Loading the Co and Fe precursors on these two supports was shown by TEM and PXRD to result in smaller and well dispersed metal particles on the hollow support material. This corresponded with high activities and C_{5+} selectivities for the Co and Fe catalysts supported on the hollow carbon spheres. TEM studies revealed that the Co and Fe particles tended to sinter significantly when dispersed on a material with a solid architecture.

Post-synthesis N-doping using a melamine precursor was shown by XPS to incorporate high quantities of nitrogen (up to 13%) on to the surface of the 30 nm thick shells of the hollow carbon spheres. On further investigation, N-doping by this method was shown to have minimal effects on the thermal stability and crystallinity of the materials. The N-doped HCSs were shown to be good anchors of Co particles as displayed by the good dispersion, activity and minimal sintering tendency of catalysts supported on N-doped HCSs.

Studies conducted herein have demonstrated the versatility of carbon spheres as a model support, and how their properties can be tailored to suit the desired specifications by simply adjusting the synthesis parameters. We have also highlighted how the chemical inertness of these materials allows for studies on metal-metal interactions at elevated temperatures for bimetallic catalyst systems. The monodisperse, morphology-tunable aspects of carbon spheres were particularly useful in modelling the effect of the support morphology in Fischer-Tropsch synthesis. It is believed that the versatility of CSs demonstrated in this study can also be exploited in other heterogeneous catalytic systems.

Dedicated to my family – emaLangeni.

"We do not need magic to change the world,

we carry all the power we need inside ourselves already:

we have the power to imagine better"

J. K. Rowling

ACKNOWLEDGEMENTS

The success of this thesis was deeply dependant on the generosity of others. The following individuals and organizations are graciously acknowledged for their contributions:

I am grateful to my supervisor Professor Neil J. Coville for sharing his immense knowledge in chemistry, and for his friendly supervision, contagious enthusiasm, guidance and never-ending support.

My co-supervisors; Professor Linda L. Jewell and Professor Dave G. Billing for their constructive criticism, kindness and encouragement.

The DST-NRF Centre of Excellence in Catalysis (c*change) and the University of the Witwatersrand are acknowledged for funding. I am grateful to Professor Michael Claeys, Professor Eric van Steen and Professor J. W. Niemantsverdriet for their advice and suggestions during c*change programme meetings.

The CATOMAT Research group members for fruitful discussions and constructive criticism during seminars and practice talks. It was a great experience and pleasure being part of the research group. Professor Nosipho Moloto, Professor Shane Durbach, Dr. Paul Franklyn and the departed Dr. Tsenolo Lerotholi are graciously appreciated for their guidance within the research group. A special thank you to Ms Colleen Coutts and the late Ms Agnes Pointeer for handling my administrative issues so well through the years.

Mr Basil Chassoulas for making sure that my FT reactor was always in a good working condition, and for sharing his vast knowledge in catalysis. And most importantly for always reminding me not to worry, but to be happy.

Microscopists Professor Alexander Ziegler, Dr. Zikhona Tetana, Dr. Manoko Maubane, Dr. Deran Reddy, Mrs. Tutuzwa Xuma and Mr. Jacques Gerber for assistance with microscopy analysis. Dr. Rudolph Erasmus is acknowledged for help with Raman spectroscopy data measurements.

Service engineers Leon De Jager, Charles Noakes and Gideon for assistance with our Micromeritics instruments (BET, TPR, Chemisorption).

My colleagues for the never-ending discussions; Farai Dziike, David Kumi, Wilson Mogodi, Lerato Hlekelele, Tumelo Phaahlamohlaka, Neo Phao, Isaac Beas, George Bepete, Ofentse Makgae, Ahmed Shaikjee, Thobeka Kente, Themba Tshabalala and Shahil Ramalall.

I also wish to thank Pastor Nkonzo Hlatjayo, Apostle Robert Kasaro and the entire Jesus Calls Worship Centre (JCWC) church for their prayers and spiritual support.

Finally, I would like to express deep gratitude to my family for all the sacrifices they have made to allow me to undertake both undergraduate and postgraduate studies. I am particularly grateful to my parents Evah Dzeliwe and the late Morris Mehlwengane Dlamini for always believing in me. My brothers, sisters and extended family are also acknowledged. I am indebted to Swazi S. Mngomezulu and my son Jay for their love, support and encouragement through the years.

List of Publications

The following is a list of publications resulting from this PhD study:

1]. M.W. Dlamini, D.O. Kumi, T.N. Phaahlamohlaka, A. Lyadov, D.G. Billing, L.L. Jewell, N.J. Coville, Carbon spheres prepared by hydrothermal synthesis – a support for bimetallic Fe Co Fischer-Tropsch catalysts, *ChemCatChem*, **2015**, 7, 3000-3011.

DOI: 10.1002/cctc.201500334

2]. T.N. Phaahlamohlaka, D.O. Kumi, M.W. Dlamini, L.L. Jewell, N.J. Coville, Ruthenium nanoparticles encapsulated inside porous hollow carbon spheres: a novel catalyst for Fischer-Tropsch synthesis, *Catalysis Today*, **2016**, 257, 76-83.

DOI: 10.1016/j.cattod.2015.11.034

3]. D.O. Kumi, M.W. Dlamini, T.N. Phaahlamohlaka, T. Lerotholi, F. Dziike, , S.D. Mhlanga, M.M. Scurrell, N.J. Coville, Selective CO methanation over Ru catalysts supported on different titania rutile morphologies, *Catalysis Science & Technology*, **2016**, (submitted for publication).

4]. M.W. Dlamini, D.O. Kumi, T.N. Phaahlamohlaka, D.G. Billing, L.L. Jewell, N.J. Coville, Post-synthesis nitrogen doping of a hollow carbon sphere support for improved cobalt Fischer-Tropsch synthesis, (In preparation).

5]. M.W. Dlamini, D.O. Kumi, T.N. Phaahlamohlaka, D.G. Billing, L.L. Jewell, N.J. Coville, Effect of the support architecture in heterogeneous catalysis: comparison of solid and hollow carbons as supports for Fischer-Tropsch catalysts, (To be submitted).

Publications from other studies:

1]. W.M. Dlamini, N.J. Coville, M.S. Scurrell, Microwave radiation in the modification of iron Fischer-Tropsch catalysts, *Journal of Molecular Catalysis A: Chemical*, **2015**, 409, 19-25.

DOI: 10.1016/j.molcata.2015.06.014

2]. M.W. Dlamini, N.J. Coville, M.S. Scurrell, Microwave treatment: a facile method for the solid state modification of potassium-promoted iron on silica Fischer-Tropsch catalysts, *RSC Advances*, **2016**, 6, 22222 – 22231.

DOI: 10.1039/c5ra26628a

List of Awards

The following is a list of awards received during the course of my PhD studies:

2016 Received the South African Chemical Institute (SACI) Postgraduate award, University of the Witwatersrand. This award is bestowed to persons considered as being "young innovative, independent and enterprising chemists", and is limited to one recipient per institution.

2016 Best poster presentation award, Wits Cross-Faculty, Wits Postgraduate Symposium

2016 Best poster presentation award, Faculty of Science, Wits Postgraduate Symposium

2015 Best oral PhD presentation award, SACI-RSC Young Chemist Symposium (Gauteng, SA)

2015 2nd Best oral PhD presentation award, Nanoscience Young Researchers Symposium, SA

2013 - 2015 Postgraduate merit award, University of the Witwatersrand, SA

2014 Best poster presentation award, Southern African Powder Diffraction Conference

2014 2nd Best poster presentation award, Faculty of Science, Wits Postgraduate Symposium

2013 Best oral PhD presentation award, Nanoscience Young Researchers Symposium

2012 Best poster presentation award, Catalysis Society of South Africa Conference, SA.

Other:

2010 Best oral MSc presentation award, Nanoscience Young Researchers Symposium

Table of Contents

Scope of the study - Overview

Crude oil, discovered in 1859 in the United States of America, has been the mainstay source of energy upon which the modern global economy has been built. It was the relatively low price and the perceived long term availability of crude oil that made the world so dependent on oil. However, the high demand for oil over recent years has put a strain on the world's crude oil reserves and has led many to predict that the oil production is peaking throughout the world. Fears of a limited supply of oil coupled with the ever increasing demand driven by rapid expansion in South East Asia and the perceived political unrest in the major oil-producing nations such as Saudi Arabia, Iran, Iraq, Venezuela and Nigeria has resulted in unstable oil prices in the last 10 years. The demand for oil-derived products has created an overwhelming push for alternative sources of fuels. Fischer-Tropsch synthesis (FTS) stands out as the most promising and proven technology that has the potential to revolutionize the fuel industry.

Fischer-Tropsch end products (chemicals and fuels) compete directly with their equivalents produced from crude oil, hence the price of crude oil is an important factor in determining the viability of the Fischer-Tropsch process. Previous estimates on the viability of commercial FT synthesis predicted that the process should be feasible at crude oil prices ~ US$20 per barrel.[1] But this value increases yearly as production and overall plant running costs continue to escalate. The oil price has been well over this value in the past decade. Recently, the oil price has been unstable. For example, the price increased to US$141/bbl in June 2008 due to fears of reduced oil supply, before it plunged to US$ 28.50/bbl in January 2016. At the time of compiling this thesis the cost of oil was US$48/bbl (Fig. 1).[2] Thus, the FT process is an attractive technology for countries with huge reserves for natural gas, shale gas, or coal.

Fischer-Tropsch synthesis provides an alternative and promising route for the production of synthetic lubricants and synthetic fuels from a variety of carbon-containing feed-stocks such as coal, biomass and natural gas. In FTS, syngas, a mixture of CO and H_2, is catalytically converted through a surface polymerisation reaction into a wide spectrum of hydrocarbons. Different transition metals have been found to be active in promoting this hydrogenation of CO, namely ruthenium, cobalt, iron and nickel. Most industrial processes have focused on Co- and Fe-based catalyst. Cobalt based catalysts are preferred for the synthesis of long-chain linear paraffins due to their high activity and selectivity towards C_{5+} hydrocarbons and low activity for the water-gas shift (WGS) reaction. Iron catalysts are generally less expensive

and they are used for the production of gasoline, hydrocarbons and linear alpha-olefins, as well as a mixture of oxygenates, such as alcohols, aldehydes and ketones. Fe catalysts also produce excessive amounts of carbon dioxide due to their high WGS activity. Catalysts which have been studied to a lesser extent in FTS are Fe-Co bimetallic systems. The use of bimetallic catalysts has been shown to influence the observed product distribution and selectivity, instead of simply giving the additive properties of the individual metals.

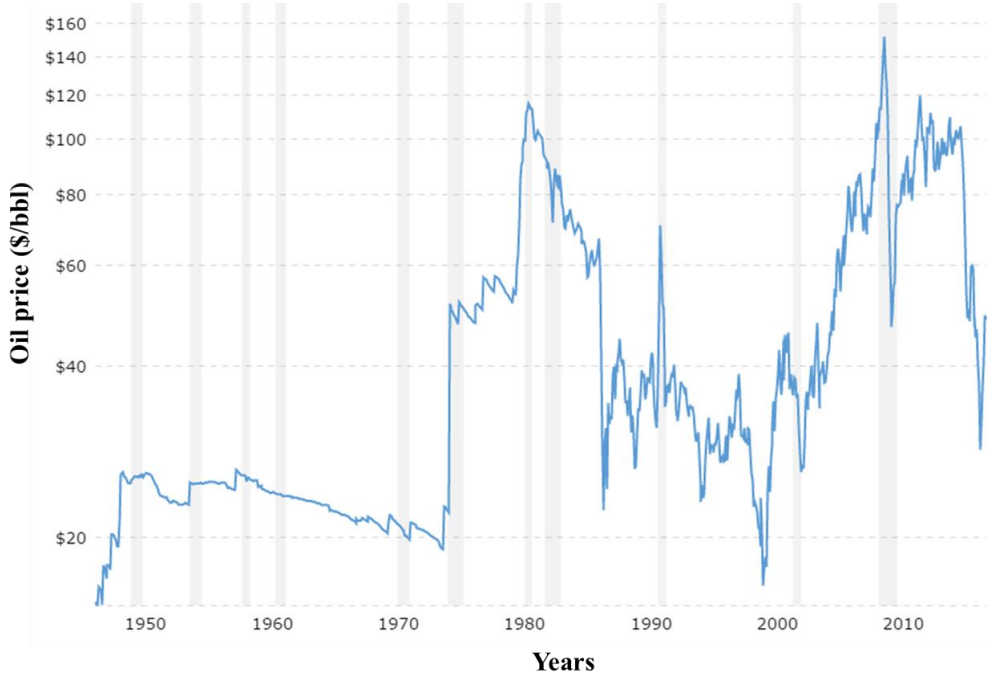

Figure 1 Crude oil prices recorded monthly for the period 1946–2016.[2]

Typically, an FT catalyst is dispersed on a support in order to enhance its catalytic performance. Metal oxides such as Al_2O_3, TiO_2, SiO_2 and MgO have been used as support materials for FT catalysts. However, the challenge with the use of these supports is that they can generate a strong metal-support interaction with the FT catalyst. This can lead to the formation of irreducible mixed compounds which are not active in the reaction, thus resulting in a loss of the expensive catalyst. Carbon-based materials, especially carbon spheres, promise to be an alternative support material for Fischer-Tropsch catalysts.

Thesis outline

The aim of this thesis was to use carbon spheres as a model support material for Co and/or Fe Fischer-Tropsch catalysts. Properties of the synthesized carbon spheres were tuned to make them ideal for application in the Fischer-Tropsch (FT) process. A break-down of the thesis chapters is given below:

Chapter 1 gives a short introduction to the basic concepts related to Fischer-Tropsch synthesis. Effects associated with the reactor design, active phase composition and the type of support material used have been highlighted. Finally, an overview on the use of carbon spheres (CSs) as a support for FT catalysts has been summarized.

Chapter 2 focuses on the different CS morphologies that are possible. Their synthesis by various approaches and their subsequent application in heterogeneous catalytic reactions has been reviewed.

Chapter 3 gives an overview of the experimental procedures involved in the synthesis of the various carbon spheres, the preparation and characterization details of the support materials and catalysts used in this study. Finally, the conditions at which catalytic evaluations were done have been given.

Chapter 4 demonstrates how the properties of solid hydrothermal carbon spheres can be tuned by a thermal treatment procedure. After establishing optimum conditions for producing the carbon spheres, the materials were then evaluated as a support for Fe-Co bimetallic FT catalysts.

This chapter was published as; MW Dlamini, DO Kumi, TN Phaahlamohlaka, AS Lyadov, DG Billing, LL Jewell, NJ Coville, Carbon spheres prepared by hydrothermal synthesis – a support for bimetallic iron cobalt Fischer-Tropsch catalysts, ChemCatChem ***2015****, 7, 3000 – 3011.*

Chapter 5 explores the use of hollow carbon spheres as a support for cobalt Fischer-Tropsch catalysts. Furthermore, details on the N-functionalization of these materials by a post-synthesis procedure are described.

Chapter 6 describes an investigation of the effect of the support morphology on the performance of a Co Fischer-Tropsch catalyst. Solid and hollow carbon spheres with comparable properties were used as the model support materials in this study.

Chapter 7 compares the use of a hollow carbon sphere and solid carbon sphere support in the preparation of a supported Fe FT catalyst.

Chapter 8 provides a summary and conclusion on the use of hydrothermal carbon spheres as a model support material for Fe and/or Co Fischer-Tropsch catalysts.

References

[1] F. Morales, B. M. Weckhuysen, *Catalysis* **2006**, *19*, 1-40.

[2] http://www.macrotrends.net/1369/crude-oil-price-history-chart, **Accessed: June 2016**.

CHAPTER 1

INTRODUCTION - Fischer-Tropsch synthesis

1.1 Background

The Fischer-Tropsch (FT) process has recently become a subject of renewed interest particularly in the context of exploitation of large reserves of stranded gas, diversification of carbon sources for transportation fuels and environmental concerns triggered by the presence of pollutants such as aromatic compounds or sulfur in crude oil.[1-2] Carbon sources such as coal, biomass or natural gas can be converted to mixtures of CO and H_2 (synthesis gas) by processes such as partial oxidation or steam reforming. The syngas can subsequently be converted to hydrocarbons in the FT process. For economic and logistic reasons, such energy conversions are best carried out in large scale projects. Therefore, the catalysts used in the FT process are required to have good activity, product selectivity as well as a long life span.

When iron catalysts are used, the FT product stream consists of large amounts of linear alpha olefins as well as long chain linear paraffins and oxygenates.[3] Sometimes it is desirable to shift the selectivity of the process during production to maximize the fabrication of chemicals rather than producing large quantities of the lower value gasoline fuel. Notably, straight-run FT gasoline has a low octane rating and low cold-flow properties since it is predominantly linear; hence require upgrading in downstream hydro-isomerization and hydrocracking refinery operations.[4-5] Maximizing the gasoline yield is usually achieved by the oligomerization of the gaseous unsaturated FT products typically performed by using non-selective acid catalysts such as phosphoric acid, followed by hydrogenation to yield branched paraffinic products which are characterized by high octane numbers.[6-7] This procedure is particularly useful for high temperature FT synthesis because of the high yield of unsaturated hydrocarbons in the C_3-C_5 fraction.

By contrast, FT-derived diesel fuel has a high cetane number (> 70 whereas the requirement is ~ 45).[7] This is because FT products are mainly linear paraffins, particularly when Co-based catalysts are used. To achieve a maximum diesel yield, the production conditions are set to favour the fabrication of waxes. For example, the use of Fe or Co catalysts at temperatures higher than 210 °C yields a product stream

rich in C_{20+} hydrocarbons. The heavy hydrocarbons are subsequently cracked to yield over 80% diesel which is free from contaminants such as CO, NO_x and particulates.[8]

Historically, discoveries associated with the Fischer-Tropsch (FT) reaction started in Germany nearly nine decades ago. As early as 1902, Sabatier and Senderens reported the formation of a hydrocarbon (methane) from the reaction of CO and H_2 over a nickel or cobalt catalyst at atmospheric pressure.[9] In 1913 the Badische Anilin und Soda Fabrik (BASF) of Ludwigshafen, Germany, discovered the production of methanol at technical scale from syngas at high temperatures and pressures.[10] Subsequently, in 1923 Franz Fischer and Hans Tropsch achieved the production of a synthol from synthesis gas at the Kaiser Wilhelm Institut für Kohlenforschung (now Max Plank Institute) in Mülheim, Germany. Synthol is a mixture of aliphatic oxygenated compounds, and was obtained over base-promoted iron chips at 150 atmospheres pressure and in the temperature range 400 – 450 °C.[11-12] The synthol produced this way was then converted into synthine, a mixture of hydrocarbons, which was later distilled for possible use as a transportation fuel. Evaluation of the fractionated distillate on a motorbike carrying two persons suggested that this product was comparable, if not better than a crude oil-derived reference fuel.[13] This invention later proved to be a key invention and the process was subsequently named the Fischer-Tropsch process in their honour. Soon thereafter, it was realised that the use of a cobalt-based catalyst in the Fischer-Tropsch process allowed for the process to be performed at much lower reaction temperatures and pressures.[14]

1.2 Industrialization of the Fischer-Tropsch process

After the establishment of the FT process, scientists started unravelling the engineering aspects of the invention. The early large-scale FT plants were all used in Germany. Developments in reactor technology by Ruhrchemie yielded the first commercial FT plant at Oberhausen, Germany in 1936. The total production capacity from the 52 reactors of this small scale-plant was 1 400 barrels per day (bbl/day). By the close of 1938, a total of nine FT plants were operational in Germany, having a combined production capacity of about 14 000 bbl/day.[15] All nine plants used Co-based catalysts for their production and operated at atmospheric pressure. This large scale production ability proved to be useful at the time because it allowed Germany to use its FT-derived fuels during the Second World War. Production at these plants

ceased after the war following the discovery of additional crude oil reserves. However, interest in the FT process remained amid fears that crude oil reserves would soon be depleted.

After World War II, Ruhrchemie and Lurgi developed a large-scale Arbeitsgemeinschaft (ARGE) process for wax production over iron catalysts. Around the same time, a technology based on a circulating fluidized bed reactor was developed at Kellogg. At this time, discoveries of large natural gas reserves in the United States of America together with declining crude oil reserves triggered interest in the Fischer-Tropsch process. Subsequently, a commercial gas-to-liquids (GTL) plant with a capacity of 7 000 bbl/day of primary product was commissioned by the Hydrocarbon Research Inc. at Brownsville, Texas. This plant utilized synthesis gas produced from the partial combustion of natural gas, and synthesis was performed in a fixed fluidized bed reactor using an iron catalyst.[6] This plant was soon shut down (1956) though because the cost of natural gas had increased sharply while crude oil became cheaper and was more readily available.[16]

In South Africa, Sasol had been tasked with exploiting the large coal deposits present in the country and to convert them to gasoline, diesel and chemicals using the German-developed Fischer-Tropsch process. In 1951 Sasol received five proposals on available reactor technologies for their planned coal-to-liquids plant. A decision was made to settle for two of the proposed designs; a circulating fluidized-bed (CFB) reactor submitted by M. W. Kellogg, and an ARGE fixed-bed system by Arbeit-Gemeinschaft Lurgi and Ruhrchemie. In 1955, Sasol started operating a large-scale FT synthesis plant at their Sasol I site in Sasolburg, South Africa, utilizing ARGE fixed-bed reactor and CFB reactor technologies. Two-thirds of the available synthesis gas was to be converted to synthetic fuels by using the Kellogg CFB system, while the ARGE fixed bed technology was used to convert the other third (at the time).[17] The catalyst used in the ARGE reactor consisted of iron supported on silica and had copper and an alkali as promoters. Unsupported iron fine powder was used as a catalyst in the CFB reactor.

The early 1970s saw drastic increases in crude oil prices and this resulted in increased profitability in operations at the Sasol I site. Thus as decision was taken to construct

two larger additional coal-to-liquid (CTL) plants in Secunda, South Africa. These were commissioned in 1980 and 1982 (Sasol II and Sasol III, respectively). The Sasol II and Sasol III plants initially used CFB reactors but these were later upgraded to newly developed Sasol advanced synthol (SAS) reactors which had diameters of 8.0 m (11 000 bbl/day) and 10.7 m (22 000 bbl/day). Production at these sites was geared up towards the synthesis of transportation fuels as they were built to counter the oil crisis which was prevalent at the time. These plants continue to be profitable due to their large-scale capacity. After these developments there followed a period in which cobalt FT catalysts were "rediscovered". These catalysts were found to be more suitable for the conversion of stranded natural gas to fuels in low temperature gas-to-liquid (GTL) FT synthesis. Soon the construction of two GTL plants started; in Mossel Bay (South Africa) and Bintulu (Malaysia), and were both commissioned in 1993. The Mossgas plant (presently PetroSA) has a capacity of 20 000 bbl/day whereas the Shell Bintuli plant produced 15 000 bbl/day of synthetic hydrocarbons using the Shell middle distillate synthesis (SMDS) process.

More recently, a joint venture between Sasol (49%) and Qatar Petroleum (51%) resulted in the construction of the $900 m Oryx GTL plant in Ras Laffan, Qatar. It was commissioned in 2006 and operated on Sasol slurry phase distillate (SPD) technology. The initial capacity for the plant was 34 000 bbl/day of hydrocarbons (24000 barrels of diesel, 9000 barrels of naphtha and 1000 barrels of liquefied petroleum gas), and used about 330 000 ft^3/day of natural gas.[18] Planned future expansions on this facility are expected to increase its capacity to a projected 450 000 bbl/day of synthetic hydrocarbons. In Qatar, Shell built the Pearl GTL plant which became fully functional in 2012, using experience gained at the Bintulu operations (Malaysia). With a total capacity of 140 000 bbl/day, this facility has about 10 times the capacity of the Bintulu plant. Just like the predecessor plant, the Pearl GTL operates on the Shell middle distillate synthesis (SMDS) process.[18] In 2014 another GTL plant was inaugurated in Escravos, Nigeria, and is owned by Chevron (75%), Sasol (10%) and the Nigerian National Petroleum Company (NNPC, 25%). This facility converts 325 million ft^3/day of natural gas to about 34 000 bbl/day of synthetic fuels, and uses the Sasol SPD and the Chevron ISOCRACKING technologies.[19-20] Many other companies are involved in the development of technologies associated with the FT process, such as ExxonMobile, ConocoPhillips,

BP, Eni/IFP, Syntroleum and Rentech. Some recent developments in FT plant operation by various companies are listed in Table 1.1.

Table 1.1 Summary of recent developments on major FT plants.[21]

Year	*Company or companies*	*Technology*	*Production level (bbl/day)*	*Country*
1955	Sasol	Sasol I	500	South Africa
1980	Sasol	Sasol II	11 000 (later 20 000)	South Africa
1982	Sasol	Sasol III	11 000 (later 20 000)	South Africa
1993	PetroSA	Sasol's slurry phase technology	20 000	South Africa
1993	Shell	Shell middle distillate synthesis (SMDS) fixed-bed technology	15 000	Malaysia
2006	Sasol and Qatar Petroleum	Sasol slurry phase distillate (SPD)	34 000 (expected: 450 000)	Qatar
2012	Shell and Qatar Petroleum	Shell middle distillate synthesis (SMDS) fixed-bed	140 000	Qatar
2014	Chevron, Sasol and Nigerian National Petroleum Company	Sasol slurry phase distillate (SPD)	34 000	Nigeria

1.3 Fischer-Tropsch chemistry

The chemistry taking place in the FT reactor is complex because it involves a variety of competing reactions.[22] The main reactions in FT synthesis are summarized in equations 1.1 to 1.3 as shown:

Paraffin formation:

$$n\mathrm{CO} + (2n+1)\mathrm{H_2} \rightarrow \mathrm{C}_n\mathrm{H}_{2n+2} + n\mathrm{H_2O} \quad (1.1)$$

Olefin formation:

$$n\mathrm{CO} + 2n\mathrm{H_2} \rightarrow \mathrm{C}_n\mathrm{H}_{2n} + n\mathrm{H_2O} \quad (1.2)$$

Water-gas shift (WGS) reaction:

$$\mathrm{CO} + \mathrm{H_2O} \leftrightarrow \mathrm{CO_2} + \mathrm{H_2} \quad (1.3)$$

where *n* is the carbon number. Several other reactions that occur include the formation of oxygenates, the Boudouard reaction, catalyst oxidation/reduction and carbide formation which have been discussed in detail elsewhere.[21] The FT process is a kinetically controlled reaction and the basic kinetics involves a step-wise chain growth process, which is essentially the polymerization of CH_x (x = 1, 2, or 3) groups on a catalyst surface to produce a broad spectrum of hydrocarbons. Chain growth during FT synthesis is still a subject of discussion; two proposals are at the forefront of this debate. The first proposal, called the carbide mechanism, involves the cleavage of the C–O bond followed by partial hydrogenation to form $CH_{x,ads}$ groups, which then polymerize to yield heavy hydrocarbons. The second proposal, called the Pichler-Schulz mechanism, describes chain growth by the insertion of CO into a metal–methyl or metal–methylene carbon bond which is subsequently hydrogenated to an alkene or alcohol.[23] Selectivities towards certain products are influenced by the ability of the catalyst used to promote either chain propagation versus chain termination reactions. The distribution of hydrocarbon products formed in the process is normally predicted using the Anderson-Schulz-Flory (ASF) model, which can be expressed as follows:

$$W_n/n = (1-\alpha)^2\alpha^{n-1}$$

where W_n is the weight fraction of hydrocarbon molecules containing *n* carbon atoms, α is the probability of chain growth (i.e. the probability that a molecule will continue reacting to form a larger chain). Generally, the value of α is determined by the characteristics of the catalyst and the specific process conditions.[24]

1.4 Fischer-Tropsch reactors

The Fischer-Tropsch reaction is well known for its high exothermicity (ΔH_R = -165 kJ/mol_{CO}).[25] It is therefore important that reactor design ensures that the heat generated during the reaction is removed efficiently from the catalyst bed. Excessive

temperatures at the catalyst surface result in high methane yields and deactivation of the catalyst due to carbon deposition and sintering. At present, reactor types utilised in commercial FT synthesis include: tubular fixed-bed reactors, slurry phase reactors, fluidized bed reactors and circulating fluidized bed reactors. Only fixed-bed reactors have been discussed in this section because of their relevance to the study.

1.4.1 Fixed bed reactors

Modern fixed bed reactors are of a multi-tubular type and consist of many narrow tubes placed vertically with a cooling medium (typically water) in the outer shell of the tubes. The catalyst is placed inside the tubes and the narrow size of the tubes ensures efficient heat removal during FT synthesis. An example of a multi-tubular fixed bed reactor currently in operation at the Sasolburg plant in South Africa is the ARGE reactor developed by Ruhrchemie and Lurgi (Germany). This type of reactor consisted of an overall diameter of 3 m, and contained 2050 tubes which had a 5 cm internal diameter and were 12 m long (Fig. 1.1).[16, 22]

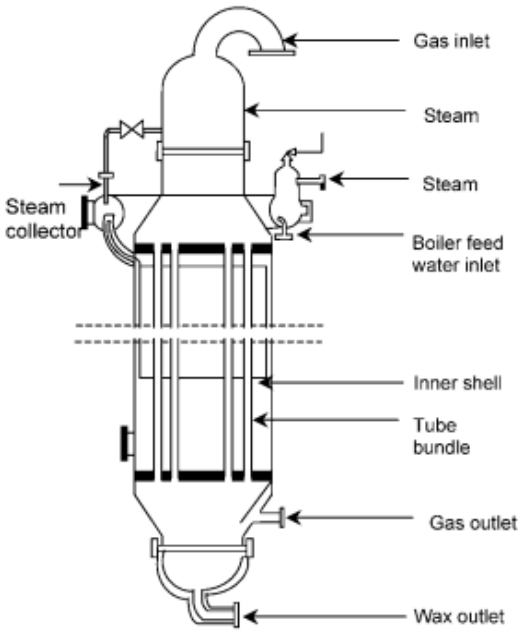

Figure 1.1 A schematic representation of a multi-tubular fixed bed reactor.[22]

Multi-tubular fixed-bed (MTFB) reactors can be operated easily as the separation of the liquid wax products and the catalyst does not require any additional instrumentation. The liquid products simply collect in ports at the bottom of the reactor. Another advantage of this type of reactor is the relative ease at which it can

be up-scaled to industrial scale and still perform similar to predictions made using a pilot scale reactor which consists of the use of a single tube. Additionally, the set-up in this reactor allows for minimal deactivation of the catalyst as a result of poisons in the feed gas. Poisoning of the catalyst only occurs in the top sections of the tubes while the rest of the catalyst remains active.

The tubes in a MTFB reactor are made with a narrow diameter to ensure efficient heat removal but this often presents challenges in the operation of the reactor. For instance, narrow tubes increase the gas compression costs which arise from trying to eliminate pressure drops across the narrow reactor tubes.[26] Furthermore, loading and unloading the catalyst can be challenging due to the narrow size of the tubes. Weak catalyst pellets tend to break under the high pressures used. Other drawbacks of multi-tubular fixed bed reactors are the high capital costs, insufficient heat transfer and the high mass-transfer limitations.[27]

1.5 Fischer-Tropsch catalysts

The FT product selectivity towards transportation fuels and chemicals is tunable by the careful selection of catalyst properties; hence catalyst design is important in optimizing the FT process. The process of selecting the active metal to be used in a particular catalyst formulation is dependent on a number of factors. These include the syngas composition (H_2/CO ratio), the price and availability of the active metal, and the desired end product. To simplify these factors, the "triangle concept" has been proposed as a suitable approach for the design of FT catalysts as it takes account of the catalytic, mechanical and chemical/physical properties (Fig. 1.5) of the catalysts.[28] For the FT process, Ni, Co, Fe and Ru catalysts are known to have sufficient performance for industrial application. It is generally agreed that nickel is not an appropriate catalyst for FT synthesis. Nickel is too hydrogenating, and produces high yields of the generally undesired methane. Furthermore, Ni forms highly toxic nickel carbonyls (volatile) at low temperatures, which results in the loss of the catalyst from the reactor.[29] Ru displays the highest activity and selectivity for heavy hydrocarbon products in FT synthesis at temperatures as low as 140 °C.[30-31] However, the low reserves for Ru worldwide and its high cost, eliminates its use for large-scale FT applications. This leaves cobalt (Co) and iron (Fe) as the only catalysts

used commercially. Details on Co, Fe and Fe-Co bimetallic catalysts are discussed in the next sections due to their relevance to this study.

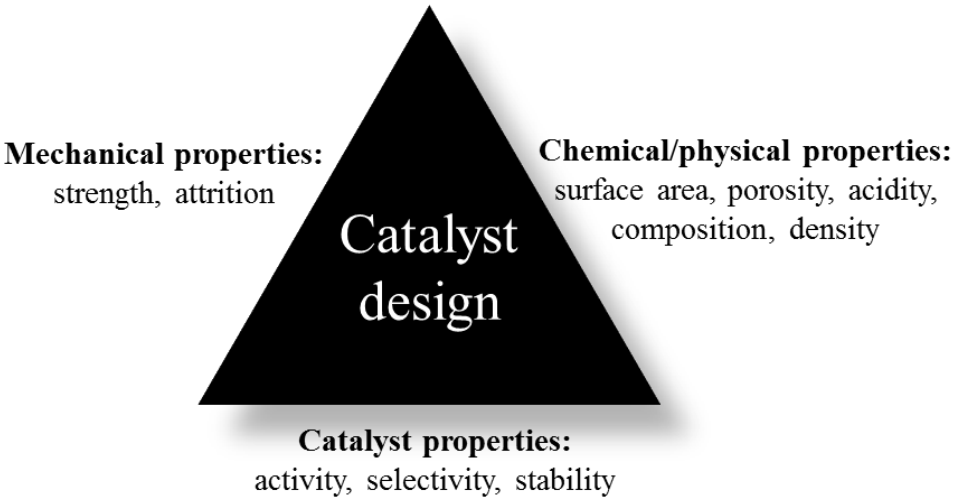

Figure 1.5 A representation of the "triangular concept" for catalyst design.[28]

1.5.1 Iron catalyst

Fe catalysts are useful in FT synthesis because of their flexibility, low cost, high abundance and low CH_4 selectivity. They are predominantly used for the production of alpha olefins as well as a mixture of oxygenated products such as ketones, aldehydes and alcohols. Apart from their high activity in the FT reaction, iron-based catalysts also produce large quantities of CO_2 due to their high water-gas shift (WGS) activity. This makes them unsuitable for use on natural gas derived synthesis gas because of environmental concerns regarding CO_2. However, they are suitable for the production of hydrocarbons from synthesis gas derived from coal or biomass, which inherently has low H_2 to CO ratios (H_2/CO ~ 1). Thus the WGS reaction is useful for the internal generation of H_2 during FT synthesis.[32-33] Furthermore, Fe catalysts typically contain chemical promoters such as copper to promote catalyst reducibility, potassium to improve CO dissociation, and structural promoters like silica or zinc oxide to improve the catalyst dispersion.[34]

Fisher-Tropsch synthesis has two operating regimes divided according to the operating temperatures. The low temperature Fischer-Tropsch (LTFT) reaction typically operates in the range 190–260 ^{o}C while the high temperature Fischer-Tropsch (HTFT) reaction operates at 300–350 ^{o}C. Fe-based catalysts are suitable for operation at both LTFT and HTFT conditions. In the HTFT process Fe-catalysts are

used for the production of both C_1–C_{15} hydrocarbons and α-alkenes, while long-chain linear alkanes are produced from the LTFT processes.[35]

During FT synthesis, a complex mixture of iron phases co-exist; metallic iron (α-Fe), iron oxides and iron carbides are present.[36] Iron carbides are essentially α-Fe species with carbon dissolved in their interstitial vacancies. Unlike Co catalysts, iron carbides are easily formed from Fe catalysts under FT working conditions. Niemantsverdriet and van der Kraan have attributed this to the low activation energy of iron carbide formation (43.9–69.0 $kJmol^{-1}$) compared to cobalt carbide formation (~145 $kJmol^{-1}$).[37] Commonly reported carbide phases include θ-Fe_3C (cementite), χ-Fe_5C_2 (Hägg carbide), ε-Fe_2C and ε'-$Fe_{2.2}C$ (hexagonal carbides). Due to the intricacy of the iron–oxygen–carbon system, the identity of the active phase(s) on Fe-based catalysts is contentious.[38] Several studies have suggested that α-Fe, bulk and surface iron carbides or Fe_3O_4 are the active phases during the FT reaction.[39] Literature also suggests that the formation of iron carbides results in a high FT synthesis activity, and that magnetite (Fe_3O_4) is the most active phase for the WGS reaction.[40-42] One of the major challenges of iron catalysts in FT is their high deactivation rate and inherently their relatively short catalyst life-time.

1.5.2 Cobalt catalysts

Cobalt is much more expensive than Fe hence Co-based catalysts are usually supported on high-surface area materials to improve their dispersion. Cobalt FT catalysts are preferred for the conversion of synthesis gas (syngas) derived from natural gas because of their higher per pass conversion, high intrinsic activity, selectivity for heavy hydrocarbon products and long lifetime relative to Fe catalysts.[43] Syngas derived from natural gas has high H_2 to CO ratios, typically ~2. Due to its high hydrogenation capability, Co catalysts allow for the production of paraffinic waxes which are then hydrocracked to make lubricants and diesel fuel with excellent cetane ratings. Large-scale plants which use Co catalysts have been in operation for over 10 years now in Qatar (Oryx GTL) and in Malaysia (Shell).

For cobalt catalysts, it is generally accepted that metallic Co is the active phase in FT synthesis. Metallic cobalt (Co^0) can exist in two different crystalline forms, namely

the hexagonal close packed (hcp) structure and the face centred cubic (fcc) structure. The phase formed usually depends on the conditions (gas composition, temperature) at which the calcined materials are reduced, and the type of cobalt species formed after activation affects the FT synthesis performance. Elbashir et al. observed that the nature of the support also determines the eventual phase; Co fcc was preferred on SiO_2, whereas the Co hcp structure was the main phase on Al_2O_3 supported catalysts after reduction.[44] In FT synthesis, higher CO conversions and C_5^+ selectivities have been measured on Co hcp catalysts relative to Co fcc samples (Table 1.2).[45] This could be associated with the larger quantity of surface defects (corners, edges) on the Co hcp structure than found on the cubic stacking (Co fcc).

Table 1.2 FT data for hcp and fcc phases of Co/SiO_2 catalysts. Reaction conditions: T = 220 °C, P = 20 bar, H_2/CO = 2/1 and syngas flow rate: 3.0 sl h^{-1} g_{cat}^{-1}.[45]

Catalyst	TOS (h)	CO conv. [%]	Selectivity		TOF (s^{-1})
			CH_4	C_{5+}	
Co hcp	16	63.1	3.5	88.2	0.095
	450	55.5	4.2	90.2	0.068
Co fcc	13	45.1	6.4	86.1	0.092
	492	32.1	7.2	82.9	0.049

From thermodynamic calculations, predictions show that the oxidation of bulk cobalt to CoO or Co_3O_4 during realistic FTS conditions is not possible. However, Co can possibly form mixed compounds such as cobalt aluminate upon interacting strongly with the support material.[46] Even though bulk oxidation of cobalt metal is not feasible thermodynamically, it has been shown from calculations that cobalt particles in the nano-regime can oxidise under typical FT synthesis conditions.[47] Visagie et al. attributed this observation to the surface energy of cobalt particles that are in the nanometre size range which contributes to overall oxidation process. On this basis it was determined that the oxidation of cobalt crystallites with sizes between 4 and 5 nm is viable under typical FT conditions, i.e. P_{H2O}/P_{H2} = 1-1.5. In similar studies, Iglesia found that the oxidation and deactivation of cobalt crystallites below 6 nm occurs rapidly under realistic FT conditions.[48-49]

1.5.3 Iron-cobalt bimetallic catalysts

As highlighted in earlier sections, Co has a high activity and selectivity to heavy hydrocarbon products but low WGS activity, whereas Fe is known to be active for the WGS reaction but its kinetic FT rate is postulated to be adversely affected by the partial pressure of water. However, when Fe and Co are used together, reports have indicated that they do not simply give the additive properties of the constituent metals.[50-52] Thus, a supported iron-cobalt (Fe-Co) bimetallic catalyst would seem to be a viable proposition for the conversion of syngas into fuels and commodity chemicals.

Several advantages of Fe-Co bimetallic systems have been highlighted in the literature. By studying co-impregnated catalysts, Holmen et al. observed that alloying Co with moderate amounts of Fe improved the FT activity of Co catalysts without a corresponding increase in the WGS activity. Hence it was concluded that the increase in the activity was due to a higher FT activity of the Fe-Co mixtures when compared to pure Co catalysts.[53] Many other studies have also reached the same conclusion.[54-56] It has also been reported that the use of a mixture consisting of Fe and Co has generated FT products with high yields of olefins and oxygenated products such alcohols, compared to individual Fe or Co catalysts.[57] For these systems, it is thought that the metallic Fe-Co alloy (formed upon reduction bimetallic precursor) is active phase in FT synthesis,[58] but this area still warrants further study because in situ characterization of these systems has been limited.

Much of what is known about the activation process or the catalytic species in bimetallic systems has mainly been inferred from indirect experimental evidence. This has been done by the post-analysis of spent or reduced-then-passivated samples. This indirect approach often results in inconclusive or contradicting reports because of the complex phase transformations that occur in such systems. For example, the formation of an alloy on these systems is still uncertain.[59] The analysis of reduced or spent catalysts by many authors has revealed the presence of reflections that correspond to the Fe_2Co, Co_7Fe_3 or Co/Fe alloys.[60-63] While elsewhere, studies have reported not detecting any features associated with alloy formation.[64] Tavasoli et al. have linked the formation small quantities of the alloy to an increase in alcohol

selectivity during FT synthesis.[57] Thus visualizing the reduction processes as they occur is key for a better understanding and development of bimetallic catalysts.

It is generally accepted that monometallic Co has a higher FT activity than Fe catalysts. However, for bimetallic Fe-Co systems it appears that several factors determine the activity of a catalyst and these include; the precursors of Fe and Co, the preparation method, the nature of the support material used, the metal addition sequence and the ratio of Co to Fe in the catalyst. For example, Vannice et al. showed that intermediate CO conversions and hydrocarbon selectivities were obtained from Fe-Co systems prepared from metal carbonyl clusters [$Fe_3(CO)_{12}$ and $Co_2(CO)_8$] as precursors.[65] The effect of the metal addition sequence has been reported by Duvenhage et al. on Fe-Co/TiO_2 catalysts prepared by the sequential impregnation of Co then Fe nitrate precursors. XPS analysis of the calcined and reduced samples revealed that the surface was richer in Fe content, indicating that the Fe had segregated from the Fe-Co system either during calcination or the reduction steps. Not surprisingly, the FT performance of this bimetallic system was comparable to that of a monometallic Fe/TiO_2 catalyst.[50]

1.6 Supports for Fischer-Tropsch catalysts

Although more than eight decades have passed since the first application of iron-based catalysts in the Fischer–Tropsch process, studies to understand and improve factors that affect the activity, selectivity and stability of a catalyst are still ongoing. The type of material used as a support for the active catalyst is critical in the FT process as it can directly influence the performance of a catalyst. Support materials are expected to play the following roles in heterogeneous catalysis: 1) to provide high surface areas for the catalytically active species; 2) to immobilize the active phase and thus minimize sintering; 3) to maintain the mechanical integrity of the material and to facilitate the mass or heat transfer in a diffusion-limited or exothermic reaction.[36] It is also desirable that surface area and pore volume of the support material be high enough to allow for a good dispersion of the active phase and eliminate mass transfer limitations. Additionally, a balanced chemical interaction must be maintained between support and the active phase. Too weak an interaction may lead to a poor dispersion of the active phase, whereas if the interaction is too strong it can cause difficulty in the reduction of the active phase precursor.[66] For example, Khodakov et

al. observed a decline in the ease of reduction from larger (20 nm) to smaller (6 nm) Co_3O_4 particles supported on silica. This effect was attributed to the differences with which large and smaller particles interact with the support.[67]

FT catalysts are typically dispersed on metal oxides that include SiO_2, TiO_2, Al_2O_3 and MgO. The chemical nature of the support material has been shown to influence FT performance. Studies on Co catalysts supported on these oxide materials by Reuel and Bartholomew found that the turnover frequency (TOF) in FT synthesis declined as follows; $Co/TiO_2 > Co/SiO_2 > Co/Al_2O_3 > Co/MgO$.[68-69] This is attributed to the presence of a strong metal-support interaction (SMSI) with the classical FT catalysts, Fe and Co. The strong interaction of these catalysts with the oxide supports has been shown to result in the formation of mixed compounds such as Co_2SiO_2,[35, 70] Co_2AlO_4,[71-72] $CoTiO_4$,[73] Fe_2SiO_4[38] or FeO-MgO,[74-75] which can only be reduced at elevated temperatures. An alternative approach to overcome challenges associated with SMSIs is to use carbon-based supports. Carbon is relatively inert hence it has a moderate interaction with the active phase particles when it is used as a catalyst support.

1.7 Carbon as a catalyst support

Carbon, the sixth element in the periodic table, has unique properties. It can form stable bonds with itself as well as most elements due to the different hybridization it can undergo; *sp*, sp^2 and sp^3.[76] And as expected, the different C-C bonding configurations possible result in materials with varying properties. For example, diamond is one of the hardest materials known to mankind, whereas graphite is a slippery material and it is used as a solid lubricant. At present, carbon materials that have been synthesized include activated carbon (AC), carbon nanotubes (CNTs), carbon spheres (CSs), glassy carbon (GCs), carbon dots (CDs) and carbon nanofibers (CNFs). These materials possess different characteristics because the properties of carbon materials are strongly influenced by their morphology. Hence, the ability to selectively fabricate carbon materials of a particular morphology is very important for their various applications. Amongst these materials, CSs stand out because of their unique properties and has become an attractive research field due to its potential applications, e.g., in catalyst supports, confined nano-catalysis, lithium-ion secondary batteries, drug delivery, and as an energy storage medium.[77-79]

1.8 Carbon spheres as a catalyst support

As a model catalyst support, advantages of CSs use are associated with their ease of synthesis which is possible without the use of catalysts, the ability to control their physical properties (size, purity, porosity), and the high yields of pure materials that can be synthesized. Due to their high surface-to-volume ratios, excellent structural stability, low electrical resistance, along with the possibility to modify their surfaces and interiors by coating and doping, CSs are well suited to be used as catalyst supports. Carbon spheres (CSs) can have different morphologies; solid, hollow, core-shell or yolk-shell/rattle-kind structure. Illustrations of the different morphologies are displayed in Fig. 1.6. Carbon spheres were used as a model support for Fischer-Tropsch catalysts in this study. Details on the synthesis and subsequent use of carbon spheres as a support in heterogeneous catalysis are given in chapter 2.

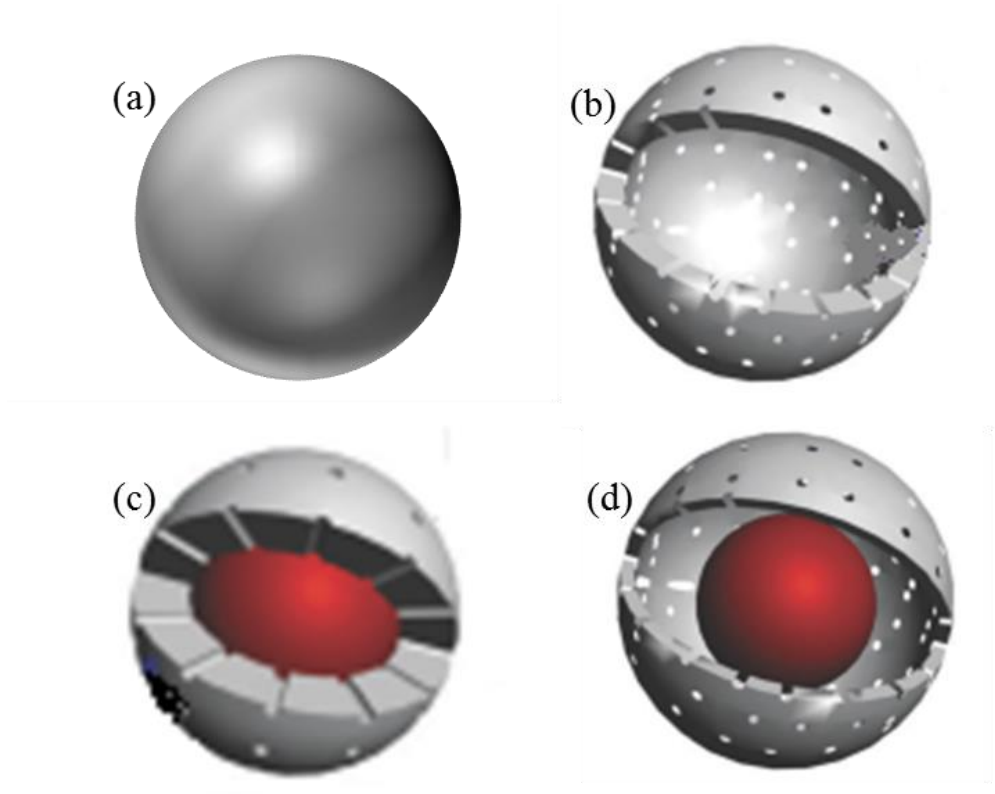

Figure 1.6 Different kinds of CS morphologies that can be fabricated; a) solid CSs, b) hollow CSs, c) core-shell CSs and d) yolk-shell CSs.[80]

1.9 Aims and objectives

The use of carbon-based materials as a model support for Fischer-Tropsch catalysts still comes short when explaining some phenomena that are actually observed in the reaction when metal oxide supports are used. This is partly because of the inability to fabricate carbons with flexible/tunable properties. These properties include surface area, pore structure, thermal stability and surface chemistry. These challenges prompted us to explore the use of hydrothermal carbon spheres as an alternative model support (to TiO_2, SiO_2, Al_2O_3) for FT catalysts, addressing issues on the control of their properties.

The specific objectives of the study were;

(i) To tailor the synthesis conditions of carbon spheres prepared by the hydrothermal method to yield materials which have high surface areas for use as model catalyst supports.

(ii) To exploit advantages related to carbon spheres in understanding phase-activity relationships for Fe-Co bimetallic systems which could be important for improving catalyst performance and efficiency.

(iii) Determine the feasibility of using hollow carbon spheres as a model support for Fischer-Tropsch catalysts. Issues on their robustness and surface functionalization were to be addressed.

(iv) Understanding the effect of the catalyst support morphology in FT synthesis by utilizing morphology-tunable carbon spheres as a model system.

(v) To prepare Co, Fe and Fe-Co catalysts supported on carbons and then characterize them by using TEM, SEM, BET, TGA, XRD, FTIR, XPS and Raman spectroscopy.

(vi) To study the reduction behaviour of the catalysts under realistic reaction conditions by using in situ powder X-ray diffraction (PXRD) and temperature programmed reduction (TPR) techniques.

(vii) To evaluate the catalytic performance of the prepared materials in the Fischer-Tropsch synthesis.

REFERENCES

[1] C. Kibby, K. Jothimurugesan, T. Das, H. S. Lacheen, T. Rea, R. J. Saxton, *Catal. Today* **2013**, *215*, 131-141.

[2] L. J. Garces, B. Hincapie, R. Zerger, S. L. Suib, *J. Phys. Chem. C* **2015**, *119*, 5484-5490.

[3] V. R. R. Pendyala, U. M. Graham, G. Jacobs, H. H. Hamdeh, B. H. Davis, *Catal. Lett.* **2014**, *144*, 1704-1716.

[4] M. E. Dry, *Appl. Catal. A* **2004**, *276*, 1-3.

[5] A. Corma, A. Martinez, S. Pergher, S. Peratello, C. Perego, G. Bellusi, *Appl. Catal. A* **1997**, *152*, 107-125.

[6] B. H. Davis, *Catal. Today* **2002**, *71*, 249-300.

[7] M. E. Dry, *Appl. Catal. A* **1999**, *189*, 185-190.

[8] M. E. Dry, in *Hydrocarb. Process., Vol. August 1982*, **1982**, pp. 121-124.

[9] P. Sabatier, J. B. Senderens, *C. R. Acad. Sci.* **1902**, *134*, 514.

[10] BASF, in *Ludwigshafen, Vol. 293*, German Patent, **1913**, p. 787.

[11] F. Fischer, H. Tropsch, *Brennst. Chem.* **1923**, *4*, 193-197.

[12] F. Fischer, H. Tropsch, *Brennst. Chem.* **1923**, *4*, 276-285.

[13] J. L. Casci, C. M. Lok, M. D. Shannon, *Catal. Today* **2009**, *145*, 38-44.

[14] F. Fischer, H. Tropsch, *Brennst. Chem.* **1926**, *7*, 97-104.

[15] M. E. Dry, *Catal. Today* **2002**, *71*, 227-241.

[16] R. Krishna, S. T. Sie, *Fuel Process. Technol.* **2000**, *64*, 73-105.

[17] D. J. Duvenhage, T. Shingles, *Catal. Today* **2002**, *71*, 301-305.

[18] www.hydrocarbons-technology.com/projects/oryx (Accessed: 20 January 2016).

[19] C. Perego, R. Bortolo, R. Zennaro, *Catal. Today* **2009**, *142*, 9-16.

[20] C. Nwaoha, D. A. Wood, *J. Nat. Gas Sci. Eng.* **2014**, *18*, 412-432.

[21] M. W. Dlamini, MSc Dissertation, University of the Witwatersrand (Johannesburg), **2012**.

[22] M. E. Dry, A. P. Steynberg, in *Studies in Surface Science and Catalysis, Vol. Volume 152* (Eds.: S. André, D. Mark), Elsevier, **2004**, pp. 406-481.

[23] R. A. van Santen, A. J. Markvoort, M. M. Ghouri, P. A. J. Hilbers, E. J. M. Hensen, *J. Phys. Chem. C* **2013**, *117*, 4488-4504.

[24] E. F. Sousa-Aguiar, F. B. Noronha, J. A. Faro, *Catal. Sci. Technol.* **2011**, *1*, 698-713.

[25] D. Gidaspow, Y. He, V. Chandra, *Chem. Eng. Sci.* **2015**, *134*, 784-799.

[26] G. Chabot, R. Guilet, P. Cognet, C. Gourdon, *Chem. Eng. Sci.* **2015**, *127*, 72-83.

[27] S. Chambrey, P. Fongarland, H. Karaca, S. Piché, A. Griboval-Constant, D. Schweich, F. Luck, S. Savin, A. Y. Khodakov, *Catal. Today* **2011**, *171*, 201-206.

[28] C. H. Bartholomew, R. J. Farrauto, in *Fundamentals of Industrial Catalytic Processes*, John Wiley & Sons, Inc., **2005**, pp. 60-117.

[29] M. E. Dry, *Catal. Lett.* **1990**, *7*, 241-251.

[30] J. M. Gonzalez Carballo, E. Finocchio, S. Garcia, S. Rojas, M. Ojeda, G. Busca, J. L. G. Fierro, *Catal. Sci. Technol.* **2011**, *1*, 1013-1023.

[31] C.-X. Xiao, Z.-P. Cai, T. Wang, Y. Kou, N. Yan, *Angew. Chem. Int. Ed.* **2008**, *47*, 746-749.

[32] K. Keyvanloo, M. K. Mardkhe, T. M. Alam, C. H. Bartholomew, B. F. Woodfield, W. C. Hecker, *ACS Catal.* **2014**, *4*, 1071-1077.

[33] B. An, K. Cheng, C. Wang, Y. Wang, W. Lin, *ACS Catal.* **2016**, *6*, 3610-3618.

[34] J. Xie, H. M. Torres Galvis, A. C. J. Koeken, A. Kirilin, A. I. Dugulan, M. Ruitenbeek, K. P. de Jong, *ACS Catal.* **2016**, *6*, 4017-4024.

[35] A. Y. Khodakov, W. Chu, P. Fongarland, *Chem. Rev.* **2007**, *107*, 1692-1744.

[36] Q. Zhang, J. Kang, Y. Wang, *ChemCatChem* **2010**, *2*, 1030-1058.

[37] J. W. Niemantsverdriet, A. M. van der Kraan, *J. Catal.* **1981**, *72*, 385-388.

[38] E. de Smit, I. Swart, J. F. Creemer, G. H. Hoveling, M. K. Gilles, T. Tyliszczak, P. J. Kooyman, H. W. Zandbergen, C. Morin, B. M. Weckhuysen, F. M. F. de Groot, *Nature* **2008**, *456*, 222-225.

[39] E. de Smit, B. M. Weckhuysen, *Chem. Soc. Rev.* **2008**, *37*, 2758-2781.

[40] G. P. van der Laan, A. A. C. M. Beenackers, *Appl. Catal. A* **2000**, *193*, 39-53.

[41] Y.-N. Wang, W.-P. Ma, Y.-J. Lu, J. Yang, Y.-Y. Xu, H.-W. Xiang, Y.-W. Li, Y.-L. Zhao, B.-J. Zhang, *Fuel* **2003**, *82*, 195-213.

[42] G. P. Van Der Laan, A. A. C. M. Beenackers, *Catal. Rev.* **1999**, *41*, 255-318.

[43] V. Subramanian, K. Cheng, C. Lancelot, S. Heyte, S. Paul, S. Moldovan, O. Ersen, M. Marinova, V. V. Ordomsky, A. Y. Khodakov, *ACS Catal.* **2016**, *6*, 1785-1792.

[44] N. O. Elbashir, P. Dutta, A. Manivannan, M. S. Seehra, C. B. Roberts, *Appl. Catal. A* **2005**, *285*, 169-180.

[45] M. K. Gnanamani, G. Jacobs, W. D. Shafer, B. H. Davis, *Catal. Today* **2013**, *215*, 13-17.

[46] P. J. van Berge, J. van de Loosdrecht, S. Barradas, A. M. van der Kraan, *Catal. Today* **2000**, *58*, 321-334.

[47] E. van Steen, M. Claeys, M. E. Dry, J. van de Loosdrecht, E. L. Viljoen, J. L. Visagie, *J. Phys. Chem. B* **2005**, *109*, 3575-3577.

[48] E. Iglesia, *Appl. Catal. A* **1997**, *161*, 59-78.

[49] E. Iglesia, in *Stud. Surf. Sci. Catal., Vol. Volume 107* (Eds.: R. L. E. C. P. N. J. H. S. M. de Pontes, M. S. Scurrell), Elsevier, **1997**, pp. 153-162.

[50] D. J. Duvenhage, N. J. Coville, *Appl. Catal. A* **1997**, *153*, 43-67.

[51] D. J. Duvenhage, N. J. Coville, *Appl. Catal. A* **2002**, *233*, 63-75.

[52] J. A. Amelse, L. H. Schwartz, J. B. Butt, *J. Catal.* **1981**, *72*, 95-110.

[53] S. Lögdberg, D. Tristantini, Ø. Borg, L. Ilver, B. Gevert, S. Järås, E. A. Blekkan, A. Holmen, *Appl. Catal. B* **2009**, *89*, 167-182.

[54] X. Ma, Q. Sun, W. Ying, D. Fang, *J. Nat. Gas Chem.* **2009**, *18*, 232-236.

[55] T. Ishihara, K. Eguchi, H. Arai, *Appl. Catal.* **1988**, *40*, 87-100.

[56] F. Tihay, A. C. Roger, A. Kiennemann, G. Pourroy, *Catal. Today* **2000**, *58*, 263-269.

[57] A. Tavasoli, M. Trépanier, R. M. Malek Abbaslou, A. K. Dalai, N. Abatzoglou, *Fuel Process. Technol.* **2009**, *90*, 1486-1494.

[58] F. Tihay, A. C. Roger, G. Pourroy, A. Kiennemann, *Energy Fuels* **2002**, *16*, 1271-1276.

[59] V. R. Calderone, N. R. Shiju, D. C. Ferre, G. Rothenberg, *Green Chem.* **2011**, *13*, 1950-1959.

[60] R. Satthawong, N. Koizumi, C. Song, P. Prasassarakich, *J. CO_2 Util.* **2013**, *3–4*, 102-106.

[61] N. Chiwaye, L. L. Jewell, D. G. Billing, D. Naidoo, M. Ncube, N. J. Coville, *Mater. Res. Bull.* **2014**, *56*, 98-106.

[62] S. Ali, N. A. Mohd Zabidi, D. Subbarao, *Chem. Cent. J.* **2011**, *5*, 1-8.

[63] V. A. de la Peña O'Shea, M. C. Álvarez-Galván, J. M. Campos-Martin, N. N. Menéndez, J. D. Tornero, J. L. G. Fierro, *Eur. J. Inorg. Chem.* **2006**, *2006*, 5057-5068.

[64] A. Guerrero-Ruiz, A. Sepúlveda-Escribano, I. Rodríguez-Ramos, *Appl. Catal. A* **1992**, *81*, 81-100.

[65] A. Chen, M. Kaminsky, G. L. Geoffroy, M. A. Vannice, *J. Phys. Chem.* **1986**, *90*, 4810-4819.

[66] S. L. Soled, E. Iglesia, R. A. Fiato, J. E. Baumgartner, H. Vroman, S. Miseo, *Top. Catal.* **2003**, *26*, 101-109.

[67] A. Y. Khodakov, J. Lynch, D. Bazin, B. Rebours, N. Zanier, B. Moisson, P. Chaumette, *J. Catal.* **1997**, *168*, 16-25.

[68] R. C. Reuel, C. H. Bartholomew, *J. Catal.* **1984**, *85*, 78-88.

[69] R. C. Reuel, C. H. Bartholomew, *J. Catal.* **1984**, *85*, 63-77.

[70] T. Mochizuki, T. Hara, N. Koizumi, M. Yamada, *Appl. Catal. A* **2007**, *317*, 97-104.

[71] G. Jacobs, J. A. Chaney, P. M. Patterson, T. K. Das, B. H. Davis, *Appl. Catal. A* **2004**, *264*, 203-212.

[72] B. Jongsomjit, J. Panpranot, J. G. Goodwin Jr, *J. Catal.* **2003**, *215*, 66-77.

[73] J. Li, N. J. Coville, *Appl. Catal. A* **1999**, *181*, 201-208.

[74] Y. Jin, A. K. Datye, *J. Catal.* **2000**, *196*, 8-17.

[75] M. Boudart, A. Delbouille, J. A. Dumesic, S. Khammouma, H. Topsøe, *J. Catal.* **1975**, *37*, 486-502.

[76] A.-H. Lu, G.-P. Hao, Q. Sun, X.-Q. Zhang, W.-C. Li, *Macromol. Chem. Phys.* **2012**, *213*, 1107-1131.

[77] J. Liu, S. Z. Qiao, Q. H. Hu, G. Q. Lu, *Small* **2011**, *7*, 425-443.

[78] J. Liu, Q. Yang, L. Zhang, H. Yang, J. Gao, C. Li, *Chem Mater.* **2008**, *20*, 4267-4277.

[79] J. Liu, S. Bai, H. Zhong, C. Li, Q. Yang, *J. Phys. Chem. C* **2010**, *114*, 953-961.

[80] J. Liu, S. Z. Qiao, J. S. Chen, X. W. Lou, X. Xing, G. Q. Lu, *Chem. Commun.* **2011**, *47*, 12578-12591.

CHAPTER 2

LITERATURE REVIEW: Recent advances in the synthesis and application of spherical carbons in heterogeneous catalytic reactions

2.1 Introduction

The future development of material science hinges on the ability to control the synthesis of nanomaterials with distinctive morphologies and functional properties.[1] Carbon chemistry is an integral part of the recent revelations seen in nanotechnology for several reasons. These include its abundance and its ability to form many allotropes like diamond, graphite, nanotubes or graphene which exhibit different physical and chemical properties.[2-3] Carbon, the sixth element in the Periodic Table, is unique in the number and variety of ways in which it can bond, leading to a wide range of carbonaceous structures with quite different properties. Carbon has the ability to form long chains of interconnecting C–C bonds and can form covalent bonds with other elements, which are strong and stable. Carbon can have different hybrid orbitals *sp*, sp^2, and sp^3, which allow it to form pentagonal, hexagonal, and heptagonal carbon rings. These distinctive and diverse arrangements allow carbon to form an almost infinite number of compounds and build up to form various shaped carbon materials.[4] Among these materials are an intriguing set of spherical nanostructures called carbon spheres (CSs). The tunable diameter, structural architecture, surface functional groups, porosity and thermal stability of carbon spheres has attracted much attention from material scientists because of their potential applications in catalysis, as adsorbents, and in drug delivery, gas storage and as electrode materials.

Carbon spheres can essentially be thought of as a 0D material composed of curling graphitic flakes with a random twist,[5] with subsequent layers deposited in a manner that follows the curvature of the sphere (Fig. 2.1). The spherical curvature within a layer is due to the different carbon ring sizes that coexist. While flat regions are composed of hexagonal rings, pentagonal or heptagonal carbon rings result in inward positive curvature (+60°) or outward curvature (-60°) respectively.[6] However, the layers within a CS are not closed. This

---

This chapter is still to be submitted for publication as a review article.

arrangement gives CSs many applications in catalysis due to the presence of surface defects.[7] Studying the application of carbon spheres in heterogeneous catalysis is particularly interesting because about 90% of the world's chemical manufacturing processes involve a heterogeneous catalyst in their synthesis methodology. Examples of products from heterogeneous catalytic processes are plastics, polymers, agricultural products, pharmaceuticals, synthetic fibres, paper products, materials for energy production, modern building materials and its well documented use for environmental protection such as in DeNOx catalysts, filters for diesel engines or in photo-catalysis for the treatment of pollutants in wastewater.[8]

Typically, the active phase of a heterogeneous catalyst is dispersed on a porous carrier to enhance its surface area. The nature of the support material is an essential component of a heterogeneous catalyst. It provides mechanical integrity and stabilizes the dispersed catalyst precursor nanoparticles. The use of metal oxides such as TiO_2, SiO_2, MgO or Al_2O_3 as catalyst support materials both industrially and in academia is well documented. However, these oxides possess a strong metal-support interaction which results in the formation of irreducible compounds and therefore attenuates catalyst performance.[9-11] Recent focus has been turning to the use of carbon-based supports because of their relative chemical inertness and the ability to tailor their properties to suit the intended use.

In this section, recent method developments in the synthesis of CSs with various architectures are described. Particular attention has been paid to summarize how synthesis methods of the CSs can be tailored to maximize their potential applications in catalytic systems either by; (1) controlling the size and pore structure, (2) improving their surface chemistry through functionalizing, or (3) improving their thermal stability and degree of graphitization.

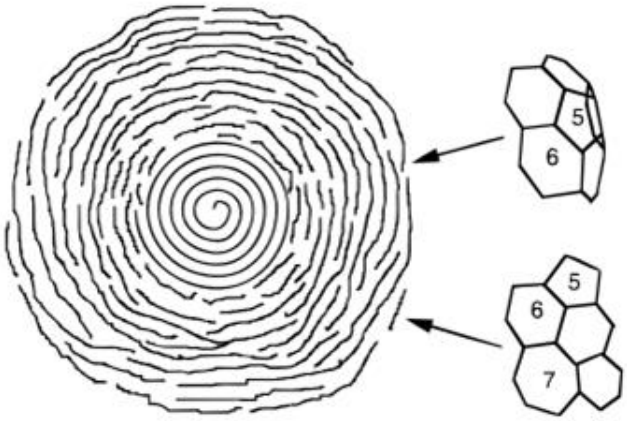

Figure 2.1 Scheme for the formation of a large carbon sphere.[5]

Carbon spheres can generally be categorized using the following criteria:

(a) Their architecture can either be solid, core-shell, yolk-shell or hollow.
(b) The spatial arrangement of the carbon layers can be radial, concentric or consist of random layers.
(c) The sphere diameter: less than 2 nm (fullerenes), 2 – 20 nm (well graphitized spheres), 50-1000 nm (less graphitized spheres) while those larger than 1000 nm are called carbon beads.
(d) Average diameter (d) of pores in their structure: microporous (< 2 nm), mesoporous (2<d<50 nm) or macroporous (> 50 nm).
(e) The method used in CS fabrication.

While these different methods are used for CS classification, it is generally believed that the architecture of CSs influences its properties since the other methods of classification are tunable. Hence CSs have been classified according to their architecture in this work but the other classes of classification have also been discussed.

2.2 Synthesis approaches for the different architectures

2.2.1 Solid carbon spheres

Numerous methods have been developed for the synthesis of solid CSs, including chemical vapour deposition (CVD),[12-13] pyrolysis of organic compounds,[14-15] ultrasonic treatment,[16] a solution plasma process,[17] arc-discharge,[18] polymerization,[19] a microwave-assisted method[20] and hydrothermal synthesis.[21-22] The hydrothermal carbonization method is one of the common approaches for synthesizing monodispersed solid carbon spheres. The hydrothermal synthesis route can be considered to be similar to the natural processes involved in the formation of coal.[23] It involves the decomposition of cheap carbon-containing precursors from the carbohydrate family (e.g. glucose, sucrose, and fructose) or raw lignocellulosic biomass using autogenic pressure and mild reaction temperatures (100 – 300 °C) with subsequent conversion of the carbon source into carbonaceous materials in high-pressure reaction vessels. The synthesis is considered to be "green" as it does not incorporate the use of any organic solvents, catalysts or surfactants.[24] The reaction mechanism for the formation of the carbon spheres involves the dehydration of the carbohydrate into a furan-like molecule (furfural aldehyde and/or 5-(hydroxymethyl)-2-furaldehyde)[25-26] followed by polymerization[27] and carbonization steps. Typically, the prepared materials are hydrophilic in nature as they have several surface functionalities (vide infra).

Ouzzine et al. prepared solid CSs by the hydrothermal treatment of three carbohydrates; glucose (a monosaccharide), sucrose (a disaccharide) and cellulose (a polysaccharide). The CS size (0.72 μm – 12 μm) was shown to be dependent on the carbohydrate concentration. They found that activation by H_3PO_4, KOH, NaOH and CO_2 all improved the textual properties of the carbons, with specific surface areas higher than 3,100 m^2/g.[28] These findings were in agreement with previous reports.[29-30]

The pyrolysis of carbon-rich polymer spheres is also a popular method among scientists for the fabrication of solid CSs. High-temperature carbonization converts the polymer analogues to carbon when performed under inert reaction conditions. For instance, Liu et al. reported the synthesis of monodisperse CSs via an extension of the well-established Stöber method

used in the preparation of colloidal silica spheres. Their approach involved the initial synthesis of resorcinol-formaldehyde (RF) resins by a sol-gel procedure which used ammonia as a catalyst. Subsequently, carbonization done at 600 °C for 4 h converted the polymer resins to high surface area (> 500 m^2/g) carbon spheres with tunable sizes (200 – 1000 nm).[19] Additionally, support materials with large pore sizes are normally required for heterogeneous catalysis applications as they allow smooth diffusion of large reagent molecules through the catalyst bed.[31-33] In the past, nitrogen-doped solid CSs with large mesopores (~16 nm) were synthesized by the self-polymerization of dopamine and the spontaneous co-assembly of polystyrene-*block*-poly(ethylene oxide) [PS-*b*-PEO] micelles (Fig. 2.2). These N-doped carbon materials possess high electrocatalytic activity and stability which is comparable to Pt/C catalysts.[34]

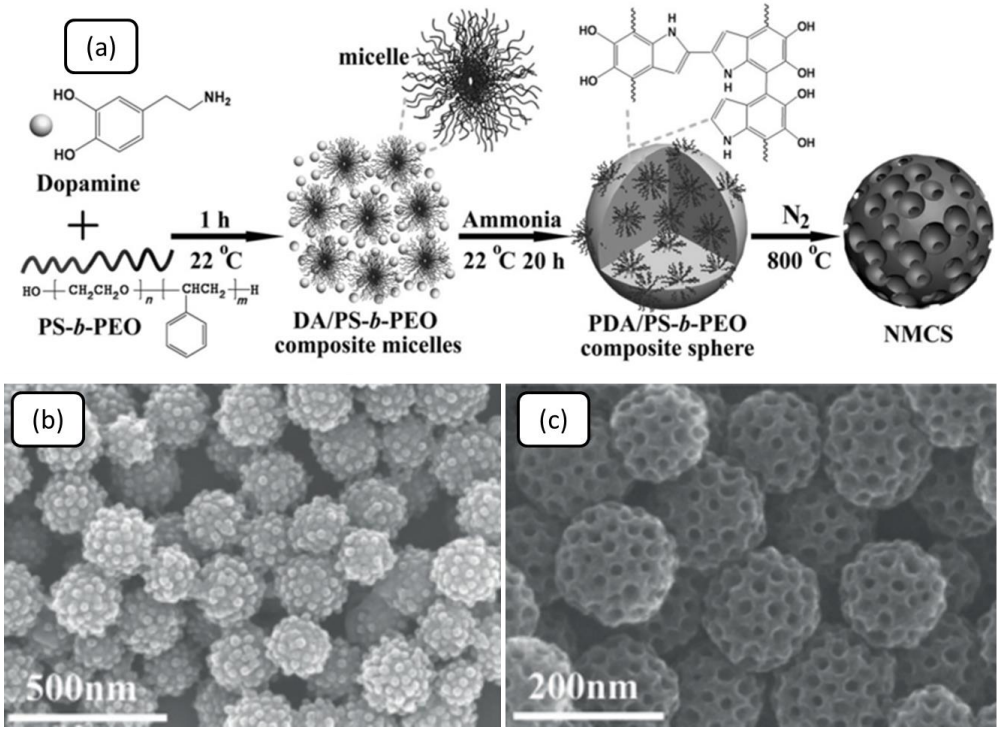

Figure 2.2 (a) Scheme for the formation process of N-doped solid CSs with large pores, and SEM images of (a) PDA/PS_{173}-*b*-PEO_{170} composite spheres before carbonization, (b) N-doped solid CSs after thermal treatment at 800 °C.[34]

Solid CSs are also synthesized by the CVD method which involves the decomposition of a carbon source at high reaction temperatures. This method is non-catalytic hence the products

are of high purity and contain no metal impurities.[35] Qian et al. reported the synthesis of solid CSs by non-catalytic pyrolysis of toluene to produce carbon materials with diameters in the range 60 nm to 1 μm. The sizes of these CSs were controlled by changing the flow-rate and carrier-gas composition.[36] Jin et al. have shown that CVD synthesis of CSs can use a range of hydrocarbons as carbon precursors, such as styrene, toluene, benzene, hexane, cyclohexane or ethene and all produce significant quantities of CSs (diameter: 50 nm to 1 μm) without the use of a catalyst.[15] It has also been proposed that high temperature treatment of CVD-synthesized CSs can alter their properties. For instance, annealing them at 2,800 °C was observed to change their spheroidal morphology into a well-defined polyhedral shape which possess long-range order (Fig. 2.3).[37] Recently, studies investigating the feasibility of large-scale (pilot plant scale) production of solid CSs have been described by Jiménez and co-workers. They successfully generated up to 43 g sample per run by the pyrolysis of benzene in the absence of a catalyst. The CSs also displayed good thermal stability and crystallinity, however, they had low surface areas (< 7 m^2/g) and low pore volumes (< 0.1 cm^3/g).[38]

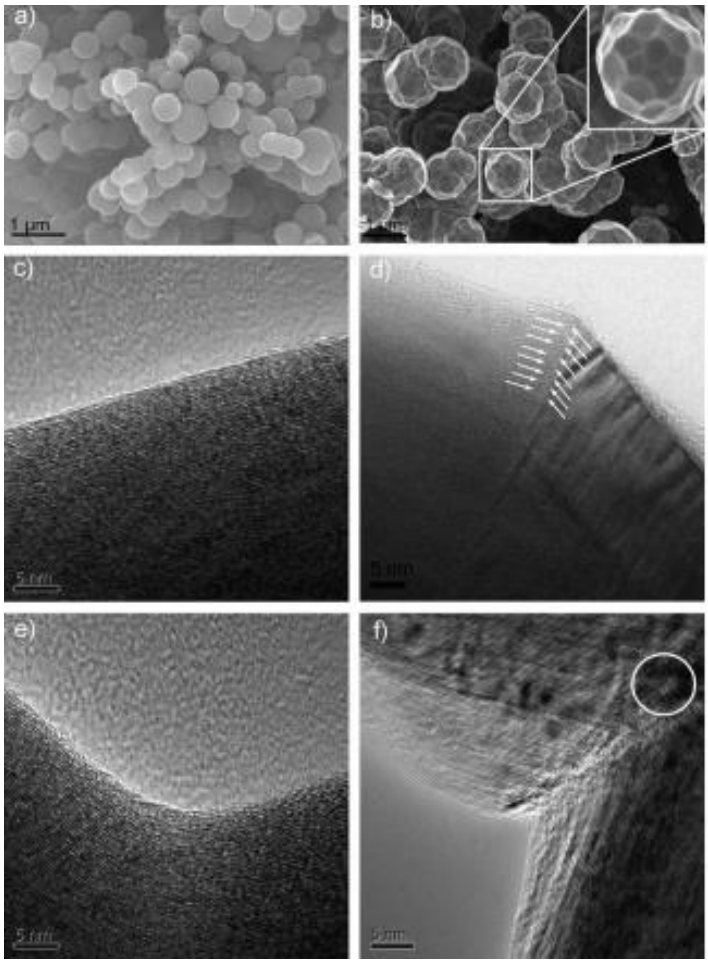

Figure 2.3 SEM images of (a) as-synthesized (CVD) CSs, (b) annealed CSs. Also displayed are HRTEM images of (c) edge of as-prepared CS, (d) edge of annealed CS, (e) coalescence region of two as-prepared CSs, (f) coalescence region of two annealed CSs.[37]

2.2.2 Hollow carbon spheres

The field of hollow structures, which consist of a large interstitial void surrounded by a permeable shell, has been extensively pursued by several research groups because of their unique properties. These include their low density, high surface area and the large variable-sized inner voids. Consequently, these materials find applications in many fields, such as drug storage and delivery,[39] catalysis,[40] energy storage,[41] lithium-ion batteries,[42] water treatment,[43] fuel cells,[44-45] confined synthesis[46] and in optics and electronics.[47] In particular, hollow structures made of carbon, hollow carbon spheres (HCSs), are interesting to synthesize for use as supports for heterogeneous catalyst supports.

For the synthesis of HCSs, templating or scaffolding is the most frequently adopted approach. Synthesis of nanomaterials via the templating approach requires (1) production of the template should be reproducible and be of low cost; (2) simple modification of the surface of the templates; (3) accurate encapsulation of the template by the shell precursor to ensure a uniform layer; and (4) a facile method for the selective removal of the template.[46, 48] Fabrication of HCSs by the template approach is done using either the soft- or hard-template routes as illustrated in Fig. 2.4.

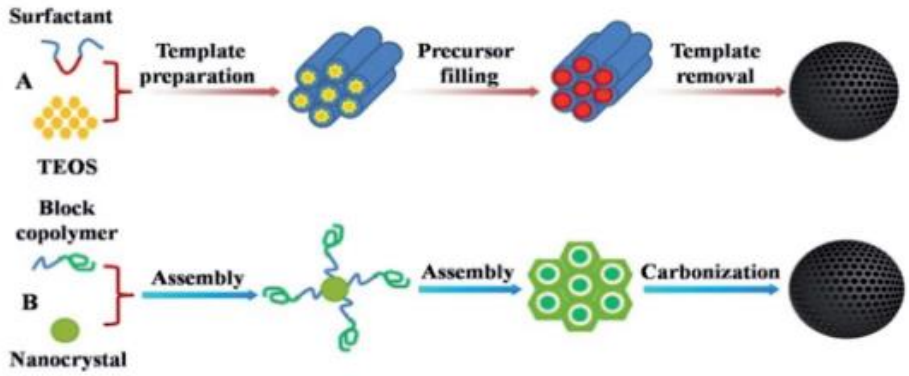

Figure 2.4 Scheme illustrating the differences between (A) hard templating and (B) soft templating approaches.

2.2.2.1 Soft-templating approach

This is a bottom-up synthesis route that uses soft matter, that is, organic molecules or amphiphilic supramolecules such as surfactants and block copolymers which can form vesicle structures that act as templates during synthesis. Vesicle structures typically form through hydrogen bonding and hydrophilic/hydrophobic interactions in aqueous media.[49] The ability of these organic structures to self-organize into a range of supermolecular structures allows for easy manipulation of the pore structure of the nanomaterials. Cooperative interaction between suitable carbon precursors around the supermolecular structures gives a well-defined organic-organic structure.[50-51] The soft template can then either be consumed at later stages of the synthesis or removed by extraction or calcination procedures. It is also possible that the organic molecules can make emulsion droplets which can act as the template in a procedure called self-templating. The latter scenario does not require an additional template removal step.

In the past, reports showed that HCSs in the size range 50 nm to 3 μm can be prepared by the hydrothermal treatment of glucose in the presence of sodium dodecyl sulfate (SDS) as the anionic surfactant.[52] However the synthesized HCSs were polydispersed. Yang and co-workers reported a hydrothermal fabrication of HCSs with a tunable size (200 - 400 nm) and shell thickness (50 - 80 nm) from *α*-cyclodextrin as a carbon precursor and Pluronic F127 as a soft template.[53-54] The HCSs were found to be mesoporous and had high surface areas (>400 m^2/g) and a high specific charge capacity (>450 mAh/g) when applied as an anode material in lithium ion batteries. Elsewhere, small-sized (~20 nm) HCSs also called carbon dots (CDs) have been prepared in a one-step procedure involving mannose as the carbon precursor, octadecene as a non-coordinating solvent and oleylamine as a capping agent.[55] The authors believe that water vapour-generated nanobubbles are the soft template in this procedure. Xu et al. have fabricated uniformly small HCSs (69 nm) with exceptionally high surface areas (3022 m^2/g) by using Triton X-100 surfactant as a template and utilizing aniline and pyrrole as co-monomers (Fig. 2.5). The large surface areas measured on these HCSs were obtained by carbonizing the polyaniline-co-polypyrrole (PACP) intermediate for 20 h, which simultaneously reduced the outer diameter from 106 nm (PACP) to 69 nm.[56]

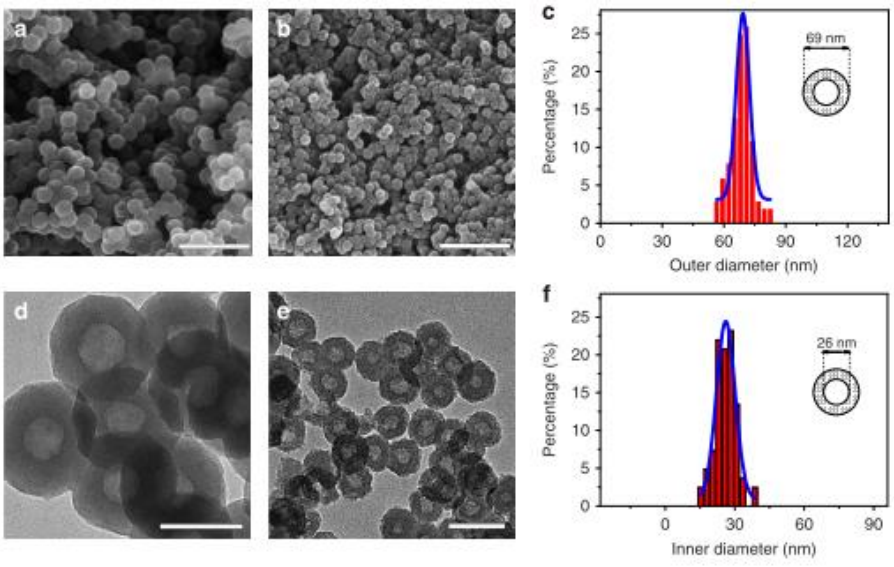

Figure 2.5 Scanning and transmission electron microscopy images of (a, d) PACP intermediate and (b, e) HCSs after a 20 h carbonization procedure. The outer and inner diameters of the HCSs are displayed in (c) and (f) respectively. Scale bars: 500 nm (a, b), 100 nm (d) and 200 nm (e).[56]

General advantages of soft-templating are that it does not require the use of hazardous chemicals such as HF or NaOH for template removal and it also has less synthesis steps which enhances its scalability prospects. The major drawback associated with this approach is the lack of reproducibility when synthesis is done in large quantities.

2.2.2.2 Hard-templating approach

The hard templating technique involves prior preparation of solid particles which are used as a template. This approach requires an additional synthesis step for the removal of the sacrificial template after the formation of the carbon shells around them. This is achieved via dissolution, etching or calcination procedures. Properties of the HCSs such as their diameter, dispersity and morphology are inherited from the template hence controlling these properties usually requires tuning the synthesis conditions for the hard template.

Monodispersed silica spheres with a size range of 50 to 2000 nm[57] have been widely used as a solid template for HCS synthesis. These spheres are typically fabricated using the Stöber method or with slight variations, to gives silica spheres which are uniform in size and monodispersed. The method is highly reproducible. In the Stöber method, colloidal silica spheres are produced through the hydrolysis of silicon alkoxides such as tetraethyl orthosilicate (TEOS) in an ethanolic solution (water-ethanol) by utilizing ammonia as a catalyst (Eq. 2.1) and the concurrent condensation of silanol groups to produce siloxane bonds (Si─O─Si) and the by-products which are alcohol (Eq. 2.2) and water (Eq. 2.3).[58] Not only does ammonia catalyze the hydrolysis and condensation steps of this sol-gel synthesis, it also inhibits aggregation of the silica particles by forming a positively charged layer of NH_4^+ ions on their surface.

Hydrolysis: $\equiv Si{-}OR + H_2O \leftrightarrows \equiv Si{-}OH + ROH$ (2.1)

Alcohol condensation: $\equiv Si{-}OR + HO{-}Si\equiv \leftrightarrows \equiv Si{-}O{-}Si\equiv + ROH$ (2.2)

Water condensation: $\equiv Si{-}OH + HO{-}Si\equiv \leftrightarrows \equiv Si{-}O{-}Si\equiv + H_2O$ (2.3)

where R is an alkyl group, C_nH_{2n+1}

Varying the sizes of silica spheres produced this way entails changing the water-to-alcohol ratio, TEOS and ammonia concentration or the chain length of the alcohol used. For example, Malay et al. compared the use of methanol, ethanol, propanol and butanol as the alcohol in colloidal silica fabrication. After monitoring the particle sizes using dynamic light scattering (DLS) they were able to demonstrate that the diameter of the particles increased with an increase in the molecular weight of the alcohol solvent.[59]

Encapsulation of the silica with a carbon precursor can be done using one of these methods; hydrothermal synthesis, polymerization or chemical vapour decomposition. Here, the most commonly used carbon precursors include hydrocarbons such as toluene, benzene or styrene and low molecular weight polymeric mixtures of formaldehyde like phloroglucinol-formaldehyde (or PF resin), phenol-formaldehyde (or resol) and resorcinol-formaldehyde (or RF resin). Recently, Tang et al. synthesized N-doped HCSs with large mesopores (~20 nm) via a dual-template approach involving colloidal silica and the amphiphilic block copolymer polystyrene-b-poly(ethylene oxide) [PS_{173}-*b*-PEO_{170}].[60] These materials present new potential applications in heterogeneous catalysis because of their large and tunable pore sizes (Fig. 2.6).

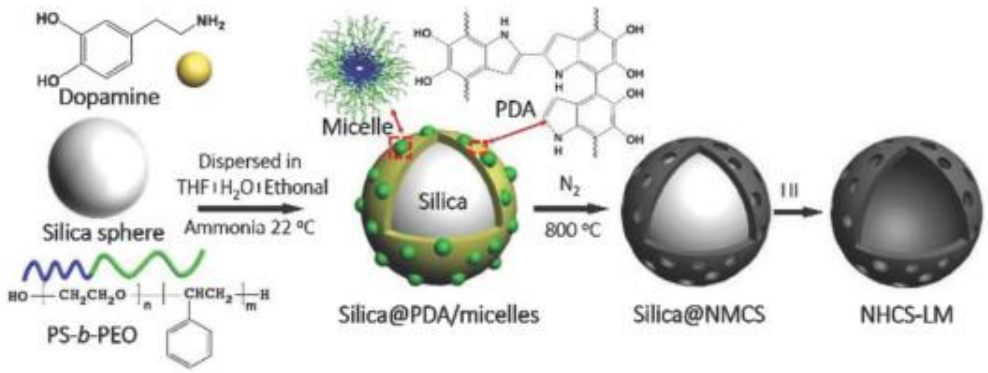

Figure 2.6 Schematic illustration of the preparation of N-doped HCSs with large mesopores.[60]

It is often desirable to functionalise the surface of the template in order to tailor specific surface area, pore size and the pore structure of the final nanostructure. In 2011, Chen et al. functionalized silica spheres with a mesoporous layer of silica to form a SiO_2@m-SiO_2 template (Fig. 2.7). The procedure utilized the surfactant CTAB (cetyltrimethylammonium bromide) as a structure directing agent. The authors observed two effects associated with CTAB use; first it promoted carbon deposition onto the silica template which led to higher yields, and secondly, it resulted in high surface area (771 m^2/g) mesoporous hollow carbon spheres which had a pore structure identical with that of MCM-41.[61]

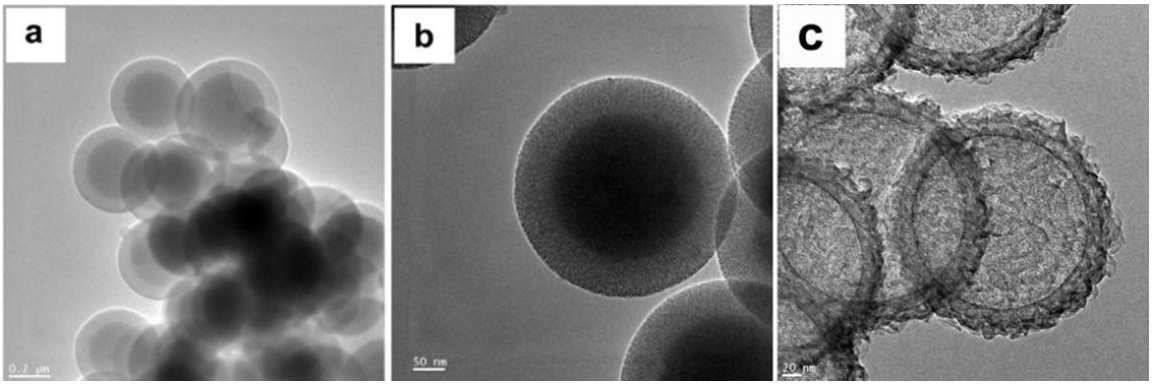

Figure 2.7 TEM images of (a, b) SiO_2@m-SiO_2 and (c) mesoporous HCSs.[61]

2.2.3 Core-shell carbon spheres

Core-shell structures involve the innovative encapsulation of a core by a shell which is chemically different and therefore allows for the fabrication of materials with multiple functionality such as hydrophilic/hydrophobic amphiphilicity. Uniform core–shell nanoparticles with different functional compositions are being widely investigated because of their potential applications in drug delivery, catalysis, photonic crystals, bio-diagnostics and energy storage.[62] The interest in core-shell structured materials arises due to the advantages which result from having the encapsulated cores being of different chemical compositions from the polymeric or inorganic shell. Core-shell mesoporous spheres comprising of an active metal precursor as the core and a mesoporous shell are a suitable candidate for nanoparticle immobilization in catalysis because the porous shell prevent particle agglomeration and their thin shells ensures a short diffusion distance of reagent molecules.[63] The use of carbon-based shells to encapsulate metallic cores is particularly interesting because of carbon's relative chemical inertness and its tunable pore structure.

Fabrication of core-shell structures involves the carbon-encapsulation of pre-formed metallic cores (M) by polymerization of carbon precursors such as polydopamine,[64] resorcinol-formaldehyde,[65] or polystyrene, poly(acrylic acid).[66] The formed composites (referred to as M@polymer) are then carbonized at high temperature to give the M@C core-shell nanostructures. For instance, Zhang and co-workers reported the synthesis of monodisperse Fe_3O_4@C spheres via the polymerization of a resorcinol-formaldehyde carbon source on the surface of pre-formed Fe_3O_4 particles as shown in Fig. 2.8.[67] The uniform carbon shell's thickness on these spheres was tunable (20 – 100 nm) by a simple variation of the Fe_3O_4 to RF ratio.

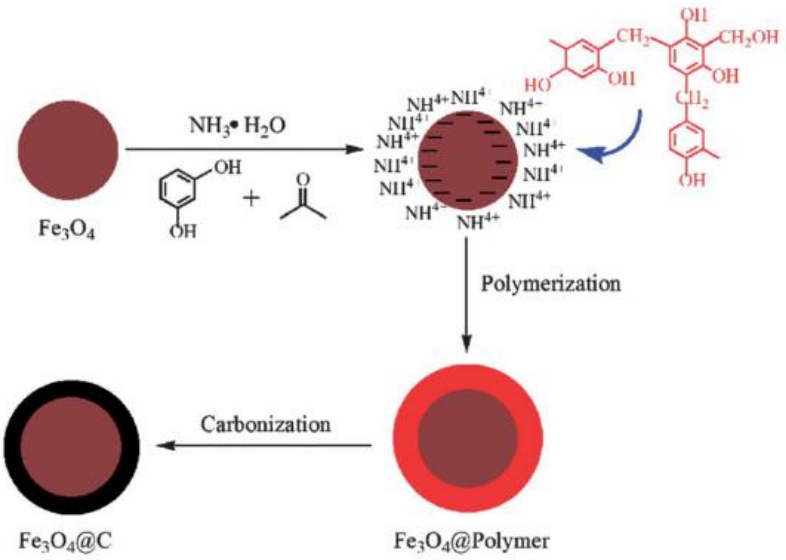

Figure 2.8 Representation of the mechanism for the fabrication of Fe_3O_4@C core-shell spheres.[67]

Elsewhere, core-shell spheres of the form M@C (M = Au, Pt, Pd) have been fabricated via a one-step synthesis method involving a 30 minutes reflux of an aqueous mixture composed of the metal precursor, carbon source and ammonia as the catalyst (Fig. 2.9). The authors reported increased shell thickness (~20 nm to ~150 nm) by controlling the carbon source concentration, while the metal core size (28 nm - 53 nm) was shown to be related to the amount of the ammonia catalyst added during the synthesis.[68] The proposed method was

shown to be versatile as it worked uniformly irrespective of whether the core metal particles were for Au, Pt or Pd.

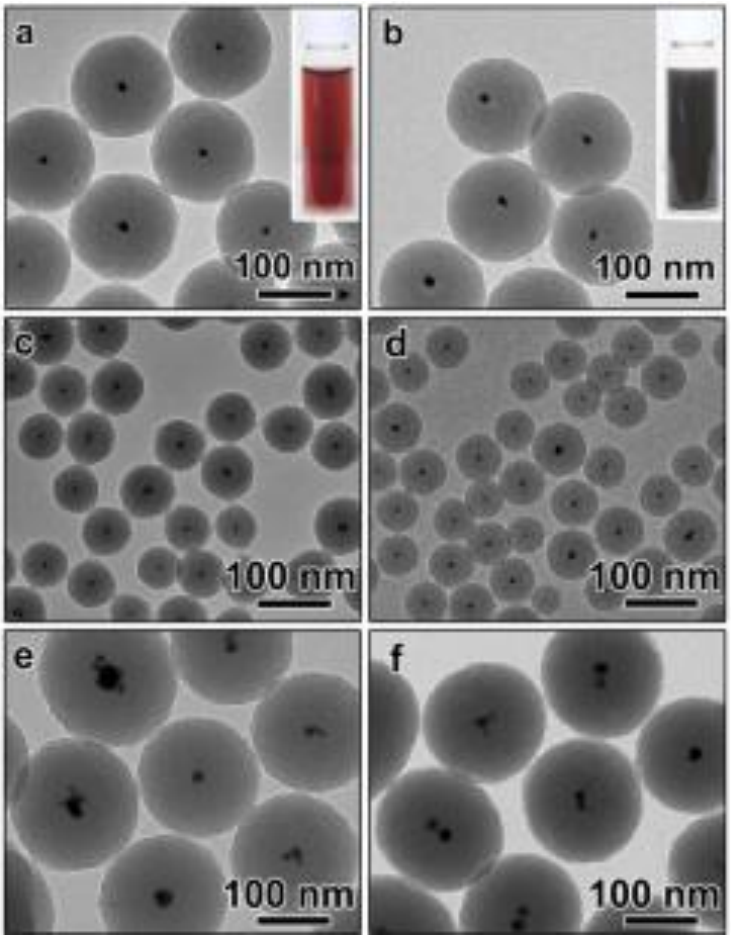

Figure 2.9 TEM images of M@RF and M@C core-shell spheres, (a-b) Au@RF and Au@C, (c-d) Pt@RF and Pt@C, (e-f) Pd@RF and Pd@C.[68]

2.2.4 Yolk-shell (or rattle-type) carbon spheres

For nanostructures with a core-shell morphology, the core materials are compactly stuck to the shell materials, and therefore their catalytic performance compromised to some extent. Structures with a yolk-shell architecture promise to be a solution to this challenge.[69] Yolk-shell structures (also called rattle-type structures) are a special type of the core-shell morphology, the distinction being that they possess tunable interstitial spaces between the metallic core and the porous carbon shell. The cores of such novel materials can be considered to be "moveable" hence they are also referred to as rattle-type structures (Fig. 2.10).

Yolk-shell structures are an innovative and promising approach for making stable catalysts, and are based on the incorporation of the metal nanoparticles into a porous shell thus limiting particle leak and sintering during high temperature reactions.[8] The properties of the shell can then be engineered accordingly for improved performance in their applications. These include: (1) to have high porosity, (2) have a specific pore structure, and (3) be stable at the temperatures at which the reactions will be conducted. For example, Fang and co-workers showed the efficient use of mesoporous carbon@mesoporous silica rattle-like nanospheres for loading anticancer multidrug-based combination therapy systems. The advantage of this architecture was that the hydrophobic mesoporous carbon cores were found to have good affinity with water-insoluble drugs, whereas the biocompatible hydrophilic mesoporous silica shell had good affinity with water-soluble drugs.[70]

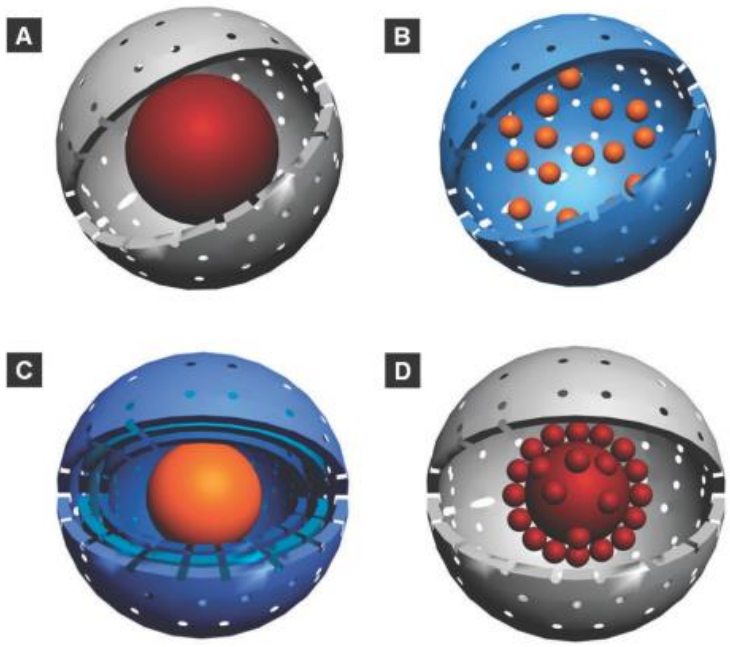

Figure 2.10 Representation of yolk-shell nanoparticles with different structures: (A) structure with a single core, (B) structure with multiple cores, (C) structure with multiple shells, and (D) structure with a raspberry-like core.[71]

Synthesis of yolk-shell carbon-based materials can be done either by the selective etching (dissolution method) or by the bottom-up approach which uses soft templating. The selective

etching method is the more common of the two. In this process, a pre-synthesized metal core is encapsulated by two chemically different layers, the inner layer is typically silica while the outer layer is carbon (represented as metal@silica@C). This three-layered structure has an egg-like composition similar to the 'yolk, egg white, and eggshell'.[72] Subsequently, the inner silica layer (i.e. the egg white) is selectively etched out using an appropriate solvent or by calcination to yield the rattle-type 0D material which is represented as metal@C structure. The outer carbon shell on this type of architecture serves as a barrier for preventing nanoparticle leak and coalescence during high temperature reactions. By using this approach, Liu et al. fabricated Ag@C yolk-shell nanoparticles by the carbonization of a resorcinol-formaldehyde composite (i.e. Ag@SiO_2@RF) followed by the selective etching of silica.[73] This one-pot synthesis approach is made possible by the by the different polymerization rates of silica and resorcinol-formaldehyde even when performed under identical reaction conditions (similar solvents, room-temperature synthesis, ammonia catalyst).[74] Silica quickly polymerises to form a Ag@SiO_2 core-shell structure, while the polymerization of resorcinol-formaldehyde to form Ag@SiO_2@RF is a slower process. Wang et al. also used a similar approach to prepare rattle-structured Fe_3O_4 spheres by selectively etching out silica from a Fe_3O_4@SiO_2@RF hybrid structure.[75]

The selective etching method has also been employed in the synthesis of rattle-type materials by evaporation of the inner (egg white) layer. Hong and Kang recently proposed the fabrication of Sn@C hybrid structures by a simple two-step method which included the evaporation of Zn which was embedded in the core of the material.[76] They first prepared core-shell SnO_2-ZnO@C spheres by a one-pot spray pyrolysis process which were later transformed into yolk-shell Sn@C microspheres by heat-treatment at 1000 °C under reducing conditions. The vaporization of reduced Zn metal generated a large void between the carbon shell and the Sn metal (Fig. 2.11).

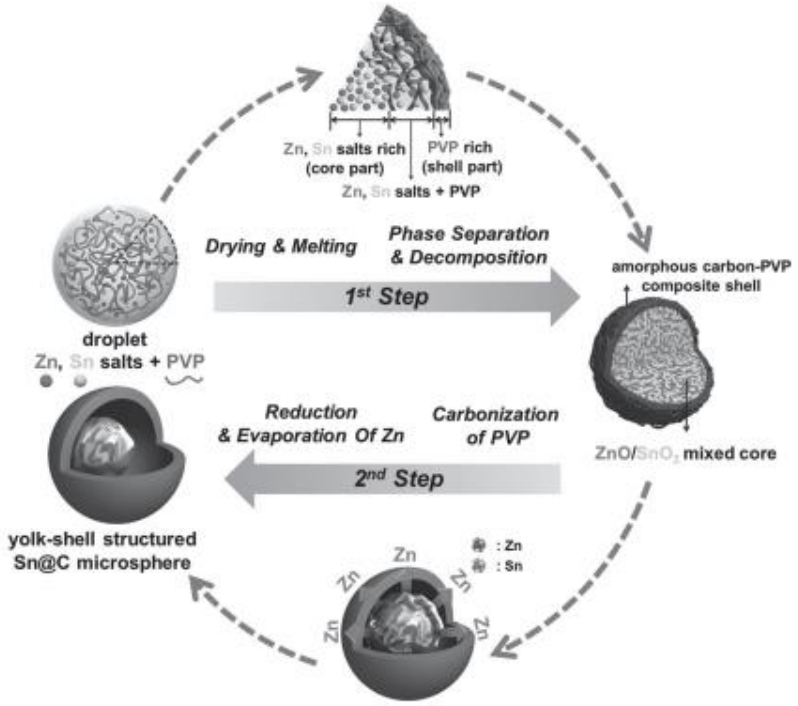

Figure 2.11 Schematic representation of the formation mechanism of yolk-shell Sn@C carbon spheres.[76]

Synthesis of yolk-shell structures can also be achieved via the bottom-up approach which utilizes soft templates. Kao et al. have demonstrated a facile approach to prepare such rattle-type nanomaterials in which Ag nanoparticles are the core enclosed in a carbon shell.[77] They first encapsulated the Ag nanoparticles (31 ± 5 nm) in a sodium dodecyl sulphate (SDS) surfactant to form a Ag@SDS core-shell structure. A layer of carbon was then introduced to the Ag@SDS composite by the hydrothermal treatment of a glucose carbon precursor. The size of the interstitial void in the yolk-shell Ag@C hybrid structure was determined by the concentration of the SDS anionic surfactant.

Carbon-based core-shell nanostructures can also be fabricated to possess multiple core particles per hollow carbon sphere. For instance, Zheng et al. reported the synthesis of core-shell carbon spheres with multiple cores of the form M@carbon (M = Sn, Pt, Ag, Fe–FeO nanoparticles) via ultrasonic spray pyrolysis of aqueous solutions containing sodium citrate and corresponding inorganic metal salts.[78] The mechanism involves first the generation of

metal nanoparticles by reduction of the metal salts using hot sodium citrate, followed by the formation and subsequent carbonization of sodium citrate to form the outer carbon shell. Residual water-soluble by-products are removed by a simple washing step. Fuertes et al. reported the synthesis of M@carbon (M = Fe_2O_3, Fe_3O_4, $CoFe_2O_4$, NiO, Cr_2O_3) by a simple impregnation of the inorganic precursors dissolved in ethanol into pre-synthesized hollow carbon spheres. [79] The generated core-shell materials had large surface areas (> 500 m^2/g), high pore volumes (> 0.3 cm^3/g) and the pore structure was mainly composed of mesopores. Recent studies by Hao and co-workers have also proposed a procedure for the synthesis of yolk-shell hybrid materials M@carbon (M = Cu, NiO) via a one-step co-pyrolysis method which utilized a metal-oleate complex and phenolic resin monomers as raw materials (Fig. 2.12).[80]

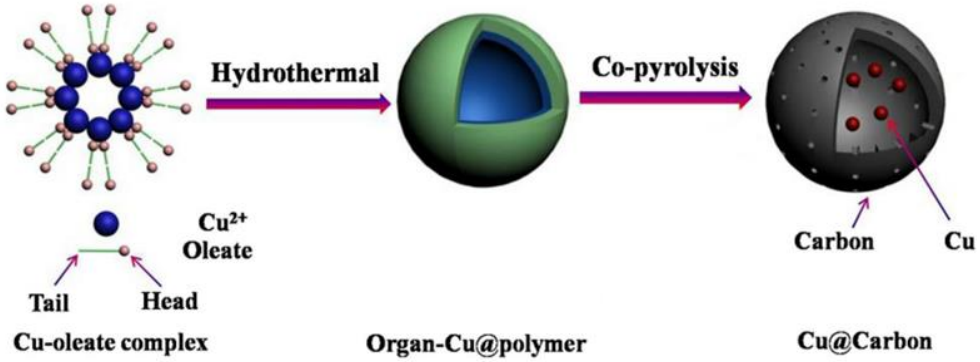

Figure 2.12 Schematic illustration for the preparation of Cu@C yolk-shell nanospheres with multiple cores.[80]

Recently, the procedures for the fabrication of yolk-shell particles have been extended for use in the synthesis of nanostructured materials with multiple (two or more) shells and are expected to have better performances over their single-shelled counterparts for various applications. For example, Wang and co-workers synthesized multiple-shells of Co_2SnO_4 and SnO_2 (Fig. 2.13) which have a mesoporous pore structure by annealing $CoSn(OH)_6$ under inert conditions. These multiple-structured nanomaterials displayed superior activity for the degradation of organic pollutants since they are photocatalysts. This morphology increased the surface area of the material and thus the available active sites for adsorption of the organic pollutants, while the thin shells enhanced diffusion of electron-hole pairs which are generated on the surface of the photocatalysts.[81]

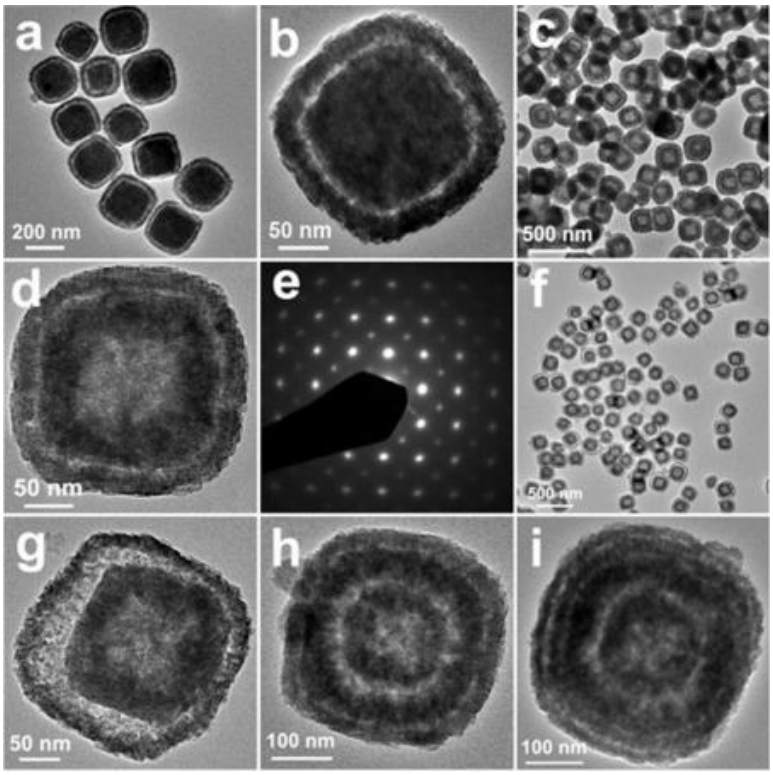

Figure 2.13 Transmission electron microscopy images of $CoSn(OH)_6$ with multiple-shell hollow structures: (a, b) yolk–shell particles; (c, d) double-shelled structures; (e) SAED pattern of a double-shelled structures; (f, g) double-shelled structures with larger inter-shell cavities; (h) a triple-shelled structure; and (i) a quadruple-shelled structure.[81]

2.3 Functionalization of carbon spheres

The functionalization of spherical carbons is a vital step in tailoring their properties for their intended use. The widely used procedures for functionalizing CSs involve surface oxidation and heteroatom introduction which can be done during synthesis or via post-synthesis treatments.

2.3.1 Oxidative treatments

This is a non-selective liquid-phase procedure for introducing various oxygen-containing groups such as carboxyl group, quinone, ether, phenol, lactone, acidic anhydride or ketones to the surfaces of the carbons. The presence of these oxygen-containing functional groups on carbon surfaces increases the surface acidity and adsorption ability.[82-84] Due to the relative

chemical inertness of carbon, post-synthesis introduction of these functional groups is usually done under harsh reaction conditions using oxidizing agents like hot nitric acid, sulphuric-nitric acid mixture, potassium permanganate or hydrogen peroxide. The one-pot hydrothermal synthesis of CSs yields materials with surface oxygen-containing functional groups and hence oxidative treatments are not required.[85-86]

2.3.2 Heteroatom introduction (doping)

The introduction of heteroatoms such as nitrogen, boron, phosphorous or sulphur into the carbon framework of carbons (called doping), continues to draw extensive attention, because it brings additional advantages such as creation of more active sites and allow the introduction of new properties such as increased electrochemical catalytic activity, hydrophilicity, electrical conductivity and higher selectivity towards selected catalysis applications.[87] Interest in doping of carbons originates from the ability to modify the electron donor/acceptor characteristics of carbons and this results in the enhancement of the electro-chemical properties of carbon.

Doping carbons with nitrogen endows the materials with additional surface nucleation sites which, in catalysis, can serve as anchorage sites thereby improving the dispersion of catalyst nanoparticles on the support material. Additionally, nitrogen-doped materials have a stronger metal-support interaction relative to pristine ones which can be advantageous as it enhances the stability of the catalyst for reactions done at elevated temperatures. These benefits are due to the attributes of nitrogen which include the strong electron donor behaviour of nitrogen which leads to enhanced bonding. The incorporation of N into a carbon lattice can take one of three common bonding configurations, i.e., quaternary (or graphitic), pyridinic and pyrrolic. Nitrogen-rich compounds such as acetonitrile,[88] phenylenediamine,[89] polyaniline,[90] and melamine[91] are typically used as precursors for the fabrication of N-doped nanomaterials. Generally, catalysts supported on N-doped CSs display improved activity and selectivity which has been attributed to: (a) the nitrogen functionalized surface influences particle deposition by altering nucleation and particle growth kinetics thereby resulting in smaller, more uniform nanoparticles which tend to be highly dispersed on the support material, (b) modified electron donor/acceptor characteristics on the surface on the material, and (c)

improved stability of the catalyst during the reaction because of the lone pair of electrons on N which acts as an anchor for the nanoparticles and minimizes sintering at high reaction temperatures.

In the past, boron has also been suggested as a dopant for carbon materials because it is only one electron less than C, has a comparable atomic radius to carbon and can therefore be easily incorporated into the carbon framework. Doping carbons with boron is of interest because it improves the mechanical and electrical properties of carbon.[92-95] During the interaction between a tri-coordinate boron centre and an adjacent π-electron system, the vacant p_z B-orbital exerts a strong π-acceptor effect which results in an extension of the π-conjugation pathway. The interaction is more pronounced in the ground state LUMO than the HOMO thereby resulting in a decrease of the HOMO-LUMO gap. This decrease renders the boron-doped carbon material a better electron acceptor.[96-98] It has been shown using electron energy loss spectroscopy (EELS) that B-doped carbon materials have a lower Fermi energy level which creates new empty π states into which the 1s electrons can be excited.[99] It is these exciting properties that have allowed boron-doped carbons to be utilized as an efficient metal-free electro-catalyst for the oxygen reduction reaction in fuel cells instead of the precious Pt metal.[100]

Pioneering work by Mondal et al. proposed the synthesis of boron-doped CSs by non-catalytic chemical vapour deposition (800 °C) using acetylene as a carbon source and boron trifluoride in methanol as the boron source. The B-doped materials which were prepared this way had significantly different electrical conduction properties relative to pristine carbon spheres.[101] Subsequent work on the fabrication of boron-doped hollow carbon spheres has also been done via CVD injection method. This was achieved by the injection of a solution containing boron trichloride and heptane/toluene onto pre-synthesized Stöber silica spheres (900 °C). The boron-doped HCSs displayed enhanced thermal stability in oxidizing conditions relative to the undoped material.[102-103]

While N-doping of carbon materials tends to decrease the thermal stability, B-doping has been shown to improve the thermal stability of the materials relative to the pristine ones.

Furthermore, Chen et al. compared DFT calculations of palladium adsorption on N- and B-doped carbons. While it was observed that both doped materials displayed improved Pd adsorption, the authors found that the enhancement of Pd adsorption was more significant on B-doped support than it was for when nitrogen was utilized as the dopant under similar conditions.[104]

2.4 Applications of CSs in catalysis

Spherical carbons of varying architectures can be utilized in several heterogeneous catalytic reactions which vary in terms of complexity, selectivity towards products, liquid/gas phase reactions and as metal-free catalysts. For instance, Wang et al. recently reported a novel PtCo bimetallic yolk-shell catalyst with excellent catalytic performance for the hydrogenolysis of 5-hydroxymethylfurfural (HMF) to 2,5-dimethylfuran (DMF) (98% yield after 2 h), a biomass-derived liquid fuel.[105] From the many applications of CSs in heterogeneous catalysis, particular attention has been given to Fischer-Tropsch synthesis, oxidative reactions, photocatalysis, reductive and hydrogenation reactions.

2.4.1 Fischer-Tropsch (FT) synthesis

The use of carbon spheres as a support for FT catalysts is due to their advantages of minimal surface energies, controllable sizes and morphologies, tunable chemical properties and high mechanical stability of the CSs. Unlike conventional metal oxide supports like TiO_2, SiO_2 or Al_2O_3 which tend to react with the cobalt FT catalyst precursor to form the $CoTiO_4$, Co_2SiO_2 or Co_2AlO_4 complexes, the relative chemical inertness of carbon supports makes them ideal model supports for FT catalysts. CVD-synthesized solid carbon spheres have been shown to be a better support for Co FT catalysts than carbon nanotubes because they are easier to prepare and contain no metal impurities.[106] Studies by Moyo et al. showed that oxidative treatment of the solid CSs using $KMnO_4$ was superior to the traditional HNO_3 treatment as it produced more functional groups on the carbon surface and these materials showed higher selectivities towards heavy hydrocarbons during FT synthesis.[107] Recently, yolk-shell Ru@C catalysts were demonstrated to be highly active in FT synthesis. In this yolk-shell architecture the ruthenium nanoparticles are partially embedded in the carbon support thus

anchoring them. This minimizes sintering during the reaction as the mobility of the nanoparticles is reduced.[108]

2.4.2 Oxidative reactions

Solid carbon spheres have been successfully used as a catalyst support for several oxidative reactions. Han et al. have used low surface area solid CSs (*d*: 0.42 – 4.5 μm) to disperse Pd-Fe bimetallic catalysts with good activity for low temperature CO oxidation. The authors demonstrated that the sphere diameter affected catalyst activity and a catalyst supported on smaller spheres achieved complete oxidation at 75 °C while larger spheres achieved it at 50 °C.[109] Hollow carbon sphere supports have also been utilized in oxidative reactions. For example, Ravat and co-workers showed that HCSs are excellent support materials for palladium catalysts for use in the solvent-free oxidation of benzyl alcohol into benzaldehyde because up to 90% conversions are possible. Additionally, doping the HCSs with boron was seen to improve the activity of the catalysts as complete conversion of benzyl alcohol was observed.[102] Meanwhile Zhang et al. found that Pt supported on N-doped HCSs had better activity, CO tolerance and stability than Pt supported on N-doped porous carbon or a commercial Pt/C catalyst in the methanol oxidation reaction (MOR) for fuel cells application.[110]

2.4.3 Photocatalysis

The spherical morphology of CSs combined with surface defects which are generated during synthesis make them suitable for use in photocatalysis. Mahajan et al. has used undoped solid spheres as a photocatalyst for the degradation of methylene blue dye which was used as a model organic pollutant under UV–vis light irradiation. This study was significant as it illustrated that CSs can quickly (5 h) degrade organic pollutants up to 65% without the use of costly noble metals as catalysts.[111] In the past, CdS quantum dots (QDs) dispersed on N-doped HCSs displayed superior activity and photostability in visible-light-induced H_2 production compared to other materials (e.g. CdS/SiO_2).[112] The authors attributed this behaviour to the promoted separation and mobility rate between the CdS QDs and the N-HCSs.

2.2.4 Reduction reactions

In the past, transition metals supported on spherical carbons have been used to catalyse reduction processes. For example, Zheng et al. utilized Au-loaded solid CSs to catalyse the reduction of 4-nitroaniline into 4-phenylenediamine by $NaBH_4$ with 100% conversions, while the unstable Au nanoparticles only resulted in 72% conversions (Fig. 2.14).[113] Zhang et al. reported the use of a novel RGO@Pd@C yolk-shell structure to catalyse the reduction of 4-nitrophenol to 4-aminophenol. These double-shelled structures are composed of reduced graphene oxide (RGO) as inner shell and a carbon (C) layer as the outer shell, and were used to encapsulate Pd nanoparticles. The use of RGO@Pd@C nanoparticles allowed the reduction process to be completed within 30 seconds even with only a 0.28 wt% loading of Pd.[114] This reduction (4-nitrophenol to 4-aminophenol) has also been catalysed by Au@C yolk-shell nanoparticles and fast reaction kinetics were observed.[62, 115] Core-shell structured carbon spheres have also been used to catalyse reduction reactions. For example, Kim et al. used Pd@C core-shell catalysts for the reduction of nitrobenzene to aniline in the presence of sodium borohydride. Higher nitrobenzene conversions were observed on the core-shell catalyst than on unsupported Pd particles due to improved catalyst dispersion.[116]

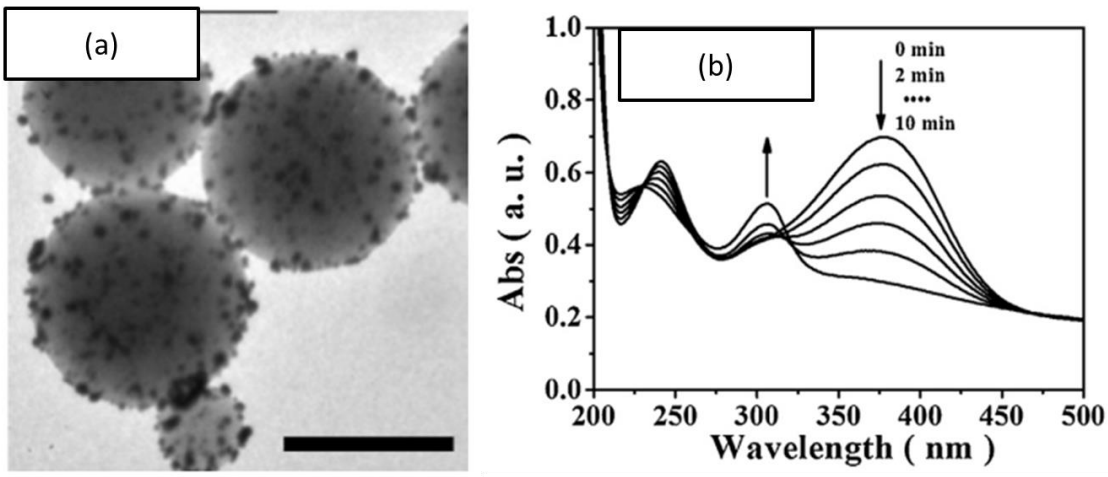

Figure 2.14 (a) TEM image of Au-loaded solid CSs, (b) UV-vis spectra of the Au/CSs catalyzed reduction of 4-nitroaniline (380 nm) into 4-phenylenediamine (320 nm). Scale bar: 200 nm.[113]

2.2.5 Hydrogenation reactions

The excellent properties of CSs have also been exploited in hydrogenation reactions. For example, high surface area (445 m^2/g) Pd@C yolk-shell nanoparticles have been employed to catalyse the industrially important hydrogenation of chlorobenzene to benzene. Conversions of around 72% were measure after 90 min, with complete selectivity for the benzene product. This material was very stable during the reaction as the chlorobenzene conversion rate and selectivity remained unchanged after 5 cycles. For comparison, a Pd catalyst supported on activated carbon was also evaluated under similar conditions. While the latter catalyst displayed a higher conversion rate for the first cycle (81%), the catalyst was unstable and a conversion rate of 58% was measured after 5 cycles.[68]

2.5 Concluding remarks and outlook

Recent years have seen tremendous growth in the understanding of (a) the controlled fabrication of carbon spheres with different architectures and properties, (b) surface enrichment of carbons through doping with heteroatoms or functionalization, and (c) the effect that the carbon spheres nanoarchitecture and properties has in the application of the materials in heterogeneous catalysis. This understanding has fast-tracked the use of carbon spheres as support materials or metal-free catalysts in several heterogeneous catalysis reactions. However, challenges still exist in this area. For instance, while most properties of carbon spheres can be readily tuned for their intended application, this, however usually involves additional steps during their synthesis which makes large-scale production of these materials cumbersome. An example is the use of structure directing agents like surfactants for controlling the pore structure of hollow and yolk-shell carbon spheres requires several additional steps. The use of one-step or one-pot procedures which produces materials with the desired properties still remains unsolved.

Advantages associated with doping carbon spheres have been well demonstrated both on the properties of the CSs and on their performance in catalysis reactions. Recent studies have shown that doping using a post-synthesis procedure is better than in situ doping when the materials are used for catalysis applications. Post-synthesis doping is still not well understood and still warrants further study. Moreover, many reports exist in the literature on the

application of carbon spheres with different morphologies in heterogeneous catalysis. These reports have been useful in understanding how changing the properties of the nanostructure can influence its catalytic performance. Nonetheless, effects associated with the use of one morphology over another have still not been explored in detail. This is a challenge because the various morphologies require different synthesis approaches which results in materials with dissimilar inherent properties, making comparative studies difficult. In this study, we have used CSs to study certain important aspects of the FT reaction such as the Fe-Co bimetallic system. It is well documented that the activity of either Fe or Co in FT synthesis is dependent on the interfacial interaction with oxidic supports typically used. This metal-support interaction is strong in nature hence the study of Fe-Co bimetallic catalysts on oxide supports is complex. Therefore the use of a relatively inert CS support is an ideal probe on to the phases that form during calcination and activation steps of these systems.

References

[1] R. J. White, R. Luque, V. L. Budarin, J. H. Clark, D. J. Macquarrie, *Chem. Soc. Rev.* **2009**, *38*, 481-494.

[2] M. Antonietti, K. Müllen, *Adv. Mater.* **2010**, *22*, 787-787.

[3] V. G. Pol, J. Wen, K. C. Lau, S. Callear, D. T. Bowron, C.-K. Lin, S. A. Deshmukh, S. Sankaranarayanan, L. A. Curtiss, W. I. F. David, D. J. Miller, M. M. Thackeray, *Carbon* **2014**, *68*, 104-111.

[4] A.-H. Lu, G.-P. Hao, Q. Sun, X.-Q. Zhang, W.-C. Li, *Macromol. Chem. Phys.* **2012**, *213*, 1107-1131.

[5] Z. L. Wang, Z. C. Kang, *J. Phys. Chem.* **1996**, *100*, 17725-17731.

[6] S. lijima, T. Ichihashi, Y. Ando, *Nature* **1992**, *356*, 776-778.

[7] A. Nieto-Marquez, R. Romero, A. Romero, J. L. Valverde, *J Mater. Chem.* **2011**, *21*, 1664-1672.

[8] L. De Rogatis, M. Cargnello, V. Gombac, B. Lorenzut, T. Montini, P. Fornasiero, *ChemSusChem* **2010**, *3*, 24-42.

[9] N. E. Tsakoumis, M. Rønning, Ø. Borg, E. Rytter, A. Holmen, *Catal. Today* **2010**, *154*, 162-182.

[10] D. Song, J. Li, *J. Mol. Catal. A* **2006**, *247*, 206-212.

[11] J. W. Bae, S.-M. Kim, S.-H. Kang, K. V. R. Chary, Y.-J. Lee, H.-J. Kim, K.-W. Jun, *J. Mol. Catal. A* **2009**, *311*, 7-16.

[12] P. Serp, R. Feurer, P. Kalck, Y. Kihn, J. L. Faria, J. L. Figueiredo, *Carbon* **2001**, *39*, 621-626.

[13] J.-Y. Miao, D. W. Hwang, K. V. Narasimhulu, P.-I. Lin, Y.-T. Chen, S.-H. Lin, L.-P. Hwang, *Carbon* **2004**, *42*, 813-822.

[14] B. Friedel, S. Greulich-Weber, *Small* **2006**, *2*, 859-863.

[15] Y. Z. Jin, C. Gao, W. K. Hsu, Y. Zhu, A. Huczko, M. Bystrzejewski, M. Roe, C. Y. Lee, S. Acquah, H. Kroto, D. R. M. Walton, *Carbon* **2005**, *43*, 1944-1953.

[16] Z. Wang, L. Yu, W. Zhang, Z. Zhu, G. He, Y. Chen, G. Hu, *Phys. Lett. A* **2003**, *307*, 249-252.

[17] J. Kang, O. L. Li, N. Saito, *Carbon* **2013**, *60*, 292-298.

[18] W. M. Qiao, Y. Song, S. Y. Lim, S. H. Hong, S. H. Yoon, I. Mochida, T. Imaoka, *Carbon* **2006**, *44*, 187-190.

[19] J. Liu, S. Z. Qiao, H. Liu, J. Chen, A. Orpe, D. Zhao, G. Q. Lu, *Angew. Chem. Int. Ed.* **2011**, *50*, 5947-5951.

[20] S. Chandra, P. Das, S. Bag, D. Laha, P. Pramanik, *Nanoscale* **2011**, *3*, 1533-1540.

[21] M.-M. Titirici, M. Antonietti, N. Baccile, *Green Chem.* **2008**, *10*, 1204-1212.

[22] L. Yu, C. Falco, J. Weber, R. J. White, J. Y. Howe, M.-M. Titirici, *Langmuir* **2012**, *28*, 12373-12383.

[23] Q. Wu, W. Li, J. Tan, X. Nan, S. Liu, *Appl. Surf. Sci.* **2015**, *332*, 354-361.

[24] M.-M. Titirici, M. Antonietti, *Chem. Soc. Rev.* **2010**, *39*, 103-116.

[25] A. E. Stütz, *Glycoscience: Epimerisation, Isomerisation and Rearrangement Reactions of Carbohydrates*, Springer, **2001**.

[26] N. Baccile, G. Laurent, F. Babonneau, F. Fayon, M.-M. Titirici, M. Antonietti, *J. Phys. Chem. C* **2009**, *113*, 9644-9654.

[27] S. K. R. Patil, C. R. F. Lund, *Energy Fuels* **2011**, *25*, 4745-4755.

[28] A. J. Romero-Anaya, M. Ouzzine, M. A. Lillo-Ródenas, A. Linares-Solano, *Carbon* **2014**, *68*, 296-307.

[29] C. Falco, J. P. Marco-Lozar, D. Salinas-Torres, E. Morallón, D. Cazorla-Amorós, M. M. Titirici, D. Lozano-Castelló, *Carbon* **2013**, *62*, 346-355.

[30] S. Román, J. M. Valente Nabais, B. Ledesma, J. F. González, C. Laginhas, M. M. Titirici, *Microporous Mesoporous Mater.* **2013**, *165*, 127-133.

[31] H. Du, L. Gan, B. Li, P. Wu, Y. Qiu, F. Kang, R. Fu, Y. Zeng, *J. Phys. Chem. C* **2007**, *111*, 2040-2043.

[32] J. Tang, J. Liu, N. L. Torad, T. Kimura, Y. Yamauchi, *Nano Today* **2014**, *9*, 305-323.

[33] S. H. Joo, S. J. Choi, I. Oh, J. Kwak, Z. Liu, O. Terasaki, R. Ryoo, *Nature* **2001**, *412*, 169-172.

[34] J. Tang, J. Liu, C. Li, Y. Li, M. O. Tade, S. Dai, Y. Yamauchi, *Angew. Chem. Int. Ed.* **2015**, *54*, 588-593.

[35] H. Xiong, L. L. Jewell, N. J. Coville, *ACS Catal.* **2015**, *5*, 2640-2658.

[36] H.-S. Qian, F.-M. Han, B. Zhang, Y.-C. Guo, J. Yue, B.-X. Peng, *Carbon* **2004**, *42*, 761-766.

[37] Y. Z. Jin, Y. J. Kim, C. Gao, Y. Q. Zhu, A. Huczko, M. Endo, H. W. Kroto, *Carbon* **2006**, *44*, 724-729.

[38] V. Jiménez, A. Muñoz, P. Sánchez, J. L. Valverde, A. Romero, *Ind. Eng. Chem. Res.* **2012**, *51*, 6745-6752.

[39] L. Wang, Q. Sun, X. Wang, T. Wen, J.-J. Yin, P. Wang, R. Bai, X.-Q. Zhang, L.-H. Zhang, A.-H. Lu, C. Chen, *J. Am. Chem. Soc.* **2015**, *137*, 1947-1955.

[40] S.-W. Kim, M. Kim, W. Y. Lee, T. Hyeon, *J. Am. Chem. Soc.* **2002**, *124*, 7642-7643.

[41] Y. Yao, M. T. McDowell, I. Ryu, H. Wu, N. Liu, L. Hu, W. D. Nix, Y. Cui, *Nano Lett.* **2011**, *11*, 2949-2954.

[42] K. Tang, R. J. White, X. Mu, M.-M. Titirici, P. A. van Aken, J. Maier, *ChemSusChem* **2012**, *5*, 400-403.

[43] A.-H. Lu, T. Sun, W.-C. Li, Q. Sun, F. Han, D.-H. Liu, Y. Guo, *Angew. Chem. Int. Ed.* **2011**, *50*, 11765-11768.

[44] Z. L. Schaefer, M. L. Gross, M. A. Hickner, R. E. Schaak, *Angew. Chem. Int. Ed.* **2010**, *49*, 7045-7048.

[45] G. S. Chai, S. B. Yoon, J. H. Kim, J.-S. Yu, *Chem. Commun.* **2004**, 2766-2767.

[46] C. Gao, Q. Zhang, Z. Lu, Y. Yin, *J. Am. Chem. Soc.* **2011**, *133*, 19706-19709.

[47] Y. Sun, B. Mayers, Y. Xia, *Adv. Mater.* **2003**, *15*, 641-646.

[48] C. Rodriguez-Abreu, N. Vilanova, C. Solans, M. Ujihara, T. Imae, A. López-Quintela, S. Motojima, *Nanoscale Res. Lett.* **2011**, *6*, 1-7.

[49] L. Lai, G. Huang, X. Wang, J. Weng, *Carbon* **2010**, *48*, 3145-3156.

[50] Y. Wan, Zhao, *Chem. Rev.* **2007**, *107*, 2821-2860.

[51] Y. Liang, R. Fu, D. Wu, *ACS Nano* **2013**, *7*, 1748-1754.

[52] X. Sun, Y. Li, *J. Colloid. Interface Sci.* **2005**, *291*, 7-12.

[53] Z.-C. Yang, Y. Zhang, J.-H. Kong, S. Y. Wong, X. Li, J. Wang, *Chem. Mater.* **2013**, *25*, 704-710.

[54] Z.-C. Yang, C.-H. Tang, H. Gong, X. Li, J. Wang, *J. Power Sources* **2013**, *240*, 713-720.

[55] G. Wang, X. Pan, J. N. Kumar, Y. Liu, *Carbon* **2015**, *83*, 180-182.

[56] F. Xu, Z. Tang, S. Huang, L. Chen, Y. Liang, W. Mai, H. Zhong, R. Fu, D. Wu, *Nat. Commun.* **2015**, *6*, DOI: 10.1038/ncomms8221.

[57] N. M. Tun, A. N. Morozov, I. M. Izvol'skii, E. G. Rakov, *Inorg. Mater.* **2015**, *51*, 445-450.

[58] C. J. Brinker, G. W. Scherer, *Sol-gel science: the physics and chemistry of sol-gel processing*, Academic Press, San Diego, **1990**.

[59] O. Malay, I. Yilgor, Y. Menceloglu, *J. Sol-Gel Sci. Technol.* **2013**, *67*, 351-361.

[60] J. Tang, J. Liu, R. R. Salunkhe, T. Wang, Y. Yamauchi, *Chem. Commun.* **2016**, *52*, 505-508.

[61] X. Chen, K. Kierzek, Z. Jiang, H. Chen, T. Tang, M. Wojtoniszak, R. J. Kalenczuk, P. K. Chu, E. Borowiak-Palen, *J. Phys. Chem. C* **2011**, *115*, 17717-17724.

[62] R. Liu, F. Qu, Y. Guo, N. Yao, R. D. Priestley, *Chem. Commun.* **2014**, *50*, 478-480.

[63] Q. Yue, J. Li, W. Luo, Y. Zhang, A. A. Elzatahry, X. Wang, C. Wang, W. Li, X. Cheng, A. Alghamdi, A. M. Abdullah, Y. Deng, D. Zhao, *J. Am. Chem. Soc.* **2015**, *137*, 13282-13289.

[64] R. Liu, Y. Guo, G. Odusote, F. Qu, R. D. Priestley, *ACS Appl. Mater. Interfaces* **2013**, *5*, 9167-9171.

[65] L. Wang, K. Gan, D. Lu, J. Zhang, *Eur. J. Inorg. Chem.* **2016**, n/a-n/a.

[66] L. Li, T. Wang, L. Zhang, Z. Su, C. Wang, R. Wang, *Chem. Eur. J.* **2012**, *18*, 11417-11422.

[67] X.-B. Zhang, H.-W. Tong, S.-M. Liu, G.-P. Yong, Y.-F. Guan, *J. Mater. Chem. A* **2013**, *1*, 7488-7493.

[68] P. Yang, Y. Xu, L. Chen, X. Wang, Q. Zhang, *Langmuir* **2015**, *31*, 11701-11708.

[69] J. Liu, S. Z. Qiao, Q. H. Hu, G. Q. Lu, *Small* **2011**, *7*, 425-443.

[70] Y. Fang, G. Zheng, J. Yang, H. Tang, Y. Zhang, B. Kong, Y. Lv, C. Xu, A. M. Asiri, J. Zi, F. Zhang, D. Zhao, *Angew. Chem. Int. Ed.* **2014**, *53*, 5366-5370.

[71] J. Liu, S. Z. Qiao, J. S. Chen, X. W. Lou, X. Xing, G. Q. Lu, *Chem. Commun.* **2011**, *47*, 12578-12591.

[72] Y. Zhao, L. Jiang, *Adv. Mater.* **2009**, *21*, 3621-3638.

[73] R. Liu, Y.-W. Yeh, V. H. Tam, F. Qu, N. Yao, R. D. Priestley, *Chemical Communications* **2014**, *50*, 9056-9059.

[74] A. B. Fuertes, P. Valle-Vigon, M. Sevilla, *Chem. Commun.* **2012**, *48*, 6124-6126.

[75] Y.-X. Wang, J. Yang, S.-L. Chou, H. K. Liu, W.-x. Zhang, D. Zhao, S. X. Dou, *Nat. Commun.* **2015**, *6*.

[76] Y. J. Hong, Y. C. Kang, *Small* **2015**, *11*, 2157-2163.

[77] L.-H. Kao, Y.-C. Chang, P.-W. Hung, H.-T. Lee, P.-H. Chi, *Colloids Surf. A* **2012**, *410*, 170-177.

[78] R. Zheng, X. Meng, F. Tang, L. Zhang, J. Ren, *J. Phys. Chem. C* **2009**, *113*, 13065-13069.

[79] A. B. Fuertes, M. Sevilla, T. Valdes-Solis, P. Tartaj, *Chem. Mater.* **2007**, *19*, 5418-5423.

[80] P. Hao, J. Ren, L. Yang, Z. Qin, J. Lin, Z. Li, *Chem. Eng. J.* **2016**, *283*, 1295-1304.

[81] Z. Wang, Z. Wang, H. Wu, X. W. Lou, *Sci. Rep.* **2013**, *3*, 1391.

[82] H. P. Boehm, *Carbon* **1994**, *32*, 759-769.

[83] H. P. Boehm, *Carbon* **2002**, *40*, 145-149.

[84] J. L. Figueiredo, M. F. R. Pereira, M. M. A. Freitas, J. J. M. Órfão, *Carbon* **1999**, *37*, 1379-1389.

[85] Q. Wang, H. Li, L. Chen, X. Huang, *Carbon* **2001**, *39*, 2211-2214.

[86] R. Demir-Cakan, N. Baccile, M. Antonietti, M.-M. Titirici, *Chem. Mater.* **2009**, *21*, 484-490.

[87] X. Duan, Z. Ao, H. Sun, S. Indrawirawan, Y. Wang, J. Kang, F. Liang, Z. H. Zhu, S. Wang, *ACS Appl. Mater. Interfaces* **2015**, *7*, 4169-4178.

[88] Y. Xia, Z. Yang, R. Mokaya, *J. Phys. Chem. B* **2004**, *108*, 19293-19298.

[89] Y. Li, T. Li, M. Yao, S. Liu, *J. Mater. Chem.* **2012**, *22*, 10911-10917.

[90] J. Han, G. Xu, B. Ding, J. Pan, H. Dou, D. R. MacFarlane, *J. Mater. Chem. A* **2014**, *2*, 5352-5357.

[91] W.-H. Lee, J. H. Moon, *ACS Appl. Mater. Interfaces* **2014**, *6*, 13968-13976.

[92] C. K. Acharya, C. H. Turner, *J. Phys. Chem. C* **2007**, *111*, 14804-14812.

[93] C. K. Acharya, C. H. Turner, *J. Phys. Chem. B* **2006**, *110*, 17706-17710.

[94] T. Hamada, K. Suzuki, T. Kohno, T. Sugiura, *Carbon* **2002**, *40*, 1203-1210.

[95] L. R. Radovic, M. Karra, K. Skokova, P. A. Thrower, *Carbon* **1998**, *36*, 1841-1854.

[96] T. W. Hudnall, F. P. Gabbaï, *J. Am. Chem. Soc.* **2007**, *129*, 11978-11986.

[97] A. Sundararaman, K. Venkatasubbaiah, M. Victor, L. N. Zakharov, A. L. Rheingold, F. Jäkle, *J. Am. Chem. Soc.* **2006**, *128*, 16554-16565.

[98] A. Lorbach, A. Hubner, M. Wagner, *Dalton Trans.* **2012**, *41*, 6048-6063.

[99] E. J. Mele, J. J. Ritsko, *Phys. Rev. B* **1981**, *24*, 1000-1005.

[100] L. Yang, S. Jiang, Y. Zhao, L. Zhu, S. Chen, X. Wang, Q. Wu, J. Ma, Y. Ma, Z. Hu, *Angew. Chem. Int. Ed.* **2011**, *50*, 7132-7135.

[101] K. C. Mondal, A. M. Strydom, Z. Tetana, S. D. Mhlanga, M. J. Witcomb, J. Havel, R. M. Erasmus, N. J. Coville, *Mater. Chem. Phys.* **2009**, *114*, 973-977.

[102] V. Ravat, I. Nongwe, N. J. Coville, *ChemCatChem* **2012**, *4*, 1930-1934.

[103] V. Ravat, I. Nongwe, R. Meijboom, G. Bepete, N. J. Coville, *J. Catal.* **2013**, *305*, 36-45.

[104] G.-X. Chen, J.-M. Zhang, D.-D. Wang, K.-W. Xu, *Physica B* **2009**, *404*, 4173-4177.

[105] G.-H. Wang, J. Hilgert, F. H. Richter, F. Wang, H.-J. Bongard, B. Spliethoff, C. Weidenthaler, F. Schüth, *Nat. Mater.* **2014**, *13*, 293-300.

[106] H. Xiong, M. A. M. Motchelaho, M. Moyo, L. L. Jewell, N. J. Coville, *J. Catal.* **2011**, *278*, 26-40.

[107] M. Moyo, M. A. M. Motchelaho, H. Xiong, L. L. Jewell, N. J. Coville, *Appl. Catal. A* **2012**, *413–414*, 223-229.

[108] T. N. Phaahlamohlaka, D. O. Kumi, M. W. Dlamini, L. L. Jewell, N. J. Coville, *Catal. Today*, *257*, 76-83.

[109] W. Han, Z. Tang, P. Zhang, G. Lu, *RSC Adv.* **2014**, *4*, 23262-23270.

[110] J. Zhang, L. Ma, M. Gan, F. Yang, S. Fu, X. Li, *J. Power Sources* **2015**, *288*, 42-52.

[111] M. Mahajan, G. Singla, K. Singh, O. P. Pandey, *J. Solid State Chem.* **2015**, *232*, 108-117.

[112] D. Zheng, G. zhang, X. Wang, *Appl. Catal. B* **2015**, *179*, 479-488.

[113] W. Zheng, Z. Guo, Z. Huang, J. Zhuang, W. Yang, *Colloids Surf. A* **2015**, *484*, 271-277.

[114] Z. Zhang, F. Xiao, J. Xi, T. Sun, S. Xiao, H. Wang, S. Wang, Y. Liu, *Sci. Rep.* **2014**, *4*, 4053.

[115] R. Liu, S. M. Mahurin, C. Li, R. R. Unocic, J. C. Idrobo, H. Gao, S. J. Pennycook, S. Dai, *Angew. Chem. Int. Ed.* **2011**, *50*, 6799-6802.

[116] Y.-J. Kim, R. Ma, D. A. Reddy, T. K. Kim, *Appl. Surf. Sci.* **2015**, *357, Part B*, 2112-2120.

CHAPTER 3

General Experimental Methods

3.1 Introduction

This chapter highlights the differences related to the preparation of the various carbon materials, the preparation and characterization of mono- and bimetallic catalysts, as well as their evaluation in the Fischer-Tropsch synthesis process. Noteworthy, synthesis of all the carbons used in this study was achieved by the hydrothermal process, although the procedures were slightly modified to fabricate the different morphologies. It was desirable to improve the properties of the as-synthesized materials, and this was achieved by annealing them under inert conditions. The conditions and optimization details of the annealing step are described in chapter 4. The optimized conditions were also used to fabricate the materials used in chapter 5, 6 and 7.

3.2 Synthesis of carbon spheres (CSs) materials

Carbon spheres with solid and hollow morphologies were fabricated in this study. Solid carbon sphere synthesis was achieved by the use of glucose and resorcinol-formaldehyde (RF) carbon precursors, while hollow carbon sphere synthesis was restricted to the use of a RF carbon source.

3.2.1 Synthesis of solid carbon spheres from a glucose precursor (CSs)

The hydrothermal method was used to synthesize solid carbon spheres from a glucose carbon source (CSs).[1, 2] In this method, a 0.3 M sucrose solution was added to a Teflon-lined stainless-steel autoclave maintaining a 90% filling ratio. The temperature of the autoclave reactor was slowly raised to 190 °C using a ramping rate of 1 °C/min, and was maintained at this temperature for 4 h. The recovered product was sequentially washed and centrifuged with distilled water and absolute ethanol to obtain a black powder. Subsequently, the black powder

was purified by utilizing Soxhlet extraction for the removal of polyaromatic hydrocarbons (PAHs). For this extraction procedure, toluene was used as the solvent. The CSs were then oven dried at 70 °C for 12 h. Then, the annealing of the carbons under inert conditions was evaluated as a method for tuning their properties. For annealing experiments, the temperature was maintained at 900 °C in the flow of N_2 (20 mL/min), and the time was varied from 1 to 4 h.

3.2.2 Synthesis of solid carbon spheres from a resorcinol-formaldehyde precursor ($SCSs_{RF}$)

Solid carbon spheres were also fabricated by the extended Stöber method by utilizing a mixture of resorcinol and formaldehyde as the carbon source.[3, 4] Typically, an ammonia solution (0.5 mL, 25%) was added to an ethanolic solution consisting of deionized water (60 mL) and absolute ethanol (24 mL) and was stirred for 1 h. Subsequently, resorcinol (0.6 g) was added followed by a 30 min stirring period. Then, formaldehyde (0.84 mL) was added to the mixture and stirring was continued for 24 h at 30 °C, followed by a hydrothermal treatment step performed at 100 °C for 24 h in a Teflon-lined autoclave. The recovered brownish powder was purified by washing/centrifugation with water and ethanol, and was then dried at 70 °C for 48 h. Carbonization was performed at 900 °C for 4 h in the flow of N_2 (20 mL/min) to yield the $SCSs_{RF}$ support material.

3.2.3 Synthesis of hollow carbon spheres (HCSs)

Hollow carbon spheres were fabricated via the hard-templating approach, with the hydrothermal method employed to encapsulate the template with carbon. Silica spheres, made by the modified Stöber method, were employed as the solid template. To synthesize the template, tetraethyl orthosilicate (TEOS, 2.13 mL) was mixed with 37.5 mL of absolute ethanol. This solution was then added to a mixture containing ethanol (25 mL), deionized water (7.5 mL) and ammonia (5 mL). The contents were stirred for 1 h to allow for the formation of colloidal silica spheres. Subsequently, resorcinol (0.5 g) and formaldehyde (0.7 mL) were added to the solution to form a core-shell (SiO_2@RF) composite. This notation represents a structure whereby the SiO_2 is the core, whereas RF is the outer shell. The solution was allowed to stir for 24 h at room temperature, and then transferred into a Teflon-

lined stainless steel autoclave, and hydrothermally treated at 100 °C for 24 h. The brownish product obtained was purified by sequential washing in ethanol/water solvents, followed by centrifugation for 5 minutes, and was then dried at 70 °C for 12 h. The SiO_2@RF composites were then carbonized at 900 °C for 1 h under N_2 (20 mL/min), followed by etching of the silica core using a 10% HF solution to give the HCS support.

3.3 Catalyst preparation

All the monometallic and bimetallic catalysts (Co, Fe, Co-Fe) prepared in this study were supported on carbon spheres (CSs, $SCSs_{RF}$, HCSs, N-HCSs). For the metal precursors, nitrate salts [$Fe(NO_3)_3 \cdot 9H_2O$ and $Co(NO_3)_2 \cdot 6H_2O$] were chosen in this study due to their good solubility in water which favoured simple deposition of easy-to-reduce cobalt and iron oxides.[5] For the synthesis of monometallic samples, the homogeneous deposition technique and a metal loading of 10wt% were utilized.

Synthesis of the bimetallic catalysts on CSs was achieved by the deposition co-precipitation method using urea as the precipitating agent. A series of bimetallic catalysts were prepared by varying the Fe-to-Co ratio, and the total metal loading was kept at 10 wt.%. Typically, the metal nitrate precursors and urea (1.5 moles urea per mole of metal) were dissolved in deionized water (50 mL) and then added drop-wise to the CSs support, which was dispersed previously in deionized water (150 mL) at 90 °C. The hydrolysis of urea was allowed to proceed for 12 h with stirring, followed by drying at 70 °C under vacuum. Calcination was performed at 300 °C for 4 h in N_2 (20 mL/min). The bimetallic samples were denoted *x*Fe-*y*Co/SCSs, in which *x* and *y* were the wt% loadings of Fe and Co, respectively, in the samples. The values of *x* and *y* were 0, 0.5, 2, 5, 8 and 10 to give the catalysts 10Co/CSs, 0.5Fe-9.5Co/CSs, 2Fe-8Co/CSs, 5Fe-5Co/CSs, 9.5Fe-0.5Co/CSs and 10Fe/CSs.

3.4 Characterization

3.4.1 Raman spectroscopy

The great versatility of carbonaceous nanomaterials arises from the strong dependence of their physical properties on the ratio of sp^2 (graphite-like) to sp^3 (diamond-like) bonds. This ratio was quantified by performing Raman spectroscopy in this study. Raman spectra were measured using a Jobin Yvon T6400 micro-Raman spectrometer which used an Ar ion laser (514.5 nm) as the light source and was fitted with a liquid nitrogen-cooled charge coupled device detector (Fig. 3.1). The DuoScan attachment was used for the analysis of samples that were sensitive to burning by the laser. Power at the sample was maintained at 0.2 mW.

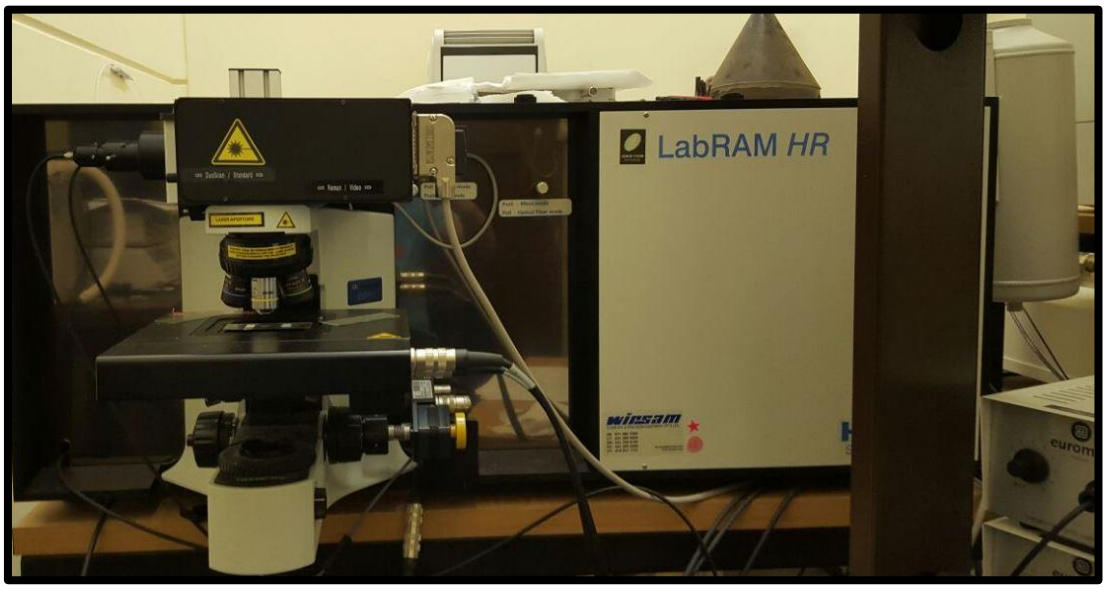

Figure 3.1 A Jobin Yvon T6400 micro-Raman spectrometer.

3.4.2 Transmission electron microscopy (TEM)

TEM analysis of the samples was done to study the morphology and sizes of the support materials or the catalyst particles. The measurements were performed on bright field mode by using an FEI Tecnai T12 instrument which was operated at an accelerating voltage of 12 kV (Fig. 3.2). Preparation of samples for TEM analysis involved the dispersion of the fine powders in ethanol by ultra-sonication until a homogeneous suspension was formed (5 minutes). In the liquid form, the samples were subsequently added drop-wise on to an SPI carbon-coated copper grid and the solvent was allowed to dry at room temperature before

introduction into the microscope. Analysis of TEM results was done using ImageJ 1.43u software. The sizes of the carbonaceous materials or the metal particles were extrapolated from histograms generated by the measurement of about 200 particles from representative TEM micrographs.

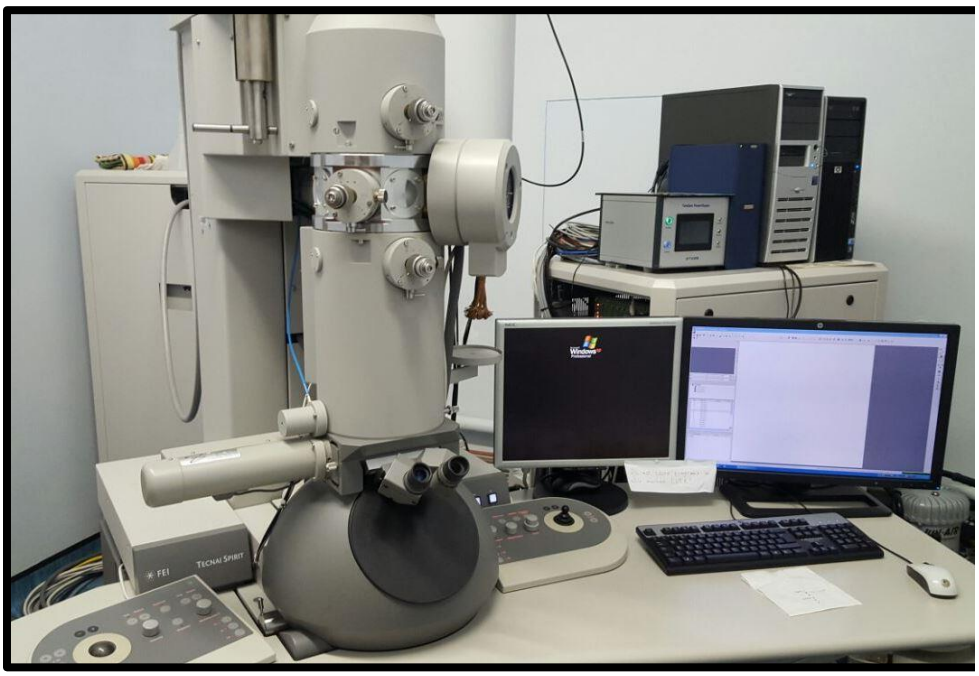

Figure 3.2 An FEI Tecnai T12 transmission electron microscope.

3.4.3 Scanning electron microscopy (SEM)

The SEM technique was used to study the external surface properties of the samples. Preparation of the specimen for analysis involved mounting them on a stub using a double-sided carbon tape. Before being introduced into the instrument, the samples were coated with successive thin layers of carbon (graphite) and gold/palladium alloy by using a sputter coater. Coating was done to ensure that the samples were electrically conductive, thus minimizing charging and other related imaging artefacts during analysis. SEM data were recorded on an FEI Nova Nanolab 600 microscope (Fig. 3.3) generally operated at 30 kV and 0.63 nA. However, the power was adjusted accordingly to improve data quality.

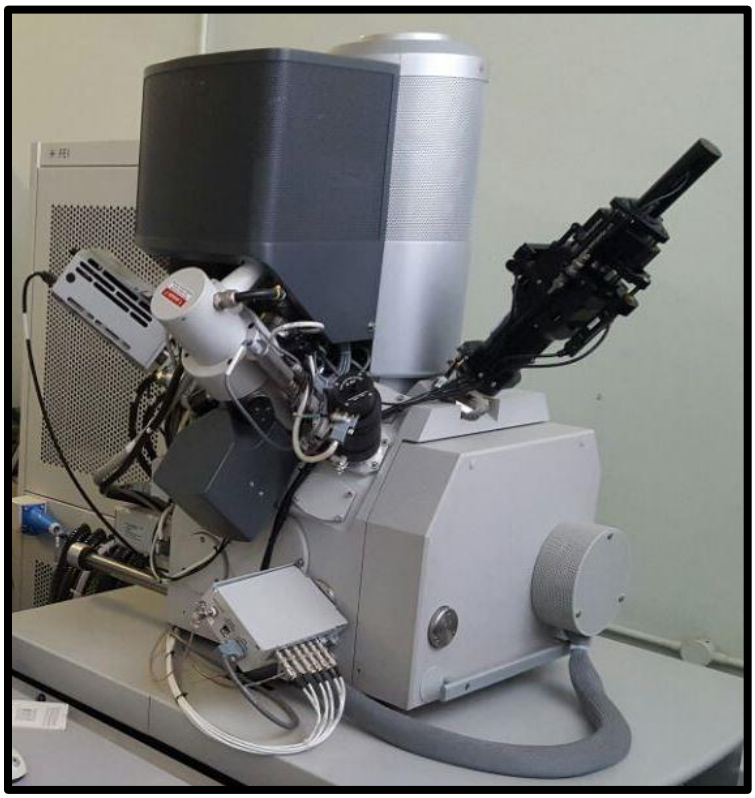

Figure 3.3 An FEI Nova Nanolab 600 microscope.

3.4.4 Energy-dispersive X-Ray (EDX) spectroscopy

EDX spectroscopy was used to map out the distributions of elements on the surface of the samples. These experiments were done on an FEI Nova Nanolab 600 SEM using the INCA Microanalysis Suit version 4.08 software package.

3.4.5 Nitrogen physisorption

Textual properties of the materials were determined by N_2 physisorption experiments using a method proposed by Stephen Brunauer, Paul Emmett and Edward Teller, abbreviated as the BET method. Prior to measurements, about 200 mg of the samples were outgassed at 150 °C for 6 h in a flow of N_2 by using a Micromeritics Flow Prep 060 unit (Fig. 3.4a). The samples were then transferred to a Micromeritics TriSta 3000 instrument for analysis (Fig. 3.4b). All N_2 adsorption measurements were performed under isothermal conditions (-196 °C) maintained by using liquid N_2, and surface area data were determined in the relative pressure range P/P_0 = 0.05-0.30. Pore volumes were determined at a relative pressure of P/P_0 = 0.995,

and pore size distributions were plotted from the desorption branches of the N_2 isotherms using the Barrett-Joyner-Halenda (BJH) method.[6]

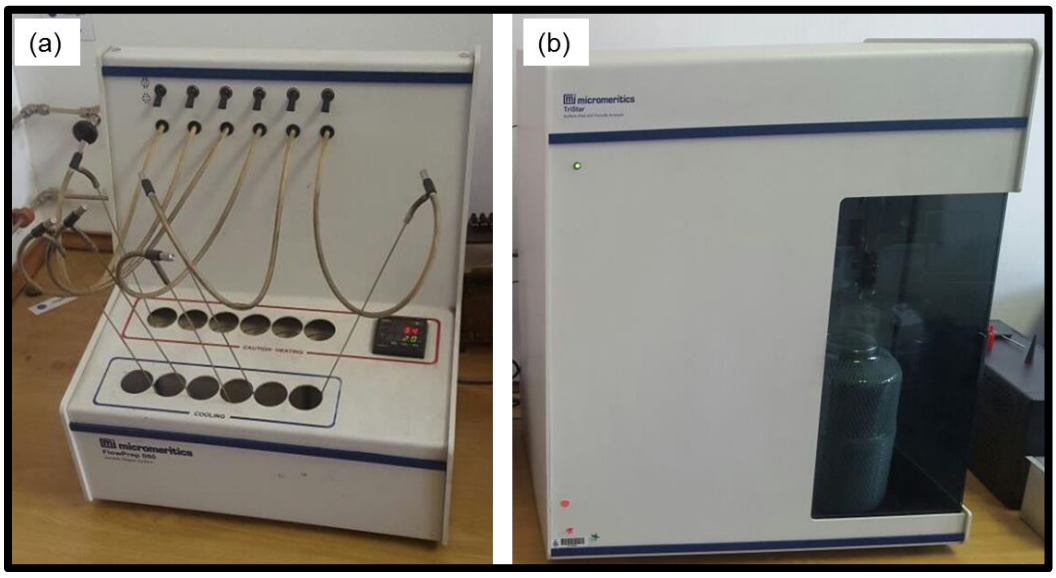

Figure 3.4 (a) Micromeritics Flow Prep 060 outgassing unit and b) Micromeritics TriStar 3000 instruments.

A detailed analysis of the pore structures of the materials was obtained by performing a multi-point BET analysis. This procedure allows for the classification of the pore structure into 6 different types possible (Fig. 3.5a). Furthermore, if hysteresis is observed on the isotherms, it can be classified accordingly as shown in Fig. 3.5b.[7]

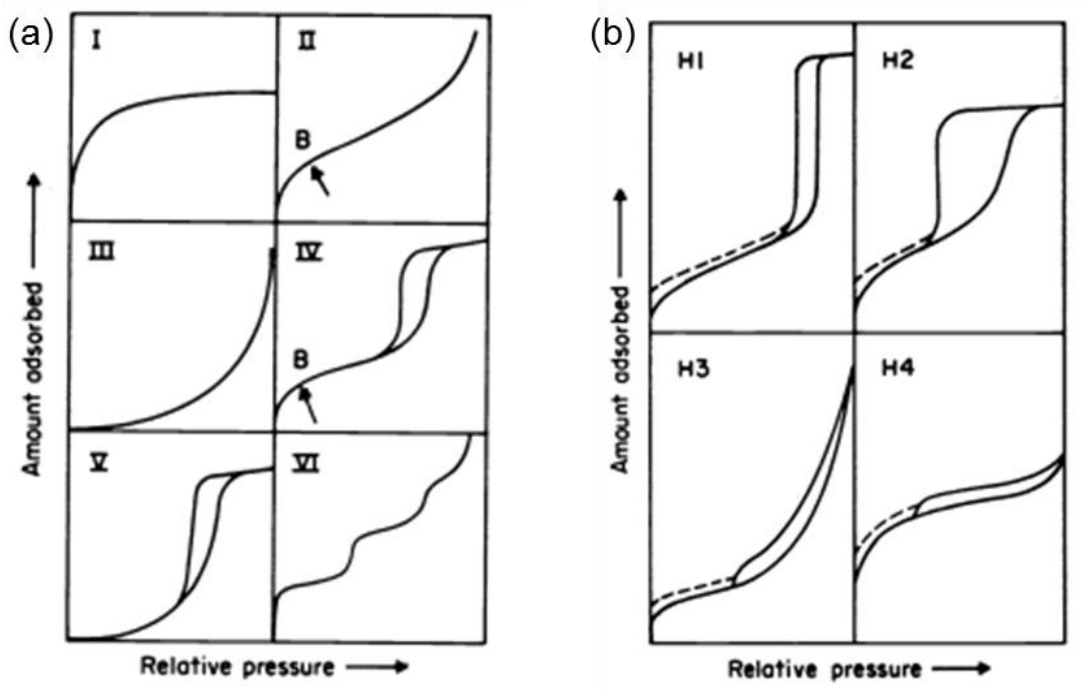

Figure 3.5 (a) types of physisorption isotherms possible and (b) a classification of the different types of hysteresis loops.[7]

3.4.6 Attenuated total reflection-Fourier transform infrared (ATR-FTIR) spectroscopy

FTIR measurements were done to determine the functional groups present on the various carbon materials. The analysis was conducted on a Bruker Tensor 27 spectrophotometer fitted with an attenuated total reflection accessory (Fig. 3.6). All spectra were collected in the range of 550-4000 cm^{-1} with a resolution of 4 cm^{-1} and an average of 64 scans per spectra.

Figure 3.6 The Bruker Tensor 27 spectrophotometer.

3.4.7 Thermogravimetric analysis (TGA)

The thermal stability of the samples was monitored by using a PerkinElmer STA6000 analyser (Fig. 3.7). Each sample (~10 mg) was heated from 50 to 900 °C at a heating rate of 10 °C/min in an oxidizing atmosphere maintained by flowing air (10 mL/min). The thermogravimetric analysis with differential thermal gravimetry (TGA-DTG) profiles were recorded from 10 mg samples without any prior treatment. TGA data provided a plot of the loss in sample weight as various components of the sample decomposed as a function of temperature, whereas DTG results allowed for an easy identification of the maximum temperature where the decomposition took place.

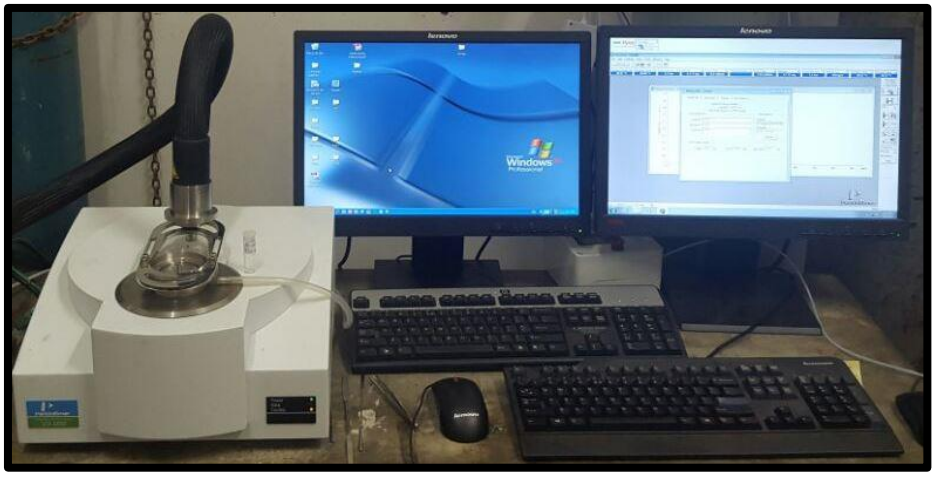

Figure 3.7 A PerkinElmer STA6000 instrument.

3.4.8 Powder X-ray diffraction (PXRD)

Ex situ PXRD measurements (low- and wide-angle) were performed on a Bruker D2 phaser which as operated at 30 kV and 10 mA (Fig. 3.8). The instrument was fitted with Ni-filtered $Co_{K\alpha}$ radiation ($\lambda_{K\alpha}$ = 0.178897 nm) and a Lynxeye detector. The scan range was 2θ = 10-90° in 0.026° steps. The phases present on the measured PXRD patterns were identified by a comparison with data stored in databases by using the EVA software package.

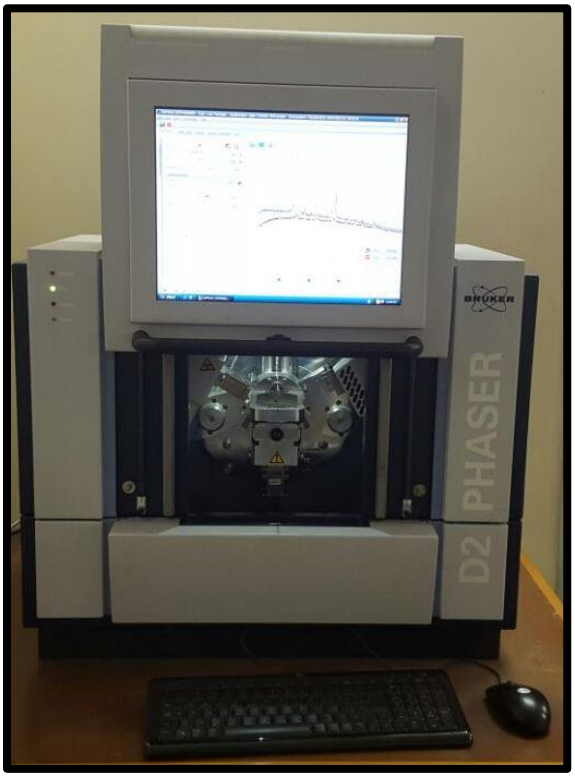

Figure 3.8 The Bruker D2 PXRD phaser.

In situ PXRD experiments were performed to gain more insight on the reduction process as it occurred on the catalysts. These measurements were performed on a Bruker D8 Advance AXS diffractometer using a $Cu_{K\alpha}$ X-ray source ($\lambda_{K\alpha}$ = 0.154084 nm) and was operated at 40 kV and 40 mA (Fig. 3.9). Data acquisition was done using a pseudo-parallel primary beam geometry achieved by fitting a Göbel mirror to the instrument. For analysis, the samples were placed in an Anton Paar XRK 900 reaction chamber and the reducing gas (5%H_2, balance N_2) was allowed to flow through at 20 mL/min. A step-wise temperature ramp from 150 to 550 °C at increments of 50 °C was used. The PXRD profiles were measured from 2θ angles of 15 to 80° by using a VÅNTEC position-sensitive detector, and the step size was kept at 0.026°.

Data analysis was done by full-profile fitting (Rietveld refinement) on the Topas 4.2 (Bruker AXS) software package, using analytical peak shape functions and starting structure models obtained from the Inorganic Crystal Structure Database.[8] Parameters such the goodness of fit (χ^2) and the weighted residual function (Rwp) were used to evaluate the quality of model used during the refinement procedure.

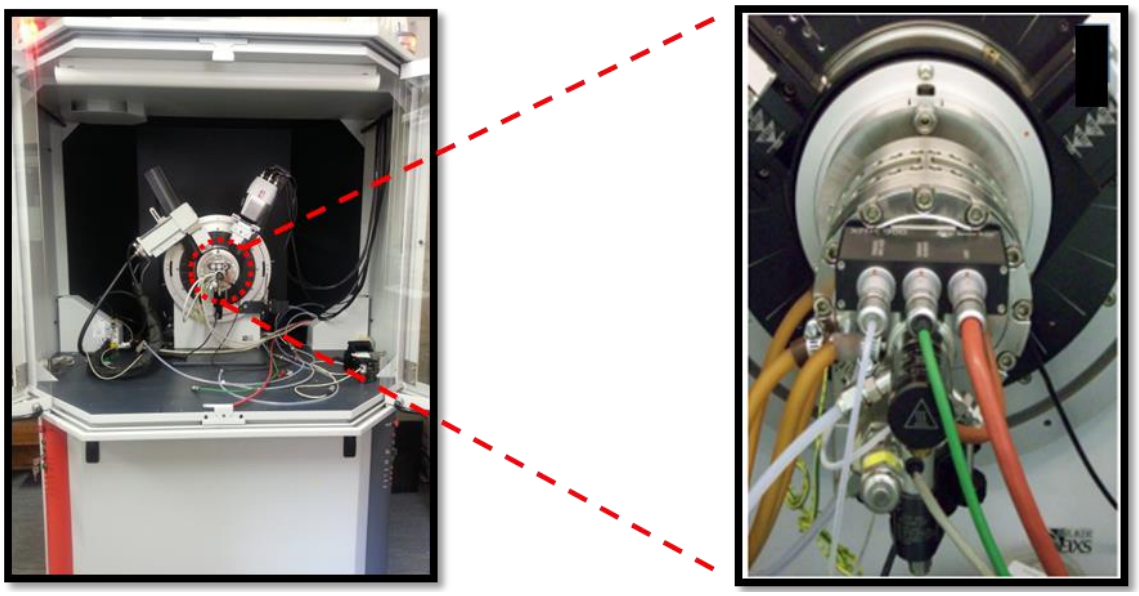

Figure 3.9 A Bruker D8 Advance AXS diffractometer fitted with an Anton Paar XRK 900.

3.4.9 Temperature programmed reduction (TPR)

TPR profiles were recorded on a Micromeritics AutoChem II instrument fitted with a thermal conductivity detector (TCD) and three Brooks mass-flow controllers. The instrument used is displayed in Fig. 3.10. Before reduction studies, about 100 mg of the samples were outgassed to remove any physisorbed solvent molecules. Outgassing was done at 150 °C for 1 h in the flow of helium. Subsequently, TPR data was measured using 5%H_2 balance Ar (45 mL/min) at temperatures between 50 and 900 °C at a ramping rate of 10 °C/min. The accurate control of reaction parameters on this unit was also exploited by studying the reduction kinetics of the different catalyst systems. For studies on reduction kinetics processes, the heating rate was varied while all other parameters were kept constant.

Figure 3.10 Micromeritics AutoChem II instrument.

3.4.10 X-ray photoelectron spectroscopy (XPS)

Analysis of the surface functional groups on the carbons was achieved by the use of X-ray photoelectron spectroscopy (XPS). These measurements were performed on a SHIMADZU KRATOS analytical AXIS SUPRA^{TM} spectrophotometer which uses momochromatic Al K_{α} radiation (1486.6 eV) and a working pressure of $1.8x10^{-8}$ torr in the measurement chamber. These experiments were performed at the University of South Africa, Florida.

3.5 Fischer-Tropsch (FT) synthesis

All catalytic evaluations performed in this study used gases provided by African Oxygen (AFROX) Ltd and were of ultra-high purity (UHP) grade. The synthesis gas (syngas) used also comprised of nitrogen for accurate mass balance calculations. Thus the composition of the syngas was $H_2/CO/N_2$:0.6/0.3/0.1.

3.5.1 FT reactor setup

The schematic representation of the rig setup utilized is displayed in Fig. 3.11. The system allows for accurate gas pressure monitoring by the use of pressure regulators (PRs) installed on different locations; on the gas cylinders, before and after the reactor. The PR placed before the reactor ensured that the gas going into the reactor was of the required pressure at any given moment. Furthermore, the PR placed after the reactor also confirmed this pressure. The reactor is made up of a 16 mm stainless steel tube with a frit and has a fixed-bed configuration. A thermocouple was inserted into the catalyst bed for temperature regulation, and Swagelok fittings were used for all connections. During FT synthesis, all lines after the reactor were maintained at 150 °C to avoid blockages. Two downstream hot and cold traps at 150 and 20 °C, respectively, were used to retain the generated wax and oil products. These products were subsequently analysed on an off-line GC-FID. For the analysis of gaseous exit products, two on-line gas chromatographs fitted with a TCD and an FID were used. Argon (20 $mLmin^{-1}$) was used as a carrier gas for the two GCs and the data from the instruments was captured and analysed using the Clarity software package. Gas flow rates on the system were measured using a soap bubble flow meter.

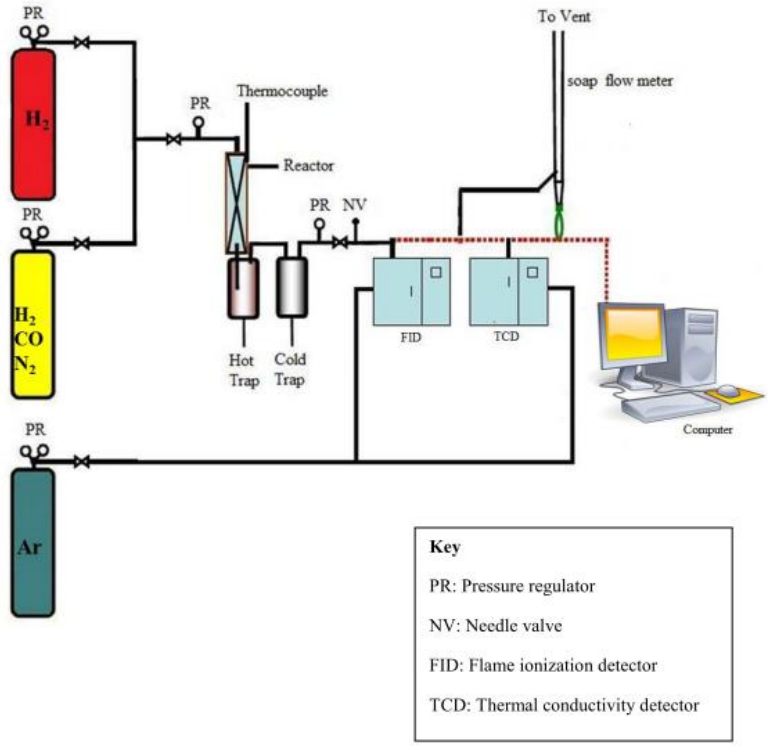

Figure 3.11 A schematic illustration of the rig reactor design.

3.5.2 Catalytic experiments

Catalytic evaluations of the catalysts were conducted on a fixed-bed reactor loaded with about 0.5 g of sample which was suspended in a thin layer of quartz wool. Prior to FT synthesis, the catalysts were activated in situ at 350 °C for 18 h under the stream of H_2 (45 mL/min, 2 bar pressure) and a ramping rate of 1 °C/min was used. After reduction, the reactor was cooled to room temperature while still in the flow of H_2. Then, synthesis gas was gradually introduced until a pressure of 10 bar and a flow rate of 20 mL/min were achieved. The reactor temperature was then increased at a ramping rate of 1 °C/min to achieve the desired FT synthesis temperatures (220, 250, 257 °C), and was maintained at this temperature initially for 100 h. However, the reactions were found to be very stable after achieving steady-state hence the reaction time was reduced to 50 h.

3.5.3 Instrument calibration and product analysis

Calibration of the gas chromatographs involved the use of two gases; syngas and a six-gas mixture. The composition of the six-gas mixture was CH_4 (2.5%), C_2H_4 (0.2%), C_2H_6 (0.5%), CO (10.0%), CO_2 (5.0%) and balance Ar, whereas the syngas consisted of H_2 (60%), CO (30 %) and N_2 (10%). Fig. 3.12, Fig. 3.13, Fig. 3.14 and Fig. 3.15 displays typical GC traces recorded from the TCD and FID detectors during calibration and FT synthesis. The peak areas measured for each analyte during calibration were used to compute the amount of that corresponding analyte in the FT product stream. The conditions at which the gas chromatographs (GCs) were operated are summarized in Table 3.1.

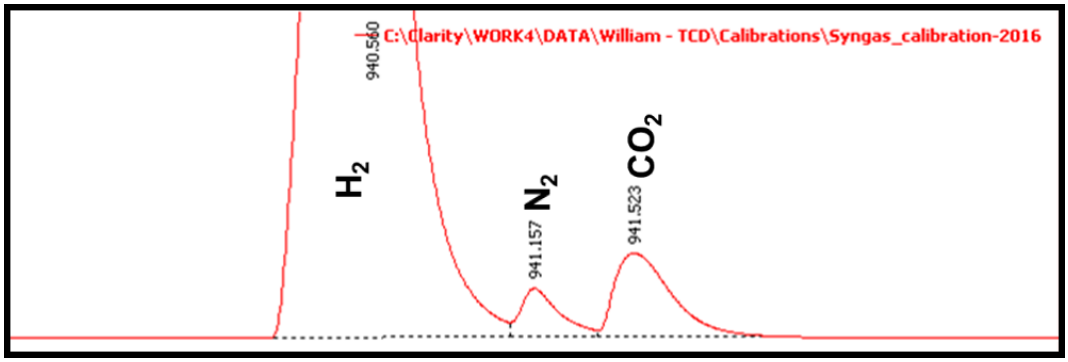

Figure 3.12 A GC-TCD trace recorded during syngas calibration.

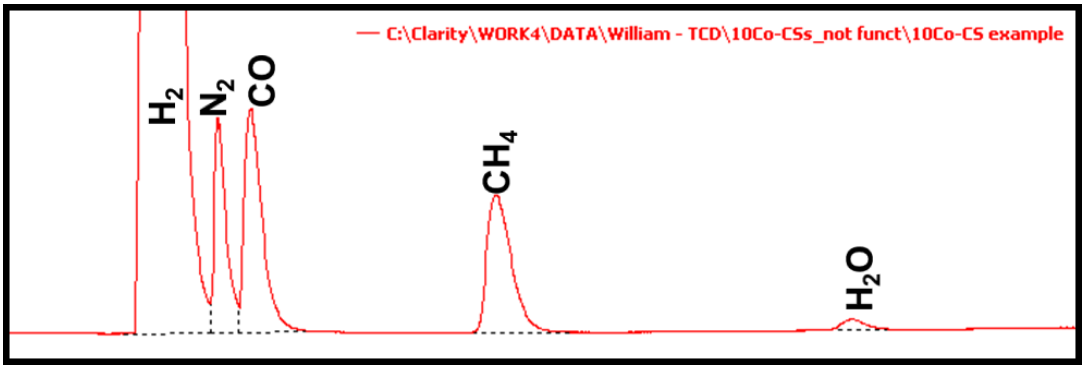

Figure 3.13 A GC-TCD trace recorded during a typical FT synthesis run.

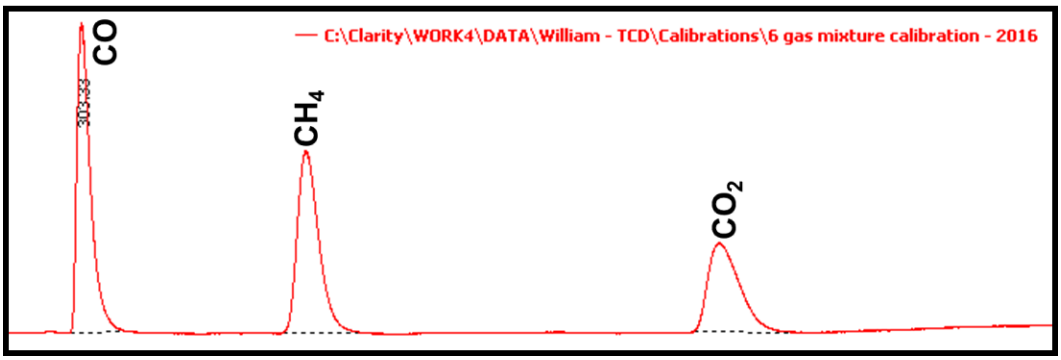

Figure 3.14 A GC-TCD trace recorded during calibration with the six-gas mixture.

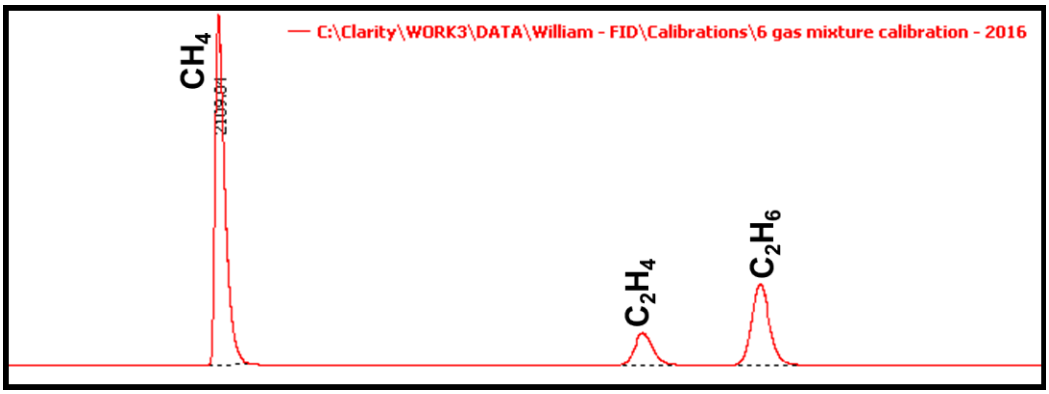

Figure 3.15 A GC-FID trace recorded during calibration with the six-gas mixture.

Table 3.1 Specifications of the GC operating conditions

Gas chromatograph (on-line)	
Make	PYE Unicam (Series 204)
Detector	Thermal conductivity detector (TCD)
Detector temperature	220 °C
Column type	Packed, stainless steel, 2 m x 2.2 mm, O.D. =1/8″
Stationary phase	Carbosieve, S-II, 60-80 mesh
Sample valve temperature	150 °C
Carrier gas	Ar, 20 mL/min
Oven temperature	250 °C (isothermal)
Gas chromatograph (on-line)	
Make	Hewlett Packard 5890
Detector	Flame ionization detector (FID)
Detector temperature	220 °C
Column type	Packed, stainless steel, 2 m x 2.2 mm, O.D. =1/8″
Stationary phase	ZB-5, 80/100 mesh
Sample valve temperature	150 °C
Carrier gas	Ar, 20 mL/min
Oven temperature	250 °C (isothermal)
Gas chromatograph (off-line)	
Make	Varian 3700
Detector	Flame ionization detector (FID
Detector temperature	350 °C
Column type	30 mx 5 μFT, O.D. = 0.53 mm
Stationary phase	ZB-1
Sample valve temperature	250 °C
Carrier gas	N_2, 20mL/min
Oven temperature program	Heat to 300 °C (ramping rate: 10 °C/min), and hold at this temperature for 3 h.

3.5.4 Mass balance calculations

The strategies used for the calculations are similar to those utilized by Bahome,[9] Hexana,[10] Phadi[11] and Muleja.[12] The fraction of carbon monoxide that was converted to hydrocarbons was calculated using data recorded on the TCD, and was expressed as a percentage as follows;

$$\% \text{ CO conversion} = \left\{\frac{CO_{in} - CO_{out} X\left[\frac{N_{2,in}}{N_{2,out}}\right]}{CO_{in}}\right\} \text{ x } 100\% \qquad \text{Eqn. 3.1}$$

where CO_{in} and $N_{2,in}$ are the calibration peak areas for CO and N_2, respectively.

CO_{out} and $N_{2,out}$ are the peak areas measured for for CO and N_2 during FT synthesis.

The inlet feed flow rate was calculated from the measured outlet flow rate (using a soap flow meter) and the gas contraction factor as follows;

$$F_{in} = \left\{\frac{X_{N_{2,out}}}{X_{N_{2,in}}}\right\} \text{ x } F_{out} \qquad \text{Eqn. 3.2}$$

where $X_{N_{2,in}}$ and $X_{N_{2,out}}$ are the mole fractions of N_2 in the calibration gas and the FT synthesis run, respectively. F_{in} and F_{out} are the total inlet and exit flow rates, respectively, and are expressed in mols/s.

Mass balance calculations were only conducted on carbon and oxygen, and the obtained results were deemed acceptable if within the range 100 ±5% in each case. By using the inlet feed flow rate (Eqn. 3.2), the total number of carbon moles in the entire mass balance time could be calculated as follows;

$$N_{C,in} = F_{in} \cdot t \cdot X_{CO,in} \qquad \text{Eqn. 3.3}$$

where $N_{C,in}$ are the total number of carbon moles fed into the reactor

F_{in} is the total feed flow rate (mol/min).

t is the overall mass balance time.

$X_{CO,in}$ is the CO mole fraction of the synthesis gas.

The rate of CO conversion (mol/min/g_{cat}) can be computed as follows;

$$-r_{CO} = \frac{F_{CO,in} - F_{CO,out}}{m_{cat}} \quad \text{Eqn. 3.4}$$

where $F_{CO,in}$ and $F_{CO,out}$ are the molar flow rates (mol/min) of CO fed into the reactor or exiting the reactor, respectively.

m_{cat} is the mass (g) of the catalyst.

For the gaseous products, the selectivity for a given carbon number was given by;

$$Sel(\theta) = \frac{[n_c]_\theta}{-r_{CO} \cdot t \cdot m_{cat}} \quad \text{Eqn. 3.5}$$

where $[n_c]_\theta$ are th moles of carbon in product θ.

The selectivity towards heavy hydrocarbons (C_{5+}) was calculated based on the moles of carbon as follows;

$$S_{S_{5+}} = 100 - \sum(S_{CH_4} + S_{C_2} + S_{C_3} + S_{C_4}) \quad \text{Eqn. 3.6}$$

where S_{CH_4} is the selectivity for methane, and S_{C_2}, S_{C_3}, S_{C_4} are the selectivities for hydrocarbons in the C_2-C_4 product range.

References

[1] S. Tang, Y. Tang, S. Vongehr, X. Zhao, X. Meng, *Appl. Surf. Sci.* **2009**, *255*, 6011-6016.

[2] T. Shaochun, V. Sascha, M. Xiangkang, *Nanotechnology* **2012**, *23*, 095603.

[3] J. Liu, S. Z. Qiao, H. Liu, J. Chen, A. Orpe, D. Zhao, G. Q. Lu, *Angew. Chem. Int. Ed.* **2011**, *50*, 5947-5951.

[4] A.-H. Lu, G.-P. Hao, Q. Sun, *Angew. Chem. Int. Ed.* **2011**, *50*, 9023-9025.

[5] G. Prieto, P. Concepción, R. Murciano, A. Martínez, *J. Catal.* **2013**, *302*, 37-48.

[6] E. P. Barrett, L. G. Joyner, P. P. Halenda, *J. Am. Chem. Soc.* **1951**, *73*, 373-380.

[7] K. S. W. Sing, in *Pure and Applied Chemistry, Vol. 57*, **1985**, p. 603.

[8] A. Belsky, M. Hellenbrandt, V. L. Karen, P. Luksch, *Acta Crystallogr. Sect. B* **2002**, *58*, 364-369.

[9] M. C. Bahome, PhD thesis, University of the Witwatersrand (Johannesburg), **2007**.

[10] W. M. Hexana, PhD thesis, University of the Witwatersrand (Johannesburg), **2009**.

[11] T. T. Phadi, PhD thesis, University of the Witwatersrand (Johannesburg), **2012**.

[12] A. A. Muleja, Y. Yao, D. Glasser, D. Hildebrandt, *Chem. Eng. J.* **2016**, *293*, 151-160.

CHAPTER 4

Carbon spheres prepared by hydrothermal synthesis - a support for bimetallic Fe Co Fischer-Tropsch catalysts

4.1 Introduction

As a gas-to-liquid reaction, the Fischer-Tropsch (FT) synthesis is a key technology in the transformation of various non-petroleum carbon resources such as natural gas, coal, or biomass into clean hydrocarbon fuels as well as valuable chemicals.[1, 2] These carbon sources provide alternative non-crude oil routes for the synthesis of petrol, diesel and chemicals. FT synthesis thus continues to receive attention from researchers, which has led to many technical advances in the FT process.[3] It is not surprising, therefore, that research in this area encompasses chemistry, chemical engineering and materials science. Recently, there has been renewed interest in the design of new FT catalysts as well as many attempts to understand and explain how catalyst composition affects the FT reaction. In most studies on FT catalysts, the focus is on monometallic catalysts, promoted to give enhanced activities and selectivities. Bimetallic systems have been investigated in detail over many decades but much less work has been expended on these systems. Developments in the characterization of catalysts has led to a more detailed understanding of these catalysts and, together with a new generation of support materials, a better understanding of these systems has become possible. Bimetallic Fe-Co systems are particularly promising as they have been shown to influence both the FT product distribution and the product selectivity.[4-7] However, details of the Fe-Co-support interaction at the microscopic level remain unclear. The design of an improved bimetallic catalyst is, therefore, a challenge as it requires an understanding of the metal-metal interactions as well as the effect that this interaction has on the catalytic properties of the catalyst.

A bimetallic FT catalyst can be influenced by many factors. Industrial FT catalysts typically use Fe- or Co-based monometallic catalysts due to their high activity, selectivity and cost.

This chapter was published as: MW Dlamini, DO Kumi, TN Phaahlamohlaka, AS Lyadov, DG Billing, LL Jewell, NJ Coville, *ChemCatChem* **2015**, 7, 3000 – 3011.

Co-based catalysts are suitable for the production of long-chain paraffins because of their high selectivity towards C_{5+} hydrocarbons. The comparatively less expensive Fe catalysts are suitable for the conversion of syngas with a low H_2/CO ratio because of their unique water-gas shift (WGS) reactivity, that is, they also catalyze the reaction between carbon monoxide and water to form hydrogen and carbon dioxide ($CO + H_2O \leftrightarrow H_2 + CO_2$).[8, 9] Additionally, Fe-based catalysts can be tuned to offer a wide range of FTS products, which include paraffins, olefins and oxygenates.

Several studies have shown that bimetallic Fe-Co systems do not possess additive properties related to the constituent monometallic Fe or Co catalysts, but have unique characteristics.[5, 10-13] Tavasoli et al. observed increased alcohol selectivity from bimetallic Fe-Co/carbon nanotubes (CNTs) catalysts compared to that of monometallic Co or Fe, which was attributed to the formation of a Co-Fe alloy.[10] Duvenhage and Coville investigated the effect of the metal precursor used to prepare supported bimetallic catalysts and compared metal nitrates with metal carbonyl complexes as precursors. Both $Fe-Co/TiO_2$ systems had similar activities in FT synthesis, but superior olefin selectivity and WGS activity was observed with the catalysts from the carbonyl systems.[14] More recently, X-ray absorption spectroscopy (X-ray absorption near edge structure, extended X-ray absorption fine structure), X-ray photoelectron spectroscopy and in situ powder X-ray diffraction (PXRD) using synchrotron radiation were used to illustrate the formation of Fe-Co species in $Fe-Co/Al_2O_3$ systems.[5]

The performance of Fe-Co systems has been shown to depend on the type of support material used. Ma et al. observed that the order for CO conversion for samples that contained 18wt% total Fe-Co catalyst loading was $9Fe-9Co/SiO_2$ > 9Fe-9Co/active carbon (AC) > $9Fe-9Co/Al_2O_3$.[15] Furthermore, studies on bimetallic Fe-Co catalysts supported on refractory oxides are often challenging due to complications associated with strong metal-support interactions. Support materials like TiO_2, SiO_2, Al_2O_3 and MgO have been shown to react with Co (or Fe) catalysts to give $CoTiO_4$, Co_2SiO_2, Co_2AlO_4 and FeO-MgO during catalyst preparation, thermal pre-treatment or catalytic reaction.[16-18] Unfortunately these mixed compounds are not active in FT synthesis[19-21] as they are only reducible at high temperatures. Carbon-based materials provide an alternative model support for FT catalysts because of their unique properties, which include high purity, high mechanical strength, high

electrical conductivity, high thermal stability and high effective surface area along with a weak interaction with the active phases.[22] As a result of their relative inertness, carbon materials are ideal to study metal-metal interactions in bimetallic systems because of their weak interaction with the active phases. Regardless of these distinct advantages, the study of carbon materials as supports for bimetallic FT catalysts remains limited.[23]

Most carbon supports that have been used in FT reactions are based on CNTs and carbon nanofibers (CNFs), typically made by chemical vapour deposition (CVD) procedures.[24] These carbons tend to be highly graphitic and hydrophobic. Thus, in nearly all studies, acid functionalization of the carbons is required before metal loading. The same applies to the study of carbon spheres (CSs) made by CVD.[25-27] The hydrothermal method is an alternative process to prepare spherical carbon materials as it uses cheap carbon sources, mild reaction conditions and is totally "green" as it involves no organic solvents, catalysts or surfactants.[28, 29] The most important advantage of CSs synthesized by the hydrothermal route is that they are hydrophilic and have useful surface functionalities, which facilitates chemical-surface modifications, a task that is challenging if CVD-synthesized carbon materials are used.[30, 31] In addition, CSs synthesized by the hydrothermal route do not need to be acid treated prior to metal loading.

In this study, we investigated the versatility of CSs synthesized by the hydrothermal method as supports for the FT reaction. We have probed the use of high-temperature treatment (annealing) as a tool to tune and improve the properties of the pristine CSs before metal loading. Furthermore, we report for the first time the application of hydrothermal carbon spheres as a model support for bimetallic Fe-Co Fischer-Tropsch catalysts. Particular attention was paid to investigate the phases formed during the reduction of the bimetallic catalysts by both temperature programmed reduction (TPR) and in situ PXRD. This was done so that the metal phases formed during reduction could be correlated to the performance of the catalysts in FT synthesis.

4.2 Results and Discussion

4.2.1 Synthesis of carbon spheres (CSs)

The carbon support was synthesized by the hydrothermal treatment of a sucrose solution at 190 °C for 4 h,[32, 33] which resulted in the formation of a black powder. Then, the black product was purified by Soxhlet extraction to give the as-prepared CSs. Typical TEM and SEM images of CSs synthesized in this study are shown in Fig. 4.1. The images illustrate that the as-synthesized carbon materials (Fig. 4.1a-b) are spherical in morphology with an average diameter of 600 nm (Fig. 4.1e). The synthesized CSs were relatively uniform in size, mono-dispersed and tended to adopt a necklace-like accreted conformation.

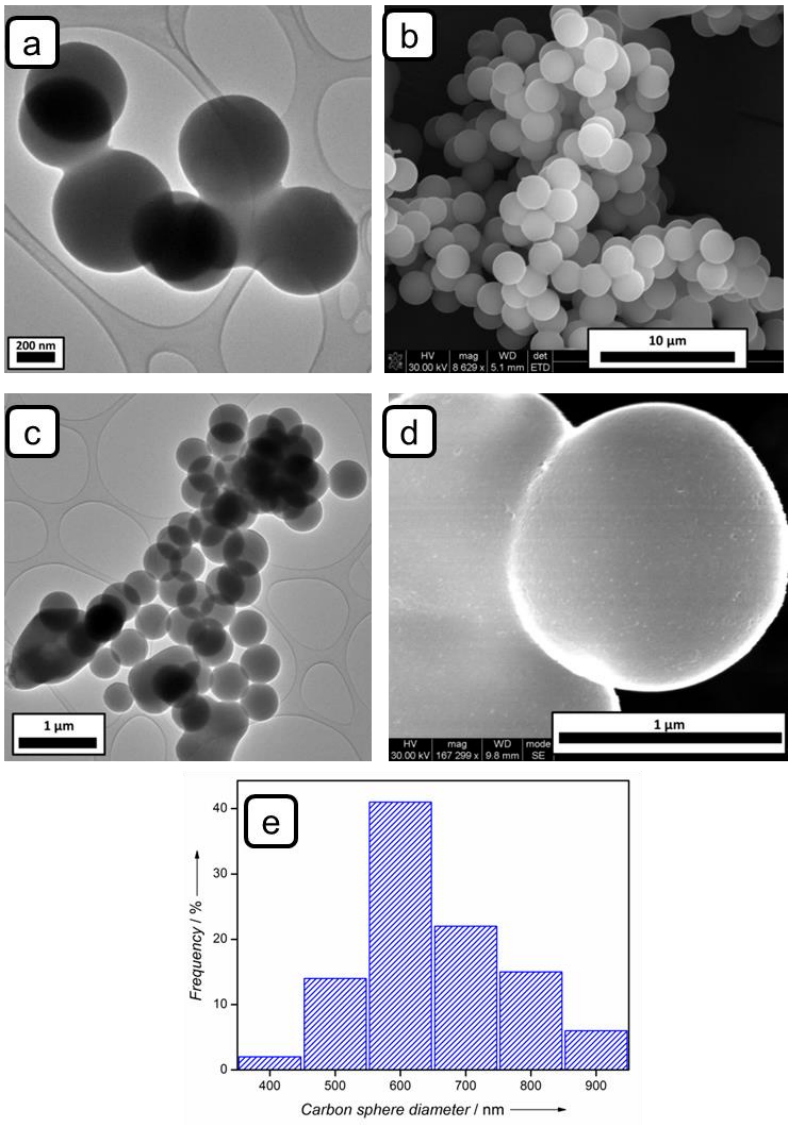

Figure 4.1 TEM and SEM images of a and b) pristine CSs, c and d) CSs annealed for 4 h at 900 °C and e) CS size distribution after annealing.

4.2.2 Effect of annealing the carbon support

Pristine carbon spheres (CSs) were annealed for 4 h at 900 °C under N_2 to enhance their properties. The morphology of the pristine and the annealed CSs was investigated by both TEM and SEM (Fig. 4.1). After annealing the samples at 900 °C for 4 hours under inert conditions, the diameter of the CSs remained constant, and an average sphere diameter of 600 nm was measured again. Notably, the surface of the as-synthesized spheres is normally smooth and well defined. However, annealing introduces some roughness on the surface of the CSs (Fig. 4.1d). This roughness is consistent with the high surface area that was recorded after the annealing step (vide infra).

The differences in the pore structure and crystallinity between the pristine and annealed samples are illustrated in Fig. 4.2. The adsorption-desorption isotherms recorded on the pristine CSs and the annealed CSs are compared in Fig. 4.2a. It can be seen that the pristine CSs display no significant increase in N_2 uptake with increasing relative pressure (P/P_o), which reveals that the surface of the as-prepared material is non-porous (type II isotherm). Correspondingly, small surface areas were recorded from the pristine material (SA_{BET} ~ 1 m^2/g). After heat treatment for 4 h, the CSs exhibit a type IV isotherm (Fig. 4.2a) with a large hysteresis loop at P/P_o = 0.4-0.7. This indicates the presence of well-defined mesopores in the sample, and consequently, the surface area of the annealed sample was found to be 452 m^2g^{-1}. The pore size distributions were calculated by the BJH method and are plotted in Fig. 4.2b. From the distributions it was also confirmed that the as-synthesized CSs were non-porous, whereas the annealed CSs were mesoporous with an average pore size of 3.4 nm.

Low-angle PXRD (Figure 4.2c) studies were performed to determine the arrangement of the pores in the carbon material after the high temperature treatment. Broad diffraction patterns were recorded before and after annealing for 4 h, which suggests that the pores are generally disordered and depict a wormhole-like structure that has short-range mesoporosity.[34] Wide-angle PXRD profiles of the as-prepared CSs (Fig. 4.2d) display a broad diffraction peak at 2θ = 23.0°, which indicates that the pristine sample had a high content of amorphous carbon. Broad diffraction peaks suggest the lack of long-range order and are characteristic of amorphous materials. Annealing improved the degree of local order in the CSs, as shown by

sharpening of peaks at 2θ =26.3 and 50.7°, which correspond to the characteristic (002) and (100) planes of graphitic carbon (Fig. 4.2d). The (002) reflection is caused by inter-layer reflection, and the (100) peak is caused by in-plane scattering and is characteristic of a turbostratic-type carbon.[31, 35] The improved crystallinity induced a slight shift in 2θ for the (002) plane because of decreases in the inter-atomic distances.

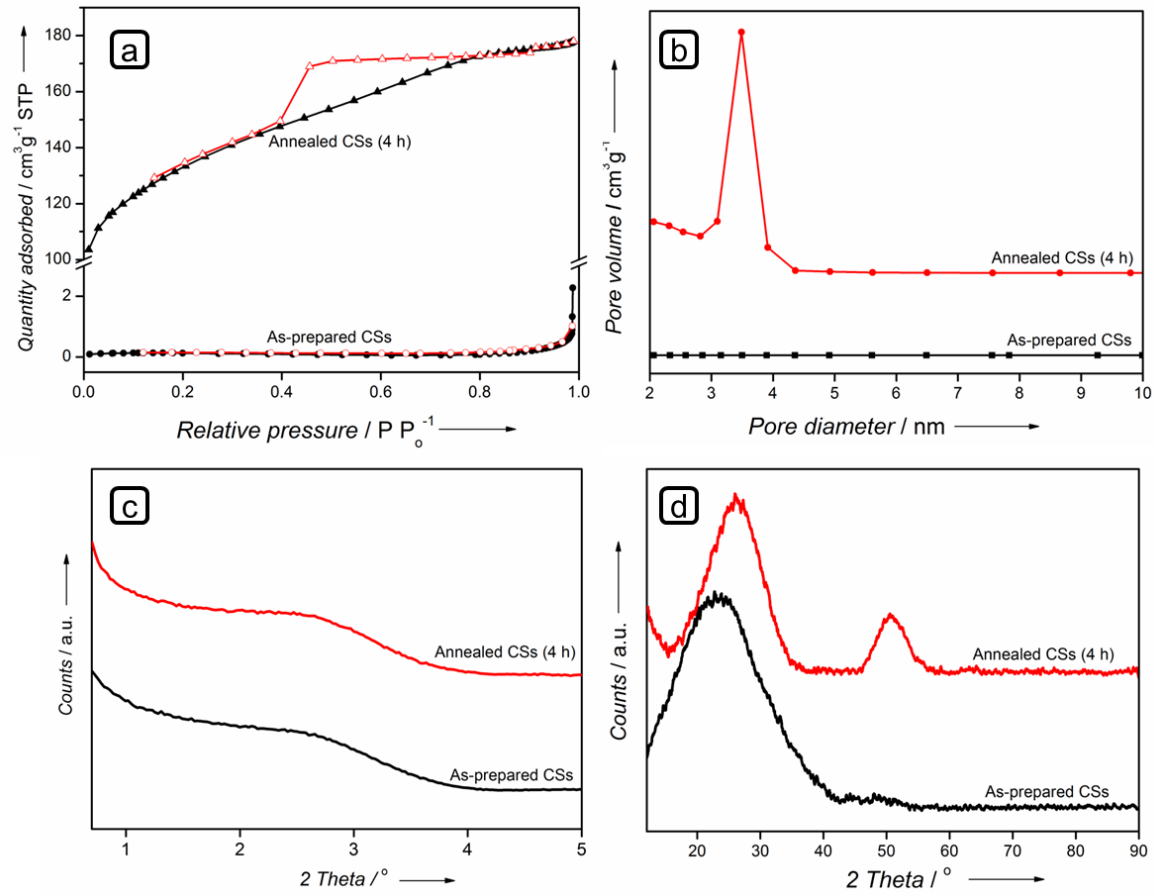

Figure 4.2 Comparisons of as-synthesized and annealed CSs; (a) Adsorption-desorption isotherms, (b) pore size distributions, (c) low-angle XRD, (d) wide-angle XRD patterns.

Fourier transform infrared spectroscopy (FTIR) was performed to determine the functional groups present on the surface of the CSs. FTIR spectra recorded from the as-prepared CSs and CSs that were annealed for 4 h are shown in Fig. 4.3. CSs synthesized by the hydrothermal method have functional groups such as hydroxyl groups evidenced by O–H bending vibrations ($\tilde{\upsilon}$ = 1169 cm^{-1}), carboxyl anhydride groups ($\tilde{\upsilon}$ = 1297 cm^{-1}), lactone groups ($\tilde{\upsilon}$ = 1365 cm^{-1}), C=C stretching of aromatics ($\tilde{\upsilon}$ = 1602 cm^{-1}), carbonyl groups ($\tilde{\upsilon}$ =

1703 cm^{-1}), C–H stretching ($\tilde{\upsilon}$ = 2915 cm^{-1}) and hydroxyl groups ($\tilde{\upsilon}$ = 3430 cm^{-1}).[29, 36, 37] These groups are lost upon heat treatment to give the annealed material.

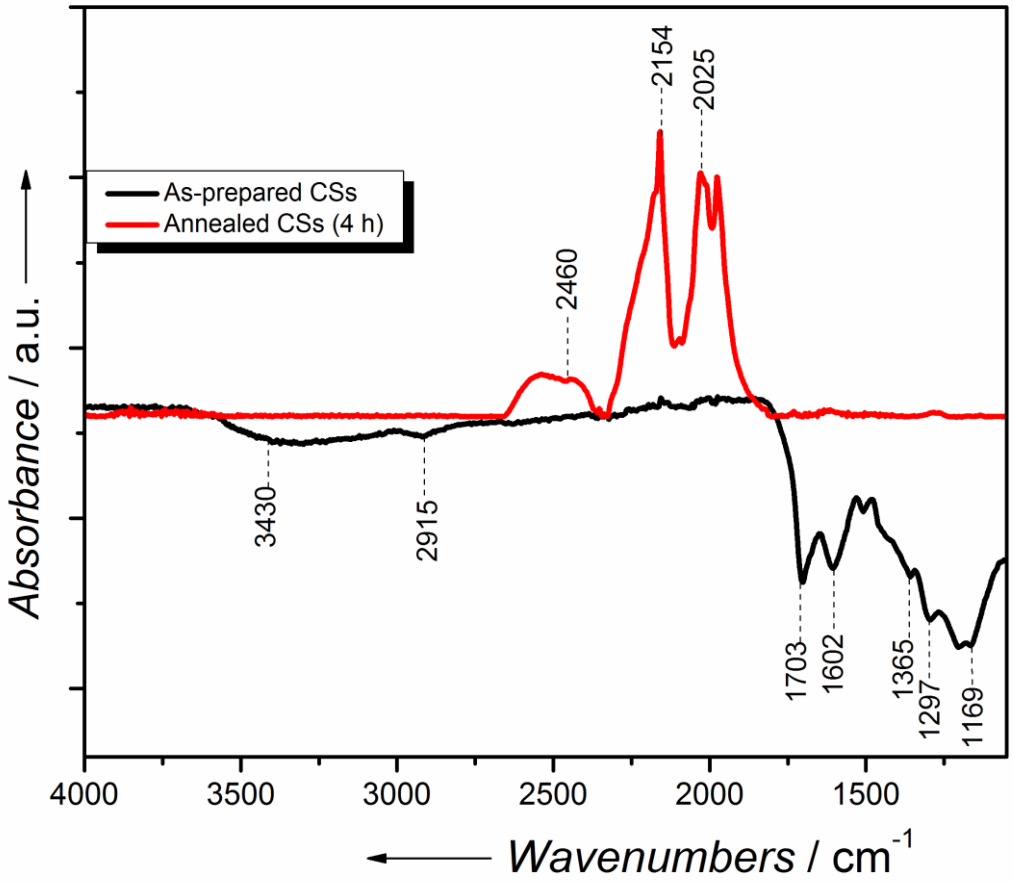

Figure 4.3 FTIR spectra of as-prepared CSs and annealed CSs (4 h).

Thermogravimetric analysis with differential thermal gravimetry (TGA-DTG) profiles of pristine CSs and CSs that were annealed for 4 h are shown in Figure 4.4, and both measurements were performed under an oxidizing atmosphere. Two notable decomposition peaks were observed for the pristine CSs (Fig. 4.4a). The low temperature decomposition peak at 344 °C is attributed to the decomposition of oxygen-containing functional groups, and the peak at 509 °C is caused by the bulk oxidation of the carbon matrix to CO_2. The annealed sample (Fig. 4.4b) only displayed one decomposition peak at 664 °C, which is caused by the oxidation of the carbon support to CO_2. It is evident that annealing the carbon spheres under inert conditions improved their thermal stability significantly. The oxidation temperature of the carbon matrix increased from 509 to 644 °C upon heat treatment because

of improved graphitization. This result is in agreement with the wide-angle PXRD observations. Notably, the residual weight after oxidation at 900 °C is ≈ 0% for both the as-prepared and the annealed CSs, which illustrated that carbon spheres synthesized using the hydrothermal method are of high purity.

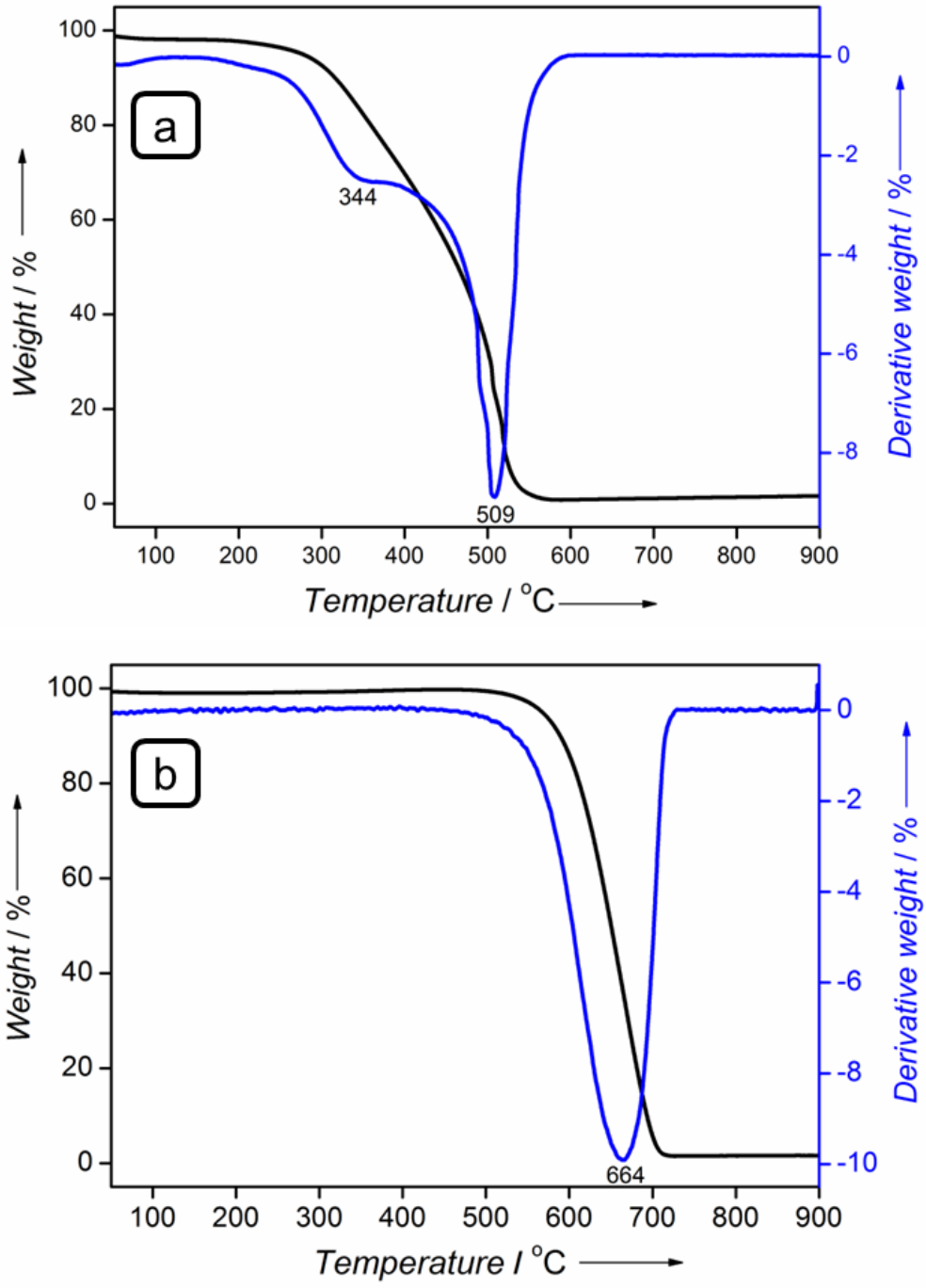

Figure 4.4 TGA-DTG profiles of a) pristine CSs and b) CSs annealed for 4 h.

The effect of the annealing time was also investigated, and the data obtained is presented in Fig. 4.5 and Fig. 4.6. Adsorption-desorption isotherms recorded after 2 and 3 h annealing periods under similar conditions are presented in Fig. 4.5a. The textual properties of the CSs as a function of the annealing period are summarized in Table 4.1. Significant N_2 uptake occurs at low P/P_o values for both samples after 2 and 3 hours annealing times (Fig. 4.5). This high N_2 uptake indicates that the carbon matrix develops pores after these thermal treatment periods. This observation suggests that some micro-channels were opened in the carbon matrix upon heating, which could be because of the burning of char-like materials. The opening of the channels in the carbon matrix resulted in the generation of high surface areas of 511 and 492 m^2g^{-1} for samples annealed for 2 and 3 h, respectively. The BET surface area decreased with continued annealing, and the average pore size increased from 2.0 to 3.4 nm. This is a significant observation as it demonstrates that the pore structure of CSs prepared by hydrothermal synthesis can be tuned by a simple variation of the duration of the thermal treatment. This could offer significant advantages in catalyst preparation as it allows for the elimination of micropores in the support material, which can cause mass-transfer limitations during Fischer-Tropsch synthesis.[2]

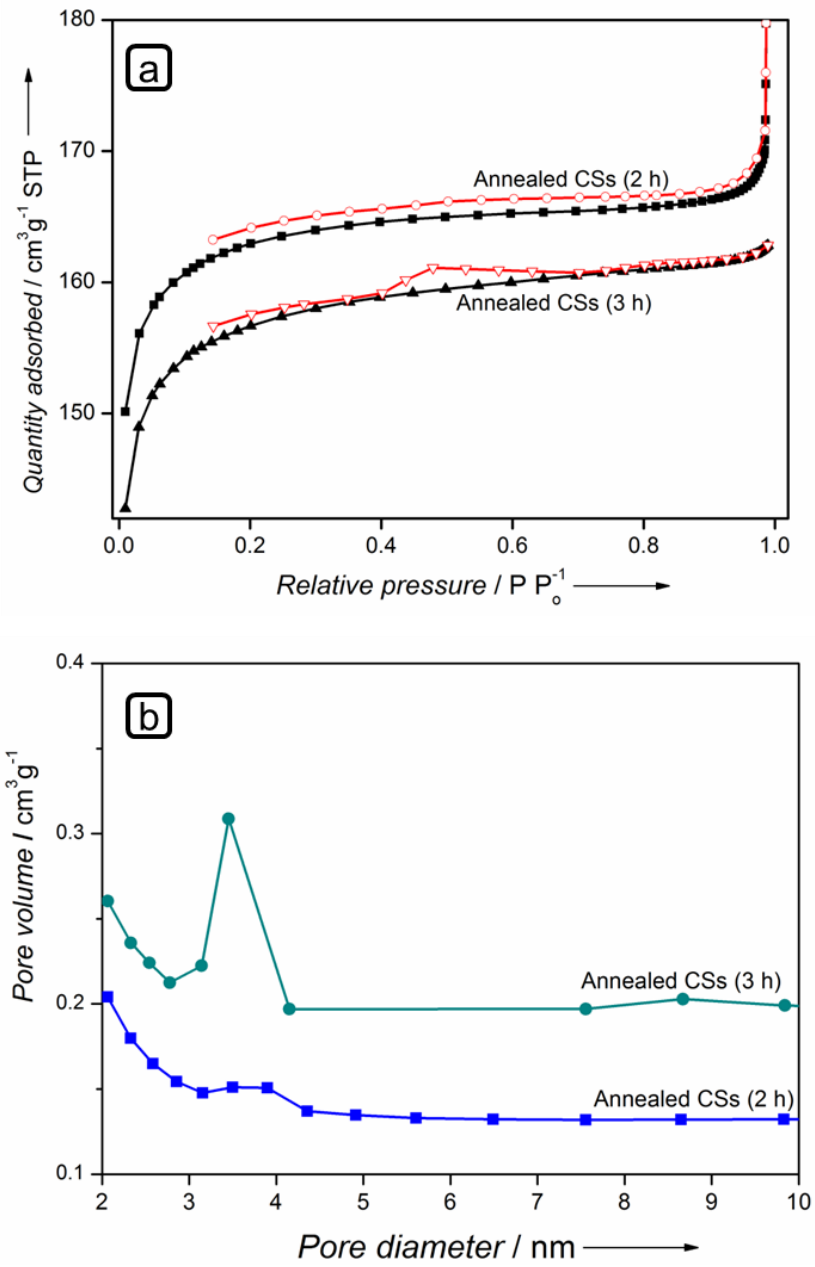

Figure 4.5 a) N_2 adsorption-desorption isotherms of CSs that were annealed for 2 h and 3 h under inert conditions. Adsorption isotherms are shown as solid symbols while desorption isotherms are shown as open symbols, and b) Pore size distributions.

Table 4.1 Textual properties of the CSs as a function of the annealing time.

Annealing time	Surface Area$_{BET}$ [m^2g^{-1}]	Pore volume [cm^3g^{-1}]	Pore diameter [nm]
0 h	1.3	0.0045	14.7
2 h	511	0.26	2.1
3 h	492	0.25	2.0
4 h	452	0.29	3.4

TGA was used to study the effect of the annealing time on the thermal stability of the CSs, and the TGA-DTG plots recorded are presented in Fig. 4.6. The carbon decomposition temperature increases from 649 to 652 and finally to 664 °C after 2, 3 and 4 h of annealing, respectively. This increase in stability is attributed to improvements in crystallinity of the carbon framework as also seen from wide-angle PXRD data. The 4 h annealing period was, therefore, chosen and for all subsequent work in this study samples were annealed for 4 h.

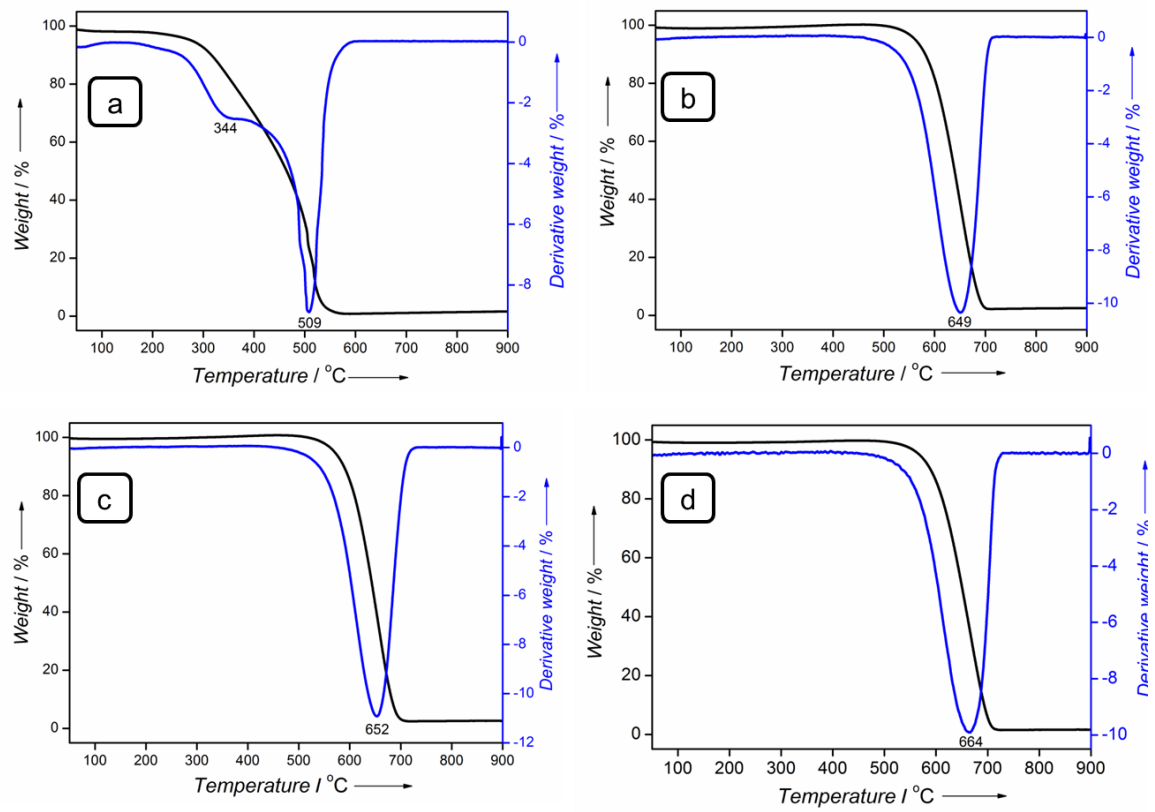

Figure 4.6 TGA-DTG profiles of a) pristine CSs, and CSs that were annealed for b) 2 h, c) 3 h and d) 4 h.

In some previous studies, CSs have been employed as FT catalyst supports. The reported CS supports were either synthesized by chemical vapour deposition (CVD)[25] or the hydrothermal method but without annealing.[26] Consequently, the reported support materials had low BET surface areas (< 5 m^2g^{-1}). Thus, generally low FT activities were reported on these support materials even after functionalizing by $KMnO_4$ or nitrogen doping. Yu et al. demonstrated that highly active FexOy@CSs can be fabricated by the hydrothermal treatment of a glucose solution that contained iron nitrate.[38] More recently, Davis et al. utilized graphitized (1900 °C) CSs prepared hydrothermally as supports for Pt-promoted Co/CS catalysts. However, the carbon support was seen to break during FT synthesis.[27] In this study, annealing at an intermediate temperature (900 °C) was used to tune the surface area, crystallinity and thermal stability of the carbon support.

4.2.3 Catalyst characterization

All the catalysts studied here were prepared by the homogeneous deposition of nitrate precursors onto carbon spheres that were annealed for 4 h. The BET surface area, pore volume and the average pore size of the different catalysts are summarized in Table 4.2. The introduction of the catalyst precursors onto the CSs decreases the surface area from 452 to 402 m^2g^{-1} for the 10Fe/CSs sample. According to the results, the average pore sizes were in the range 2.4 – 2.9 nm, which shows that the samples maintain their mesoporous pore structure even after the addition of 10% of the metal precursors.

PXRD patterns of the calcined mono- and bimetallic catalysts are shown in Figure 4.7, and the diffraction pattern of pure CSs is also shown for reference. After calcination, the 10Co/CSs sample displays diffraction lines at 2θ = 21.9, 36.2, 42.5, 52.2, 70.0 and 77.2° which correspond to the (111), (220), (311), (400), (511) and (440) characteristic peaks of face-centered cubic (fcc) Co_3O_4 [PDF No. 00-043-1003]. Similarly, peaks typical of the α-Fe_2O_3 phase were recorded for the monometallic Fe sample (10Fe/CSs). For the bimetallic systems, the samples that contained only a small amount of the second metal (0.5Fe-9.5Co/CSs and 9.5Fe-0.5Co/CSs) displayed diffraction patterns that correspond to the monometallic samples of the more abundant metal. Crystallites of the second metal, present at low concentrations in these samples, could not be detected by the PXRD technique. This observation is in agreement with energy-dispersive X-ray (EDX) mapping results that confirmed that both metals were present on the carbon support. The bimetallic samples with more second metal (2Fe-8Co/CSs, 5Fe-5Co/CSs) were composed of mixtures of the Co_3O_4 and α-Fe_2O_3 phases. It is possible that a solid solution of $(Fe_xCo_y)O_4$ was formed.

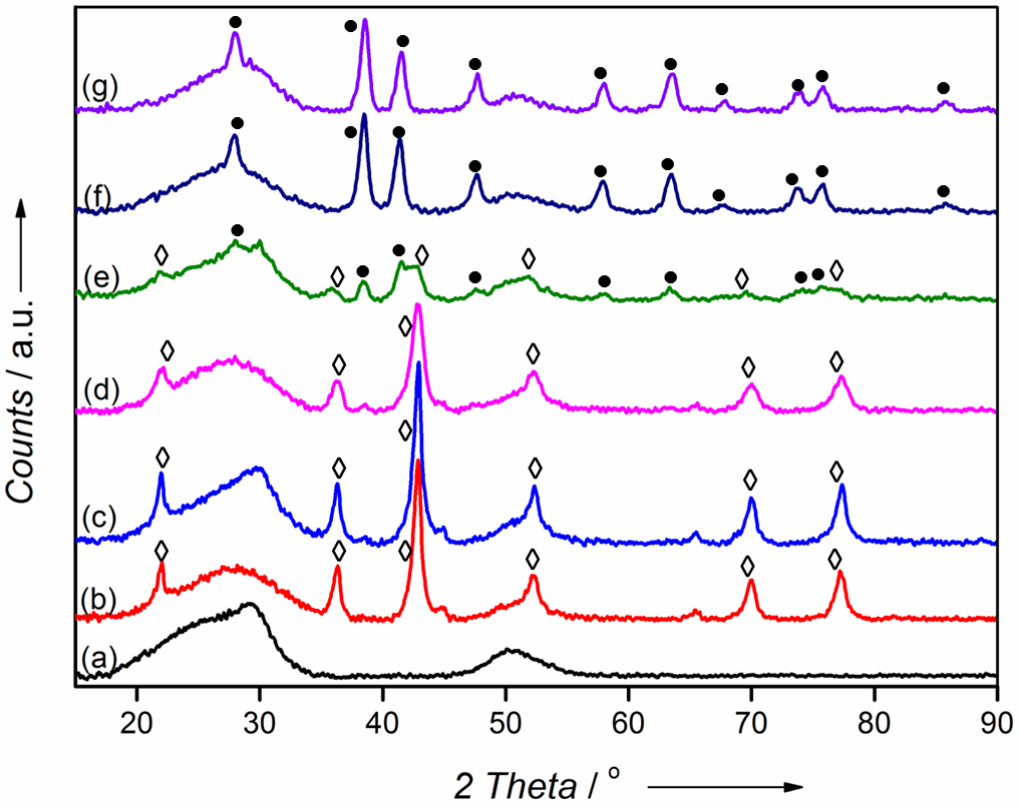

Figure 4.7 Ex situ PXRD patterns of the calcined mono- and bimetallic catalysts: (a) CS support, (b) 10Co/CSs, (c) 0.5Fe-9.5Co/CSs, (d) 2Fe-8Co/CSs, (e) 5Fe-5Co/CSs, (f) 9.5Fe-0.5Co/CSs and (g) 10Fe/CSs. The Co_3O_4 and α-Fe_2O_3 phases are marked with the symbols ◊ and ● , respectively. (X-ray source: Co, $\lambda_{K\alpha}$ = 0.179 nm)

The Co_3O_4 [or $(Fe_xCo_y)O_4$ solid solution] and α-Fe_2O_3 crystallite sizes in the mono- and bimetallic catalysts were estimated using Scherrer's equation and are presented in Table 4.2. Crystallite sizes of 7.9 and 12.9 nm were obtained for the monometallic cobalt and iron oxide catalysts, respectively. Generally, the addition of the second metal increased the crystallite size of the dominant metal oxide. This could be caused by the formation of the solid solution.

Table 4.2 Nitrogen physisorption data and crystallite sizes for the metal oxides.

Sample	BET surface area [m^2g^{-1}]	Pore volume [cm^3g^{-1}]	Pore size [nm]	Crystallite size [nm][a]	
				Co	Fe
CS support	452	0.29	3.4	-	-
10Co/CSs	423	0.28	2.9	7.9	-
0.5Fe-9.5Co/CSs	415	0.21	2.8	10.3	-
2Fe-8Co/CSs	417	0.22	2.8	9.5	-
5Fe-5Co/CSs	411	0.24	2.4	12.6	14.4
9.5Fe-0.5Co/CSs	409	0.22	2.7	-	13.1
10Fe/CSs	402	0.22	2.8	-	12.9

[a]*Crystallite sizes were estimated using the Scherrer equation.*

The deposition precipitation technique used in the catalyst preparation was shown to be a reproducible method for synthesizing well dispersed metal particles on the carbon support materials. By employing urea as a precipitating agent, this technique allows for gradual pH changes during metal deposition, which promotes small catalyst particles with a narrow particle size distribution. Representative microscopic images of the calcined catalysts are shown in Fig. 4.8. The monometallic 10Fe/CSs and 10Co/CSs catalysts (Fig. 4.8a-b) show highly dispersed metal particles on the outside of the CS support. A representative SEM image of the bimetallic 0.5Fe-9.5Co/CSs sample is shown in Fig. 4.8c, and the corresponding elemental maps for Fe and Co recorded from this image are shown in Fig. 4.8d-e, respectively. Notably, the Fe particles in this sample were dispersed uniformly even though this sample has a very small ratio of Fe to Co. EDX data (Fig. 4.8f) confirmed that the catalyst contains both Fe and Co.

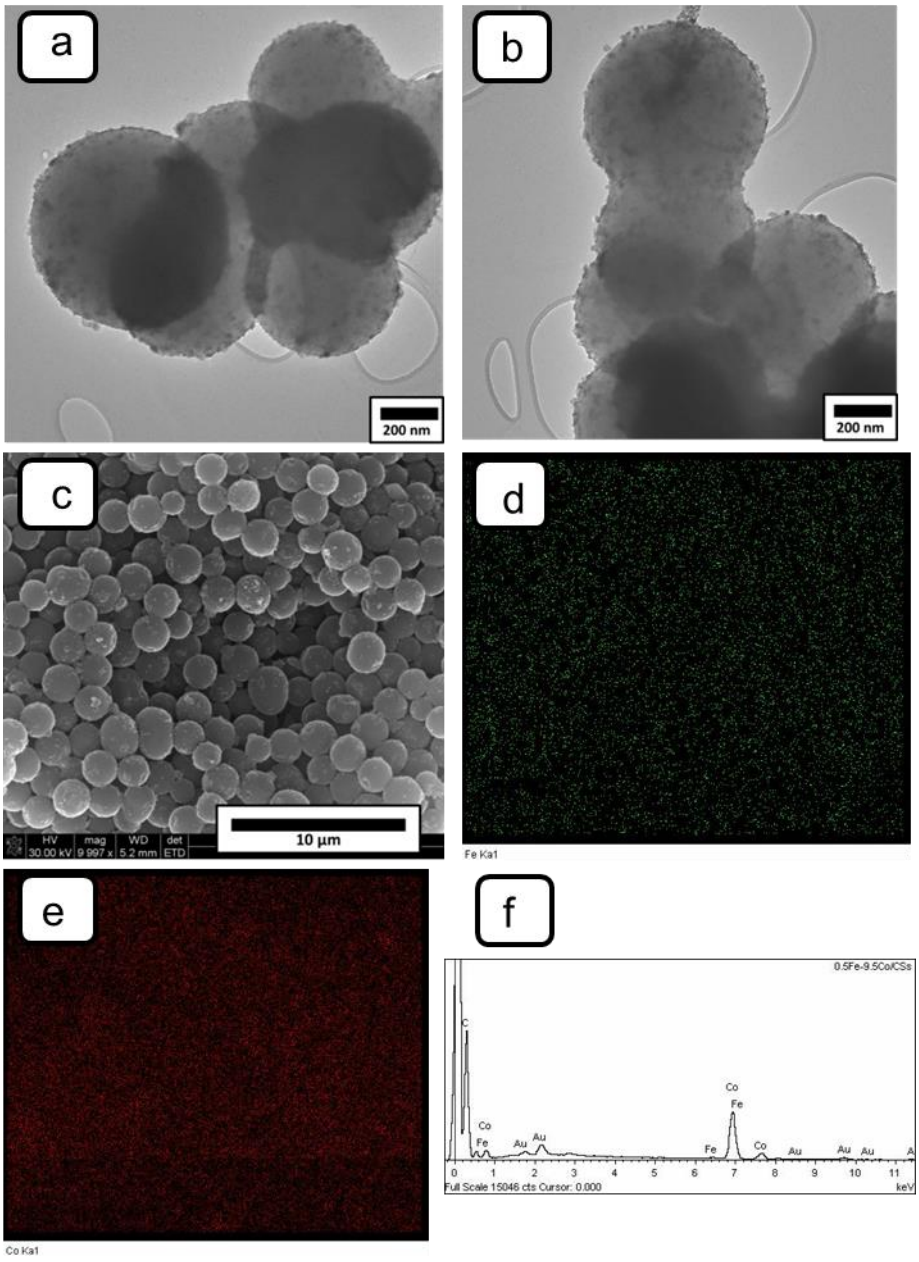

Figure 4.8 Representative TEM images of a) 10Fe/CSs and b) 10Co/CSs, and c) SEM image of the 0.5Fe-9.5Co/CSs. Representative 2D elemental maps for d) Fe and e) Co obtained from the 0.5Fe-9.5Co/CSs sample. f) EDX spectrum for the 0.5Fe-9.5Co/CSs sample.

The addition of catalyst particles onto the support material alters the thermal stability of the carbon. TGA was used to monitor the temperature at which oxidation ($C + O_2 \rightarrow CO_2$) occurs on the calcined catalysts. A general decrease in the thermal stability of the carbon support after the addition of catalyst particles was observed (Fig. 4.9). The oxidation temperature of the carbon support decreased from 664 °C observed on the annealed carbon

support to 342 °C recorded for 10Co/CSs. This decrease in thermal stability is attributed to the ability of the metal particles to catalyze carbon oxidation.[25] From the TGA profiles in Fig. 4.9, it can be seen that Co-rich samples catalyze carbon oxidation more readily than Fe-rich catalysts. Carbon oxidation over bimetallic samples occurred at intermediate temperatures. The residual weight noted at 900 °C in the TGA plots is caused by Co/Fe oxide particles and confirmed that the metal loading was approximately 10 wt% in all of the catalysts.

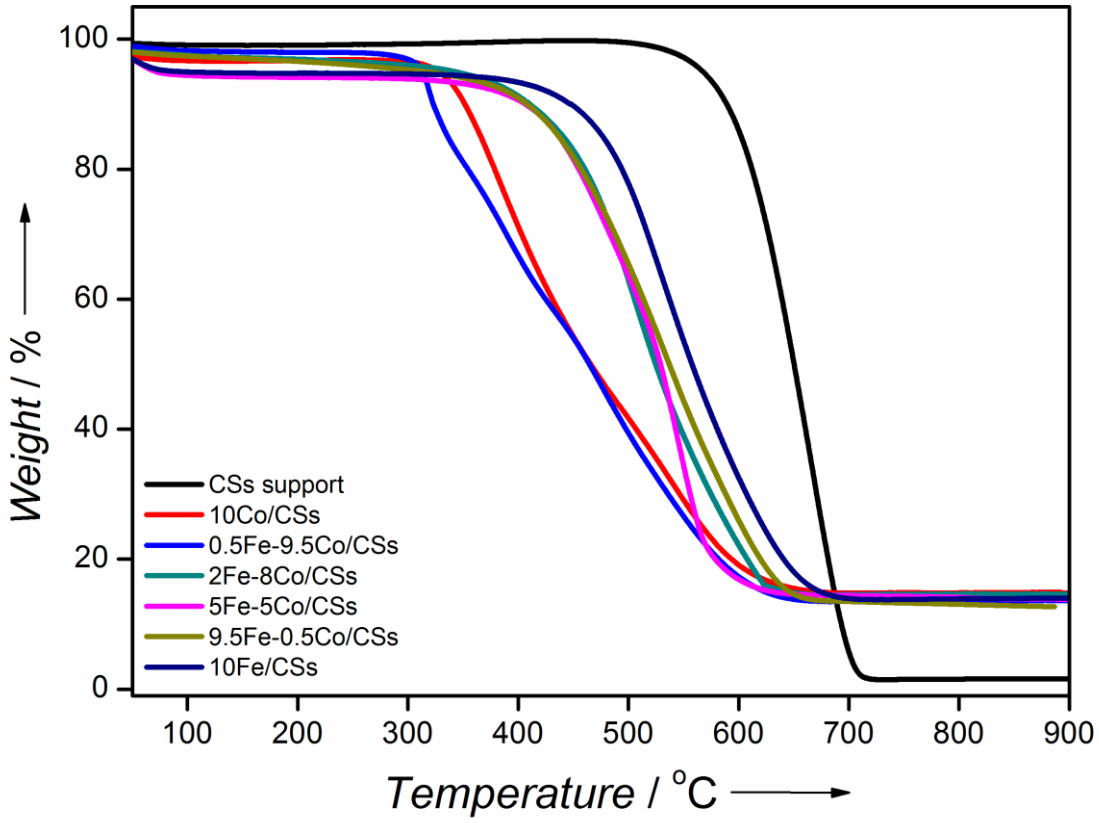

Figure 4.9 TGA profiles of the CS support and the calcined catalysts (measured in air).

4.2.4 Catalyst reducibility

TPR profiles of the various calcined samples are shown in Fig. 4.10. The monometallic Co sample displays two reduction peaks (4.10a). These peaks in the 252 – 360 °C range are caused by the stepwise transformation of Co_3O_4 to metallic cobalt ($Co_3O_4 \rightarrow CoO \rightarrow Co^o$).[39, 40] The low temperature peak at 252 °C is rather small because of the ability of the carbon support to partially auto-reduce the cobalt oxide phase.[41] The monometallic Fe sample

displays two distinct reduction peaks at 331 and 501 °C. Generally, the reduction of iron oxides proceeds as follows: $Fe_2O_3 \rightarrow Fe_3O_4 \rightarrow FeO \rightarrow Fe$. The FeO phase is thermodynamically unstable hence it converts quickly to metallic Fe and, therefore, is not normally detected by the TPR instrument.[42] The low-temperature peak at 331 °C can, therefore, be assigned to the transformation of Fe_2O_3 to Fe_3O_4, whereas the broad high-temperature peak indicates the reduction of Fe_3O_4 to metallic Fe (presumably via FeO; Fig. 4.10f).

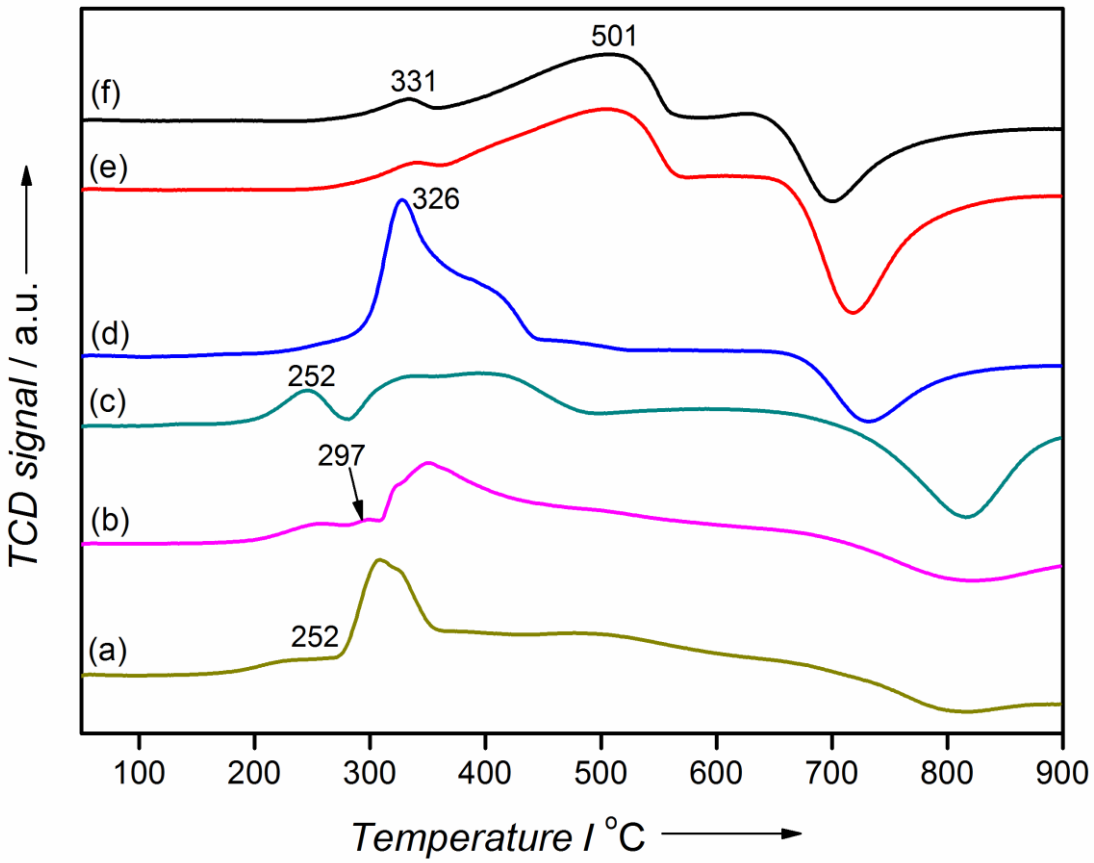

Figure 4.10 H_2-TPR profiles of the mono- and bimetallic catalysts: a) 10Co/CSs, b) 0.5Fe-9.5Co/CSs, c) 2Fe-8Co/CSs, d) 5Fe-5Co/CSs, e) 9.5Fe-0.5Co/CSs and f) 10Fe/CSs.

The addition of small quantities of cobalt (0.5 wt. %) to pure Fe_2O_3 produces no significant changes in the reduction profile (Fig. 4.10e). Conversely, the addition of a similar quantity of Fe to a Co-rich sample has a significant effect on the reducibility of the catalyst (Fig. 4.10b). The cobalt reduction peaks shift to higher temperatures on the 0.5Fe-9.5Co/CSs sample relative to the monometallic Co sample, and remarkably, an additional reduction peak is

observed at 297 °C. This peak can be associated with an alloy which is formed by reduction of a well-mixed metal Fe/Co oxide (solid solution) at high temperatures (see below). More complex H_2 consumption profiles were observed for the 2Fe-8Co/CSs (Fig. 4.10c) and 5Fe-5Co/CSs (Fig. 4.10d) because of the reduction of the different bimetallic oxide phases present. For the 2Fe-8Co/CSs sample, the peak at 252 °C is attributed to the transformation of Co_3O_4 to CoO, whereas the broad peak from 297 to 466 °C is caused by both the reduction of CoO and a Co/Fe oxide mixture, which is formed at high temperatures. The 5Fe-5Co/CSs sample mainly shows the reduction of the Co-Fe mixed oxide at 326 °C. This oxide mixture is assumed to be well mixed (a solid solution) and different from the Co-Fe core-shell structure reported recently.[7, 43]

Unlike typical metal oxide supports, TPR profiles of the catalysts supported on CSs display a broad negative peak at temperatures above 600 °C caused by the gasification of the carbon material ($C + 2H_2 \rightarrow CH_4$). Generally, Fe-rich samples catalysed the methanation reaction better than their Co-rich analogues, as displayed by the lower gasification temperatures for Fe samples. The 10Fe/CSs and 10Co/CSs samples showed gasification minima at 698 and 809 °C, respectively. The bimetallic samples had intermediate minima temperatures at 805, 815, 731 and 719 °C for 0.5Fe-9.5Co/CSs, 2Fe-8Co/CSs, 5Fe-5Co/CSs and 9.5Fe-0.5Co/CSs, respectively. Fe catalysts have better methanating ability than Co catalysts, hence the more facile gasification in the Fe-rich samples.

The reducibility of the catalysts was also monitored in situ using PXRD in an Anton Paar XRK 900 reactor chamber. Non-ambient PXRD studies lead to a set of closely related diffraction patterns, measured as a function of temperature, pressure, chemical environment or even time. This technique can afford a remarkable amount of chemically and physically meaningful data concerning the properties and behaviour of the samples under investigation.[44] The reduction patterns of monometallic Co and Fe samples as a function of temperature are displayed in Fig. 4.11. Cubic Co_3O_4 was the dominant phase at low temperatures (T < 250 °C) in the Co sample (Fig. 4.11a). At higher reduction temperatures, peaks at 2θ = 36.4, 42.3 and 61.2° were seen, which correspond to the characteristic (111), (200) and (220) peaks of CoO [PDF No. 01-070-2856]. At temperatures above 350 °C, the CoO phase was further reduced to fcc metallic Co [PDF No. 01-089-4307]. For the

monometallic Fe sample, the α-Fe_2O_3 to Fe_3O_4 transformation started from 350 °C (Fig. 4.11b), and the Fe_3O_4 to metallic Fe conversion was only seen after 9 h at 550 °C (data not shown). The trends in the reduction behaviour observed for the monometallic samples by in situ PXRD experiments are consistent with our TPR results and other literature reports.[45, 46] Slightly higher reduction temperatures were observed from the PXRD data than the TPR data because of the differences in the methodologies (for example, ramping and flow rates) used in these techniques.

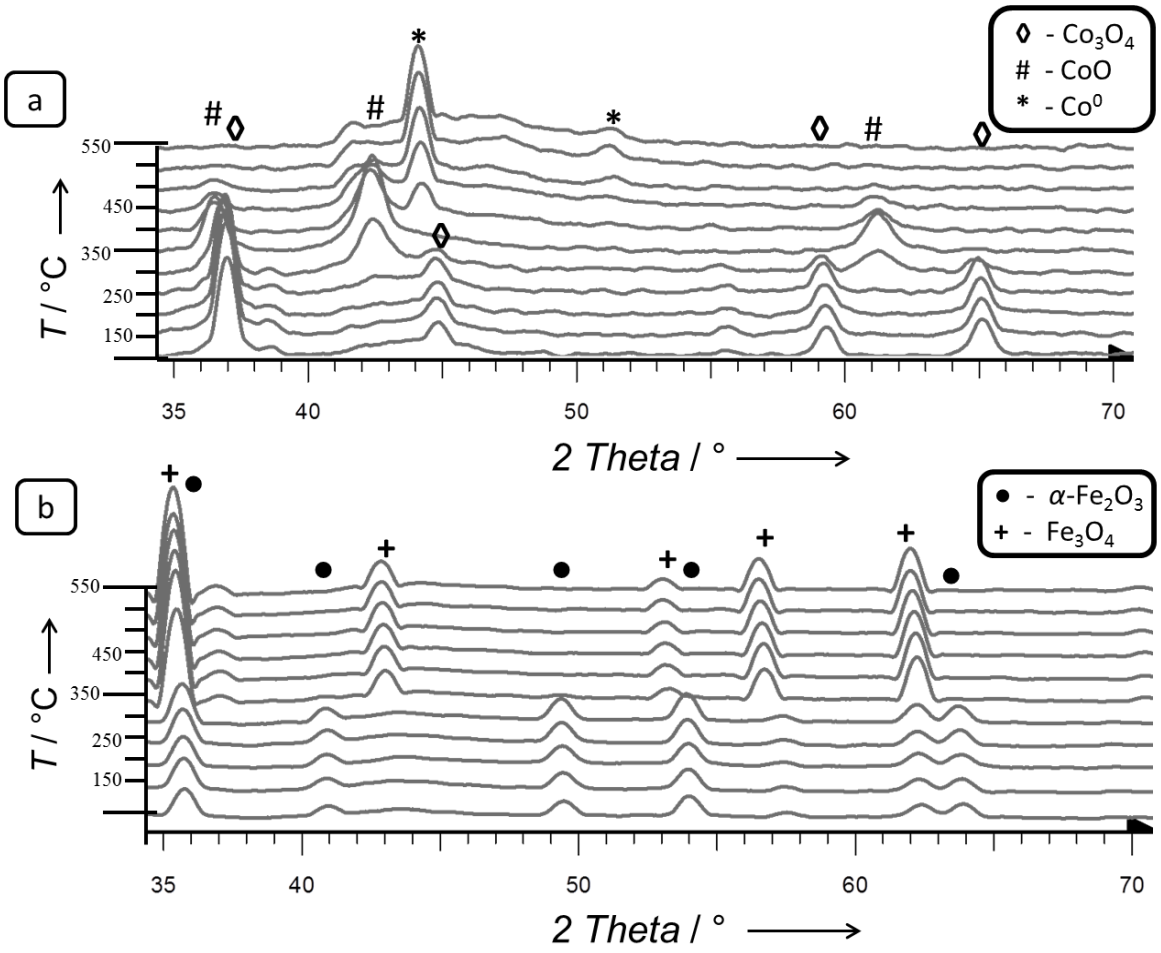

Figure 4.11 In situ PXRD patterns of the monometallic samples, a) 10Co/CSs and b) 10Fe/CSs samples. (X-ray source: Cu, $\lambda_{K\alpha}$ = 0.154 nm)

The four in situ PXRD reduction profiles of the bimetallic samples are displayed in Fig. 4.12. Notably, the addition of small quantities of Fe to the Co-rich sample (0.5Fe-9.5Co/CSs) introduced changes in the reduction behaviour compared to the monometallic Co sample (Fig. 4.12a). The final reduction step (CoO → Co) was shifted to a higher temperature (400

°C), and remarkably, a shoulder appeared at a 2θ = 44.9°, which corresponds to the (110) plane of the CoFe alloy, wairauite [PDF No. 00-044-1433]. The formation of this alloy phase at 550 °C was unexpected at such a low Fe ratio in the sample. For samples with increased iron ratios (Fig. 4.12b-c), the peak at 2θ = 44.9° was even more pronounced and an additional characteristic Co-Fe alloy peak at 2θ = 65.2° (200) was seen. For the 5Fe-5Co/CSs sample, the Co-Fe alloy formation was favoured over the formation of either metallic Co or Fe at high reduction temperatures. In this sample, a residual Fe_3O_4 diffraction peak at 2θ = 35.6° was also observed at the end of the experiment (Fig. 4.12c). The residual Fe_3O_4 was estimated to be approximately 0.68% using Rietveld refinement. This observation was unexpected as the alloy formed has a 1:1 ratio of Fe to Co and the sample contains equal amounts of the two metals. This could suggest that the alloy adopts a core-shell type of structure that has a higher Fe content in the shell.[13, 14]

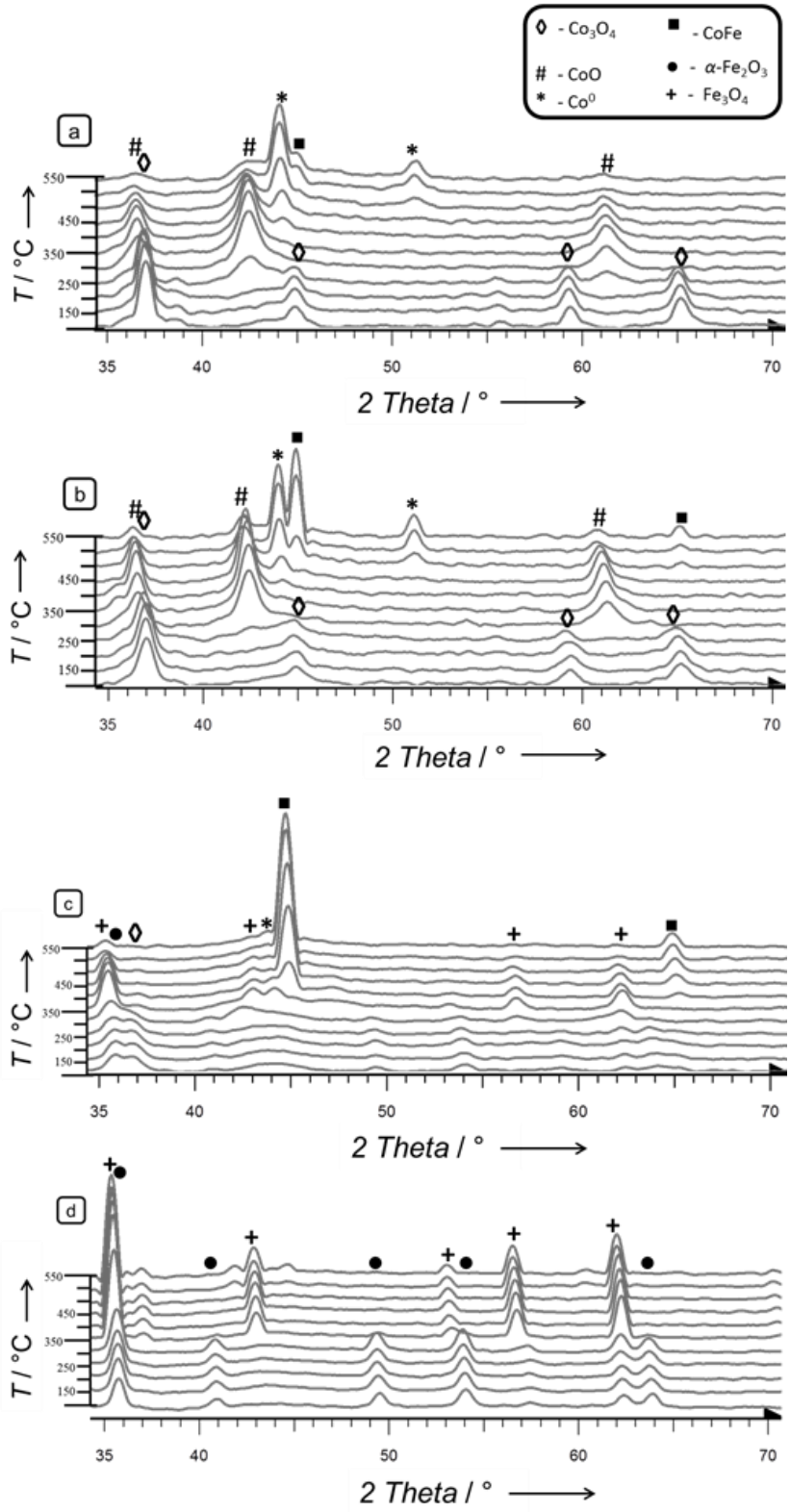

Figure 4.12 In situ PXRD patterns of the bimetallic samples, a) 0.5Fe-9.5Co/CSs, b) 2Fe-8Co/CSs, c) 5Fe-5Co/CSs and d) 9.5Fe-0.5Co/CSs samples (X-ray source: Cu, $\lambda_{K\alpha}$ = 0.154 nm).

The relative abundances of the Co-Fe alloy in the reduced bimetallic samples after in situ PXRD experiments were estimated using Rietveld refinement (Table 4.3). The relative abundance of the alloy in the samples was noted to increase as the Fe/Co ratio approached 5:5.

Table 4.3 Relative abundances of Co-Fe, Co, CoO and Fe_3O_4 on reduced bimetallic samples.

	Relative abundance [%]					**Rwp[a]**
Sample	Carbon	Co-Fe	Co	CoO	Fe_3O_4	**(χ^2)[b]**
0.5Fe-9.5Co/CSs	88.7	1.70	9.47	0.13	-	1.17 (1.50)
2Fe-8Co/CSs	90.6	2.76	5.83	0.81	-	1.32 (1.50)
5Fe-5Co/CSs	91.28	8.40	0.12	-	0.18	1.78 (1.82)

[a]Rwp is the weighted residual function. *[b]χ^2 is the goodness of fit.*

Alloy formation on bimetallic Fe-Co FT systems has long been proposed in the literature. Reports differ on the exact nature of the alloy formed presumably because of the limited in situ or in operando characterization of the bimetallic FT catalysts. Bragança et al. reported the formation of a mixed metal oxide (Co-Fe_2O_4) on Fe-Co/SBA-15 and Fe-Co/HMS catalysts after calcination at 400 °C in air.[47, 48] Other alloys that have been reported on Fe-Co systems include Fe_2Co, Co_7Fe_3 and Co/Fe supported on $CaCO_3$, SiO_2 and TiO_2, respectively.[11, 49-51] It appears that the nature of the support material used could influence the exact structure of the resultant alloy. To the best of our knowledge, there have been no literature reports on the in situ characterization of Fe-Co systems supported on carbons. Studies have been limited to PXRD characterization of samples that were reduced ex situ at elevated temperatures. Consequently, contradictory findings have been reported. Guerrero-Ruiz and co-workers reported that no features associated with an alloy were observed by PXRD on Fe-Co/C samples that were reduced ex situ at 400 and 450 °C.[52] Elsewhere, a Co/Fe alloy was observed on Fe-Co/CNTs catalysts that were reduced and passivated prior to PXRD

analysis.[10] A detailed analysis of the challenges associated with ex situ versus in situ reduction has been reported.[53] Notably, pure Fe (bcc) and Co-Fe alloy have similar diffraction patterns. Hence, the assignment of diffraction peaks in a bimetallic sample that was reduced ex situ can be challenging since both of these phases could be present. In this study, Fe_3O_4 was the dominant phase at 550 °C during the in situ reduction of monometallic Fe samples. Therefore the Fe-Co alloy peaks could be assigned unambiguously. The PXRD measurements performed in this study showed that wairauite (Co-Fe and possibly Co_xFe_y) was the alloy formed during the reduction of bimetallic Fe-Co/CSs catalysts.

4.2.5 Fischer-Tropsch reactor studies

The catalytic performance of the *x*Fe-*y*Co/CSs catalysts reduced at 350 °C for 18 h were evaluated by using a fixed-bed reactor under a set of similar conditions (220/250 °C, 10 bar, H_2/CO = 2, gas hourly space velocity (GHSV) = 2400 L kg_{cat}^{-1} h^{-1}). Two reaction temperatures (220, 250 °C) were used as these are typical reaction temperatures used for monometallic Co or Fe catalysts, respectively. The CO conversions of the catalysts as a function of time on stream are presented in Fig. 4.13. It was observed that all the catalysts investigated in this study were stable at both reaction temperatures for the time frame (100 h) used. For the monometallic catalysts, 10Co/CSs had a higher CO conversion than 10Fe/CSs catalyst under similar reaction conditions. This trend has also been reported elsewhere.[10, 48] The addition of small amounts of Fe to a Co-rich sample improved the CO conversions, and the 0.5Fe-9.5Co/CSs sample had higher conversions than all the other catalysts both at 220 and 250 °C. The increase in the activity of this bimetallic catalyst was not accompanied by any significant change in CO_2 selectivity as would be expected for an Fe catalyst. This result suggests that the bimetallic catalyst has different catalytic properties from its constituents, that is, it does not possess additive properties of Fe and Co. This observation is in agreement with conclusions drawn from other literature studies. A further increase in the Fe ratio in the samples had a negative effect on the FT conversion. CO conversions recorded over 2Fe-8Co/CSs and 5Fe-5Co/CSs were even lower than that measured on the monometallic Fe sample. Notably, the addition of small quantities of Co to a predominantly Fe-based catalyst did not yield any drastic effects on the performance of the catalyst. Thus a similar catalytic behaviour was observed between 9.5Fe-0.5Co/CSs and 10Fe/CSs. These observations are

also in agreement with our TPR results, in which similar reduction profiles were recorded for these two samples.

The steady-state CO conversions and product selectivities of the different samples in FT synthesis are summarized in Table 4.4. A plot of C_{5+} hydrocarbons as a function of the reaction temperature and the catalyst composition is shown in Fig. 4.14. Relatively high C_{5+} selectivities (77 – 87%) were displayed by the Co-rich samples at 220 °C. An increase of the reaction temperature to 250 °C generally resulted in a significant decline of C_{5+} hydrocarbons for all the Co-rich samples in favour of lighter hydrocarbon products. Consequently, methane selectivity for the 10Co/CSs sample increased from 10 to 23% at the higher reaction temperature. Monometallic cobalt catalysts are typically (industrially) evaluated in the temperature range 220 – 240 °C to achieve a high selectivity towards heavy hydrocarbons. In the present study, a reaction temperature of 250 °C was also evaluated to allow a comparison with Fe-rich samples that generally require higher reaction temperatures.

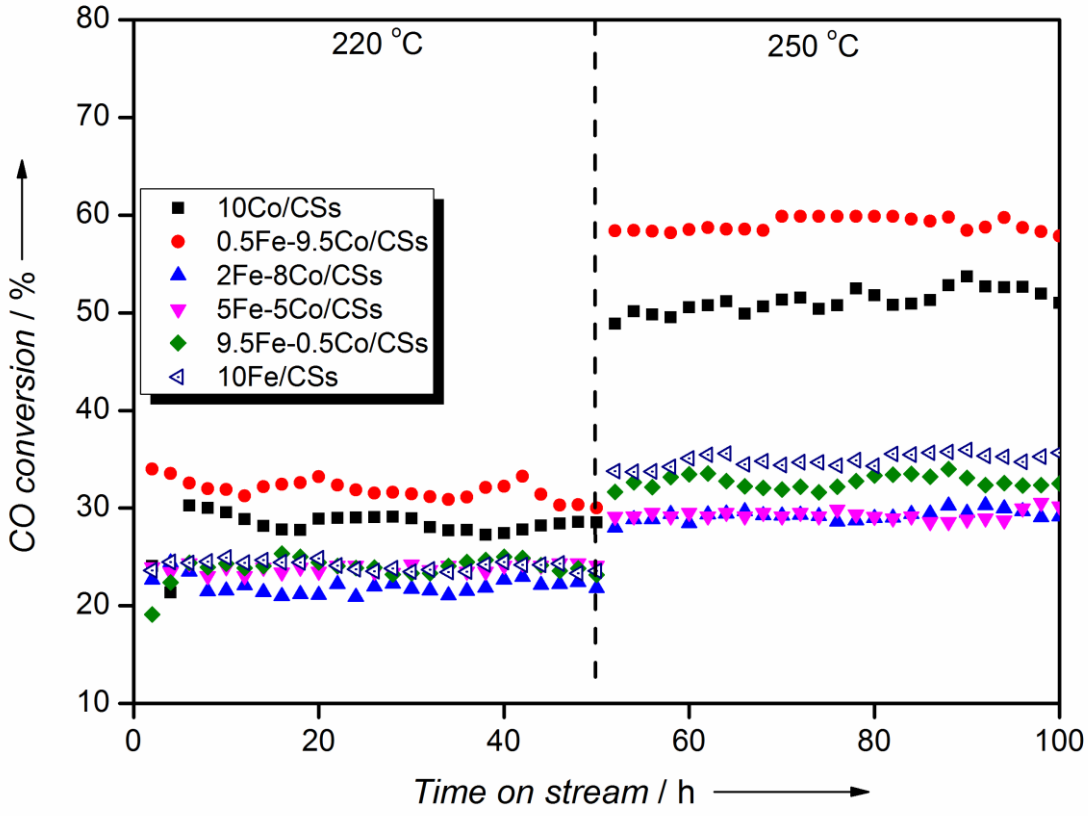

Figure 4.13 CO conversions as a function of time in FT synthesis for the mono- and bimetallic catalysts (P = 10 bar, H_2/CO = 2).

Table 4.4 FT performance data of the different catalysts.

Sample	T [°C]	CO conversion [%]	Hydrocarbon selectivity [%]			CO_2
			C_1	C_2-C_4	C_{5+}	
10Co/CSs	220	29	13	9	78	0
	250	51	23	8	69	6
0.5Fe-9.5Co/CSs	220	32	17	6	77	0
	250	60	22	10	68	10
2Fe-8Co/CSs	220	21	8	5	87	0
	250	29	18	10	72	15
5Fe-5Co/CSs	220	24	11	9	80	0
	250	29	17	9	74	8
9.5Fe-0.5Co/CSs	220	24	18	11	71	11
	250	33	19	13	68	17
10Fe/CSs	220	25	18	12	70	9
	250	36	19	14	68	20

As expected, Fe-rich samples exhibited comparatively lower C_{5+} hydrocarbon selectivities than Co-rich samples. Fe catalysts are typically promoted with an alkali metal like potassium to enhance selectivity towards long chain hydrocarbons.[54] Remarkably, the intermediate samples (2Fe-8Co/CSs, 5Fe-5Co/CSs) had the highest selectivity towards C_{5+} products at the lower temperature, that is, 87 and 80% respectively. As expected, these samples were also sensitive to the reactor temperature as significant declines in C_{5+} selectivity were observed with increased temperature. For example, the selectivity towards the heavy hydrocarbons decreased from 87 to 72% and from 80 to 74%, respectively. A corresponding increase in the methane fraction was also observed for these samples at 250 °C and intermediate WGS activity was seen for these samples. A more detailed analysis of the product distributions for selected hydrocarbons was obtained using off-line GC (Fig. 4.15).

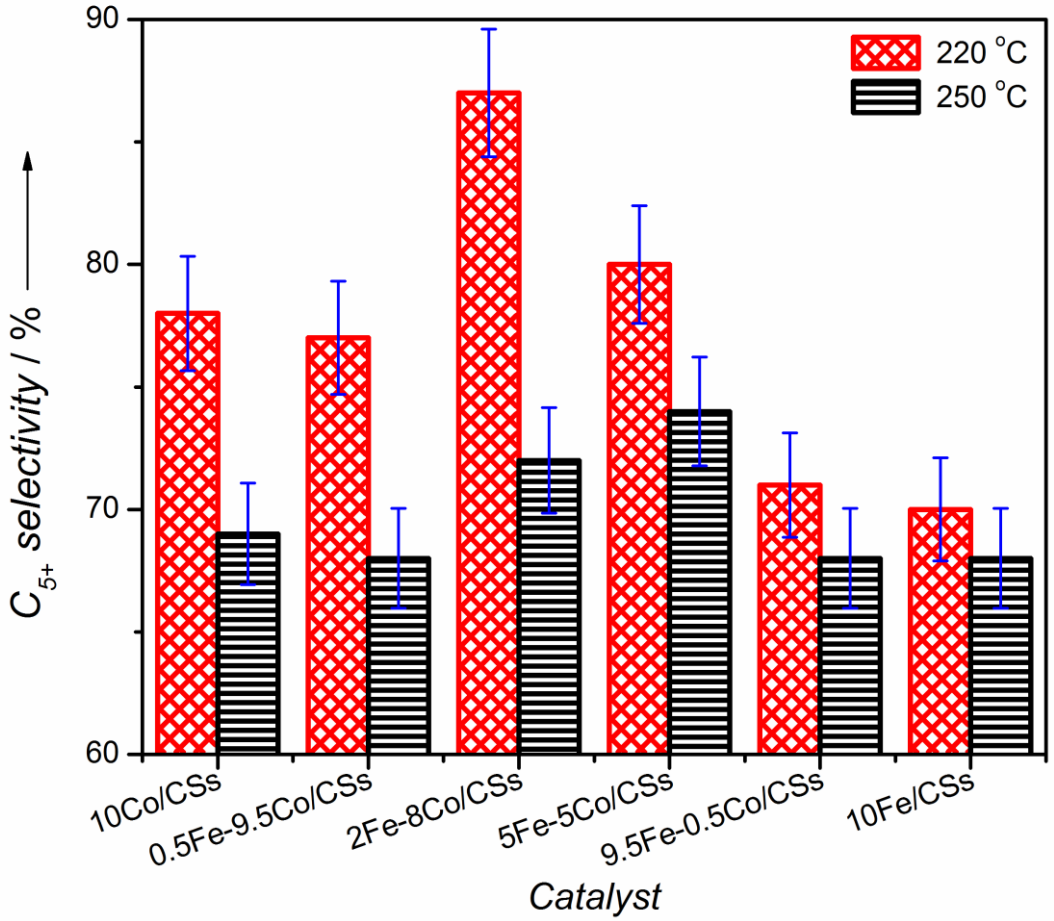

Figure 4.14 C_{5+} product selectivities calculated at 220 and 250 °C for the different catalyst compositions.

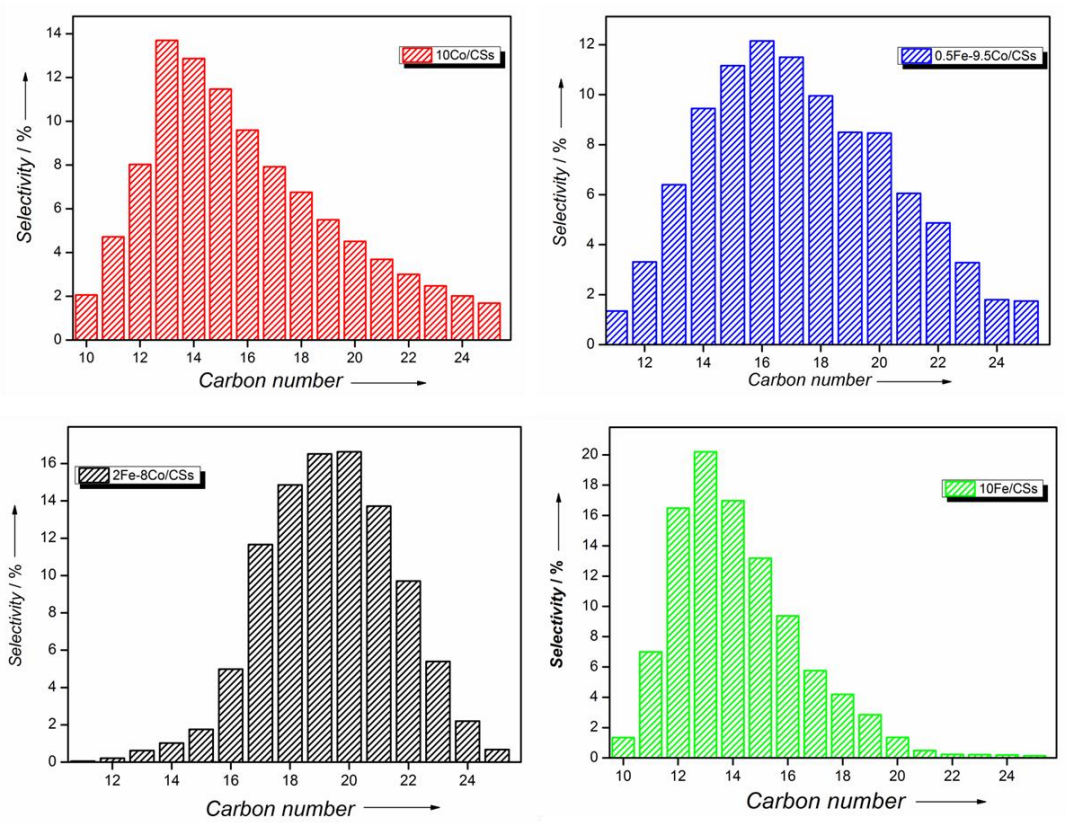

Figure 4.15 Liquid hydrocarbon product distributions obtained over the indicated catalysts.

4.2.6 The spent catalysts

Analysis of the spent catalyst was performed after FT synthesis to determine which phases had formed on the catalyst during the reaction. Ex situ PXRD patterns of selected spent catalysts, 10Co/CSs, 2Fe-8Co/CSs and 5Fe-5Co/CSs, are shown in Fig. 4.16. Two diffraction peaks at 2θ = 52.4 and 77.3° were observed on the spent bimetallic catalysts (2Fe-8Co/CSs and 5Fe-5Co/CSs), which correspond to the (110) and (200) diffraction planes of the Co-Fe (or Co_xFe_y) alloy (wairauite) [PDF No. 00-044-1433]. These data confirm that a Co-Fe alloy was present under FT conditions. It could be that the alloy formed during the prolonged reduction (18 h) before FT synthesis. However, alloy formation during FT synthesis cannot be ruled out. The Co-Fe alloy has been previously reported on spent Fe-Co/SiO_2 catalysts.[55, 56] Diffraction peaks due to the alloy were absent on the monometallic Co sample (10Co/CSs; Fig. 4.16). Other phases which were observed on the spent catalysts include CoO, metallic Co, Co_3C and Fe_2C.

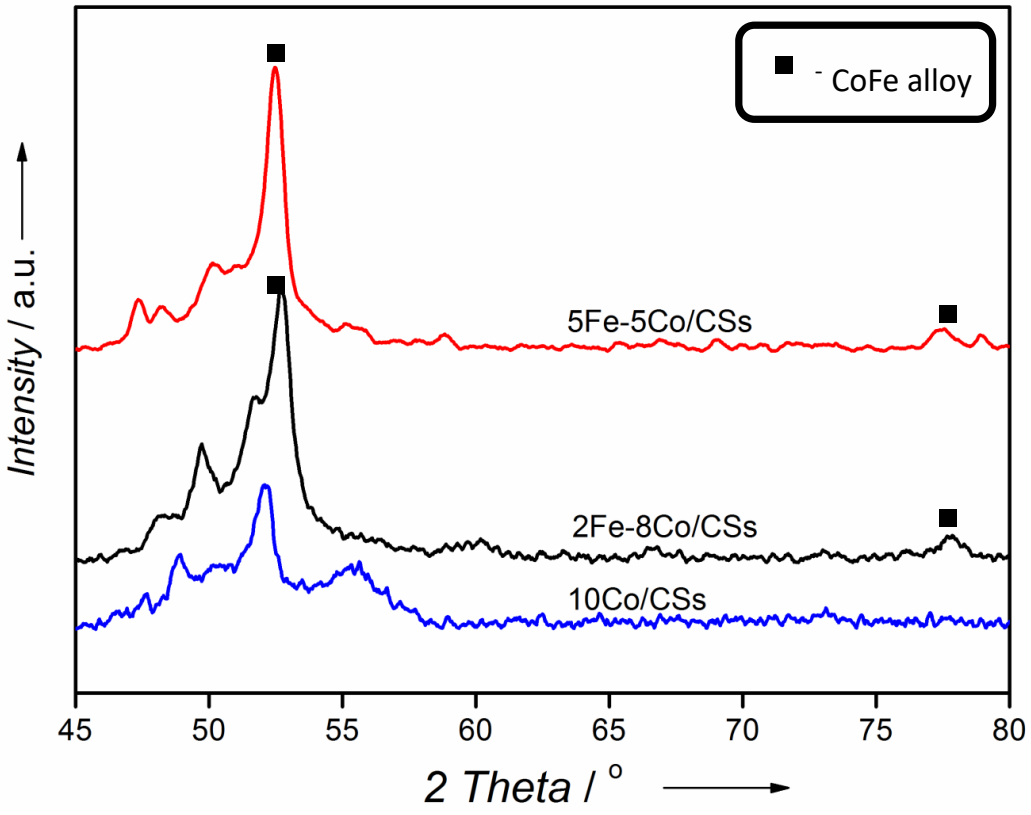

Figure 4.16 Ex situ PXRD patterns of selected spent catalysts. (X-ray source: Co, $\lambda_{K\alpha}$ = 0.197 nm).

4.2.7 Influence of the alloy on the CO conversion and selectivity

Findings made in this study indicate that the Co-Fe (or CoxFey) alloy is not observed before reduction of the bimetallic precursors, that is, on the calcined samples. Characterization by different techniques provided insight into the conditions that favour alloy formation. TPR, TGA and in situ PXRD show that the alloy forms 1) at high temperatures and/or 2) under reducing conditions. In situ PXRD data illustrate that the relative abundance of the alloy increased as the Fe/Co ratio of the reactants tended to unity.

The data summarized in Table 4.4 show that the presence of the Co-Fe alloy reduces the FT CO conversion relative to the monometallic Co catalysts; little change relative to pure Fe catalysts is seen. These results are in agreement with findings reported elsewhere.[48, 57] Bragança and co-workers also reported that 10Fe-14Co/HMS and 13Fe-15Co/SBA-15

catalysts prepared by incipient wetness impregnation had lower CO conversions than the corresponding 23Co/HMS and 24Co/SBA-15 monometallic catalysts.[48]

The CO conversions recorded at 220 °C all lie within the range 26 ± 5%. In this study (using similar reaction conditions) both Co and Fe catalysts showed a higher-hydrocarbon selectivity. The addition of 2% Fe to the Co catalyst enhanced the C_{5+} selectivity but further addition resulted in a lower C_{5+} selectivity. This behaviour is consistent at both reaction temperatures (220, 250 °C; Fig. 4.14).

The data thus indicates that the 1:1 FeCo alloy is not a key component to enhance the selectivity (or activity) of the catalysts. Rather, it appears that an alloy with a ratio closer to that of Co_2Fe is important. This data suggests a surface rich in Co; possibly with a structure similar to the core shell Fe@Co catalyst reported recently.[7, 43, 58]

4.3 Conclusions

We have synthesized solid carbon spheres (CSs) successfully by the hydrothermal method. It was found that the properties of the CSs can be tuned to make them model catalyst support materials by a simple high-temperature treatment under inert conditions (900 °C, 4 h, N_2). The results show that the surface area, pore size, thermal stability and crystallinity of the carbon support can be tuned by annealing for different periods. We have demonstrated that the CSs synthesized hydrothermally can be tuned to have higher BET surface areas and pore diameters than most reported CSs, which are typically synthesized by chemical vapour deposition. The annealing of the CSs allowed for the preparation of high-surface-area mono- and bimetallic catalysts with high dispersions. In situ powder XRD of the bimetallic Fe-Co catalysts showed that a Co-Fe-type alloy (wairauite) formed. Furthermore, the bimetallic catalysts with > 2 % Fe exhibited the best C_{5+} selectivity in Fischer-Tropsch synthesis, which suggests that the Co-rich and Fe-poor alloy formed during reduction favours the production of higher-hydrocarbon products. However, the relative abundance of the alloy is not correlated directly to the selectivity towards C_{5+} products. Notably, the alloy was formed under reducing conditions. Characterization of the calcined bimetallic catalysts in an

oxidizing atmosphere showed intermediate properties between Fe and Co. However, completely different properties were seen under reducing conditions, which confirmed the formation of a Co-Fe-type alloy. The use of the relatively inert hydrothermal CS support was particularly advantageous in this regard as it allowed in situ monitoring of the different phase transformations without forming complex mixed compounds with the bimetallic catalysts, which is normally the case with metal oxide supports. Additionally, it appears that the versatility of hydrothermal CSs can be exploited in the study of other complex bimetallic systems.

4.4 Experimental Section

4.4.1 Synthesis of carbon spheres (CSs)

The hydrothermal method was used for the synthesis of solid carbon spheres, and sucrose was used as the carbon precursor. Typically, a 0.3 M sucrose solution was added to a 100 mL Teflon-lined stainless-steel autoclave (filling ratio; 90%). The autoclave was heated to 190 °C at a heating rate of 1 °Cmin^{-1}, and synthesis was continued at this temperature for 4 h. The obtained powder was successively washed and centrifuged with water and absolute ethanol. Subsequently, purification of the product was performed by Soxhlet extraction to remove polyaromatic hydrocarbons (PAHs). For this extraction procedure, toluene was used as the solvent. The CSs were then dried at 70 °C for 12 h. As-prepared carbon spheres were then annealed under inert conditions to improve their properties. Annealing was performed at 900 °C under N_2 (20 mLmin^{-1}), and the annealing time was varied from 1 to 4 h.

4.4.2 Catalyst preparation

All catalysts in this study were supported on annealed CSs. Preparation of monometallic catalysts (10Fe/CSs, 10Co/CSs) was achieved by the homogeneous deposition precipitation method and the metal loading of 10 wt% was used in the synthesis. Nitrate precursors [$Fe(NO_3)_3 \cdot 9H_2O$ and $Co(NO_3)_2 \cdot 6H_2O$] were used as Fe and Co sources, respectively. Urea (Sigma) was used as the precipitating agent.

The bimetallic Fe-Co/CSs catalysts were also synthesized by the deposition co-precipitation technique using urea as the precipitation agent. A series of bimetallic catalysts were prepared by varying the Fe-to-Co ratio, and the total metal loading was kept at 10 wt%. Typically, the metal nitrate precursor(s) and urea (1.5 moles urea per mole of metal) were dissolved in deionized water (50 mL) and then added to the CS support, which was dispersed previously in deionized water (150 mL) at 90 °C. The hydrolysis of urea was allowed to proceed for 12 h with stirring, followed by drying at 70 °C under vacuum. Calcination was performed at 300 °C for 4 h in N_2 (20 $mLmin^{-1}$). The bimetallic samples are denoted *x*Fe-*y*Co/CSs, in which *x* and *y* are the wt% loadings of Fe and Co, respectively, in the samples. The values of *x* and *y* were 0, 0.5, 2, 5, 8 and 10, to give the catalysts 10Co/CSs, 0.5Fe-9.5Co/CSs, 2Fe-8Co/CSs, 5Fe-5Co/CSs, 9.5Fe-0.5Co/CSs and 10Fe/CSs.

4.4.3 Characterization

Transmission electron microscopy (TEM) analysis was carried out using an FEI Tecnai T12 Spirit operated at an accelerating voltage of 120 kV. Scanning electron microscopy (SEM) and energy-dispersive X-ray spectroscopy data were collected by using a FEI Nova Nanolab 600 instrument. Low- and wide-angle ex situ powder X-ray diffraction (PXRD) patterns were recorded by using a Bruker D2 diffractometer, which used Co Kα radiation ($\lambda_{K\alpha}$ = 0.178897 nm) and a Lynxeye detector. The scan range was 2θ = 10-90° with 0.026° steps. Surface area and porosity data were measured from 200 mg samples by using a Micromeritics TriStar 3000 instrument operated at -196 °C. Before analysis, samples were degassed at 150 °C in N_2 for 6 h. The specific surface area was calculated by the BET method from N_2 adsorption data in the relative pressure range P/P_o = 0.05-0.30. Total pore volumes of the samples were calculated at a relative pressure of P/P_o = 0.995. The Barrett-Joyner-Halenda (BJH) pore size distributions were calculated by analysing the desorption branches of the N_2 isotherms. Thermogravimetric analysis (TGA) was performed under oxidizing conditions by using a PerkinElmer STA6000 analyser. Analysis was performed in the temperature range 50-900 °C using a 10 °$Cmin^{-1}$ heating rate.

The reduction behaviour of catalysts was monitored both by H_2-temperature programmed reduction (TPR) and in situ PXRD techniques. TPR profiles of the catalysts were recorded by

using a Micromeritics AutoChem II unit fitted with a thermal conductivity detector (TCD). The TPR reactor was heated from RT to 900 °C at a heating rate of 10 °Cmin^{-1} in a flow of reducing gas (5%H_2/95%Ar) at flow rate of 45 mLmin^{-1}. In situ PXRD experiments were conducted by using a Bruker D8 Advance AXS diffractometer with Cu radiation ($\lambda_{K\alpha}$ = 0.154084 nm) fitted with a Göbel mirror to produce a pseudo parallel primary beam and operated at 40 kV and 40 mA. For these experiments, samples were placed in an Anton Paar XRK 900 reaction chamber and diffraction patterns were collected in the range of 2θ = 15-80° using a VÅNTEC position-sensitive detector. Reduction was performed under a flow of H_2 (5%H_2, balance N_2) using a step-wise temperature ramp from 150-550 °C with increments of 50 °C. The temperature was then maintained at 550 °C for 2 h, and the catalyst phase composition was monitored. Analysis of the in situ PXRD data by the Rietveld refinement method was performed by using the TOPAS 4.2 (Bruker AXS) software package, using analytical peak shape functions and starting structure models obtained from the Inorganic Crystal Structural Database.[59] The quality of the model used for refinement was evaluated using the goodness of fit (χ^2) and the weighted residual function (Rwp) parameters.

4.4.4 Fischer-Tropsch synthesis

Before the FTS reaction, the catalysts (0.5 g) were suspended on a plug of quartz wool in a tubular fixed-bed stainless-steel reactor (i.d. = 16 mm). Reduction was performed in situ using ultra high purity H_2 gas (45 mLmin^{-1}). Catalyst reduction was performed at 350 °C (ramping rate: 1 °Cmin^{-1}) for 18 h and 2 bar pressure. Subsequently, FT synthesis was performed at two reaction temperatures (220, 250 °C) using a synthesis gas flow rate of 20 mLmin^{-1} and a total pressure of 10 bar. Synthesis gas with a H_2/CO ratio of 2 was used and 10% N_2 was used as the internal standard. Exit-gas products were analysed by two online gas chromatographs fitted with a thermal conductivity detector (TCD) and a flame ionization detector (FID). Two hot and cold traps kept at 150 and 20 °C, respectively, were used to collect wax and oil products. The composition of the liquid hydrocarbons was determined using an off-line GC-FID.

Acknowledgements

This work was financially supported by the DST-NRF Centre of Excellence in Catalysis (c*change) and the University of the Witwatersrand. We also wish to thank the Microscopy and Microanalysis Unit (MMU) at the University of the Witwatersrand for assistance with microscopy studies.

References

[1] Y. Liu, J. Luo, M. Girleanu, O. Ersen, C. Pham-Huu, C. Meny, *J. Catal.* **2014**, *318*, 179-192.

[2] S. Sartipi, K. Parashar, M. Makkee, J. Gascon, F. Kapteijn, *Catal. Sci. Technol.* **2013**, *3*, 572-575.

[3] S. Sartipi, M. Makkee, F. Kapteijn, J. Gascon, *Catal. Sci. Technol.* **2014**, *4*, 893-907.

[4] T. Das, G. Deo, *J. Phys. Chem. C* **2012**, *116*, 20812-20819.

[5] A. Griboval-Constant, A. Butel, V. V. Ordomsky, P. A. Chernavskii, A. Y. Khodakov, *Appl. Catal., A* **2014**, *481*, 116-126.

[6] S. Lögdberg, D. Tristantini, Ø. Borg, L. Ilver, B. Gevert, S. Järås, E. A. Blekkan, A. Holmen, *Appl. Catal., B* **2009**, *89*, 167-182.

[7] V. R. Calderone, N. R. Shiju, D. Curulla-Ferré, S. Chambrey, A. Khodakov, A. Rose, J. Thiessen, A. Jess, G. Rothenberg, *Angew. Chem.* **2013**, *125*, 4493-4497.

[8] Y. Yang, H. Xiang, R. Zhang, B. Zhong, Y. Li, *Catal. Today* **2005**, *106*, 170-175.

[9] E. de Smit, B. M. Weckhuysen, *Chem. Soc. Rev.* **2008**, *37*, 2758-2781.

[10] A. Tavasoli, M. Trépanier, R. M. Malek Abbaslou, A. K. Dalai, N. Abatzoglou, *Fuel Process. Technol.* **2009**, *90*, 1486-1494.

[11] D. J. Duvenhage, N. J. Coville, *Appl. Catal., A* **1997**, *153*, 43-67.

[12] R. Satthawong, N. Koizumi, C. Song, P. Prasassarakich, *J. CO_2 Util.* **2013**, *3–4*, 102-106.

[13] V. R. Calderone, N. R. Shiju, D. C. Ferre, G. Rothenberg, *Green Chem.* **2011**, *13*, 1950-1959.

[14] D. J. Duvenhage, N. J. Coville, *J. Mol. Catal., A* **2005**, *235*, 230-239.

[15] X. Ma, Q. Sun, F. Cao, W. Ying, D. Fang, *J. Nat. Gas Chem.* **2006**, *15*, 335-339.

[16] J. Li, G. Jacobs, T. Das, Y. Zhang, B. Davis, *Appl. Catal., A* **2002**, *236*, 67-76.

[17] M. Boudart, A. Delbouille, J. A. Dumesic, S. Khammouma, H. Topsøe, *J. Catal.* **1975**, *37*, 486-502.

[18] T. Mochizuki, T. Hara, N. Koizumi, M. Yamada, *Appl. Catal., A* **2007**, *317*, 97-104.

[19] A. Y. Khodakov, W. Chu, P. Fongarland, *Chem. Rev.* **2007**, *107*, 1692-1744.

[20] B. Jongsomjit, J. Panpranot, J. G. Goodwin Jr, *J. Catal.* **2001**, *204*, 98-109.

[21] A. Tavasoli, R. M. Malek Abbaslou, A. K. Dalai, *Appl. Catal., A* **2008**, *346*, 58-64.

[22] Y. Liu, O. Ersen, C. Meny, F. Luck, C. Pham-Huu, *ChemSusChem* **2014**, *7*, 1218-1239.

[23] B. Sun, K. Xu, L. Nguyen, M. Qiao, F. Tao, *ChemCatChem* **2012**, *4*, 1498-1511.

[24] H. Xiong, L. L. Jewell, N. J. Coville, *ACS Catal.* **2015**, *5*, 2640-2658.

[25] M. Moyo, M. A. M. Motchelaho, H. Xiong, L. L. Jewell, N. J. Coville, *Appl. Catal., A* **2012**, *413–414*, 223-229.

[26] H. Xiong, M. Moyo, M. A. Motchelaho, Z. N. Tetana, S. M. A. Dube, L. L. Jewell, N. J. Coville, *J. Catal.* **2014**, *311*, 80-87.

[27] U. M. Graham, G. Jacobs, M. K. Gnanamani, S. M. Lipka, W. D. Shafer, C. R. Swartz, T. Jermwongratanachai, R. Chen, F. Rogers, B. H. Davis, *ACS Catal.* **2014**, *4*, 1662-1672.

[28] M.-M. Titirici, M. Antonietti, *Chem. Soc. Rev.* **2010**, *39*, 103-116.

[29] Z. Chen, L. Ma, S. Li, J. Geng, Q. Song, J. Liu, C. Wang, H. Wang, J. Li, Z. Qin, S. Li, *Appl. Surf. Sci.* **2011**, *257*, 8686-8691.

[30] M.-L. Sham, J.-K. Kim, *Carbon* **2006**, *44*, 768-777.

[31] L. Yu, C. Falco, J. Weber, R. J. White, J. Y. Howe, M.-M. Titirici, *Langmuir* **2012**, *28*, 12373-12383.

[32] S. Tang, Y. Tang, S. Vongehr, X. Zhao, X. Meng, *Appl. Surf. Sci.* **2009**, *255*, 6011-6016.

[33] S. Tang, S. Vongehr, X. Meng, *Nanotechnology* **2012**, *23*, 095603.

[34] P. R. Karandikar, Y.-J. Lee, G. Kwak, M. H. Woo, S.-J. Park, H.-G. Park, K.-S. Ha, K.-W. Jun, *J. Phys. Chem. C* **2014**, *118*, 21975-21985.

[35] L. Zhao, N. Baccile, S. Gross, Y. Zhang, W. Wei, Y. Sun, M. Antonietti, M.-M. Titirici, *Carbon* **2010**, *48*, 3778-3787.

[36] P. E. Fanning, M. A. Vannice, *Carbon* **1993**, *31*, 721-730.

[37] R. Demir-Cakan, N. Baccile, M. Antonietti, M.-M. Titirici, *Chem. Mater.* **2009**, *21*, 484-490.

[38] G. Yu, B. Sun, Y. Pei, S. Xie, S. Yan, M. Qiao, K. Fan, X. Zhang, B. Zong, *J. Am. Chem. Soc.* **2010**, *132*, 935-937.

[39] R. Phienluphon, L. Shi, J. Sun, W. Niu, P. Lu, P. Zhu, T. Vitidsant, Y. Yoneyama, Q. Chen, N. Tsubaki, *Catal. Sci. Technol.* **2014**, *4*, 3099-3107.

[40] H. Zhang, C. Lancelot, W. Chu, J. Hong, A. Y. Khodakov, P. A. Chernavskii, J. Zheng, D. Tong, *J. Mater. Chem.* **2009**, *19*, 9241-9249.

[41] H. Xiong, M. Moyo, M. K. Rayner, L. L. Jewell, D. G. Billing, N. J. Coville, *ChemCatChem* **2010**, *2*, 514-518.

[42] H. Wang, Y. Yang, B.-S. Wu, J. Xu, M.-Y. Ding, H.-L. Wang, W.-H. Fan, H.-W. Xiang, Y.-W. Li, *J. Molec. Catal., A* **2009**, *308*, 96-107.

[43] V. R. Calderone, N. R. Shiju, D. Curulla-Ferré, S. Chambrey, A. Khodakov, A. Rose, J. Thiessen, A. Jess, G. Rothenberg, *Angew. Chem. Int. Ed.* **2013**, *52*, 4397-4401.

[44] D. G. Billing, A. Katrusiak, *Acta Cryst., B* **2014**, *70*, 399-400.

[45] Y. Yang, L. Jia, B. Hou, D. Li, J. Wang, Y. Sun, *Catal. Sci. Technol.* **2014**, *4*, 717-728.

[46] M. K. Rayner, D. G. Billing, N. J. Coville, *Acta Cryst.* **2014**, *B70*, 498-509.

[47] L. F. F. P. G. Bragança, R. R. Avilez, M. I. P. d. Silva, *Colloid. Surf., A* **2010**, *358*, 79-87.

[48] L. F. F. P. G. Bragança, M. Ojeda, J. L. G. Fierro, M. I. P. da Silva, *Appl. Catal., A* **2012**, *423–424*, 146-153.

[49] N. Chiwaye, L. L. Jewell, D. G. Billing, D. Naidoo, M. Ncube, N. J. Coville, *Mater. Res. Bull.* **2014**, *56*, 98-106.

[50] S. Ali, N. Mohd Zabidi, D. Subbarao, *Chem. Cent. J.* **2011**, *5*, 68.

[51] V. A. de la Peña O'Shea, M. C. Álvarez-Galván, J. M. Campos-Martin, N. N. Menéndez, J. D. Tornero, J. L. G. Fierro, *Eur. J. Inorg. Chem.* **2006**, *2006*, 5057-5068.

[52] A. Guerrero-Ruiz, A. Sepúlveda-Escribano, I. Rodríguez-Ramos, *Appl. Catal., A* **1992**, *81*, 81-100.

[53] F. Huber, Z. Yu, S. Lögdberg, M. Rønning, D. Chen, H. Venvik, A. Holmen, *Catal. Lett.* **2006**, *110*, 211-220.

[54] M. E. Dry, G. J. Oosthuizen, *J. Catal.* **1968**, *11*, 18-24.

[55] X. Ma, Q. Sun, W. Ying, D. Fang, *J. Nat. Gas Chem.* **2009**, *18*, 354-358.

[56] X. Ma, Q. Sun, W. Ying, D. Fang, *J. Nat. Gas Chem.* **2009**, *18*, 232-236.

[57] J. A. Díaz, H. Akhavan, A. Romero, A. M. Garcia-Minguillan, R. Romero, A. Giroir-Fendler, J. L. Valverde, *Fuel Process. Technol.* **2014**, *128*, 417-424.

[58] T. Asefa, *ChemCatChem* **2013**, *5*, 1698-1700.

[59] A. Belsky, M. Hellenbrandt, V. L. Karen, P. Luksch, *Acta Cryst., B* **2002**, *58*, 364-369.

CHAPTER 5

Post-synthesis nitrogen doping of a hollow carbon sphere support for improved cobalt catalyst stability in Fischer-Tropsch synthesis

5.1 Introduction

Crude oil-derived liquid fuels are the overwhelming source of energy in the current transportation structure. However, the price of crude-oil is inherently unstable and is also influenced by economic and political factors.[1] The Fischer-Tropsch (FT) synthesis is an alternative route for producing clean transportation fuels and building-block chemicals from non-petroleum carbon resources such as coal, natural gas or biomass. Because of the economic significance of the FT process, it still receives world-wide attention from researchers in an attempt to improve its efficiency and profitability. Industrial catalysts for the process typically consist of Fe or Co particles dispersed on metal oxides like TiO_2, Al_2O_3 or SiO_2 which provide excellent thermal stability and mechanical integrity.[2] Supported cobalt remains the catalyst of choice for the FT reaction due to its high per pass activity, high C_{5+} selectivity, longer catalyst lifetime, low oxygenate and CO_2 selectivity and at present it accounts for a combined estimated production capacity of 250 000 barrels per day.[3-6] In contrast, iron catalysts are active in the water-gas-shift reaction and also favour the production of by-products like oxygenates and isomers.

Recently, carbon-based materials have been successfully employed as model support materials for cobalt FT catalysts due to their unique properties, such as a tunable surface area, high thermal stability and tailorable surface chemistry. Their potential applications in catalysis, gas/energy storage, as adsorbents, and sensors have been reported.[7] The properties of carbon materials are strongly influenced by their morphology,[8] currently reported morphologies include carbon spheres, carbon nanotubes, carbon nanofibers, carbon nanocoils, carbon nanowires, graphene, bamboo-like carbon and diamond like carbon. Hollow carbon spheres (HCSs) are particularly interesting because of their porous structure,

---

This chapter is still to be submitted for publication.

high surface area and low densities. The low densities of HCSs coupled with the high surface to volume ratios make them ideal support materials for the synthesis of highly dispersed catalysts. Additionally, the relatively inert carbon framework provides an ideal platform for studies on metal-support interactions, catalyst size effects and surface functionalization.

The surface chemistry of carbon materials can be tailored by doping them using a heteroatom such as nitrogen or oxygen. Nitrogen doped carbons are more interesting as they have displayed superior activity when compared to oxygen functionalized carbons when used as supports for Fischer-Tropsch catalysts. It has been reported that nitrogen-doped carbons generate a favourable metal-support interaction, resulting in improved catalyst performance. Three effects are believed to result in the improved performance of N-doped catalyst supports: (1) modified nucleation and growth kinetics during catalyst nanoparticle deposition, which favours the formation of smaller catalyst particle sizes and therefore gives increased dispersion, (2) increased the metal-support interaction which led to improved catalyst stability during the reaction, and (3) modification of the electronic structure of the catalyst nanoparticles, which might enhance intrinsic catalytic activity.[9] N-doping has been shown to increase the catalytic performance of FT catalysts supported on CNTs,[10-11] CSs[12] and more recently graphene.[13] However, most of these carbons were functionalized via in situ N-doping. Maldonado and Stevenson have demonstrated that in situ N-doping of CNFs can decrease the thermal stability of N-CNFs by ~90 °C relative to the pristine material due to increased disorder of the carbon framework.[14]

Recently, N-doped carbons in which the doping was done by a post-synthesis methodology have been shown to be a superior support material. This is attributed to the better mechanical and thermal stability of the post-doped carbons. In a typical post-doping procedure, carbon materials are treated with a nitrogen-containing precursor, such as ammonia or melamine at high temperatures, which decomposes the precursor to give free radicals like NH_2, NH, atomic nitrogen and hydrogen. The free radicals then attack the carbon matrix to form nitrogen-containing functional groups such as –CN, -NH_2, pyrrolic and quaternary nitrogen.[15] In this study we have explored the robustness of hollow carbon spheres by using them as a support material for Co FT catalysts under harsh reaction conditions (high temperature, pressure). Furthermore, the surface properties of hollow carbon spheres were

modified by a post-synthesis nitrogen doping procedure which led to N-HCSs. The effect of this surface functionalization procedure was studied by comparing pristine HCSs with nitrogen doped N-HCSs as a support material for a cobalt Fischer-Tropsch catalyst.

5.2 Experimental methods

5.2.1 Chemicals: Tetraethyl orthosilicate (TEOS, Sigma-Aldrich), ammonia solution (25%), absolute ethanol (99.6%), resorcinol (Merck), formaldehyde, hydrofluoric acid (HF, 10%), melamine, methanol, cobalt nitrate (Sigma-Aldrich), urea (Promark Chemicals) were obtained from the sources listed and used as received.

5.2.2 Synthesis of hollow carbon spheres (HCSs)

Hollow carbon spheres were synthesized by the hydrothermal method, utilizing a solid silica template as the core. The solid template was made using a modified Stöber method.[16-17] HCS synthesis started with the fabrication of core-shell SiO_2@RF composites. In a typical synthesis, 2.13 mL TEOS was mixed with 37.5 mL of absolute ethanol. This solution was then added to a mixture containing ethanol (25 mL), deionized water (7.5 mL) and ammonia (5 mL). The contents were stirred for 1 h to allow for the formation of colloidal silica spheres which were used as a template. Subsequently, resorcinol (0.5 g) and formaldehyde (0.7 mL) were added make the core-shell structures. The solution was allowed to stir for 24 h at room temperature, and then transferred into a Teflon-lined stainless steel autoclave, hydrothermally treated at 100 °C for 24 h. The product was washed/centrifuged successively with water and ethanol, followed by drying at 70 ^{o}C for 12 h. Carbonization of the SiO_2@RF composites was done at 900 ^{o}C for 1 h under N_2 (20 mL/min), followed by etching of the silica core using a 10% HF solution to give pristine HCSs.

5.2.3 Synthesis of nitrogen-doped hollow carbon spheres (N-HCSs)

N-HCSs were prepared following a post synthesis procedure. The core-shell SiO_2@RF composites were fabricated as explained above and were then mixed with melamine which was used as the nitrogen precursor. In particular, 2.82 g of melamine was allowed to dissolve

in methanol (200 mL) and then 4.7 g of SiO_2@RF composites were added to the solution under stirring. The mixture was allowed to stir at room temperature and the methanol allowed to evaporate. Subsequently, the SiO_2@RF-melamine composites were then carbonized under N_2 (20 mL/min) for 1 h. Carbonization was done at two temperatures; 600 and 900 °C. The samples were then etched using a 10% HF solution to give N-doped HCSs which are labelled as N-$HCSs_{600}$ and N-$HCSs_{900}$ in accordance with the 600 and 900 °C carbonization temperatures used.

5.2.4 Catalyst preparation

Cobalt Fischer-Tropsch catalysts supported on carbon materials (10% Co loading) were prepared in this study. Three different carbon supports were used; pristine hollow carbon spheres (HCSs), N-doped hollow carbon spheres carbonized at 600 °C (N-$HCSs_{600}$) and N-doped hollow carbon spheres carbonized at 900 °C (N-$HCSs_{900}$). The corresponding cobalt catalysts prepared from these supports have been labelled as 10Co/HCSs, 10Co/N-$HCSs_{600}$ and 10Co/N-$HCSs_{900}$. All the catalysts were prepared by the homogeneous deposition precipitation method utilizing urea as the precipitating agent and cobalt nitrate [$Co(NO_3)_2.6H_2O$] as the cobalt precursor. In a typical synthesis, the prepared carbon support was dispersed in 200 mL deionized water in a round-bottom flask and the temperature was raised to 90 °C. A solution composed of calculated amounts of the cobalt precursor and urea dissolved in deionized water (20 mL) was then added drop-wise under stirring. The hydrolysis of urea was allowed to proceed under these conditions for 12 h, after which the solvent was removed under vacuum on a rotary evaporator at 70 °C. Subsequently the catalyst was dried and then calcined at 300 °C for 4 h under N_2.

5.2.5 Catalyst characterizations

Powder X-ray diffraction (XRD) measurements were done using a Bruker D2 phaser with Co Kα radiation (λ = 0.178897 nm), scan range 10-90° (2θ) with 0.026° steps. The instrument was operated at 30 kV and 10 mA. Scanning electron microscopy (SEM) and energy dispersive X-ray spectroscopy (EDX) analysis was done on an FEI Nova Nanolab 600 instrument. Sample preparation for transmission electron microscopy (TEM) analysis was as follows: the powder sample was dispersed in ethanol by sonication for 5 minutes.

Subsequently, the sample was added drop-wise to a carbon coated copper grid prior to analysis. Bright-field TEM images were recorded on a CCD detector fitted on a FEI Tecnai T12 Spirit operating at an accelerating voltage of 120 kV.

Nitrogen adsorption measurements were carried out on a Micromeritics Tristar 3000 analyser operated at -196 °C. Prior to analysis, samples were degassed at 150 °C under N_2 flow for 12 h. Pore size distributions were determined by the BJH (Barrett-Joyner-Halenda) method while pore volumes were calculated at a relative pressure of 0.995 (P/P_o) by assuming that the pores were filled with the condensate in the liquid state. Raman spectroscopy analysis was carried out on an InVia Raman spectrometer fitted with a DuoScan attachment. The spectra were recorded at a laser wavelength of 514.5 nm and the power at the sample was 0.2 mW. X-ray photoelectron spectroscopy (XPS) measurements were done on a SHIMADZU KRATOS analytical AXIS SUPRA^{TM} XPS system with monochromatic Al K_α radiation (1486.6 eV). The working pressure in the measurement chamber was kept at 1.8×10^{-8} torr.

H_2-temperature programmed reduction (TPR) experiments were done on a Micromeritics Autochem II instrument fitted with a thermal conductivity detector (TCD). Samples were outgassed in Ar at 150 °C for 30 minutes prior to the analysis with 5% H_2 bal. Ar in the temperature range 50-900 °C. Brooks mass flow controllers were used to maintain the flow rate at 45 mL/min during the the analysis. The reducibility of the catalyst was also monitored by the in situ PXRD technique. A Bruker D8 Advance AXS diffractometer fitted with an Anton Paar XRK 900 reaction chamber was used for data collection. The diffractometer was operated at 40 kV, 40 mA and used a Cu radiation source ($\lambda_{K\alpha}$ = 0.154084 nm). Variable temperature measurements were done in the range 150-550 °C using 50 °C step-wise increments; subsequently the temperature was maintained at 550 °C for 2 h. Phase information was recorded on a VÅntec position sensitive detector in the 2 theta range 15-80°. The Rietveld refinement method incorporated in the TOPAS 4.2 (Bruker AXS) software package was used to analyse the in situ PXRD data.

5.3 Results and discussion

5.3.1 Synthesis and doping of hollow carbon spheres (HCSs)

Shown in Fig. 5.1 are TEM and SEM images of the SiO_2 spheres, SiO_2@RF composites and HCSs made in the study. Highly uniform and spherical silica templates were synthesized which had an average sphere diameter of 320 ± 20 nm (Fig. 5.1a-b). It was observed that the surface of the silica sphere was smooth and well defined. A carbon-coating process which involved resorcinol and formaldehyde as carbon precursors resulted in the formation of a SiO_2-resorcinol-formaldehyde composite, denoted as SiO_2@RF. The composite was then carbonized at 900 °C under N_2 to convert the polymeric RF to a layer of carbon. It can be seen from Fig. 5.1c-d that the composite consists of a silica core which is uniformly encapsulated by a carbon shell with a thickness of 30 ± 5 nm. In the final synthesis step, the silica template was etched out using a 10% HF solution to yield monodispersed pristine HCSs (Fig. 5.1e-f). The HF etching process did not affect the carbon shell thickness, as expected.

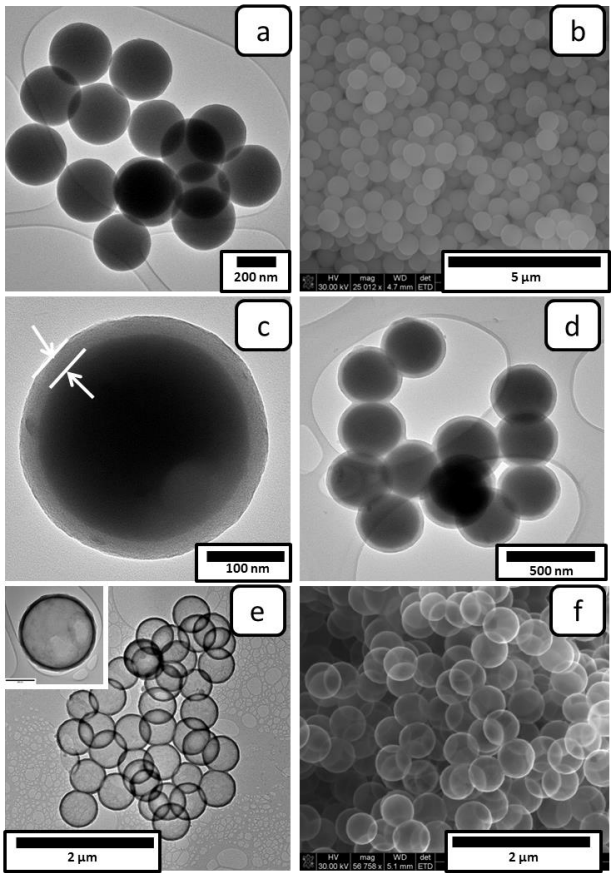

Figure 5.1 TEM and SEM images of (a,b) stöber silica spheres, (c,d) core-shell SiO_2@RF composites and, (e,f) hollow carbon spheres. The insert in Fig. 5.1e shows a single HCS.

Synthesis of N-doped HCSs was achieved through a similar protocol as that used to make the pristine HCSs but with slight variations. After the synthesis of the SiO_2@RF composite, melamine (dissolved in methanol) was added to functionalize the outer surface on the carbons with nitrogen. The materials were then carbonized in N_2 at either 600 or 900 °C to yield N-$HCSs_{600}$ and N-$HCSs_{900}$, respectively. CHNS elemental analysis was used to quantify the total nitrogen content on the materials after the carbonization steps and the results are presented in Table 5.1. The samples that were carbonized at 600 °C had a nitrogen content of 13.1% while a lower N content of 5.4% was recorded after the 900 °C heat treatment procedure. The reduced nitrogen content at higher temperatures is attributed to the cleavage of C-N bonds at the higher temperature.[18-19]

Raman spectroscopy is a useful and non-destructive technique for studying the structure and quality of carbonaceous nanomaterials. Analysis of the D band versus the G band intensities (I_D/I_G) from the Raman spectra of HCS, N-$HCSs_{600}$ and N-$HCSs_{900}$ allowed an investigation of bonding features of the carbon spheres. It can be seen from the spectra that the I_D/I_G ratio increased with the nitrogen content in the samples (Table 5.1, Fig. 5.2), consistent with the increase of defects within the carbon framework after N-doping. Correspondingly, the D-band position shifted to higher wavenumbers with an increase in the nitrogen content. The G-band peak positions remained relatively unchanged even after N-doping.

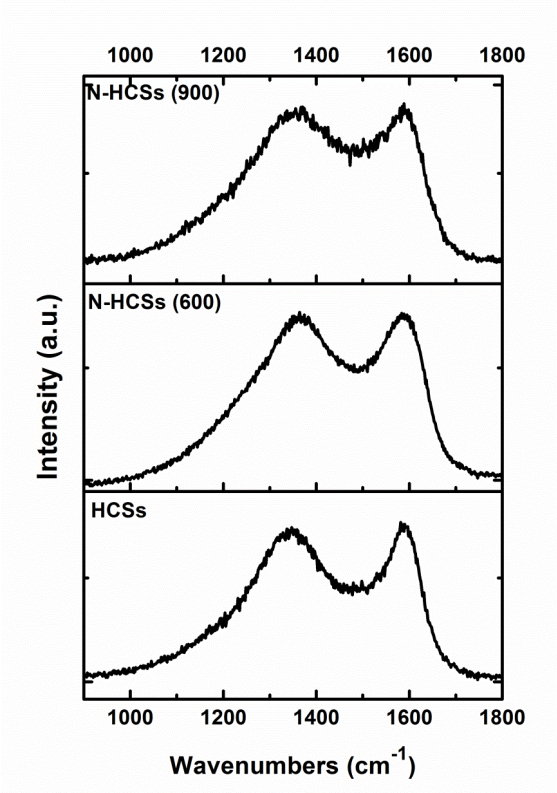

Figure 5.2 Raman spectra of the pristine and the N-doped hollow carbon spheres.

Table 5.1 Elemental nitrogen content and Raman spectroscopy data.

Sample	% N content (CHNS)	I_D/I_G	D band position (cm^{-1})	G band position (cm^{-1})
HCSs	-	0.98	1345	1593
N-HCSs$_{600}$	13.1	1.01	1369	1593
N-HCSs$_{900}$	5.4	1.00	1356	1593

Effects associated with post-synthesis N-doping on the thermal stability of the carbon supports were studied using thermogravimetric analysis (TGA). The synthesized pristine HCSs were seen to be highly stable in an oxidizing environment with a single decomposition peak at 596 °C (Fig. 5.3). This peak is attributed to the oxidation of carbon to carbon dioxide. The N-doped carbon materials also displayed good thermal stabilities with major decomposition peaks at 596 and 563 °C for the samples with 5.4 and 13.1% nitrogen

contents, respectively. It is to be noted that the major decomposition peak on the N-doped samples demonstrates the absence of residual melamine in the materials. The lower thermal stability of the N-HCSs$_{600}$ sample can be associated with two effects; (i) increased defects in the carbon framework due to nitrogen incorporation as also determined from Raman spectroscopy studies, and (ii) the lower carbonization temperature (600 °C) utilized during the preparation of this material. It was interesting to note that the N-HCSs$_{900}$ had a similar decomposition temperature as found for the pristine HCSs. This is a benefit associated with the post-synthesis procedure for N-incorporation as the nitrogen precursor is only introduced when the carbon framework is already formed. Furthermore, it was noted that all three samples had c.a. 0% residue after TGA experiments, and confirmed that the silica template was completely etched out using HF acid giving carbons with high purity. In summary, TGA experiments confirmed that these materials would be stable at Fischer-Tropsch synthesis reaction temperatures.

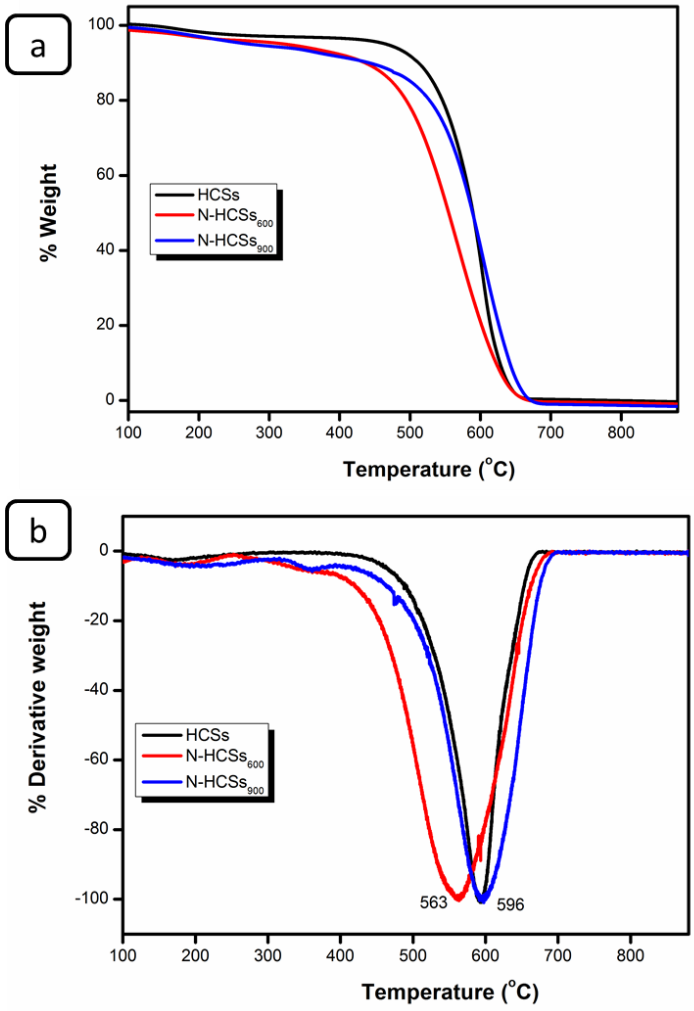

Figure 5.3 (a) TGA and (b) DTA profiles of the pristine HCSs, N-HCSs$_{600}$ and N-HCSs$_{900}$.

The doping of carbon materials has been shown to improve the performances of supported catalysts. The common structural compromise for materials doped in situ with N is reduced thermal and mechanical stability. The thermal stability of N-CNTs, N-CNFs and N-CSs doped during synthesis has been shown to decrease by up to 90 °C relative to their pristine counterparts due to increased defects within the carbon framework.[14] In this study we found that because the dopant is only introduced after the carbon spheres are already formed minimum defects are introduced on the carbon structure. The overall change in the I_D/I_G ration was found to be 0.03, which is very small for samples containing a 13% difference in the heteroatom content. As a consequence of the minimal defects introduced only a small decrease (33 °C) in thermal stability was observed even though a relatively high N content (13.1%) was incorporated into the surface of the carbon material.

5.3.2 X-ray photoelectron spectroscopy (XPS) analysis

Data measured from X-ray photoelectron spectroscopy (XPS) experiments was used to determine the elemental compositions and bonding configurations of nitrogen, carbon and oxygen on the carbon supports. As shown on the wide scans in Fig. 5.4a, the spectra confirmed the presence of N, C and O on the N-doped samples while N was not detected on the pristine HCSs as can be expected. High resolution N 1s spectra were recorded to characterize the bonding configurations of the nitrogen atoms. The N 1s spectra of the N-HCSs were deconvoluted by fitting four Gaussian peaks at 398.36, 400.87, 401.65 and 403.40 eV.[20-22] These peaks are due to pyridinic nitrogen, pyrrolic nitrogen, graphitic or quaternary nitrogen and oxidized nitrogen or pyridine oxide, respectively. It is worth noting that the N atom in pyridinic nitrogen has sp^2 hybridization with two neighbouring C atoms, while the N atom in pyrrolic nitrogen is substituted into a five-membered carbon ring. For the peaks with high binding energies, the N atom in quaternary nitrogen has sp^3 hybridization with three C atoms attached to the N because it is incorporated into a graphene layer, while the N atom in oxidized nitrogen is attached to two C atoms and one O atom.

Table 5.2 summarises the percentage contributions for the different nitrogen bonding configurations after deconvolution of the N 1s spectra which are presented in Fig. 5.4. It was observed that increasing the carbonization temperature from 600 to 900 °C changed the

bonding configurations of nitrogen atoms on the surface of the hollow carbon sphere support materials. For instance, the pyridinic nitrogen content decreased from 35.8 to 27.1% at elevated temperatures. The ratios of pyrrolic, graphitic and oxidized nitrogen increased in the N-HCSs$_{900}$ sample relative to data measured for the N-HCSs$_{600}$ support material.

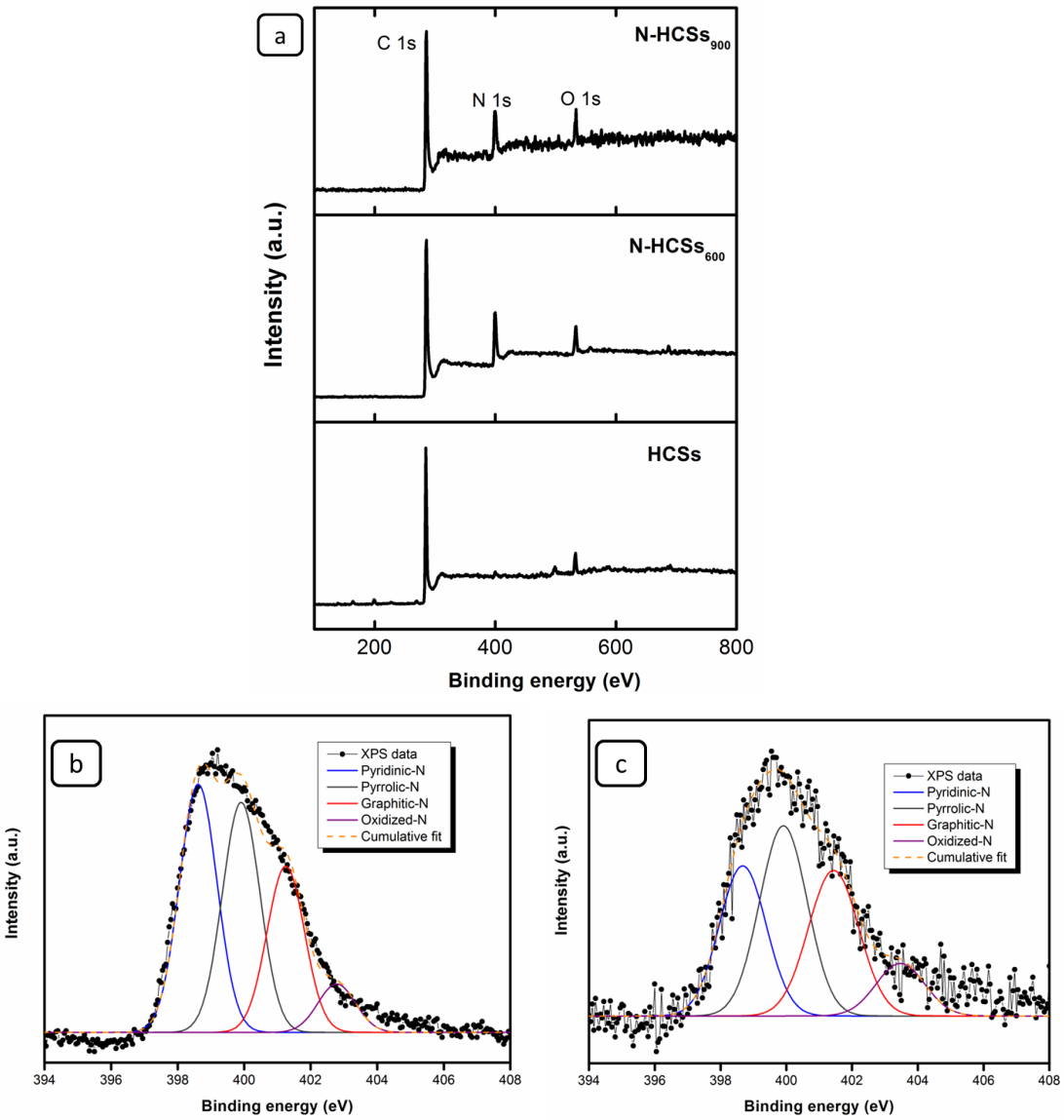

Figure 5.4 XPS data measure from the samples, (a) wide scan spectra, and high resolution N 1s spectra of (b) N-HCSs$_{600}$ and (c) N-HCSs$_{900}$.

Table 5.2 XPS N 1s spectral parameters from the deconvoluted peaks

Sample	Nitrogen bonding configurations (%)				R^2 value
	Pyridinic-N	Pyrrolic-N	Graphitic-N	Oxidized-N	
N-HCSs$_{600}$	35.8	33.2	24.0	7.0	0.989
N-HCSs$_{900}$	27.1	34.8	28.2	9.9	0.984

High resolution XPS spectra were also analysed to investigate the effect of post-synthesis nitrogen doping on the bonding configurations of the surface carbon and oxygen atoms. Fig. 5.5a-c shows C 1s spectra of the different carbon supports. The spectra were deconvoluted into three peaks with maxima at 284.64, 285.37 and 287.07 eV, corresponding to various carbon functional groups (Table 5.3).[23] The peak at 284.64 eV is attributed to pure graphitic carbon sites (C=C, C-C, C-H), the peak at 285.37 eV is due to carbon atoms with sp^2 hybridization (C-O, C-N), while the peak with a maxima at 287.07 eV is designated to the O=C-O and O=C-N surface functional groups. As shown in Table 5.3, the N-doped samples display a significant decrease of pure graphitic carbon sites and an increase in the amount of carbon with sp^2 hybridization. The sp^2 hybridized sites contain nitrogen groups and this confirms the incorporation of N into the carbon network. This observation is in agreement with Raman data where a slight increase in the sp^2 content was seen. The higher quantities of Type 2-C and Type 3-C on the N-HCSs$_{600}$ sample relative to the N-HCSs$_{900}$ sample are related to the total N content on these materials.

A similar approach was also adopted to deconvolute the high resolution O 1s spectra into three peaks corresponding to the following functional groups; -C=O (531.02 eV), C-O-C (531.95 eV) and O-C=O (533.01 eV).[24] The contributions of these functional groups to the total O content are listed in Table 5.4. It can be observed from the Table that post-synthesis N-doping favours the C-O-C (Type 2-O) and O-C=O sites, whereas the pristine HCSs display a higher –C=O content (i.e. Type 3-O).

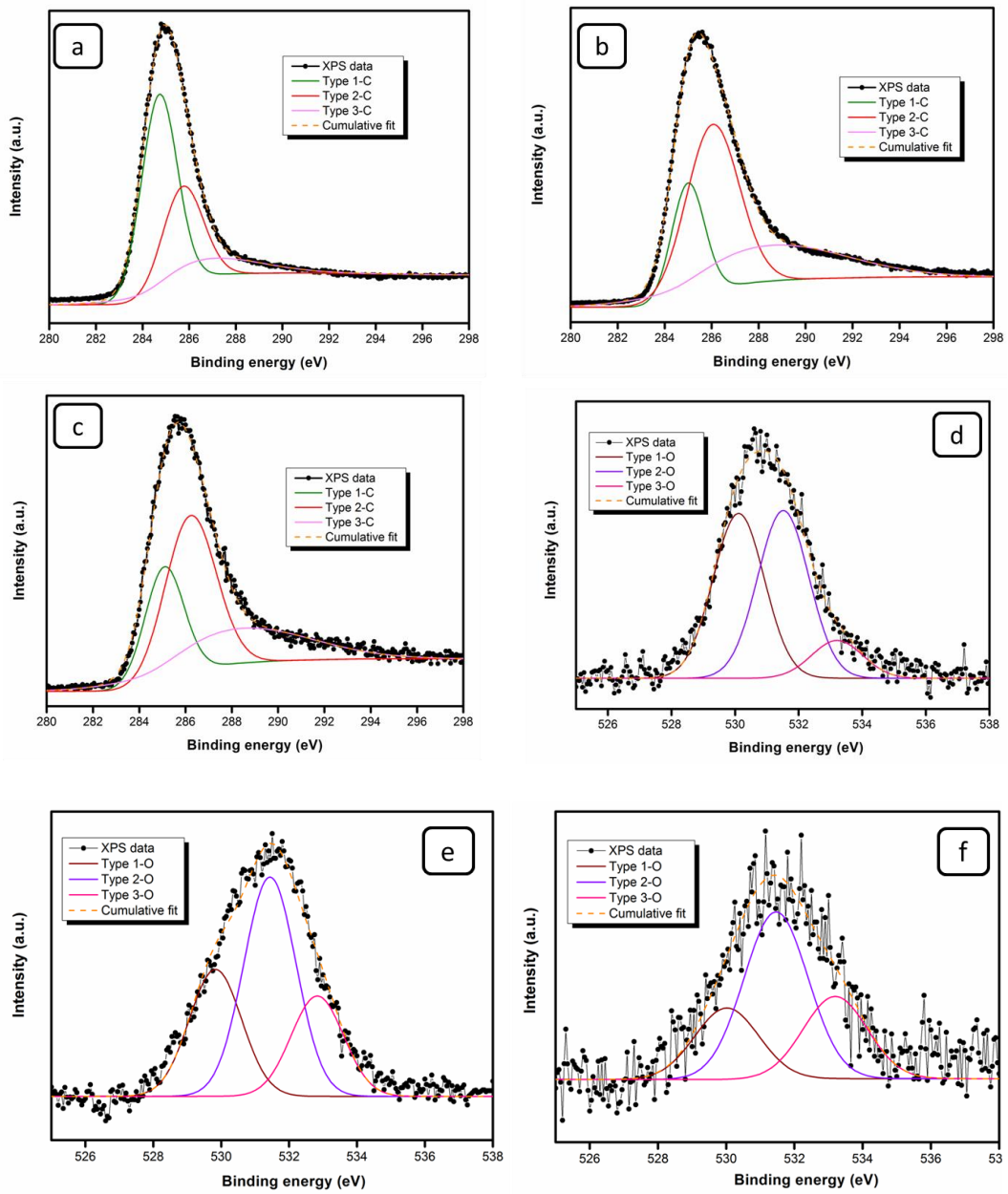

Figure 5.5 High resolution C 1s spectra for the (a) HCSs, (b) N-HCSs$_{600}$, (c) N-HCSs$_{900}$ and O 1s data for (d) HCSs, (e) N-HCSs$_{600}$ and (f) N-HCSs$_{900}$.

Table 5.3 C 1s spectra analysis

Sample	Bonding configurations (%)			R^2 value
	Type 1-C (C=C, C-C, C-H)	Type 2-C (C-O, C-N)	Type 3-C (O=C-O, O=C-N)	
HCSs	55.6	30.2	14.2	0.998
N-HCSs$_{600}$	21.3	48.9	29.8	0.998
N-HCSs$_{900}$	26.0	45.8	28.2	0.995

Table 5.4 O 1s spectra analysis

Sample	Bonding configurations (%)			R^2 value
	Type 1-O (-C=O : 531 eV)	Type 2-O (C-O-C : 532 eV)	Type 3-O (O-C=O : 533 eV)	
HCSs	44.5	45.3	10.2	0.978
N-HCSs$_{600}$	28.4	49.1	22.5	0.982
N-HCSs$_{900}$	22.3	52.1	25.6	0.962

5.3.3 Textual properties of the support materials

Specific surface areas of the carbon supports were measured by the BET method and the results are tabulated in Table 5.5. The carbon supports were found to have large surface areas (> 400 m^2/g) which are in agreement with TEM measurements that showed that these materials possess a large inner void. For instance, the pristine hollow support had a specific surface area of 507.1 m^2/g. Furthermore, incorporation of the nitrogen precursor on the outer surface of the carbons was noted to slightly decrease the surface area, possibly through pore blockage. The pore structures of all the materials displayed mesoporous characteristics as their average pore sizes were greater than 2 nm.

5.3.4 Catalyst characterization

5.3.4.1 Microscopic analysis

Fig. 5.6 shows TEM images for the 10Co/HCSs and 10Co/N-HCSs$_{900}$ catalysts and the corresponding particle size distributions. It can be seen that the cobalt nanoparticles supported on the pristine HCSs have a slightly larger average particle size (7.7 nm) while the particle size distributions are similar. For the samples supported on the N-doped HCSs, it was observed that the average particle sizes were inversely proportional to the nitrogen content on the support. Hence the 10Co/N-HCSs$_{600}$ sample had the smallest particles followed by the 10Co/N-HCSs$_{900}$ with average particle sizes of 5.7 and 6.4 nm, respectively. Generally small cobalt oxide particles were seen on all the supports and this is attributed to the low density of the hollow carbon spheres which provides a large surface for the metal precursor deposition. However, the particles appeared to be slightly better dispersed on the N-doped supports as determined from the microscopy images (Fig. 5.6d).

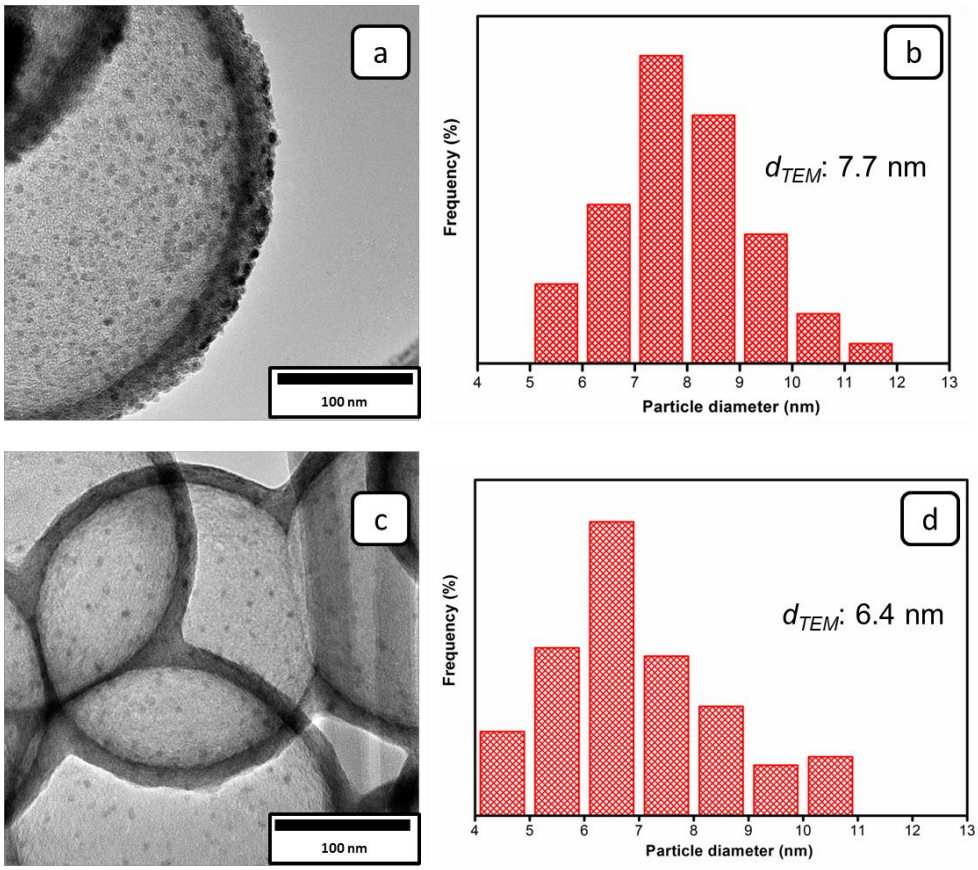

Figure 5.6 TEM images and the corresponding Co particle size distributions for (a, b) 10Co/HCSs and (c, d) 10Co/N-HCSs$_{900}$ samples.

5.3.4.2 Thermal stability of catalysts

Thermogravimetric analysis (TGA) of the catalysts was also carried out to study the influence of cobalt nanoparticles on the thermal stability of the hollow carbon supports. A plot of the TGA derivative curve allowed for the identification of points where maximum weight loss occurred during the experiments. Fig. 5.7 depicts TGA/DTA profiles of the catalysts which were measured in a flow of air using a heating rate of 10 °C/min. As can be seen from the derivative curves in Fig. 5.7b, the decomposition temperature was less than 480 °C for all the carbon supports after loading cobalt oxide. This is in contrast to oxidation temperatures greater than 560 °C recorded prior to loading the catalyst precursor. The decrease in thermal stability is attributed to cobalt nanoparticles catalizing the oxidation of carbon to carbon dioxide. The decomposition trend of the catalysts was similar to that observed prior to loading the active phase precursor, with the 10Co/N-HCSs$_{600}$ sample having the lowest stability. Meanwhile, a residue of about 16% was noted after the TGA experiments and is due to Co_3O_4 which was loaded onto the supports. This percentage residue corresponds to 11.7% Co which was close to the theoretical Co loading of 10wt.% added onto the hollow carbon spheres.

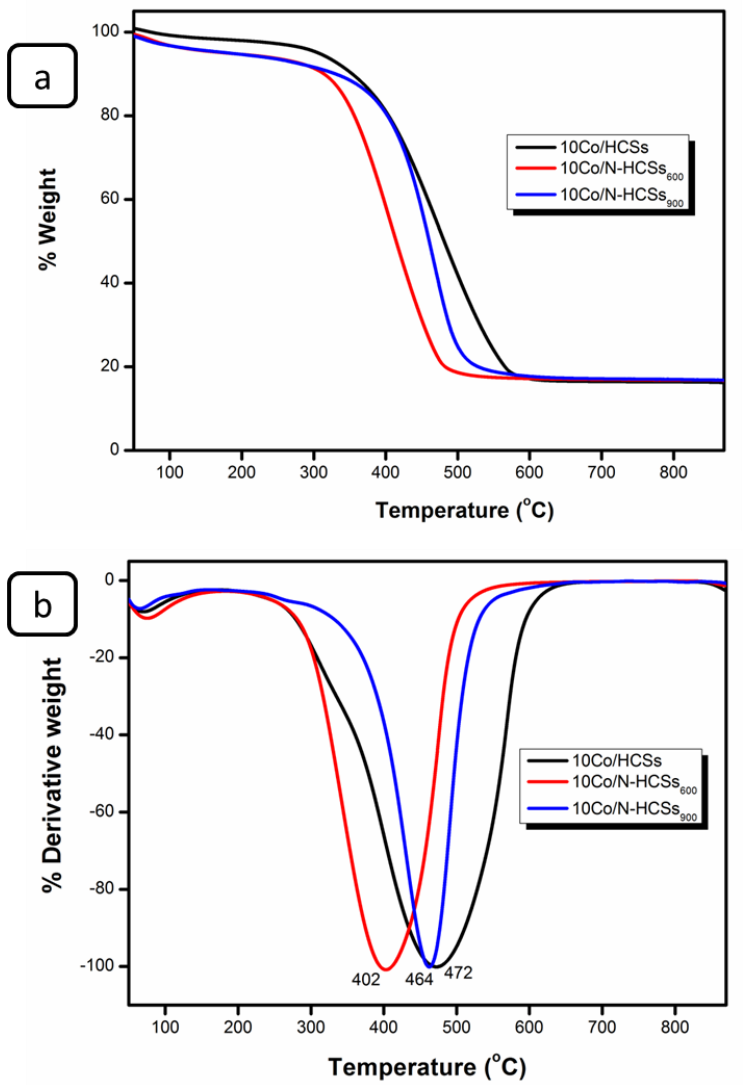

Figure 5.7 (a) TGA and (b) DTA profiles for the 10Co/HCSs, 10Co/N-HCSs$_{600}$ and 10Co/N-HCSs$_{900}$ samples.

5.3.4.3 Powder X-ray diffraction (PXRD)

Ex situ PXRD data of the calcined samples is shown in Fig. 5.8. The peaks at 2θ positions of 28.2 and 50.6° were present in all the patterns and are attributed to the (002) and (100) diffractions of graphitic carbon.[25] The 10Co/HCSs, 10Co/N-HCSs$_{600}$ and 10Co/N-HCSs$_{900}$ samples all displayed peaks at 2θ positions of 21.9, 42.5, 70.0 and 77.2° which are typically indexed as the (111), (311), (511) and (440) diffraction planes of face-centred cubic Co_3O_4 [PDF No. 00-043-1003]. It was therefore concluded that surface nitrogen functionalization did not affect the crystallographic phase of the metal precursor as the spinel phase of cobalt

oxide was detected in all three samples. Subsequently, the cobalt oxide crystallite sizes were estimated from line broadening analysis using the Scherrer equation and are listed in Table 5.5. The Co oxide crystallite sizes were seen to vary as a function of the nitrogen content on the carbon support. As can be seen in Table 5.5, the pristine support had the biggest crystallites with a size of 8.2 nm. The catalyst precursor crystallite sizes decreased with an increase in the nitrogen content of the carbon support. For instance, the sizes for the 10Co/N-$HCSs_{600}$ sample were estimated to be 5.0 nm on average. The decrease in Co size with an increase in heteroatom content is consistent with surface nitrogen atoms influencing the nucleation sites for catalyst deposition on the carbon support.

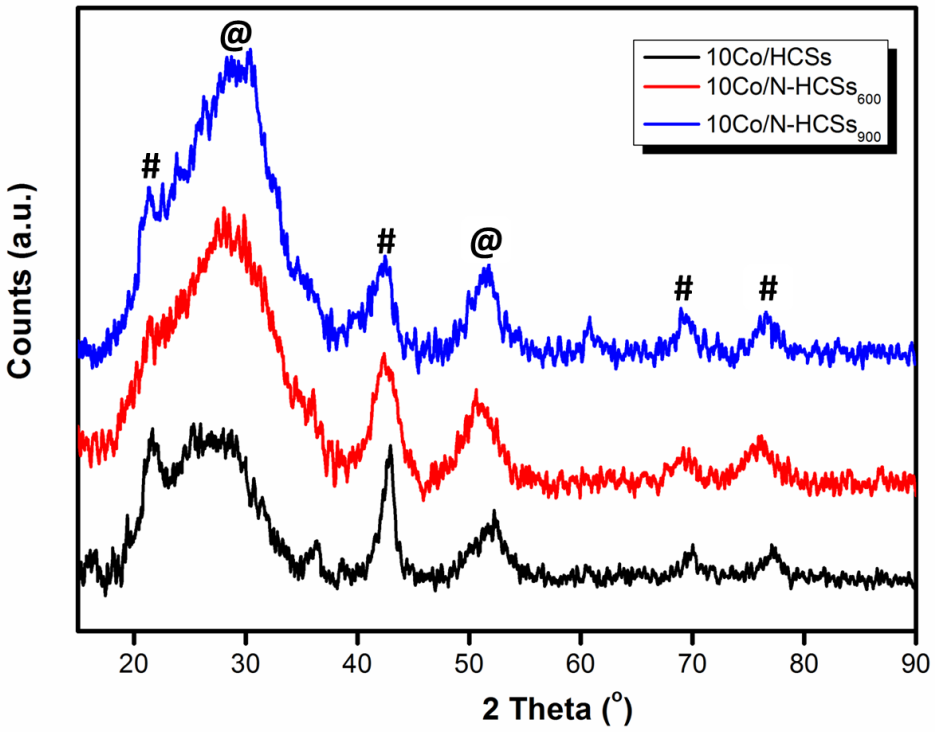

Figure 5.8 Ex situ PXRD patterns of the calcined cobalt catalysts supported on pristine and N-doped HCSs. (Carbon: @, Co_3O_4: #).

5.3.4.4 BET analysis of catalysts

Listed in Table 5.5 are the surface areas, pore volumes and pore sizes of the calcined cobalt on carbon samples as determined by the BET technique. It was observed that the specific surface areas decreased upon loading the metal precursors. This trend is to be expected because the metal precursors are loaded on the outer surface of the hollow supports and could

thus block some of the mesopores. However, all the measured surface areas are still relatively high (> 250 m^2/g) and thus ideal for FT catalysts. It was interesting to note that the mesoporous nature of the materials was retained on the catalysts as pore sizes greater than 2 nm were again measured on all the samples.

Table 5.5 Summarized textual properties of the carbon supports and the calcined catalysts.

Sample name	Textual properties			Co_3O_4 size (nm)[a]
	Surface area (m^2/g)	Pore volume (cm^3/g)	Pore diameter (nm)	
HCSs	507.1	0.406	3.20	-
N-HCSs$_{600}$	411.0	0.427	4.58	-
N-HCSs$_{900}$	436.2	0.360	3.30	-
10Co/HSCs	332.2	0.350	4.62	8.2
10Co/N-HCSs$_{600}$	266.1	0.348	4.08	5.0
10Co/N-HCSs$_{900}$	294.5	0.363	3.61	5.9

[a]*Cobalt oxide crystallite sizes were estimated from XRD data using the Scherrer equation.*

5.3.4.5 Catalyst reducibility

The effect of N-functionalization on the stepwise reduction of cobalt oxide was monitored by TPR and in situ PXRD techniques. TPR profiles of cobalt nanoparticles on the hollow carbon supports are displayed in Fig. 5.9 and the observed peak positions are given in Table 5.6. All samples show the characteristic reduction features of cobalt oxide which are ascribed to the $Co_3O_4 \rightarrow CoO$ and $CoO \rightarrow Co^0$ transformations (Eqn. 5.1 and 5.2).[26] The first reduction step ($Co_3O_4 \rightarrow CoO$) occurred at T < 400 °C, with reduction at temperatures around 282, 357 and 296 °C for the 10Co/HCSs, 10Co/N-HCSs$_{600}$ and 10Co/N-HCSs$_{900}$ samples, respectively. This reduction step evidently occurs at higher temperatures for the catalysts dispersed on N-doped hollow spheres which were determined to be smaller in size. A similar behaviour was again displayed during the $CoO \rightarrow Co^0$ reduction step with the pristine-supported Co showing the lowest reduction temperature (414 °C) while Co on the N-doped substrate had the higher reduction temperatures, with reduction at 506 and 413/495 °C for the N-HCSs$_{600}$

and N-HCSs$_{900}$ supports. For this reduction step, the peak for the 10Co/N-HCSs$_{900}$ sample was split into two peaks in the 413 – 495 °C region. The signal for the lower temperature could be due to cobalt nanoparticles which are not in direct contact with N atoms, while the peak at 495 °C can be assigned to nanoparticles that are in direct contact with N atoms on the support. The differences in cobalt nanoparticle proximity to N-rich sites are to be expected due to the lower nitrogen content on the N-HCSs$_{900}$ substrate.

$$Co_3O_4 + H_2 \rightarrow 3CoO + H_2O \qquad \text{(Eqn. 5.1)}$$

$$CoO + H_2 \rightarrow Co^0 + H_2O \qquad \text{(Eqn. 5.2)}$$

It is apparent that N-surface functionalization influenced the reduction characteristics of supported cobalt oxide nanoparticles, with reduction profiles shifting to higher temperatures with an increase in the nitrogen content. This is attributed to the strong interfacial electronic interaction between cobalt oxide nanoparticles and the N-rich hollow carbon sphere surface. The interaction promotes the transfer of electrons from the N-doped HCSs to the Co oxide particles making them harder to reduce (i.e. the reduction peaks shift to higher T).[27]

The post-synthesis functionalization procedure also affected the methanation characteristics of the carbon supports. The signals for the N-doped materials appeared to be shifted to higher temperatures corresponding with the doped nitrogen content. As a result, the pristine HCS-supported catalyst had the lowest methanation temperature (ca. 653 °C).

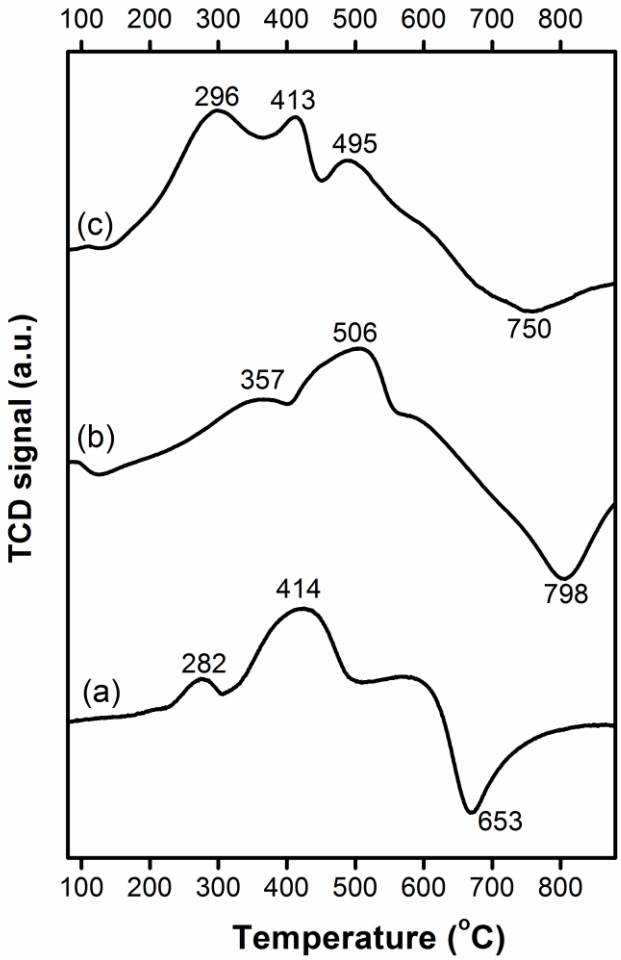

Figure 5.9 H_2-TPR profiles for cobalt nanoparticles on various hollow carbon sphere supports, (a) 10Co/HCSs, (b) 10Co/N-$HCSs_{600}$ and (c) 10Co/N-$HCSs_{900}$.

Table 5.6 Peak positions for various transformations in TPR analysis

	Reduction temperatures (°C)		**Methanation**
Catalyst	$Co_3O_4 \rightarrow CoO$	$CoO \rightarrow Co^0$	**temperature (°C)**
10Co/HCSs	282	414	653
10Co/N-$HCSs_{600}$	357	506	798
10Co/N-$HCSs_{900}$	296	413, 495	750

The reducibility of cobalt oxide dispersed on a pristine support and when also loaded onto hollow carbon spheres with a high nitrogen content was monitored by in situ PXRD measurements. Data collection was done in the temperature range 150-550 °C with 50 °C intervals between successive measurements. Fig. 5.10 depicts in situ PXRD reduction patterns for 10Co/HCSs and 10Co/N-$HCSs_{600}$ samples. Both sets of data show that the spinel phase of cobalt oxide (Co_3O_4) was the stable phase at T < 250 °C. Reduction of Co at higher temperatures followed the well-established stepwise transformation of cobalt oxide: $Co_3O_4 \rightarrow$ CoO then CoO $\rightarrow$ Co^0. However, the transformations were noted to occur at different temperatures for the two samples. Both reduction steps appeared to be delayed on the 10Co/N-$HCSs_{600}$ catalyst. As an illustration, the CoO to Co^0 reduction step has been circled to highlight the lower reduction temperature seen on the pristine HCSs-supported nanoparticles. The CoO $\rightarrow$ Co^0 transformation commenced at T = 550 °C for the 10Co/N-$HCSs_{600}$ sample while it was seen to start occurring at 500 °C for the 10Co/HCSs catalyst. Furthermore, the CoO $\rightarrow$ Co^0 reduction was still not complete on the 10Co/N-$HCSs_{600}$ catalyst at the end of the in situ studies as traces of the CoO phase are still visible (Fig. 5.10b). The higher reduction temperatures for the catalysts supported on N-doped carbons was also observed during TPR studies and this is attributed to the presence of a stronger metal-support interaction between the nanoparticles and the nitrogen functionalized hollow carbon spheres.

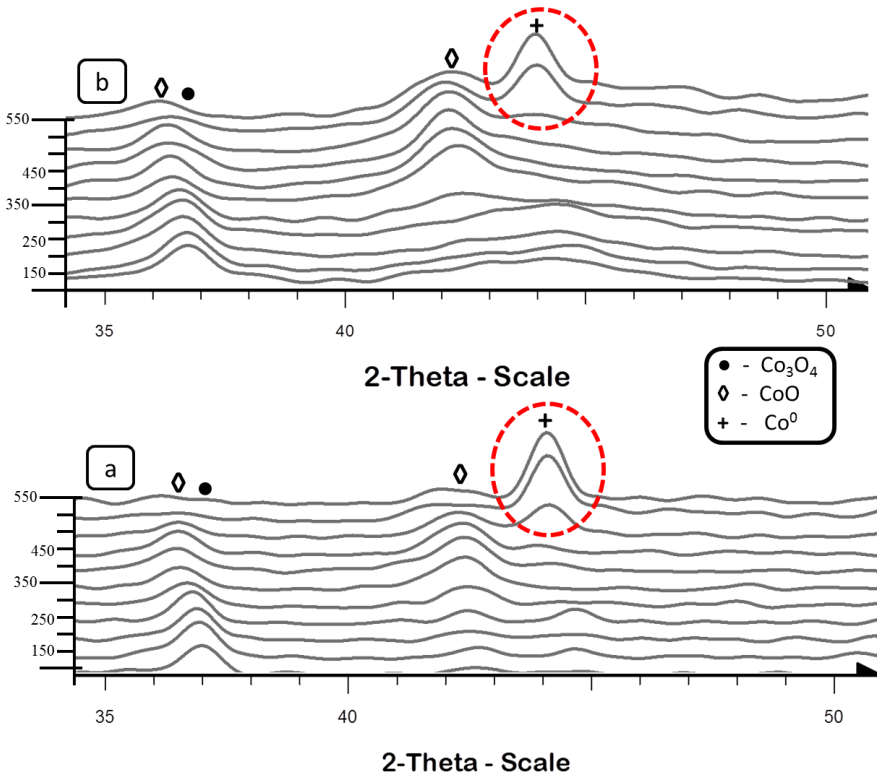

Figure 5.10 In situ PXRD patterns of (a) 10Co/HCSs and (b) 10Co/N-HCSs$_{600}$.

5.3.5 Fischer-Tropsch evaluation

All the calcined catalysts were reduced in situ with pure H_2 (UHP grade) at 350 °C prior to Fischer-Tropsch catalytic tests at 220 and 250 °C under a similar set of reaction conditions: P = 10 bar, H_2/CO = 2. Evidently all the catalysts had stable activities at both reaction temperatures as shown by the steady CO conversions for the entire period that this study was conducted (Fig. 5.11, Table 5.7). It is assumed that the catalysts maintained their structural integrity during the reaction (vide infra for details on the spent catalysts). The catalysts supported on nitrogen-doped hollow carbon spheres (10Co/N-HCSs$_{600}$, 10Co/N-HCSs$_{900}$) displayed higher CO conversions than the catalyst supported on the undoped support (10Co/HCSs). This trend was consistent under both reaction temperatures and can be attributed to the smaller particle sizes present on the doped supports as observed by both TEM and PXRD techniques. Further, as a consequence of the small cobalt oxide particle sizes on N-doped HCSs, the catalysts had a higher dispersion as confirmed by SEM and TEM analysis. It was noted that the presence of any strong metal-support interactions on the N-doped supports was compensated for by the size of cobalt particles on these catalysts hence

they had better activities than the undoped catalyst. For the catalysts supported on functionalized supports, it was observed that a higher nitrogen content did not necessarily yield the highest activity. It is evident that the strong metal-support interactions seen during TPR studies resulted in a lower activity for the 10Co/N-HCSs$_{600}$ catalyst. In addition, the activity of this catalyst could be lower because the average particle size for this catalyst was smaller than 6 nm which has been shown to be a critical Co size for Fischer-Tropsch catalysis.[4]

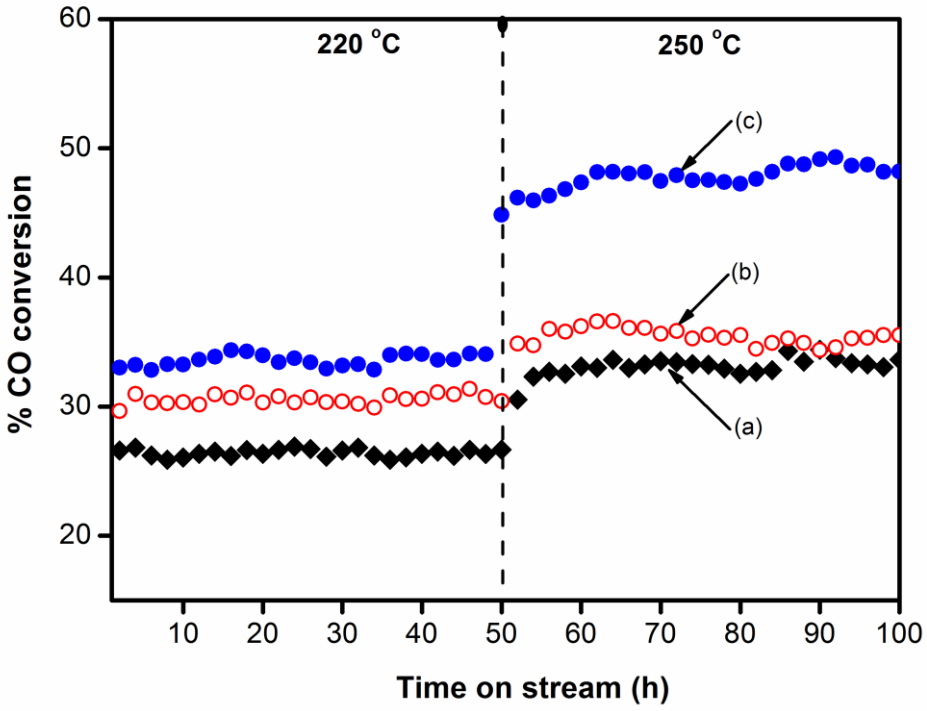

Figure 5.11 CO conversions for the Co catalysts supported on pristine and N-doped supports; (a) 10Co/HCSs, (b) 10Co/N-HCSs$_{600}$, and (c) 10Co/N-HCSs$_{900}$, (P = 10 bar, H_2/CO = 2).

Previous studies comparing FT activities for catalysts dispersed on N-doped and undoped carbons reported a continuous decrease in activity with time on stream for the sample supported on the pristine carbon support.[10] This behaviour was ascribed to significant catalyst sintering which occurred at high reaction temperatures on pristine carbon materials. In contrast in this study, catalysts dispersed on the pristine support displayed a stable activity with time on stream which was attributed to the unique properties of hollow carbon spheres. HCSs possess a low density and a high surface area which allows for higher dispersions of

the catalyst particles on the support which consequently minimizes catalyst agglomeration and favours stable CO conversions during FT synthesis.

Table 5.7 depicts the hydrocarbon selectivities for the different catalysts evaluated at 220 and 250 °C. Comparison of the product selectivities for the catalysts at 220 °C revealed that the Co supported on the pristine hollow carbon spheres had highest C_{5+} selectivity and a low C_1 selectivity. As expected, there was a significant decrease in the C_{5+} selectivity when FT synthesis was carried out at 250 °C for this sample. It must be noted that typical Co FT synthesis is done in the 220 – 240 °C temperature range, but a 250 °C reaction temperature has been evaluated in this study to accelerate possible catalyst sintering. On the N-doped samples, comparatively lower C_{5+} values were obtained while the selectivity towards C_1 increased. It was interesting to note that the C_{5+} selectivity did not decrease drastically at 250 °C for the N-doped samples, and the C_1 fraction showed a slight increase at the elevated reaction temperature.

Previous studies by Borg et al. on Co/γ-Al_2O_3 catalysts have also shown that there tends to be an increase in the C_{5+} product fraction with an increase in the Co particle size, with the highest C_{5+} values possible in the 7 – 8 nm size range.[28] In another study similar conclusions were drawn on the Co particle size effect using Co/δ-Al_2O_3 and Co/θ-Al_2O_3 catalysts.[29] In agreement with these reports, the 10Co/HCSs catalyst had the highest C_{5+} product fraction in this work and the average Co particle size was determined to be 7.7 nm by TEM analysis. It was observed that the C_{5+} selectivities on the studied catalysts were generally low due to fact that these samples were unpromoted and also possibly due to the pore structure of the hollow carbon supports utilised. By comparing cobalt catalysts dispersed on γ-Al_2O_3 supports with narrow pores (7 nm) and wide pores (13 nm), Rytter and co-workers demonstrated that wide pores favour higher C_{5+} selectivities.[30] The pore sizes for catalysts in this study were less than 5 nm (Table 5.5). Due to the smaller size of hydrogen relative to carbon monoxide, H_2 tends to diffuse much more quickly than CO in the reactor which yields higher H_2/CO ratios in certain parts of the catalyst. A higher H_2 to CO ratio favours chain termination over chain propagation resulting in a lower C_{5+} selectivity. Furthermore, the higher methane fraction measured in this work on the N-doped samples is in agreement with conclusions made by Bezemer on C_1 selectivity for small Co nanoparticles.[4]

Table 5.7 FT product selectivities for the different catalysts.

Catalyst	Temp. (°C)	% CO conversion	Hydrocarbon selectivity (%)		
			C_1	C_2-C_4	C_{5+}
10Co/HCSs	220	26	13.4	7.9	78.7
	250	33	22.8	29.9	47.3
10/N-HCSs$_{600}$	220	30	18.5	18.3	63.2
	250	36	21.9	18.5	59.6
10/N-HCSs$_{900}$	220	34	15.7	8.5	75.8
	250	48	26.2	21.0	52.8

5.3.6 The spent catalyst

Catalyst sintering is an important phenomena in FT synthesis and has been proposed as one of the major deactivation mechanisms in the FT process, alongside poisoning, reoxidation, catalyst surface rearrangement, carbon effects (e.g. carbidization, coking or fouling), attrition and the formation of metal-support compounds.[31-32] Several studies have observed the loss of catalytically active cobalt surface area due to particle growth under realistic FT reaction conditions. The tendency of smaller particles to sinter and form bigger ones is driven by thermodynamic principles associated with the lower surface energy of larger particles. Notably, sintered catalysts have lower surface concentrations of the catalytic Co phase and thus display poor performances in FT synthesis. This phenomenon of sintering is believed to occur by two mechanisms: coalescence and Ostwald ripening. Coalescence involves the random movement of intact particles on the support surface. These movements occur until the particles collide to form a single, larger nanoparticle. On the contrary, Ostwald ripening is the diffusion of atoms from smaller particles onto bigger ones as a result of differences in the chemical potentials of the particles.[33-35]

After catalytic evaluations under Fischer-Tropsch conditions, the samples were subsequently studied to infer changes which might have occurred during the reaction. Fig. 5.12 shows TEM images and corresponding particle size distributions measured on the spent catalysts

after 100 h on stream. It can be seen that the hollow carbon sphere support maintains its structural integrity even after a 100 h exposure to the high pressures and temperatures used during the FT process. Carbon breakage or fracturing was not detected on the pristine and nitrogen doped support materials. This demonstrates the robustness of the hollow carbon spheres despite that they have a thin 30 nm carbon shell. It was also interesting to note that the N-doped materials demonstrated equally good robustness under FT conditions. This observation also confirms that post-synthesis N-doping only introduced marginal defects or structural changes on the carbon framework, and is in agreement with Raman spectroscopy and XPS data discussed earlier.

The Co particle size distributions on the spent catalysts were also measured and are displayed in Fig. 12b and Fig. 12d. It was noted that the average Co particle size increased for all the samples indicating that sintering had occurred during the catalytic reaction. However, it was observed that all the catalysts displayed a generally smaller propensity to sinter as shown by the small average particle increases on the spent samples. This effect is attributed to the hollow carbon supports which offer more accessible surface per unit mass relative to conventional support materials. For example, the average particle size on the 10Co/HCSs sample increased from 7.7 to 10.2 nm after 100 h on stream. The insert in Fig. 5.12a shows that the sintered particles formed a core-shell structure with the reduced cobalt being encapsulated by an outer shell which is composed of oxidized cobalt.

The catalysts supported on N-doped HCSs displayed reduced sintering behaviour. For instance the average Co particle size increased from 6.4 to 8.9 nm on the 10Co/N-HCSs$_{900}$ spent catalyst (Fig. 5.12d). The smaller particle growth seen for the catalysts supported on the N-doped carbons is consistent with conclusions made in other reports that nitrogen atoms (or the C-N bonds) act as anchoring sites and this immobilizes the catalyst particles even at high reaction temperatures. Noteworthy, the N-HCSs-supported cobalt also had a narrow size distribution even on the spent catalyst with most particles being less than 15 nm, while pristine HCSs-supported cobalt displayed a wider size distribution on the spent catalyst with a significant percentage of crystallites with sizes greater than 20 nm.

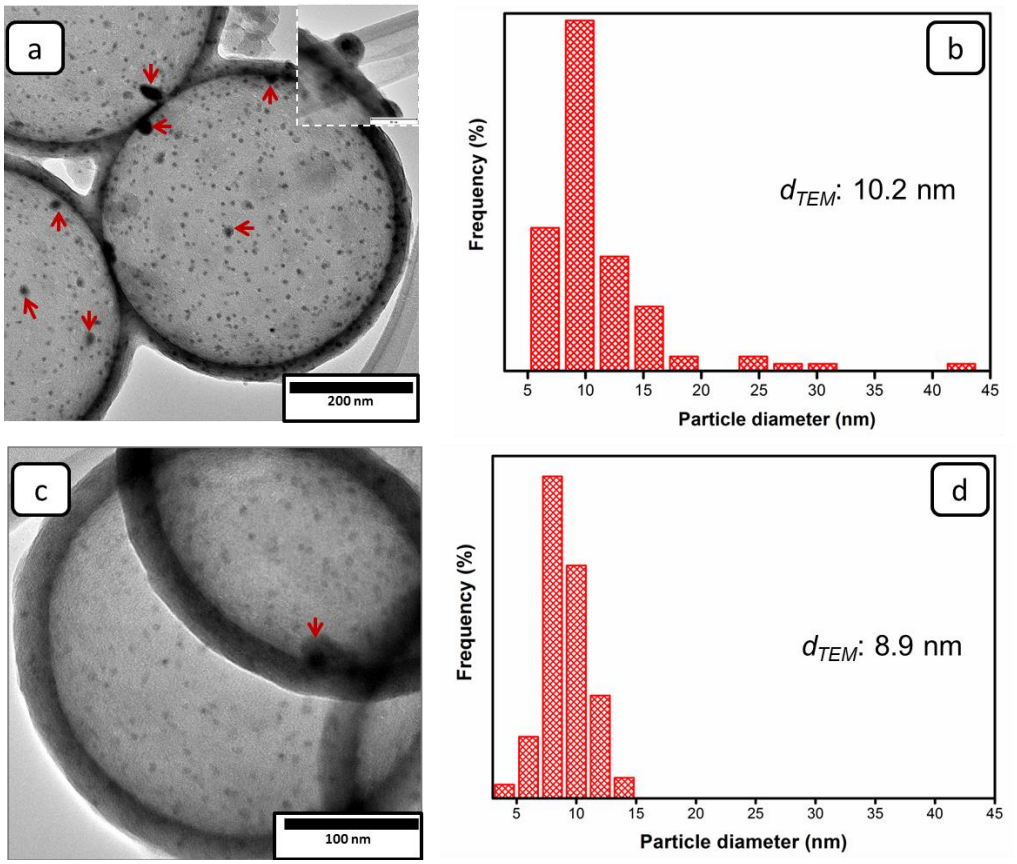

Figure 5.12 TEM images of spent catalysts, (a) 10Co/HCSs, (c) 10Co/N-HCSs$_{900}$. The corresponding particle size distributions are displayed in (b) and (d). (Insert) A high magnification image of the spent Co catalyst supported on pristine hollow carbon spheres i.e. 10Co/HCS sample.

TEM analysis of the spent samples revealed that there was general particle growth which confirmed that sintering of the supported Co particles did occur during Fischer-Tropsch synthesis (Fig. 5.12). It was also noted that the overall cobalt dispersion decreased in the spent samples. However, particle size distributions from these catalysts show only a gradual increase in the average Co particle sizes. These observations indicate that Ostwald ripening was most likely the predominant sintering mechanism at the synthesis conditions. It would have been expected that large particle size increases would be seen if particle migration (i.e. coalescence) had been the predominant sintering mechanism. Furthermore, Co particles supported on N-doped HCSs displayed less sintering behaviour which is also consistent with the Ostwald ripening sintering mechanism. Sintering by a coalescence mechanism can be completely ruled out on the N-doped samples and is in agreement with nitrogen immobilizing

the nanoparticles. However, particle growth by the coalescence mechanism cannot be completely ruled out for the catalyst supported on pristine HCSs as much larger particles were measured. It is also possible that the wider particle size distribution on this sample could be associated with both particle growth mechanisms occurring simultaneously.

5.4 Conclusions

In this study we have used hollow carbon spheres as catalyst supports and shown that they are a suitable model support material for cobalt Fischer-Tropsch catalysts. Synthesis of these materials via a solid template approach was shown to yield uniform and monodispersed HCSs with high specific surface areas and good thermal stabilities. More interestingly, a strategy for the surface N-functionalization of the materials by a method which involves the addition of a nitrogen source onto an already prepared carbon framework has been demonstrated. This simple procedure provided a unique material which is favourable for use as a carbon support for several reasons; (1) it has more catalyst anchoring sites, (2) its thermal stability is comparable to those for the pristine material hence its mechanical strength is not compromised, and (3) it immobilized the catalyst nanoparticles during the reaction leading to minimized particle agglomeration. Results from this study also showed that the surface properties of materials produced by this strategy are dependent on the carbonization temperature. These surface properties were shown to influence the metal-support interactions on the prepared catalysts. Thus the carbonization temperature can be used to tune the strength of metal-support interactions in such materials. N-functionalization effects were also evident in FT synthesis and yielded catalysts with improved activities and stabilities. We believe that the catalyst stabilizing effect produced by the post-synthesis melamine introduction to already prepared carbons can also be used to anchor other types of catalysts on carbon supports synthesized using a similar approach.

References

[1] S. Chu, A. Majumdar, *Nature* **2012**, *488*, 294-303.

[2] F. Morales, F. M. F. de Groot, O. L. J. Gijzeman, A. Mens, O. Stephan, B. M. Weckhuysen, *J. Catal.* **2005**, *230*, 301-308.

[3] E. Iglesia, *Appl. Catal. A* **1997**, *161*, 59-78.

[4] G. L. Bezemer, J. H. Bitter, H. P. C. E. Kuipers, H. Oosterbeek, J. E. Holewijn, X. Xu, F. Kapteijn, A. J. van Dillen, K. P. de Jong, *J. Am. Chem. Soc.* **2006**, *128*, 3956-3964.

[5] G. L. Bezemer, T. J. Remans, A. P. van Bavel, A. I. Dugulan, *J. Am. Chem. Soc.* **2010**, *132*, 8540-8541.

[6] M. E. Dry, *Appl. Catal. A* **2004**, *276*, 1-3.

[7] H. M. Torres Galvis, J. H. Bitter, C. B. Khare, M. Ruitenbeek, A. I. Dugulan, K. P. de Jong, *Science* **2012**, *335*, 835-838.

[8] Y. Piao, K. An, J. Kim, T. Yu, T. Hyeon, *J. Mater. Chem.* **2006**, *16*, 2984.

[9] C. Galeano, J. C. Meier, M. Soorholtz, H. Bongard, C. Baldizzone, K. J. J. Mayrhofer, F. Schüth, *ACS Catal.* **2014**, *4*, 3856-3868.

[10] J. Lu, L. Yang, B. Xu, Q. Wu, D. Zhang, S. Yuan, Y. Zhai, X. Wang, Y. Fan, Z. Hu, *ACS Catal.* **2014**, *4*, 613-621.

[11] H. J. Schulte, B. Graf, W. Xia, M. Muhler, *ChemCatChem* **2012**, *4*, 350-355.

[12] H. Xiong, M. Moyo, M. K. Rayner, L. L. Jewell, D. G. Billing, N. J. Coville, *ChemCatChem* **2010**, *2*, 514-518.

[13] X. Chen, D. Deng, X. Pan, Y. Hu, X. Bao, *Chem. Commun.* **2015**, *51*, 217-220.

[14] S. Maldonado, K. J. Stevenson, *J. Phys. Chem. B* **2005**, *109*, 4707-4716.

[15] B. Stohr, H. P. Boehm, R. Schlogl, *Carbon* **1991**, *29*, 707.

[16] S. Feng, W. Li, Q. Shi, Y. Li, J. Chen, Y. Ling, A. M. Asiri, D. Zhao, *Chemical Communications* **2014**, *50*, 329-331.

[17] A. B. Fuertes, P. Valle-Vigon, M. Sevilla, *Chemical Communications* **2012**, *48*, 6124-6126.

[18] X. Duan, Z. Ao, H. Sun, S. Indrawirawan, Y. Wang, J. Kang, F. Liang, Z. H. Zhu, S. Wang, *ACS Applied Materials & Interfaces* **2015**, *7*, 4169-4178.

[19] X. Li, H. Wang, J. T. Robinson, H. Sanchez, G. Diankov, H. Dai, *J. Am. Chem. Soc.* **2009**, *131*, 15939-15944.

[20] W. Ding, Z. Wei, S. Chen, X. Qi, T. Yang, J. Hu, D. Wang, L.-J. Wan, S. F. Alvi, L. Li, *Angew. Chem.* **2013**, *125*, 11971-11975.

[21] J. Zhang, L. Ma, M. Gan, F. Yang, S. Fu, X. Li, *J. Power Sources* **2015**, *288*, 42-52.

[22] S. Marzorati, J. M. Vasconcelos, J. Ding, M. Longhi, P. E. Colavita, *J. Mater. Chem. A* **2015**, *3*, 18920-18927.

[23] X. Y. Chen, C. Chen, Z. J. Zhang, D. H. Xie, *Ind. Eng. Chem. Res.* **2013**, *52*, 12025-12031.

[24] M. Seredych, D. Hulicova-Jurcakova, G. Q. Lu, T. J. Bandosz, *Carbon* **2008**, *46*, 1475-1488.

[25] T. Fu, R. Liu, J. Lv, Z. Li, *Fuel Process. Technol.* **2014**, *122*, 49-57.

[26] G. Prieto, P. Concepción, R. Murciano, A. Martínez, *J. Catal.* **2013**, *302*, 37-48.

[27] Y. Yang, L. Jia, B. Hou, D. Li, J. Wang, Y. Sun, *J. Phys. Chem. C* **2014**, *118*, 268-277.

[28] Ø. Borg, P. D. C. Dietzel, A. I. Spjelkavik, E. Z. Tveten, J. C. Walmsley, S. Diplas, S. Eri, A. Holmen, E. Rytter, *J. Catal.* **2008**, *259*, 161-164.

[29] S. Rane, Ø. Borg, E. Rytter, A. Holmen, *Appl. Catal. A* **2012**, *437–438*, 10-17.

[30] E. Rytter, S. Eri, T. H. Skagseth, D. Schanke, E. Bergene, R. Myrstad, A. Lindvåg, *Ind. Eng. Chem. Res.* **2007**, *46*, 9032-9036.

[31] H. Karaca, O. V. Safonova, S. Chambrey, P. Fongarland, P. Roussel, A. Griboval-Constant, M. Lacroix, A. Y. Khodakov, *J. Catal.* **2011**, *277*, 14-26.

[32] H. Karaca, J. Hong, P. Fongarland, P. Roussel, A. Griboval-Constant, M. Lacroix, K. Hortmann, O. V. Safonova, A. Y. Khodakov, *Chem. Commun.* **2010**, *46*, 788-790.

[33] K. H. Cats, J. C. Andrews, O. Stephan, K. March, C. Karunakaran, F. Meirer, F. M. F. de Groot, B. M. Weckhuysen, *Catal. Sci. Technol.* **2016**, DOI: 10.1039/c1035cy01524c.

[34] M. Sadeqzadeh, J. Hong, P. Fongarland, D. Curulla-Ferré, F. Luck, J. Bousquet, D. Schweich, A. Y. Khodakov, *Ind. Eng. Chem. Res.* **2012**, *51*, 11955-11964.

[35] D. Kistamurthy, A. M. Saib, D. J. Moodley, J. W. Niemantsverdriet, C. J. Weststrate, *J. Catal.* **2015**, *328*, 123-129.

CHAPTER 6

Morphological effects in heterogeneous catalysis: comparison of solid and hollow carbons as model supports for cobalt Fischer-Tropsch catalysts

6.1 Introduction

The Fischer-Tropsch (FT) synthesis is of great academic and industrial interest because it has proven to be the most efficient process for the production of hydrocarbons from synthesis gas (H_2/CO mixtures) generated from carbon sources such as coal, natural gas, biomass and shale gas.[1, 2] Among the transition metals used to catalyse the process, cobalt-based catalysts are ideal for low-temperature industrially FT applications because of their high intrinsic activity, high per single pass feed conversion, and better longevity when compared to iron-based FT catalysts.[3, 4] The need to disperse the Co catalyst on a support material arises frequently in FT synthesis, as it maximises the surface area, performance and stability of the active phase. However, during the reaction cobalt is known to form hard-to-reduce complexes such as Co_2SiO_4, $CoTiO_4$ or Co_2AlO_4 if the catalyst was dispersed on conventional oxides such as SiO_2, TiO_2 and Al_2O_3. This is attributed to the strong interaction of these support materials with the catalyst precursor.[5-7] As an alternative, carbon-based materials have been shown to be excellent support materials for FT catalysts partly because of their chemical inertness. Thus carbonaceous materials such as carbon nanotubes, carbon fibres, carbon spheres, carbon nano-onions, graphene and reduced graphene oxide have been utilized as supports for FT catalysts.[8-11] Despite the variation in the morphology of these carbons, their application in heterogeneous has been with varying degrees of success. Therefore, a holistic approach on understanding the effect of the support architecture in heterogeneous catalysis is still required for a better design and development of new catalysts.

A versatile approach for studies on morphology-based effects could involve the use of carbon spheres as model supports. Unlike the other carbonaceous materials which are restricted to one form, carbon spheres (CSs) can form several morphologically distinct structures. The morphology of carbon spheres can be easily manipulated by a simple variation of the

---

This chapter is still to be submitted for publication.

synthesis conditions, to give materials with morphologies such as solid, hollow, core-shell and yolk-shell.[12] This, therefore, makes CSs an attractive material for investigating support architecture-based effects in heterogeneous catalysis. For such studies though, it is critical that the materials be synthesized from identical carbon precursors and using similar preparation methods. It has been demonstrated that the carbon precursor and the preparation method plays a key role in the properties on the final carbon material[13, 14] and should therefore be carefully selected. For example, Cheng et al. demonstrated the differences in the pore structures of mesoporous carbon synthesized using starch and cyclodextrin carbon sources. The use of starch as a precursor yielded materials with a broad pore size distribution (PSD) with an average pore size of 9 nm, whereas the use of a cyclodextrin source resulted in a narrow PSD with an average pore size of 4 nm.[15] In another study, Xu et al. showed that the use of alkali propiolates carbon precursors ($HC{\equiv}CCO_2M$, M = Li, Na, K) resulted in highly porous carbon spheres with morphologies such as Janus, jellyfish and bowl-like being observed, and the architecture of the obtained product was influenced by the precursor used. Furthermore, using mixtures of these propiolate precursors yielded carbon spheres with different micro-structures.[16, 17] Recently, Xiong et al. demonstrated that N-doped carbon spheres prepared by chemical vapour deposition and hydrothermal synthesis methods had different properties.[18]

In this study, we explore the effect of the support morphology in heterogeneous catalysis by comparing the use of carbon materials with distinct architectures (solid and hollow) as model supports for Co FT catalysts. The solid carbon spheres ($SCSs_{RF}$) and the hollow carbon spheres (HCSs) used were prepared by the hydrothermal synthesis method using a resorcinol-formaldehyde carbon precursor. The synthesis conditions for these materials were tuned such that the properties of the final materials were similar, so that any differences observed in the catalyst performances can be attributed to the architectures of the support materials involved.

6.2 Experimental methods

6.2.1 Synthesis of solid carbon spheres ($SCSs_{RF}$)

Fabrication of solid carbon spheres from resorcinol and formaldehyde precursors ($SCSs_{RF}$) was achieved by the extended Stöber method.[19, 20] In a typical synthesis, an ammonia

solution (0.5 mL, 25%) was added to an ethanolic solution consisting of deionized water (60 mL) and absolute ethanol (24 mL) and was stirred for 1 h. Subsequently, resorcinol (0.6 g) was added followed by a 30 min stirring period. Then, formaldehyde (0.84 mL) was added to the mixture and stirring was continued for 24 h at 30 °C, followed by a hydrothermal treatment step performed at 100 °C for 24 h in a Teflon-lined autoclave. The recovered brownish powder was purified by washing/centrifugation with water and ethanol, and was then dried at 70 °C for 48 h. Carbonization was performed at 900 °C for 4 h in the flow of N_2 (20 mL/min) to yield the $SCSs_{RF}$ support material.

6.2.2 Synthesis of hollow carbon spheres (HCSs)

The HCS support was also fabricated from resorcinol and formaldehyde carbon precursors via the hard-templating approach, and the hydrothermal method was employed in the encapsulation of the template with carbon. Stöber silica spheres were employed as the solid template. For the template synthesis, tetraethyl orthosilicate (TEOS, 2.90 mL) was mixed with 37.5 mL of absolute ethanol. This solution was then added to a mixture containing ethanol (25 mL), deionized water (7.5 mL) and ammonia (6 mL). The contents were stirred for 1 h to allow for the formation of colloidal silica spheres. Subsequently, resorcinol (0.5 g) and formaldehyde (0.7 mL) were added to the solution to form a core-shell (SiO_2@RF) composite. This notation represents a structure whereby the SiO_2 is the core, whereas RF is the outer shell. The solution was allowed to stir for 24 h at room temperature, and then transferred into a Teflon-lined stainless steel autoclave, and hydrothermally treated at 100 °C for 24 h. The brownish product obtained was purified by sequential washing in ethanol/water solvents, followed by centrifugation for 5 minutes, and was then dried at 70 °C for 12 h. The SiO_2@RF composites were then carbonized at 900 °C for 1 h under N_2 (20 mL/min), followed by etching of the silica core using a 10% HF solution to give the HCS support.

6.2.3 Catalyst preparation

The Co catalysts were prepared by the homogeneous deposition precipitation method using $Co(NO_3)_2 \cdot 6H_2O$ as the metal precursor, $SCSs_{RF}$ and HCSs materials were used as the catalyst supports. For the catalyst deposition, urea (1.5 moles urea per mole of metal) was used as the

precipitating agent and urea hydrolysis was done for 12 h at 90 °C. The samples were then dried overnight at 70 °C, followed by calcination at 300 °C for 4 h under N_2.

6.2.4 Characterization

Transmission electron microscopy (TEM) images were taken on FEI Tecnai T12 microscope operated at 120 kV. Scanning electron microscopy (SEM) images were recorded using a FEI Nova Nanolab 600 instrument. Thermogravimetric analysis with differential thermal gravimetry (TGA-DTG) profiles were obtained on a PerkinElmer STA6000 analyser. Typically, the samples were heater from room temperature to 900 °C in an oxidizing atmosphere using a ramping rate of 10 °C/min. Powder X-ray diffraction (PXRD) measurements were performed at room temperature on a Bruker D2 phaser emitting $Co_{K\alpha}$ radiation ($\lambda_{K\alpha}$ = 0.178897 nm). Pore structure analysis was achieved by performing cryogenic nitrogen sorption measurements under isothermal conditions (-196 °C) on a Micromeritics TriStar 3000 analyzer.

6.2.5 Catalytic evaluations

Fischer-Tropsch reactor studies were performed in a 16 mm i.d. stainless steel fixed-bed reactor. Prior to measurements, the catalyst (~0.5 g) was activated in situ using a stream of pure hydrogen (UHP grade) at 350 °C for 18 h (ramping rate: 1 °C/min). FT synthesis measurements were conducted at 220 and 250 °C using syngas with the composition: $0.6H_2$, 0.3CO, bal. N_2. A total gas pressure of 10 bar and a flow rate of 20 mL/min were used during the analysis. The rig was equipped with two online GCs to monitor the composition of the gaseous products, a GC-TCD and a GC-FID. An offline GC-FID was used to analyse liquid products.

6.3 Results and discussion

6.3.1 Characterization of the carbon supports

Properties of the prepared solid and hollow carbon supports were analysed by using TEM, SEM, Raman spectroscopy, TGA and N_2 sorption techniques.

6.3.1.1 Support morphology characterization

Electron microscopy analysis was performed to verify the architectures of the synthesized solid and hollow carbon spheres (Fig. 6.1). In particular, TEM showed that the $SCSs_{RF}$ had a rigid core whereas the HCSs possessed a large inner void created by the empty core. Consequently, when these materials were analysed by SEM, and it was observed that the instrument beam could penetrate through the HCSs but not through the $SCSs_{RF}$ carbons. Thus electron microscopy verified that the materials had the designed architectures. The prepared solid carbon materials were spherical in shape and monodispersed (Fig. 6.1a-b). The average diameter of these spheres was calculated to be approximately 565 nm (Fig. 6.1c). For the hollow carbon spheres, the materials displayed a uniform size distribution and were also monodispersed (Fig. 6.1d-e). The hollow carbon spheres were slightly smaller than the solid support materials and had an average sphere diameter of 550 nm (Fig. 6.1f), while their shell thickness was ~30 nm. It was noted that the hollow carbon materials displayed a significantly narrow size distribution than the solid carbon spheres. This is because the preparation of the HCS material involved the use of Stöber silica sphere template which is characterized by a uniform distribution.

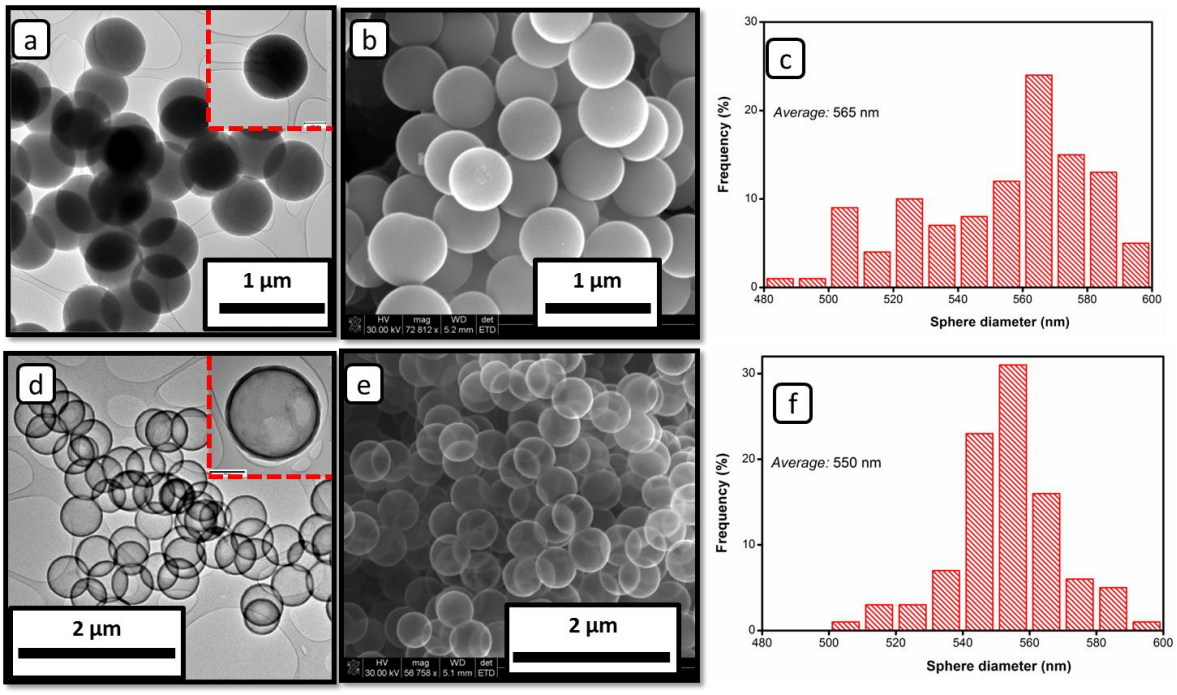

Figure 6.1 TEM and SEM images of (a,b) solid carbon spheres, and (d,e) hollow carbon spheres, the inserts show single carbon spheres of the respective morphologies. The outer carbon sphere diameters of (c) solid and (f) hollow carbon spheres, are also presented.

6.3.1.2 Raman analysis

Raman spectra of the solid and hollow CSs were recorded to study the degree of graphitization and the presence of defects within the carbon framework of the two types of supports (Fig. 6.2). Both spectra depict two peaks at about 1341 and 1581 cm^{-1}, corresponding to the D and G bands, respectively. The D band is characteristic of a disorder-induced mode of carbon while the G band is due to the high frequency E_{2g} first order mode. The intensity ratio of the D and G band (I_D/I_G) is a useful parameter for estimating the degree of graphitization in the solid and hollow CSs, and was determined to be 0.90 and 0.96 for the solid and hollow materials in this study as indicated in Fig. 6.2. These values are very similar and therefore indicate that these two carbon materials have closely related carbon structures. This is to be expected since the materials were prepared by a similar method and from using the same carbon precursor.

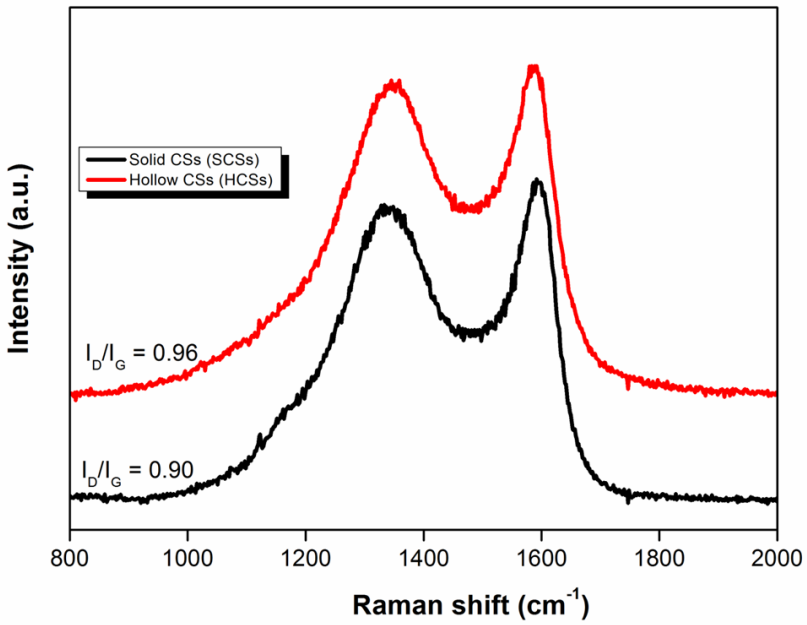

Figure 6.2 Raman spectra of solids and hollow carbon spheres materials.

6.3.1.3 Surface area analysis

N_2 adsorption-desorption isotherms were recorded to quantify the surface textual characteristics of the carbonaceous support materials (Fig. 6.3). The cryogenic N_2 sorption isotherms display similar physisorption characteristics which suggest that the materials

possess similar pore systems. The curves are characterized by a steep slope at low relative pressures, followed by steady rise which also contains a small hysteresis loop on the desorption plot in the range P/P_0 = 0.3–0.7 and P/P_0 = 0.0.4-0.6 for the $SCSs_{RF}$ and the HCSs materials, respectively (Fig. 6.3a, Fig. 6.3c). This behaviour shows that the materials possess combined characteristics of type I and Type IV materials.[21] This is consistent with materials that are largely mesoporous but also contains micropores, correspondingly, the solid and hollow supports were found to have average pore sizes of 2.7 and 2.8 nm, respectively. Finally, the isotherms also display a rapid increase in the quantity of adsorbed N_2 at high relative pressures (Fig. 6.3a,c). This could be associated with the presence of macropores in the materials which arise from the presence of large interparticle voids.

The textual properties of the materials are summarized in Table 6.1 and it can be seen that both support architectures exhibit high surface areas (> 560 m^2/g) and were therefore found to be ideal for use as support materials. The comparable porosity of these materials allow for a good comparison between solid and hollow materials when they are utilized as model support materials. Similar pore size distributions (PSD) plots were recorded from both support materials (Fig. 6.3b and Fig. 6.3d). In these plots, the PSD for the desorption isotherm data displayed a kink at a pore size of 3.5 nm which is due to an error associated with N_2 desorption.

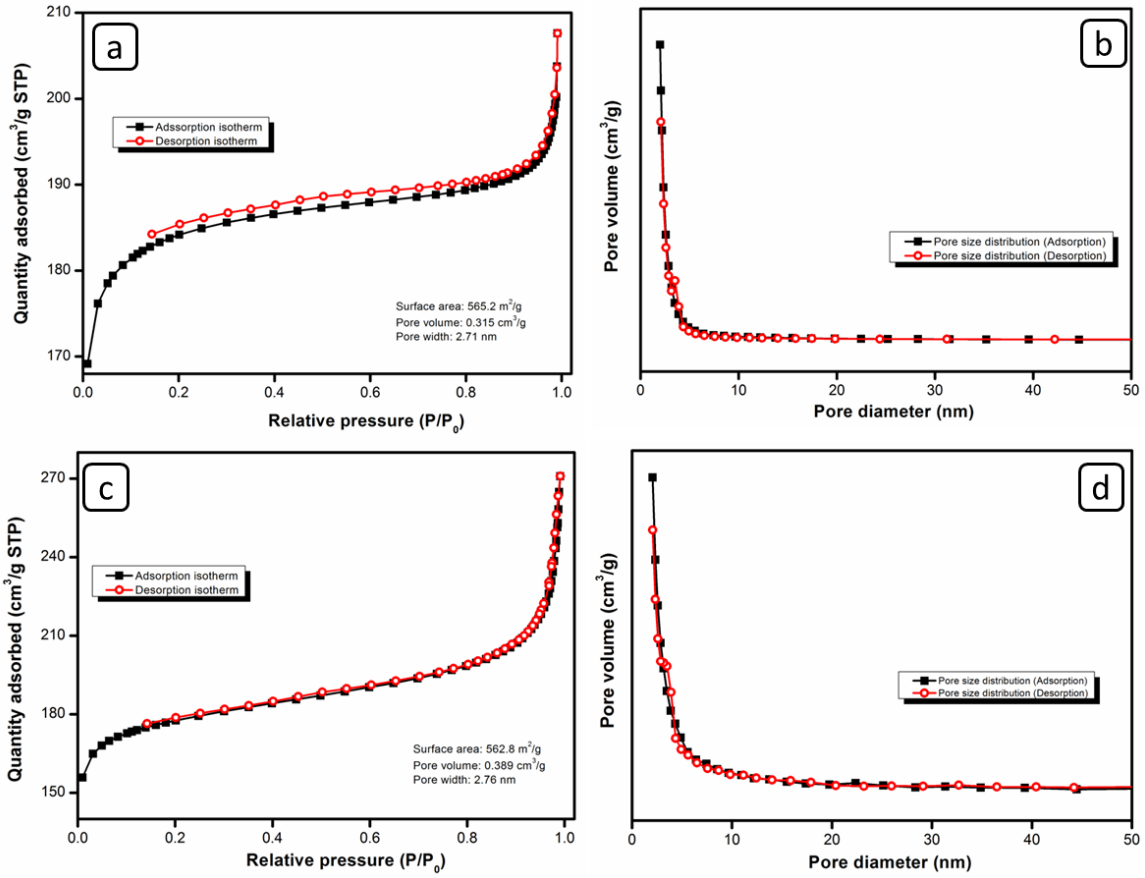

Figure 6.3 N_2 adsorption-desorption isotherms and the corresponding pore size distributions for (a, b) $SCSs_{RF}$ and (c, d) HCSs.

6.3.1.4 Thermogravimetric analysis (TGA)

Fig. 6.4 compares the thermal stabilities of the solid and hollow carbon supports in an oxidizing environment. Both profiles show a single decomposition peak which is due to the oxidation of the carbon material to carbon dioxide. It can be seen that the support materials are characterized by high thermal stabilities as the onset of oxidation for both samples is at T > 550 °C in air. It was noted that the decomposition of the solid carbon spheres occurred over a wider temperature range due to the much thicker carbon layers on this material (Fig. 6.4a). Decomposition of the hollow support occurred over a narrower temperature range and had a T_{max} at 592 °C (Fig. 6.4b). The sharp decomposition peak is associated with the thin carbon layer (~30 nm) in this material. Additionally, the residue at the end of both TGA experiments was negligible (c.a. 0%) which also verified that the carbon spheres were of high purity. This

observation is particularly useful on the hollow support material as it confirmed that the silica template was completely etched out using hydrofluoric acid. Notably, the onset of carbon oxidation occurs at high temperatures for both support materials, allowing for their use in the preparation, calcination and subsequent evaluation of Fischer-Tropsch catalysts under normal conditions.

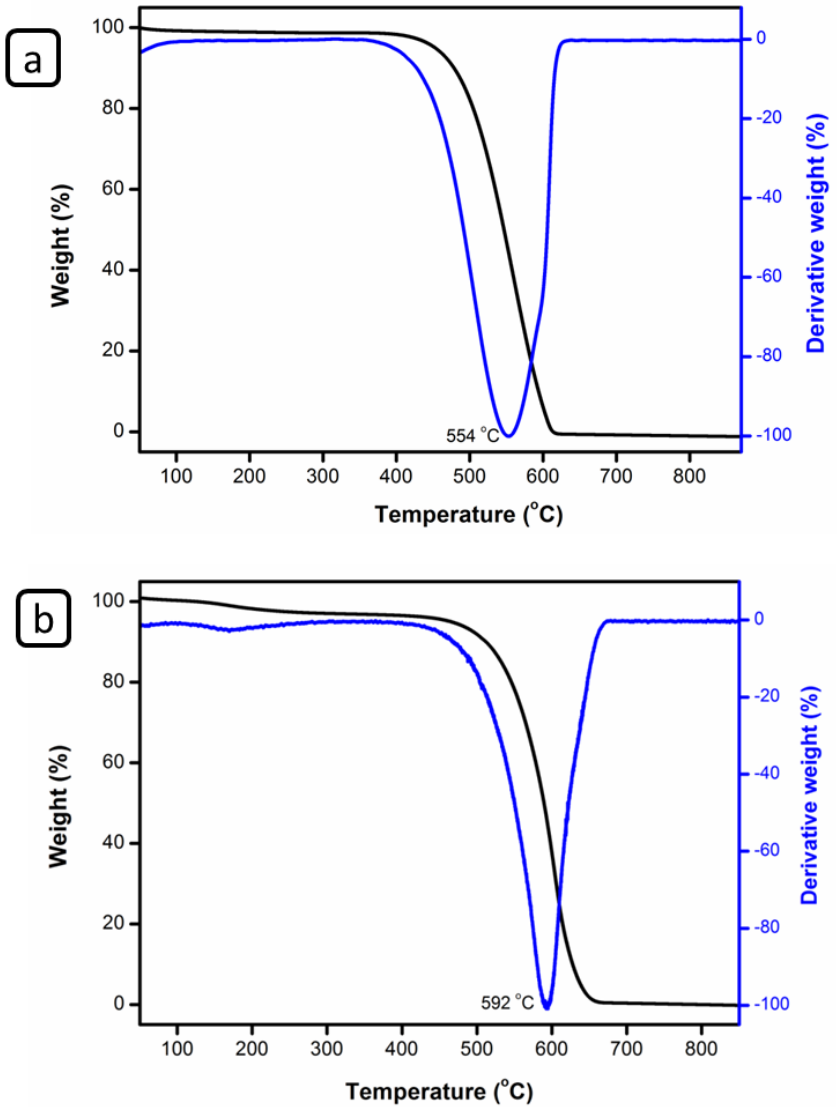

Figure 6.4 TGA/DTA profiles of (a) solid and (b) hollow carbon spheres.

6.3.2 Catalyst characterization

6.3.2.1 Transmission electron microscopy (TEM)

Bright-field TEM studies were performed to visualize the distribution of Co nanoparticles on the carbon supports (Fig. 6.5). Analysis of the TEM images verified that the metal particles were generally well dispersed on the outer surface of the support materials. This good particle dispersion is to be expected as catalyst loading was achieved through the homogeneous deposition precipitation, and is consistent with other literature reports. However, different particle sizes were obtained on the two catalyst systems; 9.4 nm versus 6.7 nm for the 10Co/SCSs$_{RF}$ and the 10Co/HCSs samples, respectively. Because of the chemical similarities in the surfaces of the support materials used, it can be assumed that the differences in catalyst particle size relate to the properties of the two different morphologies of the support materials. The HCS support is significantly less dense than its solid counterpart, allowing for a higher available surface area for catalyst deposition per mass of the support material.

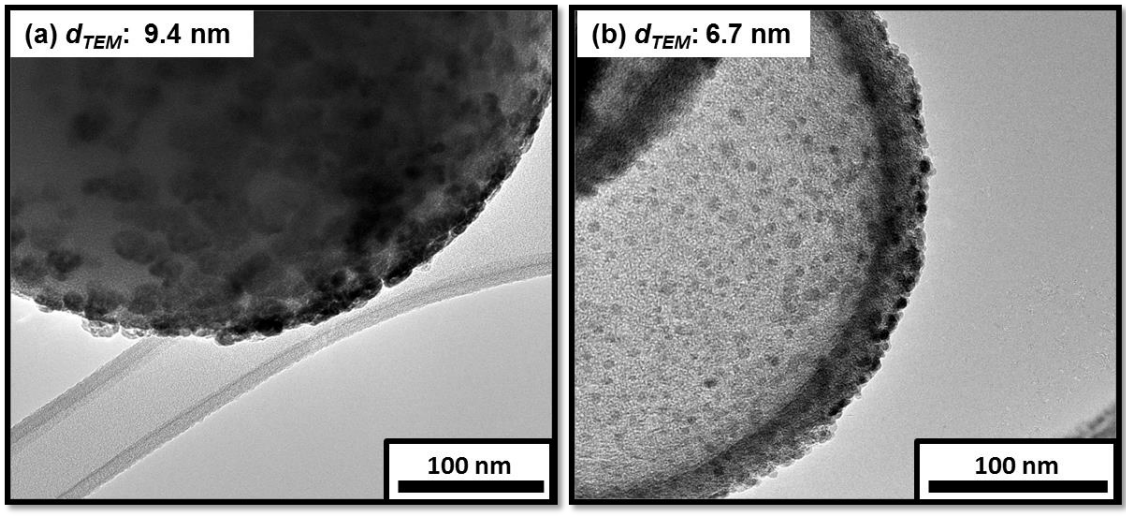

Figure 6.5 TEM images of (a) 10Co/SCSs$_{RF}$ and (b) 10Co/HCSs catalysts.

6.3.2.2 BET surface area analysis

The calcined catalysts were found to have surface areas of 369.9 and 377.3 m^2/g for 10Co/SCSs$_{RF}$ and 10Co/HCSs, respectively. The surface area declined when compared to the support materials indicating that some pore of the support material were blocked by the metal particles. After loading the metal precursor and calcination, the samples also displayed

decreases in pore volumes and pore diameters relative to the support materials. The pore volumes decreased by about 22% and 28% for 10Co/$SCSs_{RF}$ and 10Co/HCSs, respectively. The decreases in pore diameters were marginal as they were quantified to be less than 6% for both catalyst systems.

Table 6.1 Properties of the samples

Sample	N_2 physisorption data			Co_3O_4 and CS sizes	
	Surface area	**Pore volume**	**Pore size**	**PXRD[a]**	**TEM[b]**
	[m^2/g]	**[cm^3/g]**	**[nm]**	**[nm]**	**[nm]**
$SCSs_{RF}$	565.2	0.315	2.71	-	565
HCSs	562.8	0.389	2.76	-	550
10Co/$SCSs_{RF}$	369.9	0.245	2.65	9.1	9.4
10Co/HCSs	377.3	0.280	2.60	7.2	6.7

[a] *Co_3O_4 crystallite sizes were estimated from PXRD patterns using the Scherrer equation.*

[b] *Co_3O_4 and CS particle sizes were estimated from TEM images.*

6.3.2.3 Powder X-ray diffraction (PXRD)

PXRD patterns of the carbon supports had similar features, displaying a broad peak at 25.0° and another peak at 50.7°, and are attributed to the (002) and (100) reflections of graphitic carbon (Fig. 6.6). The absence of any additional peaks on the support diffraction patterns also highlighted the purity of the prepared support materials, and is in agreement with our TGA data. After loading the metal precursors and calcination, the samples displayed additional diffraction peaks at 21.9, 36.2, 42.5, 52.2, 70.0 and 77.2° which can be assigned to the (111), (220), (311), (400), (511) and (440) reflections of face-centred cubic (fcc) Co_3O_4. Identical Co oxide phases (Co_3O_4) were observed on both the solid and hollow carbon sphere support materials. The crystallite sizes of the Co_3O_4 on carbons were computed from the full width at half-maximum (FWHM) of the most intense peak at a 2θ value of 42.5° together with the Scherrer equation and are presented in Table 6.1. It can be seen that the prepared samples had crystallites in the range 7 – 10 nm. It was found that the catalyst preparation method and support architecture influenced the sizes of the Co catalyst precursor. The homogeneous deposition precipitation technique produced smaller crystallites for both types of carbon

while the hollow support also gave significantly smaller crystallite sizes relative to their solid counterparts. These observations were also in agreement with those findings made by electron microscopy.

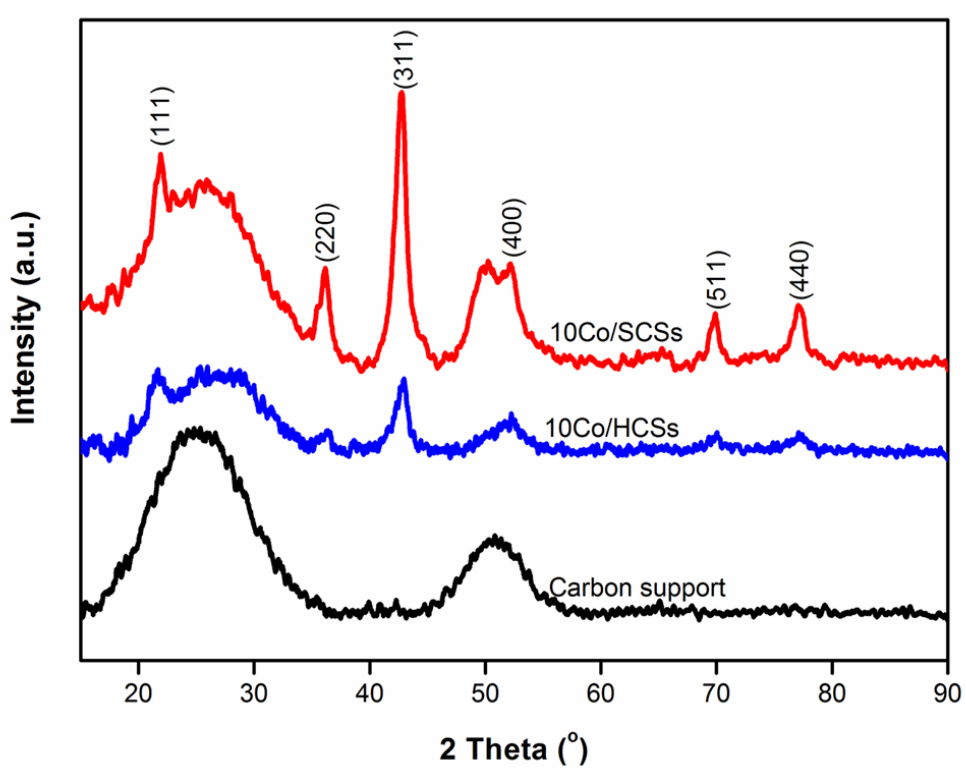

Figure 6.6 PXRD profiles of the carbon support, and the 10Co/SCSs$_{RF}$ and 10Co/HCSs samples.

6.3.2.4 Thermogravimetric analysis-differential thermal gravimetry (TGA-DTG)

Thermal stabilities of the calcined catalysts were determined by the TGA technique. Fig. 6.7 shows the recorded TGA profiles (black) and the corresponding DTG curves (blue). For the 10Co/SCSs$_{RF}$ sample, two carbon oxidation peaks ($C + O_2 \rightarrow CO_2$) were observed. The small peak at 320 °C is related to the decomposition of the less-graphitic amorphous carbon in the SCS$_{RF}$ support, whereas the peak at 396 °C is due to the bulk decomposition of the more graphitic carbon. Only one major decomposition peak was associated with the 10Co/HCSs catalyst, and was attributed to the Co-catalyzed oxidation of bulk carbon. Notably, the carbon decomposition temperatures were lower fow the catalysts than on the pristine supports (>550 °C). The presence of the metal particles catalyzes the oxidation reaction, allowing it to occur at lower temperatures.

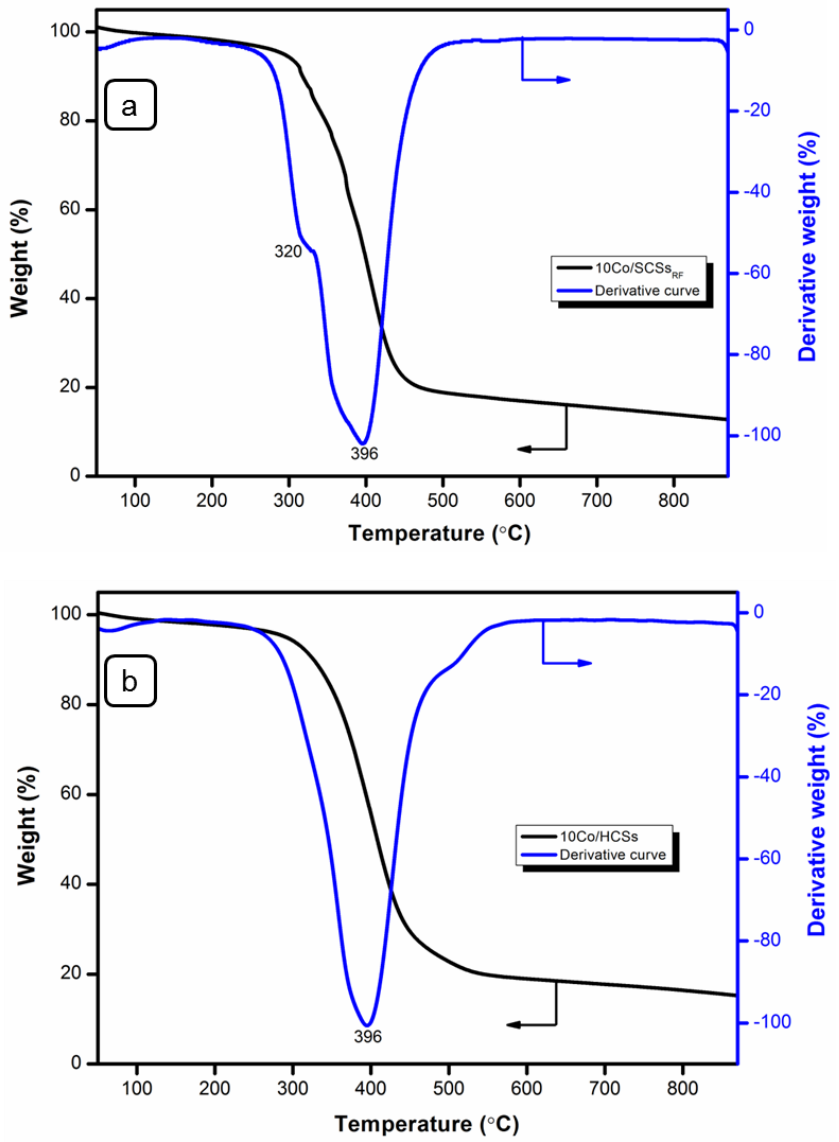

Figure 6.7 TGA-DTG profiles of (a) 10Co/SCSs$_{RF}$ and (b) 10Co/HCSs.

6.3.2.5 Temperature programmed reduction (H_2-TPR)

The influence of the support morphology on the reducibility of the cobalt oxide reduction characteristics was monitored using temperature programmed reduction. The profiles display multiple peaks as a result of the interaction of hydrogen with cobalt oxide and the carbon support (Fig. 6.8). For the 10Co/HCSs sample, Co oxide reduction was seen to proceed as follows; $Co_3O_4 \rightarrow CoO$, followed by the $CoO \rightarrow Co^0$ transformation,[2, 22] with the reductions peaks observed at 282 and 414 °C, respectively. For the 10Co/SCSs$_{RF}$ sample, similar reduction trends were seen but the reduction of the various phases was observed at higher

temperatures relative to the 10Co/HCSs sample. For instance, the $Co_3O_4 \rightarrow CoO$ transformation occurred at 309 °C and the subsequent conversion of CoO to metallic Co was seen in the 370 – 570 °C temperature range on this sample. The shift to higher reduction temperatures on the 10Co/SCSs sample is attributed to the bigger cobalt oxide particles measured on both TEM and XRD techniques. It was interesting to see a relatively small peak for the $Co_3O_4 \rightarrow CoO$ transformation on the 10Co/HCSs sample and could be associated with the ability of carbon to partially auto-reduce the cobalt oxide. This effect was not observed on the $10Co/SCSs_{RF}$ sample presumably because of the cobalt particle sizes present on this catalyst. See chapter 7 for the effect of the support morphology on the catalyst reduction kinetics.

The hydrogenation of the carbon support to methane was observed as negative peaks during TPR experiments. For the 10Co/HCSs sample, the methanation peak appeared at 653 °C as a narrow negative peak. This peak was seen to be broader on the $10Co/SCSs_{RF}$ sample with T_{max} at 760 °C. The difference in the methanation characteristics observed on the two supports is believed to be due to two effects; (1) the thickness of the carbon layer, and (2) the sizes of the cobalt oxide particles. The differences in morphology results in a narrow methanation peak on the hollow carbon sphere support, while the same effect results in a broader peak on the solid carbon sphere support. Furthermore, a cobalt catalyst is known to catalyse the hydrogenation of the carbon support (see Chapter 4). Thus the methanation of carbon on the 10Co/HCSs sample was observed at a lower temperature because the particles were better dispersed on this support and were smaller in size.

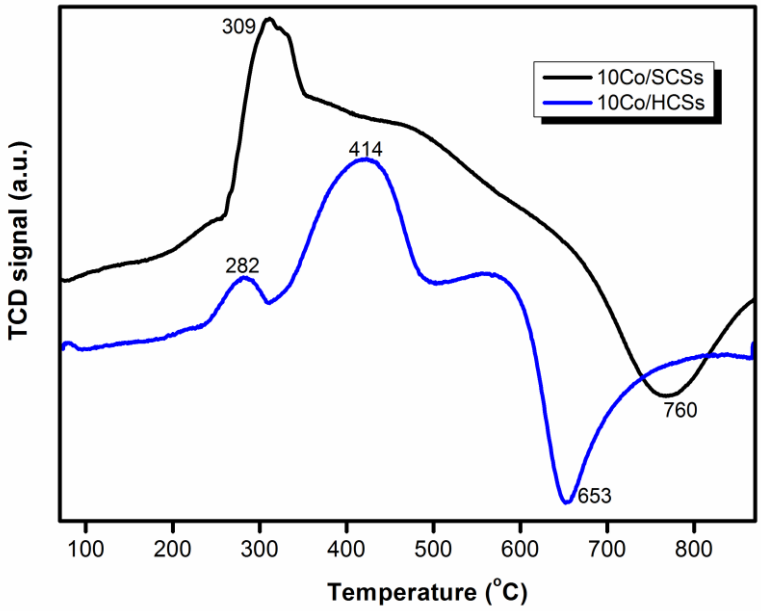

Figure 6.8 H_2-temperature programmed reduction profiles for the 10Co/HCSs and 10Co/$SCSs_{RF}$ samples.

6.3.3 Fischer-Tropsch catalytic performance evaluation

The effect of the support architecture in heterogeneous catalysis was investigated in Fischer-Tropsch synthesis at 220 and 250 °C, 10 bar and H_2/CO = 2.0. Fig. 6.9 shows changes in the CO conversion as a function of the time on stream for the two catalyst systems. The stabilities of the catalysts in FT synthesis were monitored up to 100 h on stream and the catalysts displayed steady activities at both reaction temperatures for this reaction period, irrespective of the support morphology used. The stable activities illustrate that the catalysts maintain good structural integrity during the FT experiments. Notably, the 10Co/HCSs catalyst displayed consistently higher FT activities under both reaction temperatures studied than the 10Co/$SCSs_{RF}$ catalyst. This behaviour could be attributed to the good dispersion of Co particles on the hollow support as seen on TEM results. Due to the good metal oxide dispersion, the 10Co/HCSs catalyst was characterized by smaller Co particles which can be expected to be more active in FT synthesis.[23] Furthermore, it appears that the hollow support morphology of the 10Co/HCSs sample favours the efficient removal of products from the catalytic sites, thus allowing for a higher throughput.

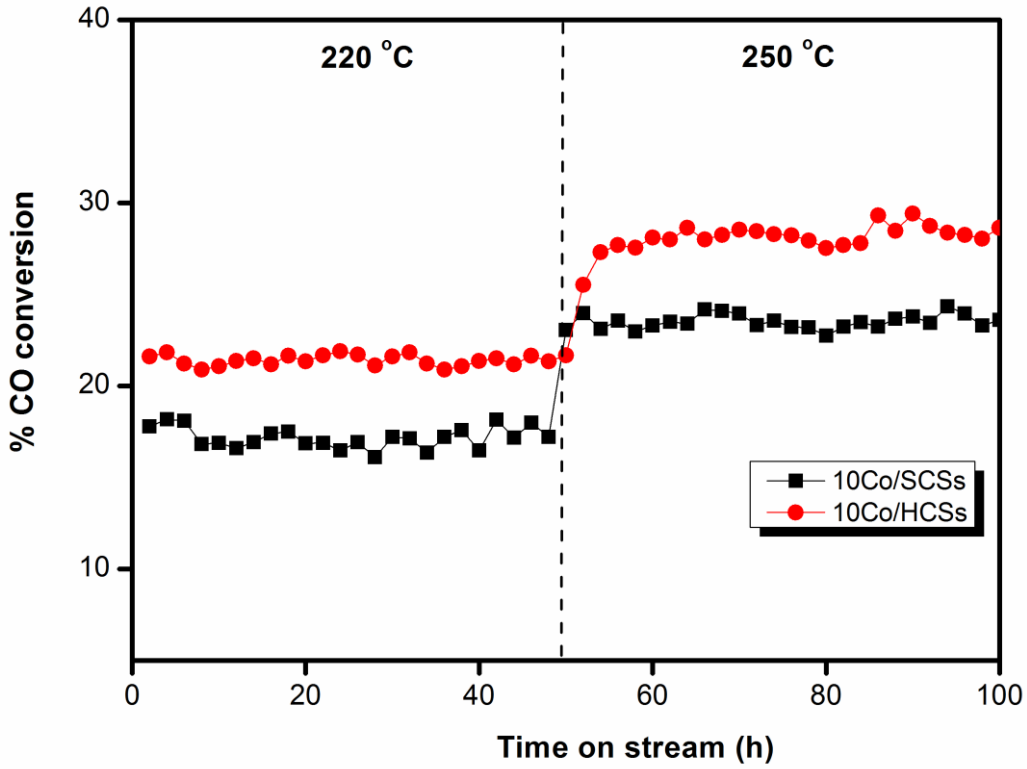

Figure 6.9 FT catalytic activity on the metal oxides dispersed on solid and hollow support morphologies.

Hydrogenation of carbon monoxide on both cobalt catalysts led to the formation of hydrocarbons and water. The hydrocarbon selectivities calculated under the different conditions are summarized in Table 6.2. Generally, high C_{5+} selectivities were recorded on both systems at typical FT conditions (220 °), with slightly higher values possible on the HCS-supported catalyst. When the reactor temperature was increased to 250 °C, a large drop in the C_{5+} product fraction were measured for both catalyst systems. These large decreases in the heavy hydrocarbon products and the corresponding increase in methane selectivity were expected because a reaction temperature of 250 °C is too high for Co FT synthesis. However, it was still interesting to see that the 10Co/HCSs sample still recorded a higher C_{5+} yield even at the high reaction temperature when compared to the 10Co/$SCSs_{RF}$ catalyst. A similar trend on the undesirable increase of the methane fraction was also seen. The high C_{5+} and low CH_4 selectivities on HCSs-supported catalyst suggest that the architecture of the support influences the product distribution. Even though most properties (size, porosity, stability) of the two distinct support materials were similar, the different morphologies affect the mass transfer properties of the catalysts which results in different product selectivities.

Table 6.2 FT product selectivities for the catalysts.

Sample	Temp. (°C)	%CO conversion	Activity (mol CO/g_{Co}.sec)	Hydrocarbon selectivity (%)		
				C_1	C_2-C_4	C_{5+}
10Co/SCSs$_{RF}$	220	16.4	$1.66x10^{-5}$	19.1	6.9	74.0
	250	22.6	$2.29x10^{-5}$	26.6	25.6	47.8
10Co/HCSs	220	21.7	$2.22x10^{-5}$	12.8	6.7	80.5
	250	29.2	$2.96x10^{-5}$	21.4	13.9	64.7

6.3.4 The spent catalysts

After FT synthesis the spent catalysts were analysed using TEM and the representative images obtained are presented in Fig. 6.10. Upon analysis of the images, it was evident that the Co particles had sintered during the reaction. For the 10Co/HCSs sample, the metal particles were still general well dispersed on the carbon support even after the high-temperature reaction. Sintering was only observed in isolated regions as highlighted with arrows in Fig. 6.10b, and an average metal particle size of 11.5 nm was measured on the spent sample which reflects a 73% increase relative to the fresh catalyst. A much higher sintering behaviour was observed for the 10Co/SCSs$_{RF}$ sample (Fig. 6.10a). The average particle size on this sample was determined to be 28.3 nm, which corresponded with a 201% particle size increase when compared to the fresh catalyst. Thus, the spent catalysts verified the differences in properties of particles dispersed on hollow and solid support morphologies. The spent samples also confirmed that the HCS support enables a better metal dispersion than the solid materials, and this reduces the tendency for metal particles to sinter during high-temperature reactions.

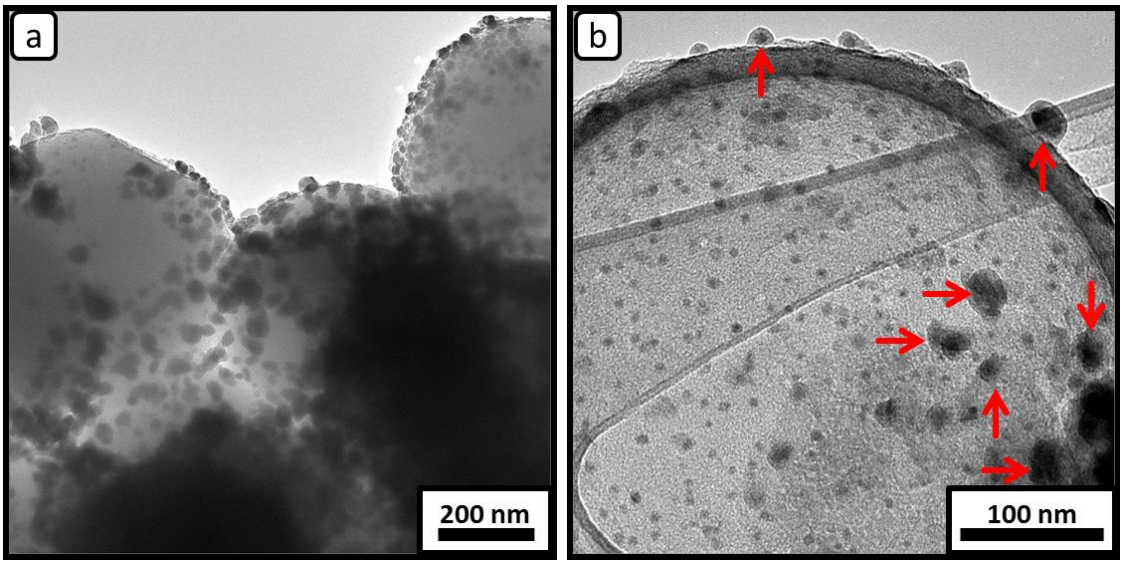

Figure 6.10 TEM images of the spent (a) 10Co/$SCSs_{RF}$ and 10Co/HCSs samples.

6.4 Conclusions

In summary, we have demonstrated a simple hydrothermal route for the synthesis spherical carbon materials. We have described how the synthesis conditions of this method can be tuned to allow for the preparation of solid ($SCSs_{RF}$) or hollow carbon spheres (HCSs). On the basis of TEM, SEM, TGA, BET and Raman spectroscopy, it can be concluded that we successfully tailored the physicochemical properties of the solid and hollow materials to be similar, allowing for an effective comparison in the study of support architecture effects in heterogeneous catalysis. Notably, the HCSs are characterized by a low density due to their hollow morphology. Thus they have a larger outer volume for the same mass of sample when compared with their solid counterparts. This difference resulted in a better metal dispersion on the calcined samples, following metal loading by the homogeneous deposition precipitation method.

Due to the morphology differences and the inherent differences in the particle properties, the catalyst supported on the solid and hollow morphologies possessed different characteristics. These include their high-temperature stabilities, reducibility and catalytic activity. The Co/HCSs catalyst was more readily reducible using hydrogen, and also displayed higher

activities and selectivities for heavy hydrocarbon products in Fischer-Tropsch synthesis. The differences in the catalytic properties were seen to be two-fold. Firstly, its because of the smaller metal particles possible on the HCS support, and secondly, due to the differences in mass transport resistance of the two support materials. Analysis of the spent FT catalysts allowed us to verify the better metal dispersion possible on the Co/HCSs, and the minimal sintering tendency achievable on this catalyst system. On this basis, it appears that the hollow support morphology enables a better catalyst performance than the conventional solid support materials.

References

[1] J. H. den Otter, H. Yoshida, C. Ledesma, D. Chen, K. P. de Jong, *J. Catal.* **2016**, *340*, 270-275.

[2] L. Wei, Y. Zhao, Y. Zhang, C. Liu, J. Hong, H. Xiong, J. Li, *J. Catal.* **2016**, *340*, 205-218.

[3] A. Y. Khodakov, W. Chu, P. Fongarland, *Chem. Rev.* **2007**, *107*, 1692-1744.

[4] V. Subramanian, K. Cheng, C. Lancelot, S. Heyte, S. Paul, S. Moldovan, O. Ersen, M. Marinova, V. V. Ordomsky, A. Y. Khodakov, *ACS Catal.* **2016**, *6*, 1785-1792.

[5] R. P. Mogorosi, N. Fischer, M. Claeys, E. van Steen, *J. Catal.* **2012**, *289*, 140-150.

[6] Y. Liu, B. de Tymowski, F. Vigneron, I. Florea, O. Ersen, C. Meny, P. Nguyen, C. Pham, F. Luck, C. Pham-Huu, *ACS Catal.* **2013**, *3*, 393-404.

[7] S. Zhang, P. N. Plessow, J. J. Willis, S. Dai, M. Xu, G. W. Graham, M. Cargnello, F. Abild-Pedersen, X. Pan, *Nano Lett.* **2016**, *16*, 4528-4534.

[8] U. M. Graham, G. Jacobs, M. K. Gnanamani, S. M. Lipka, W. D. Shafer, C. R. Swartz, T. Jermwongratanachai, R. Chen, F. Rogers, B. H. Davis, *ACS Catal.* **2014**, *4*, 1662-1672.

[9] J. Lu, L. Yang, B. Xu, Q. Wu, D. Zhang, S. Yuan, Y. Zhai, X. Wang, Y. Fan, Z. Hu, *ACS Catal.* **2014**, *4*, 613-621.

[10] T. O. Eschemann, W. S. Lamme, R. L. Manchester, T. E. Parmentier, A. Cognigni, M. Rønning, K. P. de Jong, *J. Catal.* **2015**, *328*, 130-138.

[11] Y. Cheng, J. Lin, K. Xu, H. Wang, X. Yao, Y. Pei, S. Yan, M. Qiao, B. Zong, *ACS Catal.* **2016**, *6*, 389-399.

[12] P. Zhang, Z.-A. Qiao, S. Dai, *Chem. Commun.* **2015**, *51*, 9246-9256.

[13] Y. Shirazi, M. A. Tofighy, T. Mohammadi, A. Pak, *Appl. Surf. Sci.* **2011**, *257*, 7359-7367.

[14] W.-W. Liu, A. Aziz, S.-P. Chai, A. R. Mohamed, C.-T. Tye, *Physica E* **2011**, *43*, 1535-1542.

[15] W. Shen, X. Yang, Q. Guo, Y. Liu, Y. Song, Z. Han, Q. Sun, J. Cheng, *Mater. Lett.* **2006**, *60*, 3517-3521.

[16] H. Xu, J. Guo, K. S. Suslick, *Adv. Mater.* **2012**, *24*, 6028-6033.

[17] W. Yang, S. Mao, J. Yang, T. Shang, H. Song, J. Mabon, W. Swiech, J. R. Vance, Z. Yue, S. J. Dillon, H. Xu, B. Xu, *Sci. Rep.* **2016**, *6*, 24187.

[18] H. Xiong, M. Moyo, M. A. Motchelaho, Z. N. Tetana, S. M. A. Dube, L. L. Jewell, N. J. Coville, *J. Catal.* **2014**, *311*, 80-87.

[19] J. Liu, S. Z. Qiao, H. Liu, J. Chen, A. Orpe, D. Zhao, G. Q. Lu, *Angew. Chem. Int. Ed.* **2011**, *50*, 5947-5951.

[20] A.-H. Lu, G.-P. Hao, Q. Sun, *Angew. Chem. Int. Ed.* **2011**, *50*, 9023-9025.

[21] K. S. W. Sing, in *Pure and Applied Chemistry, Vol. 57*, **1985**, p. 603.

[22] A. Y. Khodakov, J. Lynch, D. Bazin, B. Rebours, N. Zanier, B. Moisson, P. Chaumette, *J. Catal.* **1997**, *168*, 16-25.

[23] G. L. Bezemer, J. H. Bitter, H. P. C. E. Kuipers, H. Oosterbeek, J. E. Holewijn, X. Xu, F. Kapteijn, A. J. van Dillen, K. P. de Jong, *J. Am. Chem. Soc.* **2006**, *128*, 3956-3964.

CHAPTER 7

Iron Fischer-Tropsch synthesis on solid and hollow support morphologies – a comparative study

7.1 Introduction

Carbon spheres (CSs) possess unique characteristics which set them apart from other carbonaceous materials such as carbon nanotubes, carbon nanofibers or activated carbon, in that they have inherent advantages of both carbon materials and spherical colloids.[1] As a result they have tunable particle sizes, controllable pore structures, high stability in both acidic and basic environments, good electrical conductivity and allow for easy recovery of precious metals by simply burning off the carbon after the deactivation of the supported catalysts. Thus the synthesis of nanoporous CSs has been of increasing interest. To date, CS have been fabricated from a wide variety of carbon sources by employing methods such as the non-catalytic chemical vapour deposition (CVD), hard templating with silica spheres as the templates, soft templating approaches by organic-organic self-assembly, hydrothermal treatment of sugars, and more recently by the modified Stöber method.[2-5] Recent interests are focusing on the fabrication of different morphologies of CSs as the dissimilar architectures tend to possess unique characteristics, and can potentially be used in a wide range of applications.

Prior studies have reported the synthesis of CSs with solid, hollow, core-shell and yolk-shell morphologies. Mahajan et al. have fabricated solid carbon spheres with an average diameter of 43 nm by the MgO-catalyzed hydrothermal pyrolysis of acetone.[6] Chen et al. prepared hollow carbon spheres by using pre-fabricated silica spheres as the solid template, and then encapsulating it with carbon.[7] The silica spheres are typically made using the Stöber method which involves the base-catalyzed hydrolysis and condensation of alkoxysilanes such as TEOS. Recently, Liu and co-workers have shown that the Stöber method can be modified (extended) to allow for the synthesis of monodisperse solid carbon spheres.[8] This extended

---

This chapter is still to be submitted for publication.

Stöber method approach also allows for the preparation of core-shell, yolk-shell and hollow carbon spheres when a template is used during the synthesis.[9-11]

Recently, interest in the Fischer-Tropsch (FT) synthesis reaction has been revived because of instability in crude oil prices, and thus efforts are now directed towards diversifying energy sources. In the Fischer-Tropsch (FT) synthesis, syngas ($CO + H_2$) derived from feedstocks such as biomass, coal, stranded natural gas or shale gas is converted to heavy hydrocarbons, the precursors for high-quality diesel, kerosene and commodity chemicals. The FT synthesis is industrially performed over cobalt or iron catalysts. Iron catalysts are preferred for the synthesis of hydrocarbons from CO-rich synthesis gas because of their water-gas-shift activity, low price, large reserves and low sensitivity to poisoning.[12, 13] Furthermore, Fe catalysts produce a wider product spectrum than Co-catalysed reactions, the products include olefins, paraffins and oxygenates. Fe-based FT catalysts also have a flexible reaction temperature range as they can be operated under low or high temperature FT conditions. Thus the versatility of Fe catalysts still makes them favourable candidates for the conversion of synthesis gas and warrants further study in order to make better performing catalysts.

Previous studies on Fe FT synthesis have been dedicated to investigating effects associated with chemical promoters,[14, 15] Fe particle size,[14, 16-18] Fe oxide reducibility,[19] structure,[20] catalyst deactivation,[21] metal-support interactions[22] or the use of different types of catalyst support materials.[23, 24] The morphology of the support material is also a critical aspect and its effects should be well understood in catalyst design. Effects related to the catalyst support morphology have been reported on the performance of fuel cells.[25] However, the effects reported were detected by comparing carbon black with carbon nanotubes as supports for Pt catalysts, and these carbons possess different properties. Carbon spheres (CSs) are a versatile material which can be used to study morphology-related effects in heterogeneous catalysis. CSs can have morphologies such as solid, hollow, core-shell or yolk-shell structures, which are achievable by a simple variation of the synthesis conditions. The chemical inertness of these materials makes them suitable for studying effects associated with the support morphology in catalysis. In this study, we focused on studying the effects of using a solid or a hollow carbon support on the performance of Fe FT catalysts. The fabrication of the solid and hollow CSs was tuned so that they had comparable properties (size, surface area, pore

structure, thermal stabilities and crystallinity) and was also done from the same carbon precursor by using the hydrothermal method.

7.2 Experimental procedures

7.2.1 Synthesis of Solid carbon spheres ($SCSs_{RF}$) and hollow carbon spheres (HCSs)

Fabrication of the solid carbon sphere support was achieved using a procedure given in earlier section (6.2.1). Briefly, the synthesis was achieved by the room-temperature polymerization of a resorcinol-formaldehyde (RF) carbon precursor, followed by the hydrothermal treatment of the solution to yield a brown polymeric product. The polymeric material was then converted to carbon by a high temperature treatment (900 °C, 4 h) under the flow of nitrogen (20 mL/min). Unlike their solid analogues, the nanofabrication of hollow carbon spheres was performed by the use of a sacrificial silica sphere template. This scaffold was encapsulated with the polymeric material (RF) to give a core-shell SiO_2@RF composite, which was then carbonized at 900 °C for 1 h to SiO_2@C material. Removal of the template was achieved by etching it using a hydrofluoric acid solution. The prepared solid carbon spheres were abbreviated as $SCSs_{RF}$, whereas the hollow carbon spheres are labelled as HCSs.

7.2.2 Material characterizations

Transmission electron microscopy (TEM) bright-field data was obtained on an FEI Tecnai T12 instrument operated at 12 kV. Scanning electron microscopy (SEM) analysis was performed on an FEI Nova Nanolab 600 operated at 30 kV and 0.63 nA. Prior to the analysis, the samples were coated with a thin layer of Au-Pd alloy in a sputter coater. Nitrogen physisorption measurements were done on a Micromeritics TriSta 3000 analyser. The average pore sizes were determined by the Barrett-Joyner-Halenda (BJH) method, and pore volumes were measured at a relative pressure of P/P_0 = 0.995. Powder X-ray diffraction (PXRD) patterns were recorded on a Bruker D2 diffractometer operated at 30 kV and 10 mA, by using a Lynxeye detector. Thermogravimetric analysis with differential thermal gravimetry (TGA-DTG) analysis was performed with a PerkinElmer STA6000 instrument. Temperature programmed reduction (TPR) measurements were performed on a Micromeritics AutoChem II analyser equipped with a thermal conductivity detector (TCD) and Brooks mass-flow controllers.

7.2.3 Catalyst preparation and catalytic testing

Supported catalysts were prepared in this study, using $SCSs_{RF}$ and HCSs as the support materials. The homogeneous deposition precipitation method was used to load the metal particles on to the carbon supports. Precipitation was done using urea at 90 °C, and evaporation of the solvent (water) was done at 70 °C under vacuum. Drying was done at 70 °C for 12 h, followed by calcination at 350 °C for 4 h. The calcined samples were tested on 16 mm i.d. stainless steel fixed-bed reactor. Reduction of the catalyst (0.5 g) was done in situ at 350 °C for 18 h using pure hydrogen (UHP grade). Subsequently, FT synthesis evaluation was performed at 250 and 270 °C (50 h at each T) using synthesis gas $H_2/CO = 2$ and a flow rate of 20 mL/min. Gaseous products were analysed with two online GCs fitted with a TCD and an FID detector. Liquid products were analysed using an off-line GC equipped with an FID detector.

7.3 Results and discussion

7.3.1 Electron microscopy analysis

The morphology and properties of calcined catalysts were examined by using electron microscopy. Fig. 7.1 shows representative TEM and SEM images of the $10Fe/SCSs_{RF}$ and 10Fe/HCSs catalysts. It was clear that the iron oxide particles were mainly found on the outer surface of the carbon spheres on both catalyst systems, except for few isolated cases where they were also seen on the inside of broken hollow carbon spheres. Examples of broken hollow carbon spheres within the catalyst are shown in Fig. 7.1d. The metal particles were generally well dispersed on the carbon supports. Specifically, the 10Fe/HCSs catalyst displayed better dispersion of the metal oxide particles. The sizes of the particles were measured from the TEM images are the recorded size distributions are displayed in Fig. 7.1e and Fig. 7.1f. The average size of the particles was found to be 14.9 and 10.8 nm for the $10Fe/SCSs_{RF}$ and the 10Fe/HCSs samples, respectively. Because of their lower density, the HCS support offers more outer surface area for particle deposition than their solid analogues, hence the higher dispersions measured on this support material. For the same reason, the 10Fe/HCSs catalyst was also seen to have a narrower particle size distribution.

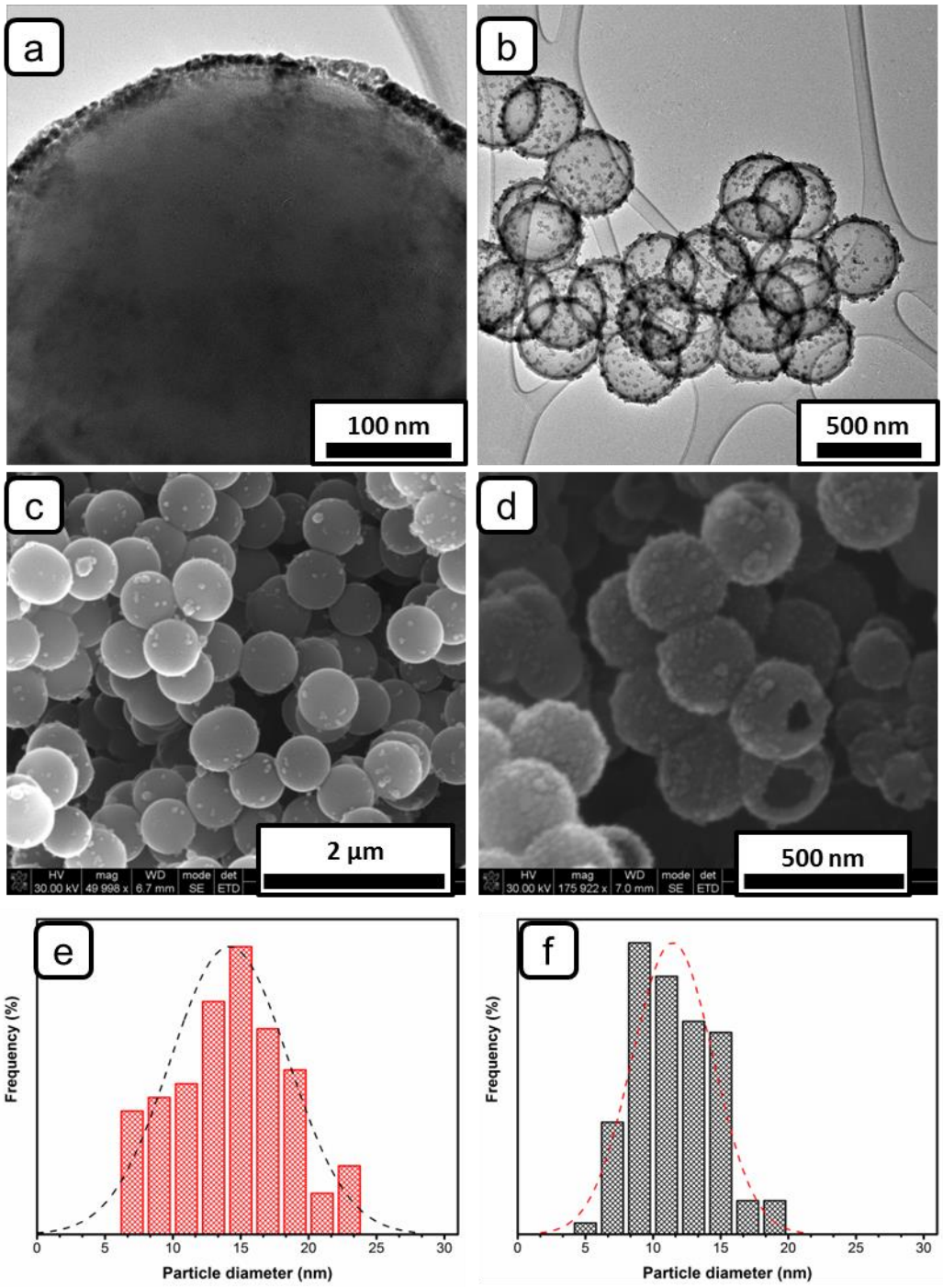

Figure 7.1 TEM and SEM images of (a,c) 10Fe/SCSs$_{RF}$ and (b,d) 10Fe/HCSs. The corresponding particle size distributions are shown as (e) 10Fe/SCSs$_{RF}$, (f) 10Fe/HCSs.

7.3.2 Energy-dispersive X-ray (EDX) spectroscopy

Fig. 7.2 shows energy-dispersive X-ray (EDX) spectra measured from the catalysts. The results verified that both the 10Fe/SCSs$_{RF}$ and the 10Fe/HCSs samples contained carbon, iron and oxygen. The palladium and gold elements detected are due to the Au-PD alloy used to coat the samples prior to their introduction into the microscope.

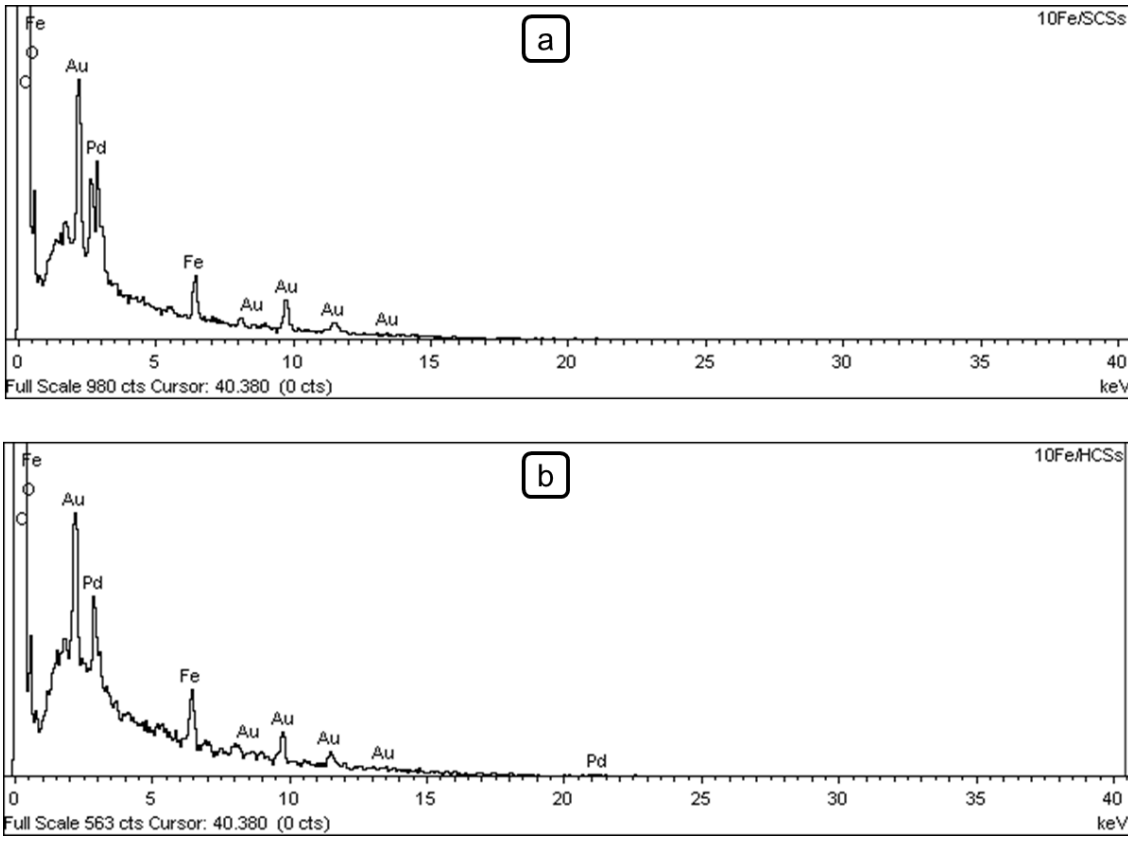

Figure 7.2 EDX spectra for the (a) 10Fe/SCSs$_{RF}$ and the (b) 10Fe/HCSs samples.

7.3.3 Nitrogen physisorption studies

Table 7.1 summarizes the textual properties of the samples. The BET results revealed that the surface areas of the catalysts decreased after the deposition of the iron oxide nanoparticles. The pore volumes and pore sizes of the calcined samples only displayed slight decreases, with measured differences of ~0.1 cm^3/g and 0.3 nm, respectively. The decrease in these properties is mainly due to the partial blockage of some pores of the carbon supports during catalyst incorporation. However, the catalysts still possess sufficiently high surface areas for

their application in the CO hydrogenation reaction. Notably, the mesoporous pore structure of the materials was retained on the calcined samples.

Table 7.1 Textual properties of the samples.

Sample	Surface area [m^2/g]	Pore volume [cm^3/g]	Pore size [nm]	PXRD[a] [nm]	TEM[b] [nm]
$SCSs_{RF}$	565.2	0.315	2.71	-	-
HCSs	562.8	0.389	2.76	-	-
10Fe/$SCSs_{RF}$	381.9	0.245	2.46	15.6	14.9
10Fe/HCSs	396.5	0.279	2.55	10.1	10.8

[a] *Fe_2O_3 crystallite sizes were estimated from PXRD patterns using the Scherrer equation.*

[b] *Fe_2O_3 particle sizes were estimated from TEM images.*

7.3.4 Thermogravimetric analysis (TGA)

In order to probe the effect of the support architecture on the thermal stability of the catalysts, TGA experiments were performed; all were done under the flow of air. Fig. 7.3 depicts TGA profiles (shown in black) and the corresponding differential thermal gravimetry curves (shown in blue) for the 10Fe/$SCSs_{RF}$ and 10Fe/HCSs samples. Two broad decomposition peaks with maxima at 580 and 687 °C were seen on the 10Fe/$SCSs_{RF}$ sample (Fig. 7.3a). These peaks are both due to the oxidation of carbon to CO_2. The low temperature peak is attributed to Fe-catalyzed carbon oxidation, whereas the peak at 687 °C is due to the decomposition of bulk carbon which was not in direct contact with the metal particles. Unlike their solid analogues, the 10Fe/HCSs sample featured only one decomposition peak at 605 °C (Fig. 7.3b). This peak is narrow in width due to the thin carbon shells of the hollow support. Only one peak was seen on this sample because carbon decomposition was mainly Fe-catalyzed. Furthermore, this carbon oxidation behaviour confirms the good dispersion of Fe nanoparticles on the carbon support. The non-zero residual weight after TGA-DTA

experiments is due to iron oxide which was about 20 wt% for both samples, and verified that the samples had similar metal loadings.

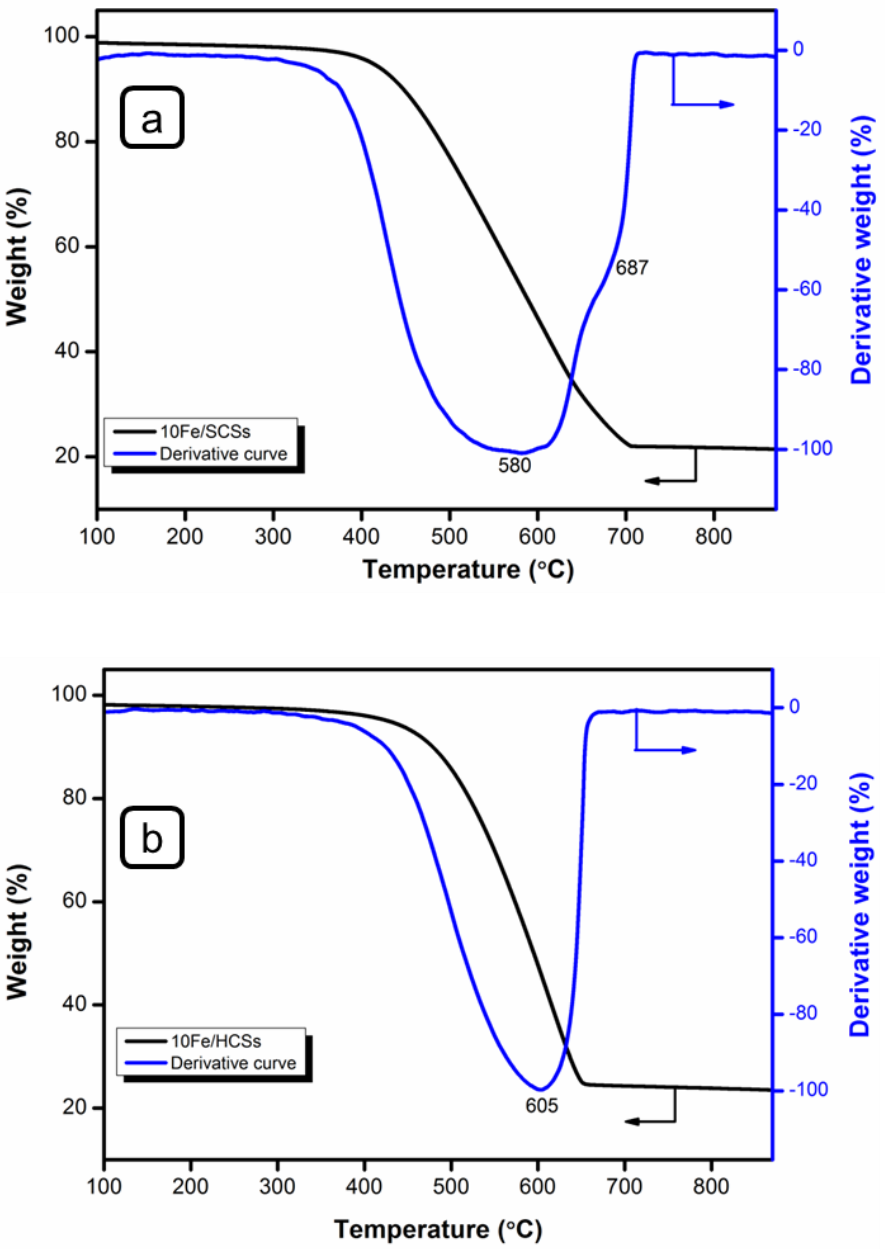

Figure 7.3 TGA profiles and derivative curves of (a) 10Fe/SCSs and (b) 10Fe/HCSs, analysis done in an oxidizing atmosphere.

7.3.5 Powder X-ray diffraction (PXRD)

The phases present on the calcined catalysts were identified by using the PXRD technique (Fig. 7.4). The diffraction peaks observed at 25.0 and 50.7° on both samples are attributed to

the (002) and the (100) signature peaks for graphitic carbon.[12] The lower degree of crystallinity on the HCS support is related to the shorter carbonization time (1 h) used during the synthesis of this material and the hollow nature of this material. In addition to the carbon signals, both samples had peaks at 38.5, 41.4, 47.6, 57.6, 63.6, 73.9 and 76.0°, and corresponded with the (104), (110), (113), (024), (116), (214) and (300) signature peaks for α-Fe_2O_3 [PDF No. 01-089-0598]. It was observed that the 10Fe/$SCSs_{RF}$ pattern had more crystalline diffraction peaks, suggesting that the iron oxide crystallites could be larger on this sample. The sizes of the iron oxide crystallites were estimated using the Scherrer equation and are displayed in Table 7.1. The smaller crystallite sizes (10.1 nm) on the 10Fe/HCSs sample are attributed to the higher particle dispersion which is aided by the hollow architecture of the support material, and are in agreement with results obtained from electron microscopy studies.

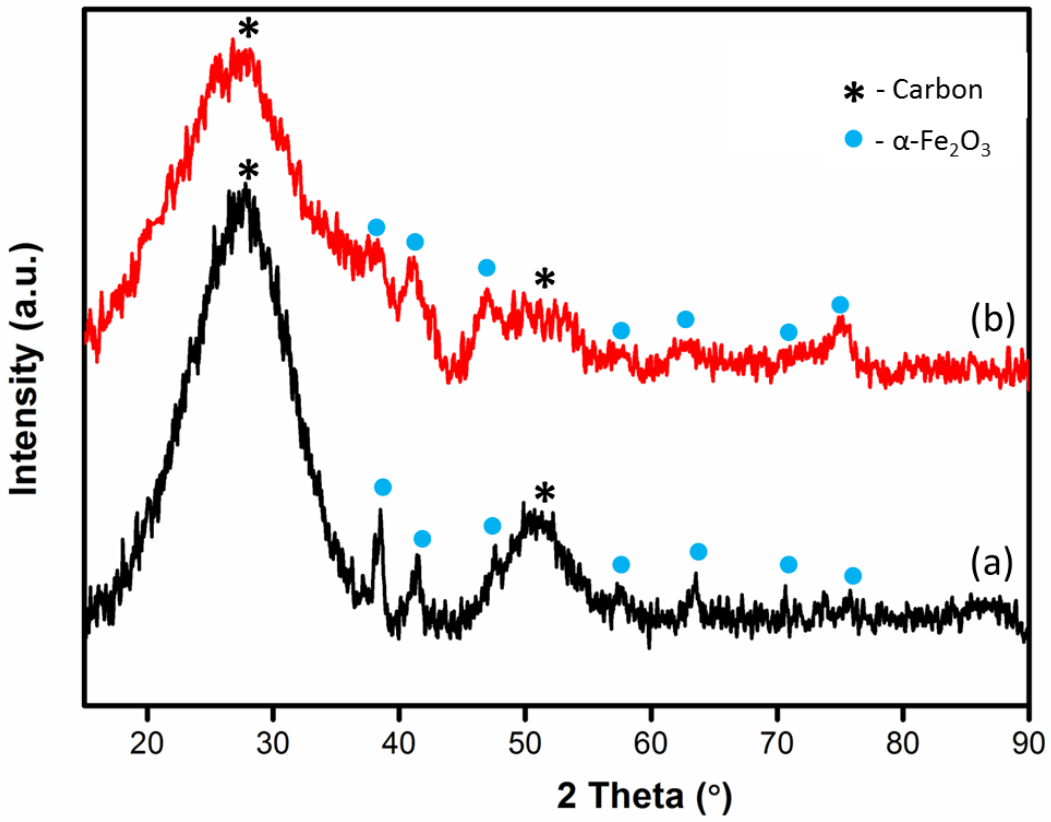

Figure 7.4 Powder X-ray diffraction patterns of (a) 10Fe/$SCSs_{RF}$ and (b) 10Fe/HCSs samples.

7.3.6 Temperature programmed reduction (TPR)

The reduction characteristics of the Fe oxide nanoparticles supported on solid and hollow carbon spheres were studied by the TPR technique. Fig. 7.5 shows reduction profiles of the 10Fe/SCSs$_{RF}$ and 10Fe/HCSs samples measured using different heating rates (2, 5, 10, 20 °C/min). The observed reduction temperatures are summarized in Table 7.2. For the 10Fe/SCSs$_{RF}$ sample, the transformation of Fe oxide was seen to proceed via a two-step mechanism as follows; $Fe_2O_3 \rightarrow Fe_3O_4$ followed by the $Fe_3O_4 \rightarrow Fe$ step.[13] These reduction steps were seen as two distinct peaks in the 300 – 500 °C region during the activation process, and were present irrespective of the ramping rate utilized. Increasing the heating rate was observed to shift the transformations to higher reduction temperatures. Furthermore, the methanation of carbon, seen as a negative peak at T > 600 °C, also shifted to higher temperatures with increased heating rates.

For the 10Fe/HCS sample, a similar reduction trend was observed as the Fe oxide nanoparticles were converted to metallic Fe (Fig. 7.5). However, the reduction peaks were not distinctive for this sample, but they were seen to overlap in the same temperature range (300 – 500 °C). The overlapping of the reduction peaks was observed even when very low heating rates (2, 5 °C/min) were used. Notably, methanation of the hollow carbon support consistently occurs at a lower temperature than the hydrogenation of the solid support material. This observation is due to two effects; 1) the thin carbon shells of this material are easily hydrogenated, and 2) the good dispersion and thus smaller metal particle sizes have a higher hydrogenation activity than the bigger metal particles characteristic of the 10Fe/SCSs$_{RF}$ catalyst. The difference in the activation characteristics might be related to differences in support morphologies for these samples.

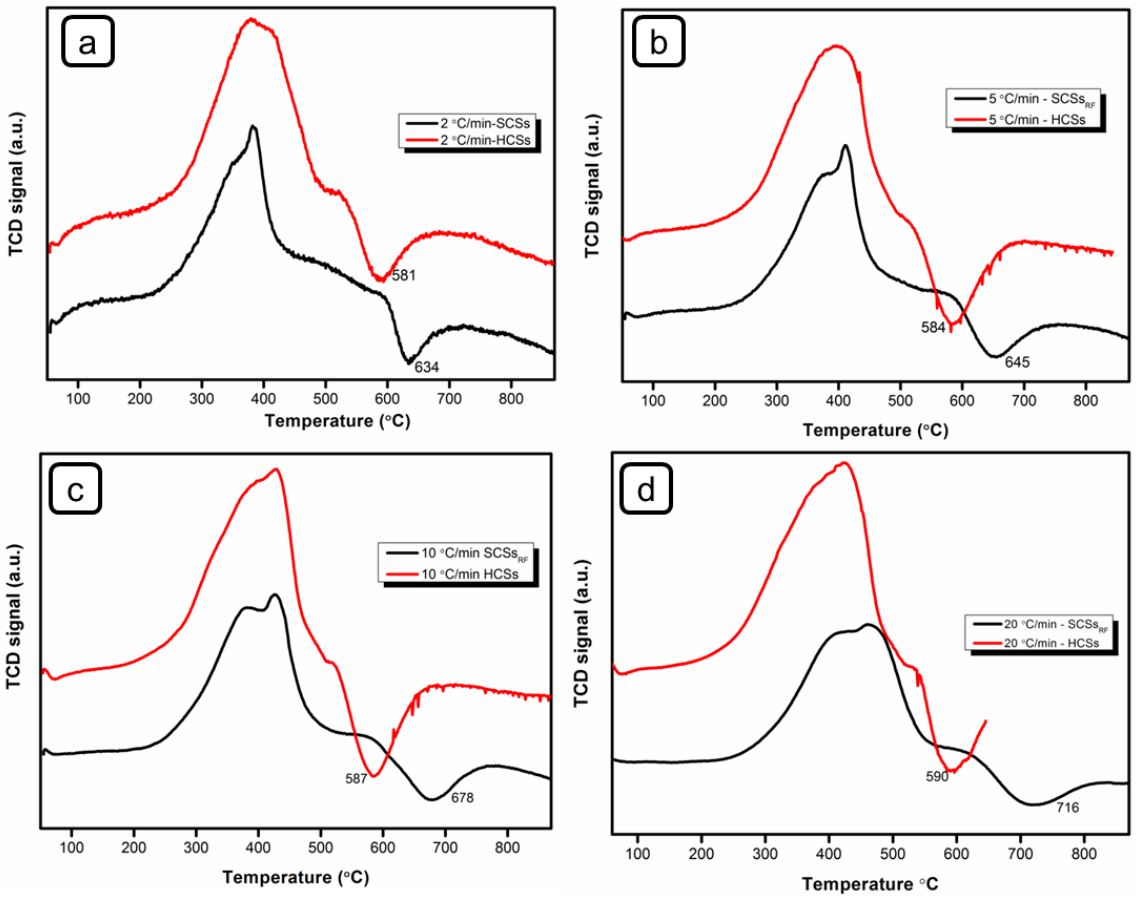

Figure 7.5 A comparison of TPR profiles for the 10Fe/SCSs$_{RF}$ and the 10Fe/HCSs catalysts that were measured using different ramping rates.

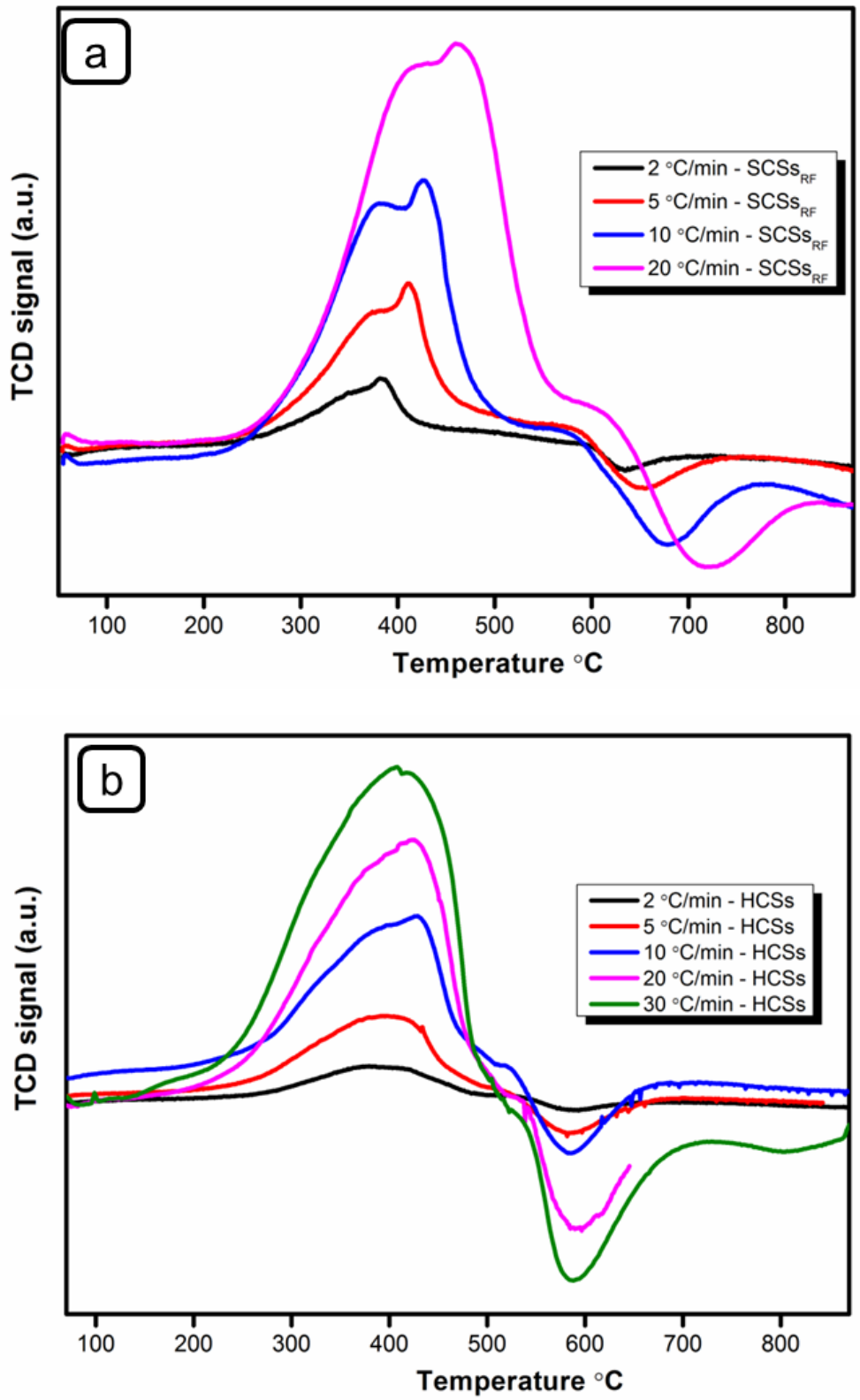

Figure 7.6 TPR profiles measured at different heating rates for the (a) 10Fe/SCSs and (b) 10Fe/HCSs catalysts.

Table 7.2 Reduction temperatures recorded under different ramping rates.

Ramping rate	Temperature of occurrence [°C]		
	$Fe_2O_3 \rightarrow Fe_3O_4$	$Fe_3O_4 \rightarrow Fe$	Methanation
2 °C/min - $SCSs_{RF}$	346.3	382.8	633.9
2 °C/min – HCSs	364.1	412.3	581.1
5 °C/min - $SCSs_{RF}$	371.3	410.3	644.9
5 °C/min – HCSs	367.0	413.9	583.5
10 °C/min - $SCSs_{RF}$	378.4	427.0	677.5
10 °C/min – HCSs	370.9	423.8	587.1
20 °C/min - $SCSs_{RF}$	413.5	464.1	716.4
20 °C/min – HCSs	377.9	426.9	589.7
30 °C/min - $SCSs_{RF}$	-	-	-
30 °C/min - HCSs	379.0	429.8	588.6

7.3.6.1 Effect of the support morphology on catalyst reducibility

Fig. 7.5 and Fig. 7.6 shows TPR profiles for the reduction characteristics of iron oxide nanoparticles dispersed on a solid and a hollow carbon support analysed using different heating rates (2, 5, 10 and 20 °C/min). For the same support material, the reduction profiles exhibited similar trends. For example, the peaks shifted to higher temperatures and the signal intensity increased with an increase in the heating rate, as expected. However, the 10Fe/HCSs catalyst consistently displayed a marginal increase in the reduction peak maxima as the ramping rate was increased. This was also true for the methanation peaks (negative signal) at the different heating rates. On this basis, it is evident that the morphology of the support material plays a role in the reducibility of the catalyst. This is withstanding the fact that the carbon supports were synthesized from the same carbon source (RF) and by using the same method (hydrothermal synthesis).

7.3.6.2 Reduction kinetics

To examine the effects of the support morphology on the catalyst reduction kinetics, the evolution of different iron species in TPR experiments was monitored using different heating rates (2, 5, 10, 20 and 30 °C/min). The Kissinger method (Eqn. 7.1) has been extensively applied in the determination of activation energies (E_a) for various processes and is represented as follows:[26]

$$ln\left(\frac{\beta}{T_m{}^2}\right) = -\frac{E_a}{RT} + ln\left(\frac{AR}{E_a}\right) \qquad \text{Eqn. 7.1}$$

where β is the linear ramping rate (K/min), T_m is the reduction peak temperature (K), A is the pre-exponential factor (s^{-1}) and R is the gas constant ($Jmol^{-1}K^{-1}$). Using Eqn. 7.1, a plot of $ln\left(\frac{\beta}{T_m{}^2}\right)$ vs $\frac{1}{T}$ results in a straight line for first order processes, and the activation energy can be determined from the slope ($m = -\frac{E_a}{R}$) of this line. Even though the Kissinger approach was originally used to determine activation energies of single-step first order kinetics, it has been extensively used to estimate the E_a for multi-step processes.

Fig. 7.7 shows plots of $ln\left(\frac{\beta}{T_m{}^2}\right)$ vs $\frac{1}{T}$ for the reduction of the iron species on the 10Fe/SCSs sample. The kinetic plots for the transformation of Fe_2O_3 to Fe_3O_4 are shown in Fig. 7.7a, whereas Fig. 7.7b displays data for the $Fe_3O_4 \rightarrow Fe$ conversion. The slopes for these Kissinger plots were found to be -13.3 K and -12.3 K, respectively for this sample. The activation energies associated with these reduction processes were determined to be 110.3 and 102.5 kJ/mol, respectively. These values are comparable to data reported for other Fischer-Tropsch catalysts. Fig. 7.8 shows of $ln\left(\frac{\beta}{T_m{}^2}\right)$ vs $\frac{1}{T}$ plots for reduction processes which occurred on the 10Fe/HCSs sample. This sample only displayed minimal increments in the peak temperatures with corresponding increases in the ramping rate. As a consequence, the Kissinger plots had slopes of -57.0 K and -73.7 K, for the first and the second reduction peaks, respectively. These values are significantly high, thus the activation energies could not be determined accurately for this sample by using the Kissinger method. However, it was clear that the two catalyst systems displayed different reduction behaviours. On this basis, it appears that the support morphology does influence the reduction kinetics of a catalyst. The origin of this effect could be two-fold; (1) the differences in gas transport characteristics on

the two supports, and (2) the inherent consequences of dissimilar iron oxide particle sizes. The surface chemistry of the carbon supports is believed not to play a major role in this as it is similar for the two materials. However, the different particle sizes of Fe oxide could interact differently with the carbon surface.

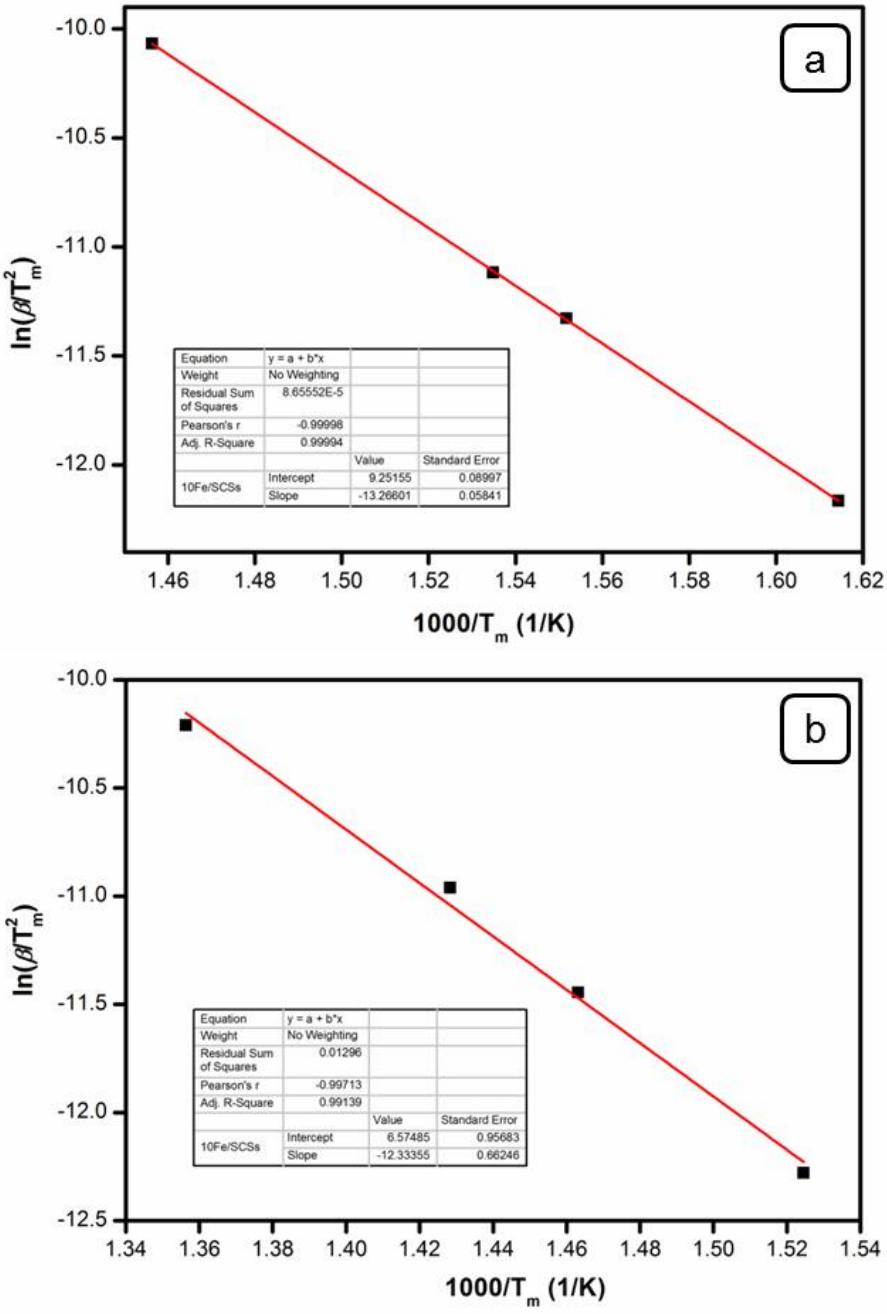

Figure 7.7 Thermokinetics of the reduction of (a) $Fe_2O_3 \rightarrow Fe_3O_4$ and (b) $Fe_3O_4 \rightarrow Fe$ for the $10Fe/SCSs_{RF}$ catalyst.

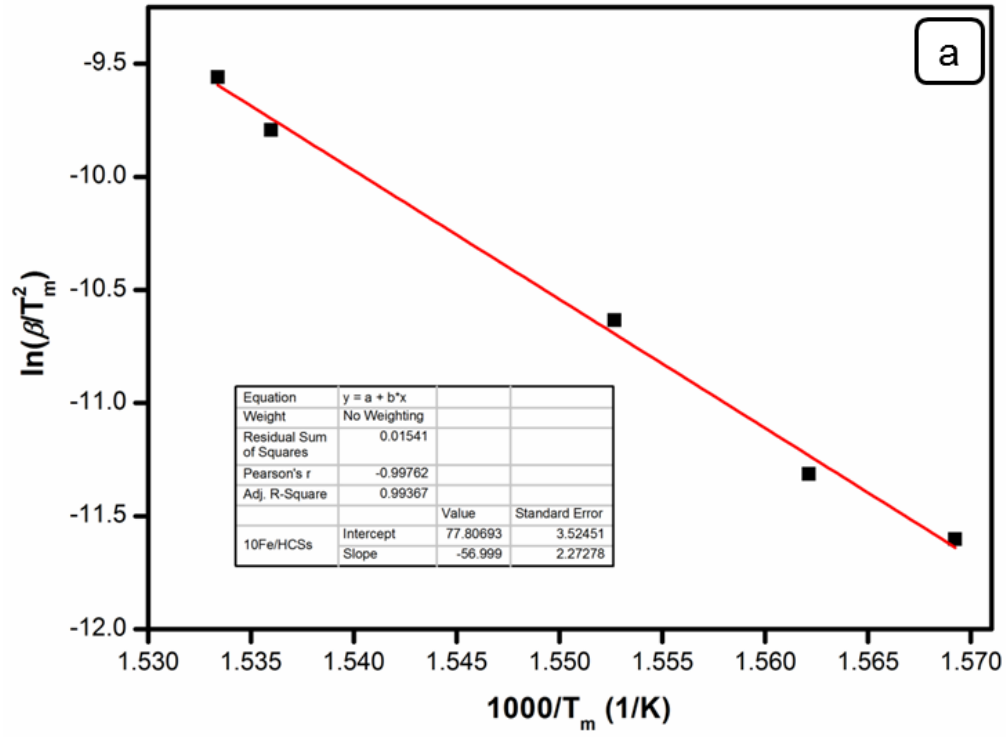

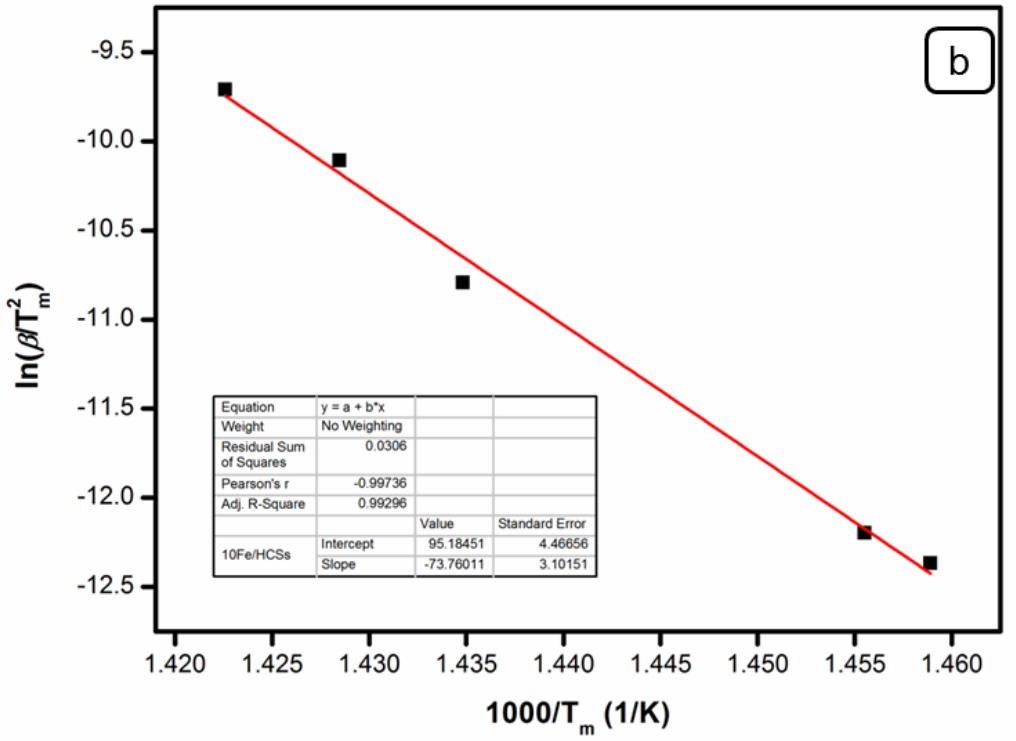

Figure 7.8 Thermokinetics of the reduction of (a) $Fe_2O_3 \rightarrow Fe_3O_4$ and (b) $Fe_3O_4 \rightarrow Fe$ for the 10Fe/HCSs catalyst.

7.3.7 Fischer-Tropsch catalytic evaluation

The FT catalytic tests were performed under the following conditions; T = 250, 275 °C, 10 bar total pressure, H_2/CO: 2, flow rate: 20 mL/min, catalyst weight: 0.5 g. Table 7.3 summarizes the steady-state activity and selectivity data for the Fe catalysts dispersed on solid and hollow carbon spheres. Significant differences were observed on the catalytic properties of these samples. For example, at similar reaction temperatures, higher CO conversions were measured for the Fe/HCS than for the Fe/$SCSs_{RF}$ sample. This trend was maintained at both reaction temperatures used and was consistent with results measured for the Co/HCSs and Co/$SCSs_{RF}$ systems. Just like with the Co measurements, these differences in activity are related to the good metal dispersion on the hollow support, and the efficient mass transfer of products from the active sites when this support architecture is used. As expected, increasing the temperature improved the activity of the different catalyst systems. However, it was noted that a bigger percentage increase was measured on the Fe/HCSs catalyst (12.5%) versus 5.8% recorded for the $SCSs_{RF}$ sample. This is related to the higher sintering tendency of Fe particles dispersed on the solid support at higher reaction temperature. Vide infra for a characterization of the spent catalysts.

Data on the product selectivity towards specific fractions is presented in Table 7.3. The Fe/HCSs sample had higher selectivity towards the C_{5+} product fraction than the Fe/$SCSs_{RF}$ sample at both reaction temperatures studied. It is evident that the two systems possess dissimilar properties as the differences in the C_{5+} selectivity measured were greater than 10% for similar analysis conditions. Furthermore, unlike the Co systems which displayed a large decrease in the C_{5+} fraction at a high reaction temperature, minimal changes (± 4%) were measured on these Fe catalysts. This is because of the flexibility of Fe as a low- and high-temperature FT catalyst.

Table 7.3 Fischer-Tropsch synthesis performance of the catalysts.

Sample	Temp [°C]	CO conversion [%]	Product selectivity [%]			
			C_1	$C_2 - C_4$	C_{5+}	CO_2
10Fe/SCSs$_{RF}$	250	20.3	15.1	22.5	62.4	16.7
	275	26.1	20.6	20.1	59.3	22.5
10Fe/HCSs	250	25.9	11.8	14.4	73.8	21.2
	275	38.4	13.0	16.2	70.8	26.2

7.3.8 Spent catalysts

After a 100 h time on stream catalytic evaluation period, the spent catalysts were subsequently characterized with TEM (Fig. 7.9). The analysis of TEM images of the spent 10Fe/SCSs$_{RF}$ catalyst revealed that there was a difference in the metal particle properties before and after the reaction. The metal particles were seen to have agglomerated on the spent sample, and the average parcel size was calculated to be 34.3 nm (Fig. 7.9a). This is a significant increase from the 14.9 nm particle size measured on the calcined fresh catalyst measured by the same technique (TEM). In the case of the Fe dispersed on hollow carbon spheres, the particles were also seen to have sintered. Thus the measured average particle size increased from 10.8 nm on the fresh catalyst to 21.1 nm after the reaction. It was observed that the tendency to sinter was lower for the 10Fe/HCSs catalyst than on the 10Fe/SCSs sample, owing to the better particle dispersion on the hollow carbon sphere support material. The insert in Fig. 7.9b depicts a metallic Fe species encapsulated in an amorphous iron oxide passivation layer, and is consistent with other reports.[27] Furthermore, the spent samples displayed no structural collapse for both the solid and hollow CS-supported catalysts. This illustrated that the support materials used maintained their structural integrity under the hydrothermal conditions present during FT synthesis.

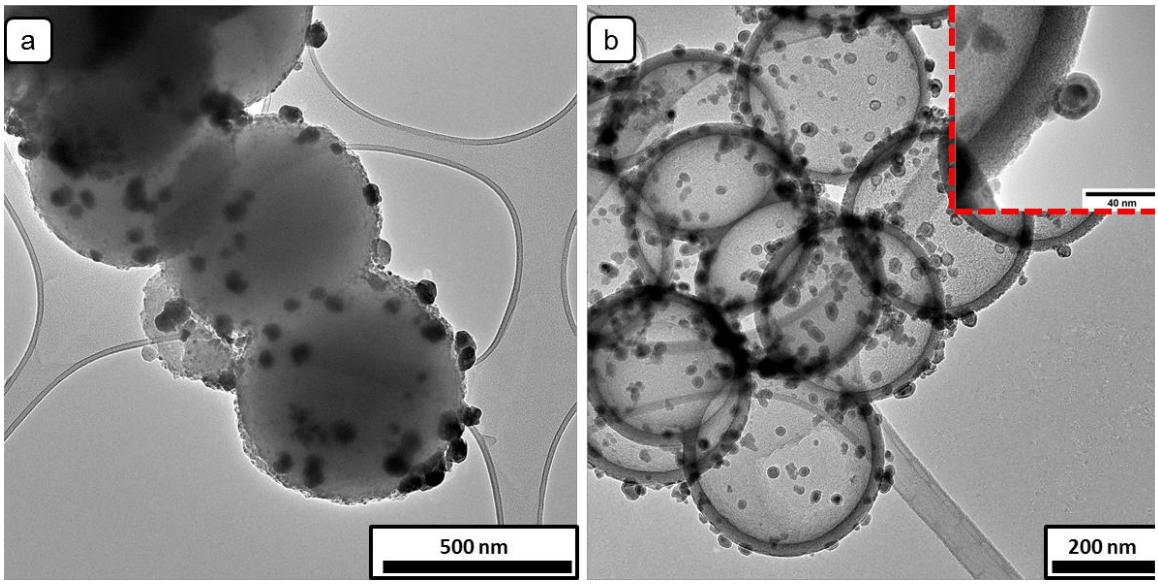

Figure 7.9 TEM images of the spent catalysts (a) 10Fe/$SCSs_{RF}$ and (b) 10Fe/HCSs. The insert shows a high magnification image of the 10Fe/HCSs spent catalyst.

7.4 Conclusions

The fabrication of solid and hollow carbon sphere support materials by similar synthesis procedures has allowed us to study and quantify the effects of the support architecture in heterogeneous catalysis. Catalysts prepared from these materials had mesoporous pore structures and high specific surface areas (> 380 m^2/g), inherent from the CS supports used. The Fe particle sizes were seen to be well-dispersed and thus smaller on the hollow support (~10 nm) than on the solid carbon spheres (~15 nm). Furthermore, the carbon supports had high thermal stabilities despite being in contact with the catalytic metal particles. Performing TPR studies allowed us to study the differences in the reducibility of iron oxide particles supported on solid or on hollow CSs.

From kinetic studies, it was observed that the reduction characteristics of the catalysts were different illustrating that they possessed dissimilar properties. Furthermore, the use of various heating rates resulted in different response trends in the TPR, providing new insights on the effect of the support architecture on the catalyst reduction kinetics. The catalytic properties of Fe particles dispersed on solid and hollow support materials were found to be different. The

Fe/HCSs catalyst generally displayed superior activity and selectivity for C_{5+} hydrocarbons both at 250 and 275 °C. Due to the higher metal dispersion on the hollow support, minimal sintering was detected.

References

[1] J. Liu, N. P. Wickramaratne, S. Z. Qiao, M. Jaroniec, *Nature Mater.* **2015**, *14*, DOI: 10.1038/nmat4317.

[2] H. Xiong, M. Moyo, M. A. Motchelaho, Z. N. Tetana, S. M. A. Dube, L. L. Jewell, N. J. Coville, *J. Catal.* **2014**, *311*, 80-87.

[3] J. Zhang, L. Ma, M. Gan, F. Yang, S. Fu, X. Li, *J. Power Sources* **2015**, *288*, 42-52.

[4] N. Li, Q. Zhang, J. Liu, J. Joo, A. Lee, Y. Gan, Y. Yin, *Chem. Commun.* **2013**, *49*, 5135-5137.

[5] B. Guan, X. Wang, Y. Xiao, Y. Liu, Q. Huo, *Nanoscale* **2013**, *5*, 2469-2475.

[6] M. Mahajan, G. Singla, K. Singh, O. P. Pandey, *J. Solid State Chem.* **2015**, *232*, 108-117.

[7] Y. Chen, H. Chen, L. Guo, Q. He, F. Chen, J. Zhou, J. Feng, J. Shi, *ACS Nano* **2010**, *4*, 529-539.

[8] J. Liu, S. Z. Qiao, H. Liu, J. Chen, A. Orpe, D. Zhao, G. Q. Lu, *Angew. Chem. Int. Ed.* **2011**, *50*, 5947-5951.

[9] A. B. Fuertes, P. Valle-Vigon, M. Sevilla, *Chem. Commun.* **2012**, *48*, 6124-6126.

[10] P. Yang, Y. Xu, L. Chen, X. Wang, Q. Zhang, *Langmuir* **2015**, *31*, 11701-11708.

[11] C. Wang, J. Chen, X. Zhou, W. Li, Y. Liu, Q. Yue, Z. Xue, Y. Li, A. A. Elzatahry, Y. Deng, D. Zhao, *Nano Res.* **2015**, *8*, 238-245.

[12] Y. Cheng, J. Lin, K. Xu, H. Wang, X. Yao, Y. Pei, S. Yan, M. Qiao, B. Zong, *ACS Catal.* **2016**, *6*, 389-399.

[13] C. Li, I. Sayaka, F. Chisato, K. Fujimoto, *Appl. Catal. A* **2016**, *509*, 123-129.

[14] J. Xie, J. Yang, A. I. Dugulan, A. Holmen, D. Chen, K. P. de Jong, M. J. Louwerse, *ACS Catal.* **2016**, *6*, 3147-3157.

[15] K. Keyvanloo, J. B. Horton, W. C. Hecker, M. D. Argyle, *Catal. Sci. Technol.* **2014**, *4*, 4289-4300.

[16] J.-Y. Park, Y.-J. Lee, P. K. Khanna, K.-W. Jun, J. W. Bae, Y. H. Kim, *J. Mol. Catal. A* **2010**, *323*, 84-90.

[17] H. M. Torres Galvis, J. H. Bitter, T. Davidian, M. Ruitenbeek, A. I. Dugulan, K. P. de Jong, *J. Am. Chem. Soc.* **2012**, *134*, 16207-16215.

[18] J. Xie, H. M. Torres Galvis, A. C. J. Koeken, A. Kirilin, A. I. Dugulan, M. Ruitenbeek, K. P. de Jong, *ACS Catal.* **2016**, *6*, 4017-4024.

[19] A. F. H. Wielers, A. J. H. M. Kock, C. E. C. A. Hop, J. W. Geus, A. M. van Der Kraan, *J. Catal.* **1989**, *117*, 1-18.

[20] T. A. Wezendonk, V. P. Santos, M. A. Nasalevich, Q. S. E. Warringa, A. I. Dugulan, A. Chojecki, A. C. J. Koeken, M. Ruitenbeek, G. Meima, H.-U. Islam, G. Sankar, M. Makkee, F. Kapteijn, J. Gascon, *ACS Catal.* **2016**, *6*, 3236-3247.

[21] V. R. R. Pendyala, U. M. Graham, G. Jacobs, H. H. Hamdeh, B. H. Davis, *Catal. Lett.* **2014**, *144*, 1704-1716.

[22] H. Wan, B. Wu, H. Xiang, Y. Li, *ACS Catal.* **2012**, *2*, 1877-1883.

[23] K. Keyvanloo, M. K. Mardkhe, T. M. Alam, C. H. Bartholomew, B. F. Woodfield, W. C. Hecker, *ACS Catal.* **2014**, *4*, 1071-1077.

[24] D. B. Bukur, X. Lang, D. Mukesh, W. H. Zimmerman, M. P. Rosynek, C. Li, *Ind. Eng. Chem. Res.* **1990**, *29*, 1588-1599.

[25] M. M. Waje, W. Li, Z. Chen, Y. Yan, *ECS Trans.* **2006**, *3*, 285-294.

[26] H. E. Kissinger, *Anal. Chem.* **1957**, *29*, 1702-1706.

[27] Y. Jin, A. K. Datye, *J. Catal.* **2000**, *196*, 8-17.

CHAPTER 8

General conclusions and recommendations

8.1 General conclusions

It has been demonstrated in the literature that the hydrothermal method could be used to prepare carbon spheres. This low-temperature synthesis approach usually yields reproducible materials with solid and hollow architectures. But the as-prepared materials are typically non-porous, with surface areas of ~1 m^2/g being commonly reported in the literature. In this study, we have shown that properties of carbon spheres (such as surface area, pore structure, thermal stability or crystallinity) can be improved by annealing the materials at 900 °C under inert conditions (N_2, 20 mL/min). Tuning these properties involved a simple variation of the annealing period between 1 to 4 hours. The annealing procedure proved to be key in optimising the properties of the carbon materials to enable their use as model catalyst supports.

The improved properties of the annealed carbon spheres prompted us to use them as a model support material for bimetallic Fe-Co FT catalysts. The relative inertness of this material was to be exploited in an endeavour to understand this complex system. From the literature, reports of a seemingly contradictory nature were found on various aspects of this catalyst system. These included the identity of phases present after calcination, the phases formed during catalyst activation and the role of a possible alloy on the overall performance of the catalyst. These aspects seemed to be heavily influenced by the support material used. On the inert carbon spheres, the calcined bimetallic catalysts were determined to consist of Fe and Co oxides (α-Fe_2O_3 and Co_3O_4). No alloy of the two metals was detected on the calcined samples. During the activation of these catalysts as monitored by the H_2-TPR and in situ PXRD techniques, the relatively inert carbon support allowed for an insight on the transformations possible for such systems. Combining H_2-TPR and operando PXRD data allowed us to trace for the first time the transformations as they occur and to relate the phases formed during reduction to the Fe to Co ratios used. Activation of Co-rich samples led to the formation of the alloy wairauite (Co-Fe and possibly Co_xFe_y). When the Fe/Co ratio tended to unity, the relative abundance of the alloy increased. However, this specific alloy was not the

key component for improved catalyst activity or selectivity. Instead an alloy with a higher Co content closer to Co_2Fe seems more important.

In order to investigate the effect of the support morphology in heterogeneous catalysis carbon spheres were used as a model support. Carbon spheres were particularly useful in this regard because their architecture can easily be varied by simply changing the synthesis conditions. The conditions were chosen carefully to allow for the fabrication of carbon spheres with a solid or a hollow morphology. Synthesis of these materials with distinct morphologies was done by the hydrothermal method by using a mixture of resorcinol and formaldehyde as the carbon precursor in both instances. The synthesis conditions were tuned to enable the fabrication of solid and hollow carbon spheres with comparable properties such as their size, porosity and surface chemistry. Once optimized, the solid and hollow materials were then used as supports for monometallic Co and Fe catalysts. Conventional catalysts are typically dispersed on support materials with a solid morphology, while hollow materials have only recently found use as catalyst supports. Studies on the effects associated with the different support morphologies are still limited in the literature yet understanding this will be important in the rational design of the next generation of catalysts.

Catalysts dispersed on solid and hollow carbon spheres had different properties, although similar trends were observed for similar support morphologies when either Co or Fe was used. The low-density HCSs enabled the preparation of catalysts with highly dispersed metal particles compared to its solid counterpart. The result of the good dispersion was evident in the catalytic performance of both Co and Fe supported on HCSs. The higher activities and heavy hydrocarbon selectivities recorded for the Co/HCSs and Fe/HCSs catalysts are related to the smaller metal particles on these systems after calcination and the ease of mass product transfer favoured heavy hydrocarbon products. Analysis of the spent catalysts by the TEM technique revealed that sintering was more pronounced for the particles supported on the SCS_{RF} than on the HCS material, with increases in the average particle size of over 200% being possible on the solid sphere-supported catalyst.

The surface chemistry of the hollow carbon spheres was enhanced by doping them with nitrogen by using a post-synthesis procedure. This was achieved by the addition of aqueous melamine to SiO_2@RF composites, followed by a carbonization step at 600 or 900 °C under inert conditions. The use of these two carbonization temperatures incorporated 13.1 and 5.4% N for the N-$HCSs_{600}$ and the N-$HCSs_{900}$ samples. Furthermore, the types of incorporated N species were determined by X-ray photoelectron spectroscopy (XPS). The lower temperature treatment favoured a higher content of pyridinic and pyrrolic nitrogen, whereas the 900 °C treated samples had a higher pyrrolic and graphitic nitrogen content. TGA analysis revealed that post-synthesis N-doping did not significantly compromise the thermal stability of the materials because they were determined to be similar to those measured for the pristine hollow material.

PXRD and TEM data revealed that the Co particles deposited on the N-doped supports were significantly smaller in size than those dispersed on the pristine HCSs. The high N content of the doped materials was seen to result in a moderate metal-support interaction during the reduction of the catalyst precursors by the TPR and in situ PXRD techniques. However, this interaction was not too strong to inhibit the activity of the Co species in FT synthesis. Thus the highest FT performance (activity, selectivity) was recorded from the Co/N-$HCSs_{900}$ and Co/N-$HCSs_{600}$ samples. Analysis of the catalysts after FT synthesis revealed than the moderate metal-support interaction induced by N-doping promoted the anchoring of Co particles thus minimizing sintering at high temperatures.

8.2 Recommendations

It can be clearly seen from studies conducted in this work that the versatility of carbon spheres makes them ideal model support materials for investigating Fe, Co and Fe-Co catalyst systems. Further studies on the use of these materials are recommended but a carbon precursor alternative to resorcinol-formaldehyde is suggested because the porosity carbons synthesized from RF is harder to tune if the use of a surfactant is to be avoided. Secondly, additional studies are still required for a better understanding of bimetallic Fe-Co systems. For example, the use of promoters on such catalyst systems is still rarely reported. It is believed that this system would be better understood if a carbon support utilized, particularly

carbon spheres because of benefits associated with their tunability. Finally, the effect of the support morphology in catalysis still has to be explored on similarly-sized catalyst particles to eliminate particle size effects.

Appendix 1 – List of symbols

The following is a list of abbreviations that were used in the thesis:

ASF	-	Anderson-Schulz-Flory
BET	-	Brunauer-Emmett-Teller
CNTs	-	Carbon nanotubes
CSs	-	Carbon spheres
CVD	-	Chemical vapour deposition
EDX	-	Energy dispersive X-ray spectroscopy
FID	-	Flame ionisation detector
FTIR	-	Fourier transform infrared spectroscopy
FT	-	Fischer-Tropsch
GC	-	Gas chromatography
GHSV	-	Gas hourly space velocity
HCSs	-	Hollow carbon spheres
N-HCSs	-	Nitrogen doped hollow carbon spheres
PXRD	-	Powder X-ray diffraction
RF	-	Resorcinol-formaldehyde
SEM	-	Scanning electron microscopy
TCD	-	Thermal conductivity detector
TEM	-	Transmission electron microscopy
TEOS	-	Tetraethyl orthosilicate
TGA-DTA	-	Thermogravimetric analysis with differential thermal gravimetry
TPR	-	Temperature programmed reduction
WGS	-	Water gas shift
wt.%	-	Weight percentage
XPS	-	X-ray photoelectron spectroscopy

Appendix 2 - H_2-TPR profile for the CS support material.

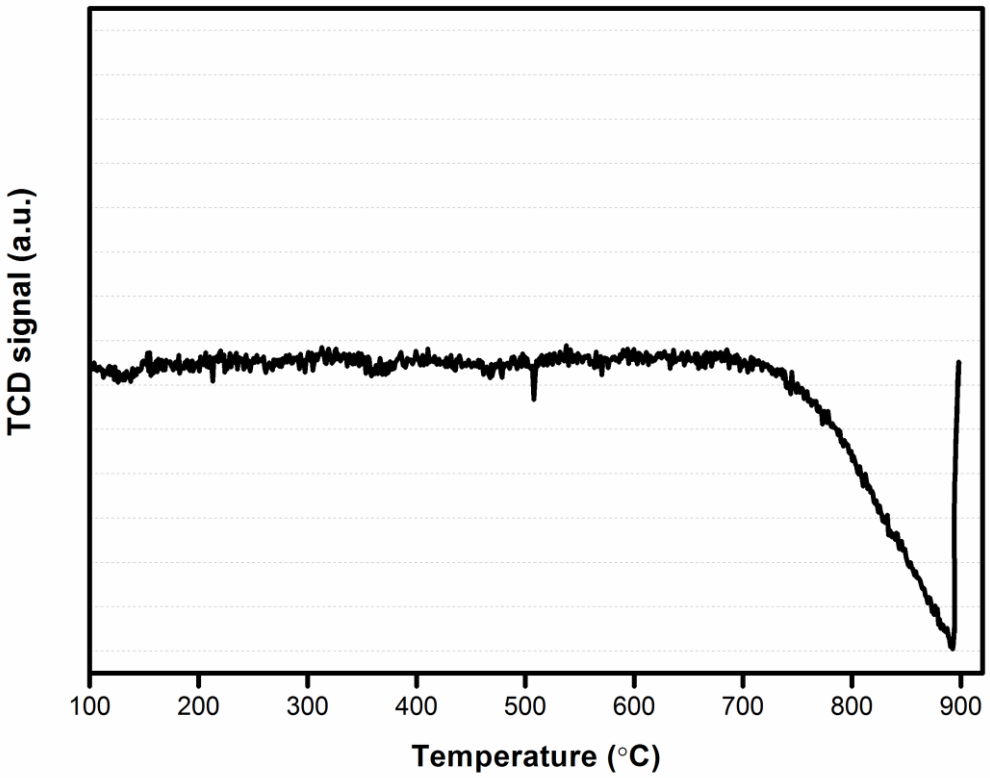

Figure S1 – H_2-TPR profile of the HCSs support sample. This profile illustrates that the negative peak observed at higher temperatures (methanation signal) was due to the carbon supports.

Appendix 3 – A summary of FT performance data of all the studied catalysts.

Catalyst	Temp. [°C]	CO conversion [%]	Hydrocarbon selectivity [%]			
			C_1	C_2-C_4	C_{5+}	CO_2
10Co/CSs	220	29	13	9	78	0
	250	51	23	8	69	6
0.5Fe-9.5Co/CSs	220	32	17	6	77	0
	250	60	22	10	68	10
2Fe-8Co/CSs	220	21	8	5	87	0
	250	29	18	10	72	15
5Fe-5Co/CSs	220	24	11	9	80	0
	250	29	17	9	74	8
9.5Fe-0.5Co/CSs	220	24	18	11	71	11
	250	33	19	13	68	17
10Fe/CSs	220	25	18	12	70	9
	250	36	19	14	68	20
10Co/HCSs	220	26	13	8	79	0
	250	33	23	30	47	0
10Co/N-HCSs$_{600}$	220	30	19	18	63	0
	250	36	22	19	60	0
10Co/N-HCSs$_{900}$	220	34	16	9	76	0
	250	48	26	21	53	0
10Co/SCSs$_{RF}$	220	16	19	7	74	0
	250	23	27	26	48	0
10Co/HCSs	220	22	13	7	81	0
	250	30	21	14	65	0
10Fe/SCSs$_{RF}$	250	20	15	23	62	17
	275	26	21	20	59	23
10Fe/HCSs	250	26	12	14	74	21
	275	38	13	16	71	26